Smart Sensors, Measurement and Instrumentation 28

Masoud Ghandehari

Optical Phenomenology and Applications

Health Monitoring for Infrastructure Materials and the Environment

Springer

Smart Sensors, Measurement and Instrumentation

Volume 28

Series editor

Subhas Chandra Mukhopadhyay, Beecroft, NSW, Australia

More information about this series at http://www.springer.com/series/10617

Masoud Ghandehari

Optical Phenomenology and Applications

Health Monitoring for Infrastructure Materials and the Environment

Springer

Masoud Ghandehari
New York University
Six Metrotech Center
Brooklyn, NY
USA

ISSN 2194-8402 ISSN 2194-8410 (electronic)
Smart Sensors, Measurement and Instrumentation
ISBN 978-3-319-70714-3 ISBN 978-3-319-70715-0 (eBook)
https://doi.org/10.1007/978-3-319-70715-0

Library of Congress Control Number: 2017958829

Printed on acid-free paper

This Springer imprint is published by the registered company Springer International Publishing AG part of Springer Nature
The registered company address is: Gewerbestrasse 11, 6330 Cham, Switzerland

Acknowledgements

There are many individuals I would like to acknowledge for their role in making this book possible. Foremost among them are Prof. Surendra Shah and Prof. Sridhar Krishnaswamy who led me on this path some years ago. No less deserving of mention are my students, co-authors and research colleagues, without whom this work would not have been possible. They are too numerous to name them all here, but there are a few who stand out for a special mention. Christian Vimer, Alexey Sidelev, Engui Lui and Filip Mlekicki spent many tireless hours producing the experimental methods and results in this book. Special mention must be made of the contributions of my co-authors Christian Brückner, Gamal Khalil, and Peter Spellane, who elevated the field of optical sensing with their exceptional work in chemical sensing. This cross disciplinary work is an example of how certain engineering challenges can be addressed. I would also like to recognize special collaborations with my co-authors Karina Gin, Hao-Ming Fang, Bavigadda Viswanath, Mircea Petre in Singapore, with my colleagues from NYU Mohsen Hossein and Dino Kostarelos, for their work in environmental engineering, and Weihua Jin for his exceptional work in material sciences for sustainability, as well as my other colleagues at NYU who have served as mentors over the year. Thanks to Frederica Rossi, Anna Laura Pisello and Marco Ferrero, Yilmaz Akkaya and Ioannou Ioannis for their excellent work in the field of building energy and materials. Numerous undergrad and high school students have made major contributions, including Narrisa Puran, now a physician and Shijie Zheng, now a University faculty, both who studied hard and delivered quality work. I also want to thank those who generously tutored me when I was a student, including Liu-Sheng Wang at Northwestern University. My editor, Amy Stinchcombe, deserves very special acknowledgment for her skill and attention in producing this book. Over the years this research has benefitted from the strong financial backing of government, academic and industry research grants and contracts; the NSF, NIH, DOE, DOT, New York State, New York University, as well as Consolidated Edison, National Grid, all have been generous in their support of advancing engineering science.

January 2018 Masoud Ghandehari

Contents

About the Author

Masoud Ghandehari is Associate Professor of Urban Systems Engineering at New York University. His research, teaching and outreach are focused on the application of advanced instrumentation and data analysis. Through the application of sensing, and modeling, he is developing methodologies that generate multi-scale data on the physical, environmental and human systems. He works on topics ranging from developing the taxonomy for those systems to platform integration. This work is resulting in novel approaches for understanding the condition, inter-dependencies, and health of cities and urban inhabitants. He believes in cross disciplinary collaboration to produce creative solutions for complex problems; and he is interested in partnership with the industry and government agencies, with the aim of generating insights to inform policy and security.

Part I
Concepts and Tools for Optical Sensing in Materials

Chapter 1
Optical Phenomenology for Materials Health Monitoring

Masoud Ghandehari

Abstract Advances in photonics has led to remarkable growth in the development of optical sensors and components. These developments, combined with recent advances in optical materials, have helped convert bench-top-style optical instruments into compact sensors and sensor systems. These technologies are likely to have a significant impact on the quantitative analysis of the environment enabling deeper insights into materials performance in service. Ultimately, this will lead to better scheduling of infrastructure remediation and repair cycles, as well as the identification and quantification of species of concern in the environment, with potentially significant benefits to population health. It is expected that the applications of advanced optical diagnostics to phenomenology across the domains of infrastructure and environment will address knowledge gaps in both theory and practice.

1.1 Introduction

Monitoring existing conditions and predicting the serviceability and future condition of infrastructure and the environment addresses key objectives of safety, health and cost. For example, with a thorough understanding of materials in service, safety can be improved through advanced materials design and by optimizing maintenance and remediation programs. The costs of maintaining the aging infrastructure is high and replacement cost of degraded structures is even higher (George 2016; Parfomak 2013; Laursen et al. 2007; Jackson 2017; NACE Intl. 2002; ASCE 2009; DOT 2016). Reliable tools for the diagnosis and prognosis of the health and service life of the civil infrastructure and its environs are essential for safety and cost effective infrastructure health maintenance (Minsker et al. 2015; Hutchison et al. 2012; Böhni 2005; Alsubaie et al. 2016). This argument can be applied across systems for predictive maintenance of the total environment, including transportation, sanita-

M. Ghandehari (✉)
New York University, Six Metrotech Center, Brooklyn, NY 11201, USA
e-mail: masoud@nyu.edu

M. Ghandehari, *Optical Phenomenology and Applications*,
Smart Sensors, Measurement and Instrumentation 28,
https://doi.org/10.1007/978-3-319-70715-0_1

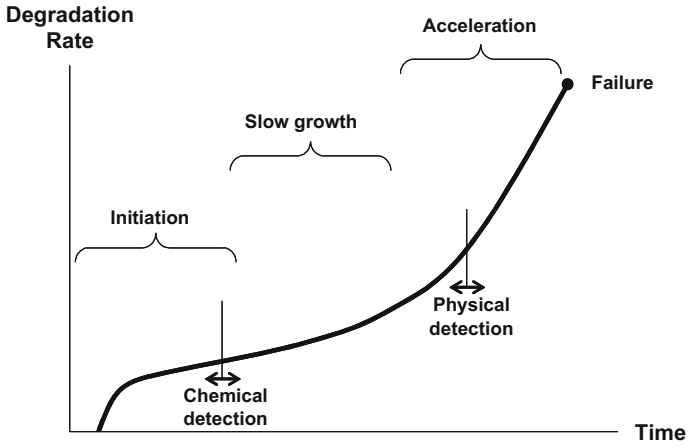

Fig. 1.1 Typical stages of materials degradation such as metal corrosion

tion, waste disposal, water resources, utilities and the environment within which they are situated (Zimmerman 2004; Mostafavi et al. 2014; D'Agostino et al. 2010).

The focus of this book is on the material level of this system and the developments in the application of optical methods for evaluation of materials damage and detection of chemical species relevant to civil and environmental science and engineering (Burgess 1992; Wolfbeis 2005; Wang and Wolfbeis 2014, 2013; Torres-Luque et al. 2014; Montemor et al. 2006; Higazy et al. 1994). These include species that catalyze aging, such as moisture, oxygen and extreme pH levels; those that are symptoms or byproducts of such aging, such as dissolved ions arising from metal dissolution; as well as the species that are a result of subsurface physical failures, such as leaks of hydrocarbons or waste products from sanitation and waste-storage facilities and pipelines.

Degradation processes in materials are often catalyzed by, or accompanied by chemical reactions (Bentur et al. 1997; Czarnecki and Woyciechowski 2013; Malvar et al. 2002). Therefore, direct monitoring of these processes, in advance of the emergence of the corresponding physical damage, is an effective means of enhancing infrastructure serviceability (Fig. 1.1). Complementing existing knowledge of materials performance, which is based on historical patterns and theoretical principles, real time, in situ or remote analysis of the chemical and physical states of materials with optical sensors can be instrumental in improving health management practices for the infrastructure and environment.

Synergetic Developments in Photonics

Applications of photonics to spectrometry have resulted in remarkable developments in the life sciences. For example, fluorescent microscopy has been used with exquisite sensitivity and selectivity to reveal the diffusion and localization of

intracellular substances through cell membranes. Bringing the sensor to the sample has led to applications in areas that were not possible before such as chemical sensing probes for in situ analysis and remote imaging of living tissue, blood oxygen, calcium, and gastric fluid, etc. Modern chemical sensor technology has moved from the experimental stage to real world applications, and is on the verge of taking a leap from the lab to the field. The development of these devices represents a new opportunity for civil infrastructure health monitoring.

Optical sensor technology, characterized by its versatility and potential for miniaturization, has been assisted by advances in fiber-optics and imaging. This has helped convert bench-top style optical instruments into compact optical sensors and sensor systems (Wolfbeis 2000). The availability of low-cost components such as light sources and detectors, is leading to widespread field implementation of such devices as portable hand-held spectrometers. These advances offer a promising future for materials health monitoring. (Wolfbeis 2000; Seitz and Sepaniak 1988; Norris 1989; Lakowicz 2010; Elster et al. 1999; Ge et al. 1993; Feng 1994).

While tools developed for pharmacy and biology provide useful models, they are not directly applicable to civil applications. Emphasizing durability requirements, it is expected that the content presented in this book will be an asset to the evaluation, monitoring and health of the materials, infrastructure and the environment in the way that remote chemical analysis and surgical endoscopies have been for the medical profession. The work presented is expected to serve applications in the laboratory and the field. In the remainder of this chapter, we will present a description of the fundamental science of optical phenomenology for civil and environmental applications as well as case studies. In all case studies the reader will be directed to the chapter or chapters where more in depth information can be found.

1.2 Optical Sensing

1.2.1 Transduction Strategies

We focus on the applications of optical methods for materials diagnostics, ranging from Ultraviolet through Infrared (Fig. 1.2). In all cases, the methods presented will involve transduction of electromagnetic radiation either by optical waveguides or by imaging systems. Chapter 2 will provide some detail on the application of optical fibers for in situ sensing, and Chap. 3 will discuss opportunities in imaging systems for remote sensing.

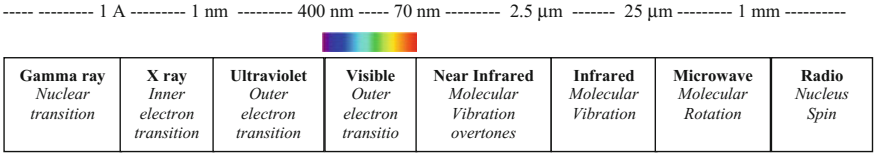

Fig. 1.2 The electromagnetic spectrum and wave length assignments

1.2.2 Recognition Strategies

Regardless of the transduction strategy, sampling of the target environment is carried out either by inherent properties of the target as it interacts with electromagnetic radiation, or it is mediated using an indicator specifically applied to the sensor that is responsive to the target species. Chapter 2 provides further detail on these molecular probes.

1.2.2.1 Direct Recognition of Matter Based on Intrinsic Electromagnetic Properties

In contrast to chemical sensing using customized indicators (such Litmus for pH or antibodies for bacteria), the intrinsic properties of materials can also be used for its identification, practically applicable to all wavelengths, where the energy is selectively absorbed according to the material property. There are also cases where there is intrinsic fluorescence. In this book we present applications where the intrinsic optical properties of materials detected in wavelengths ranging from Ultraviolet to Infrared are used. For example, the intrinsic fluorescence of microbial contaminants in water in the Ultraviolet and Visible wavelengths is described, and the selective absorption of Infrared wavelengths are used for detection of airborne gases. The intrinsic sensing can be carried out at a point or along a distance, using optical fibers or imaging. Many of these approaches have been in practice for some time, in some form, for example Infrared (molecular-vibration) spectroscopy has been a classic analytical tool for the characterization of organic compounds (Barton 2003; Settle 1997; Siesler 2006; Martin 2002; Poupard et al. 2004; Baumann et al. 2000; Milori et al. 2005; Wlodarczyk et al. 1987).

Molecular vibration spectroscopy: Vibration spectroscopy by Infrared analysis is based on the principle that each material is a unique combination of atoms producing a unique 'signature', and that two compounds don't produce exactly the same Infrared signature. Therefore, Infrared spectroscopy can result in qualitative identification of numerous materials. For example, water is a nonlinear polyatomic molecule; here, nonlinear refers to the non-collinear bonds of the hydrogen atoms to the oxygen atom. The inserted diagrams in Fig. 1.3 show the fundamental modes of vibration of the water molecule. In such structures, the number of vibration degrees of freedom is given by $3N-6$, where N is the number of atoms. However, the absorption of Mid-Infrared (wavelength greater than 2500 nm) radiation by water however, is often too strong for typical in situ applications using optical fibers. The Near-Infrared region of the electromagnetic spectrum (750–2500 nm) which contains "echoes" of the fundamental Mid-Infrared vibrations, offers signal levels suitable for most engineering applications. Additionally, this wave length range is efficiently handled by most compact spectrometers and waveguides.

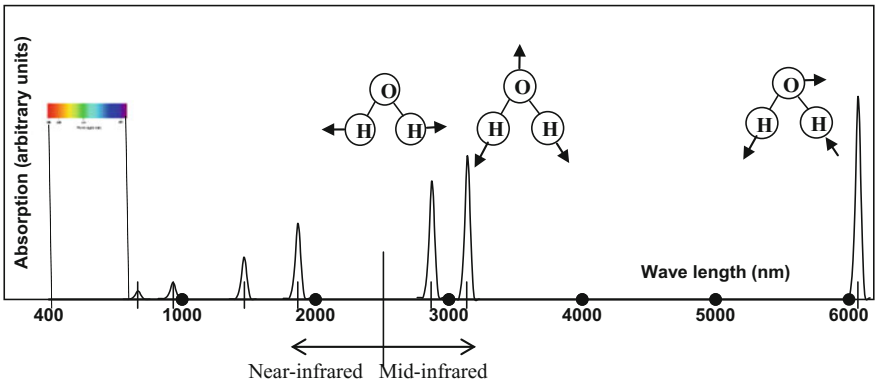

Fig. 1.3 Fundamental modes of vibrations of the water molecule and respective strength in the Mid-Infrared and Near-Infrared region of the electromagnetic spectrum

Sensing Moisture

Moisture and chlorides continue to be one of the critical conditions effecting the built environment. Moisture detection is relevant to the durability of most engineering materials. For example, the duration and distribution of moisture in concrete pores has a great deal of influence on shrinkage, creep, thermal conductivity, hydration rate and the long-term durability of cementitious materials. Water also carries with it chemical species, such as chlorides, that lead to accelerated corrosion of the steel in reinforced concrete. Sensing moisture also has important applications for subsurface water resource monitoring.

Near-Infrared (NIR) spectroscopy is a powerful tool for remote analysis of aqueous species (Grant et al. 1989; Siesler 2006; Zhang et al. 2015). Strong NIR absorption bands of water are located at 1930–1940 nm ($\nu_2 + \nu_3$ combination), 1430–1440 nm ($\nu_1 + \nu_3$), 975–985 nm ($2\nu_1 + \nu_3$) and 740–750 nm ($3\nu_1 + \nu_3$). Figure 1.3 shows a schematic of the fundamental modes and the overtone in the Near and Mid-Infrared region of the EM spectra. Figure 1.4 shows experiments using the NIR spectroscopy for sensing the desorption of water from a cement mortar sample during drying. The Near-Infrared absorption spectra of water in cement paste, centered at 1947 nm, are shown in Fig. 1.4. The shift in absorption peak from the theoretical 1928 nm for pure water to 1947 shown in the figure, is due to the ionic species present in the hydrated cement pore solution. The decrease of absorption intensity shown in the figure indicates decreasing moisture content by desorption. The moisture concentrations shown were first measured by collecting a reference spectrum at the fully saturated conditions, followed by scans during the drying process up to 24 h. Chapter 8 provides an extended view of how this approach can be used for measuring transport of liquid phase moisture in cement based materials. Chapter 9 highlights the application to ground water.

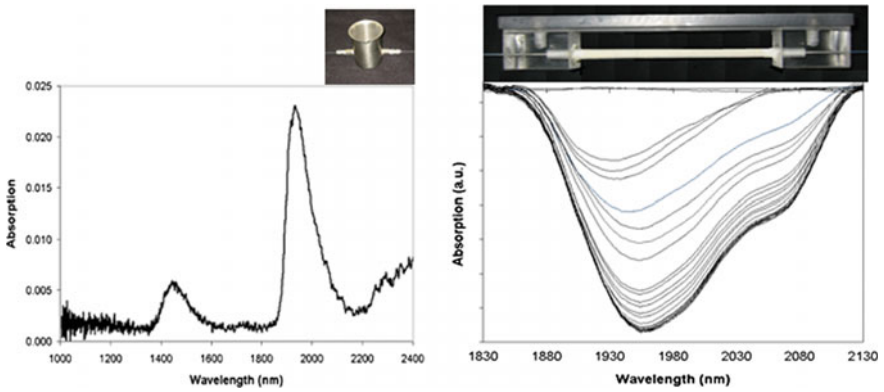

Fig. 1.4 (Left) Absorption spectra of water showing first two overtones schematized in Fig. 1.3. The spectra measured through fiber evanescent field with 10 cm length of fiber with porous cladding in water. (Right) Fiber embedded in cement paste, cured and saturated. Results show desorption of moisture during 24 h of drying. Specimen dimensions 5 mm diameter and 100 mm long, w/c = 0.5

Water has the ability to break down other substances such as sodium chloride (NaCl) (Fig. 1.5). In water, the ionic bonds of a sodium chloride molecule are broken easily because of the competitive action of the numerous water molecules, the process stops at the solubility limit of the salt. Inorganic ions such as chlorides are known to affect the IR spectrum of the water in which they are dissolved. These compounds, commonly known as "structure breaking reagents," can cause measurable modifications to the absorption bands of water by perturbing its molecular structure. One reason for these modifications is how this process effects the hydrogen bonds in the water "polymer." (The use of the term "polymer" here refers to the dynamic collection of individual water molecules joined together by hydrogen bonds). Sodium and calcium chlorides are among the strongest structure-breaking reagents, a quality which is used for de-icing agents. Previous works in literature report use of NIR spectroscopy in determining the NaCl concentrations (Grant et al. 1989; Siesler 2006).

The effect of salts on the hydrogen bond of water is measurable and can be used for quantitative analysis of the chloride content. Figure 1.6 shows the sensitivity of this measurement to chloride concentrations from 0.5 to 6%. Chapter 7 provides a complete description of tests on the measurement of chlorides, high alkalinity and temperature using the intrinsic absorption properties of water.

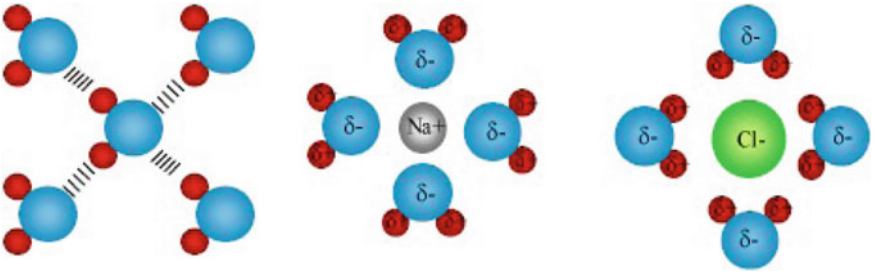

Fig. 1.5 (Left) water molecule and hydrogen bonds, (Right) effect of dissolution of NaCl on hydrogen bonds

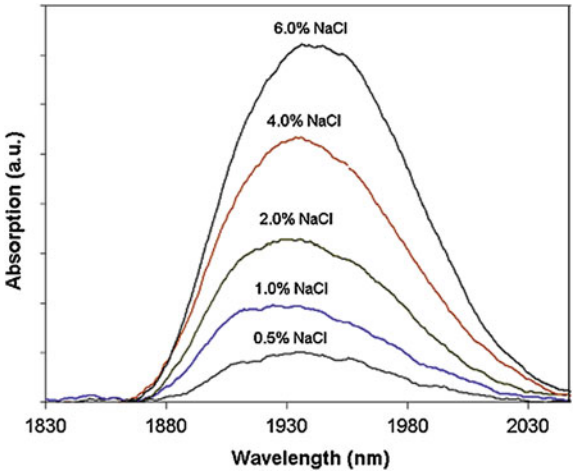

Fig. 1.6 NIR spectra of sodium chloride solution showing effect of NaCl concentration. Measurements taken by fiber in solution over a sensing length of 10 cm

Sensing Liquid Hydrocarbons

Organic compounds also exhibit distinct Mid-Infrared and Near-Infrared absorption signatures. As in water, overtones of the Mid-Infrared modes of vibration of organic compounds appear in the higher energy Near-Infrared region. The NIR absorption spectrum of methanol (CH_4O), for example, is shown in Fig. 1.7. For methanol, the main CH overtone occurs at wave length 2300 nm with higher order overtones at 1740 and 2100 nm. Similar signals are also available for gas phase hydrocarbons but much weaker. Results shown in Fig. 1.7 were obtained using an optical fiber with silica core where the polymer cladding was replaced with a lipophilic polymeric cladding over a 7 cm length. Chapter 12 provides details on how this approach can be used for applications to the subsurface/soil environment.

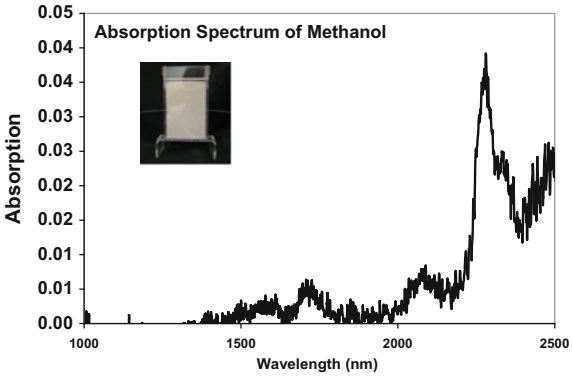

Fig. 1.7 Near-Infrared absorption of Methanol transduced along 7 cm fiber length

Gas Plume and Surface Temperature Imaging

Figure 1.3 shows the fundamental modes of molecular vibration (in the Mid-Infrared region) are stronger than the overtones that take place in the Near-Infrared regions. However, in the case of in situ monitoring applications, optical fibers attenuate the Mid-Infrared energy significantly, hence the use of Near-Infrared overtones occuring at wavelengths that can be guided through optical fibers, for liquid phase detection.

In open air sensing applications the longer wavelengths and stronger signals present an opportunity for gas sensing where the concentrations are lower. This presents opportunities for field spectroscopy to be utilized in the field in a fashion similar to what has been practiced in the laboratory. When carried out with imaging, this can result in full field imaging of surface temperatures (Sidelev and Ghandehari 2017) and for applications to imaging spectroscopy for gas plume detection (Ghandehari et al. 2017) as shown in Fig. 1.8. The imaging spectroscopy was carried out with a hyperspectral camera 7.6–13.4 μm spectral range which corresponded to the peak IR emissions for temperatures between 220 and 380 K and many gaseous compounds; the example of Freon is shown in Fig. 1.8.

Performance Evaluation of Protective Coatings

Thermal energy results in the emission of electromagnetic radiation, with emission spectra that is temperature dependent. In ambient temperatures, this radiation is in the Infrared region of EM radiation, not visible by eye. Infrared thermography is the practice of the measurement of Infrared radiation for mapping surface temperatures. The surface temperature may, for variety of applications, include mapping energy fluxes in buildings as shown in Fig 1.8 or mapping subsurface defects as shown in Fig. 1.9. Unlike the hyperspectral camera referred to in the gas plume imaging example given, cameras used for conventional thermography are broad band. This means that they register and integrate the intensity of a range of Infrared energy

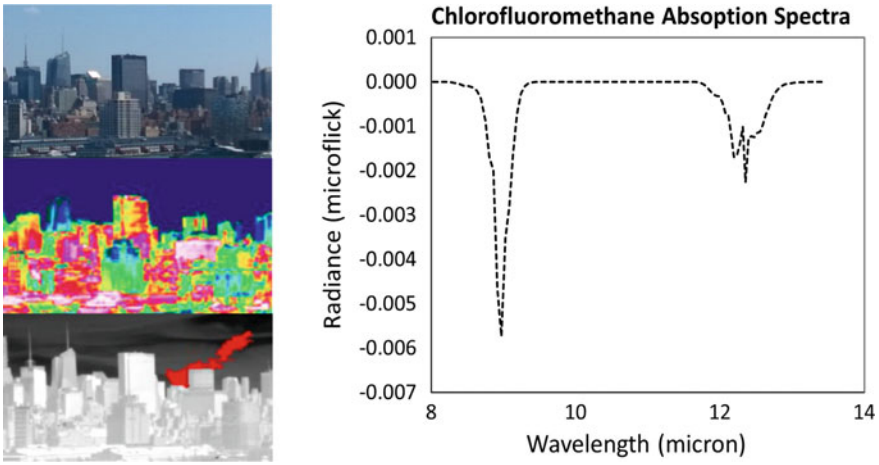

Fig. 1.8 Infrared imaging spectroscopy for identification of fugitive gases, (Left from Top to Bottom) visible image, pseudo color image of infrared radiance at 10 μm, post processed hyperspectral image of Freon gas plume. (Right) Absorption spectra of Freon detected

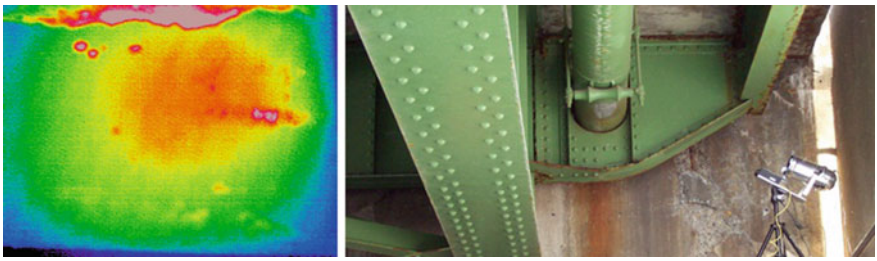

Fig. 1.9 Broad band Infrared imaging of defect identification under coatings

without discriminating the wavelength. The camera used in Fig. 1.9 registered energy at all wavelengths from 8 to 13 μm.

Mapping Interiors of Solid Bodies

Computerized axial tomography known as CT scan is known for its applications to medical and material sciences. It is a technique by which the internal structure of object be reconstructed in three dimensions using an X-ray beam that rotates around the object. In a similar way that the absorption of Near-Infrared energy is used for sensing moisture, transmission (or absorption) of X-rays through the object maps its density distribution (Liu et al. 2015; Sarida et al. 2016). The composite of many slices (each made of many line scans) forms a three-dimensional model of the object. Figure 1.10 shows image of one slice through a mortar sample.

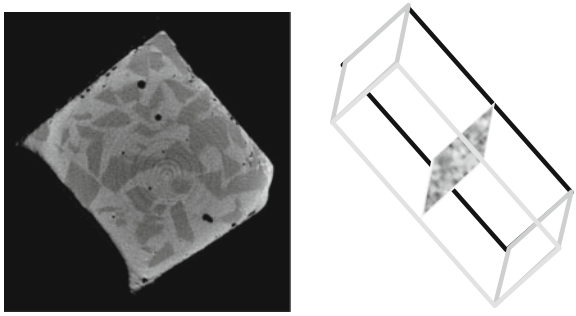

Fig. 1.10 CT scan of a slice within a piece of mortar

1.2.3 Indirect (Indicator-Based) Recognition

Here, indicators (or sensor molecules) are synthesized and used to detect the target species. The indicators are brought into contact with the target analyte, either on the surface for full field imaging or integrated with optical-fiber sensors for remote in situ sensing. The idea is to use the optical activity of the sensor molecule to indicate the presence or the concentration of target chemical species (Lakowicz 2010). In general, indicators either change color (by absorption) or emit light (by fluorescence). A classic example of an indicator is litmus, which changes color as a function of pH level. In general, the color change of a substance arises from changes to the orbiting electron structure of the atoms making up that substance. In sensing, such "electron shifts" are caused by the interaction of the indicator and the analyte. Some examples of this approach, which is often called electronic spectroscopy, are shown in the following experimental results for detection of gas leaks and products of metal corrosion.

Sensing of Gases in the Subsurface Environment

The strategy demonstrated here takes advantage of a well-developed technique for measuring oxygen concentration (Khalil et al. 1989; Sweet et al. 2002). The utility of oxygen measurement for gas leak detection is based on the concept that the environment surrounding a gas pipeline normally contains a constant or slowly fluctuating amount of oxygen. In the event of a gas leak, the oxygen concentration in the vicinity of the leak suddenly and noticeably decreases through displacement of oxygen by the gaseous organic compound.

The approach involves synthesis of an oxygen sensor compound that is integrated with an optical fiber. Optical fibers, in this application, provide the utility for subsurface distributed sensing of leaks. Further details on the mechanism of signal transduction to and through the optical fiber is given in Chap. 2. The fiber fabrication involves synthesizing an oxygen-sensitive molecule within the fiber cladding. The cladding is composed of oxygen-permeable (hydrophobic) membrane containing the luminescent *platinum porphyrin* as the sensor molecule (Khalil 2004). Porphyrins are macro cyclic organic molecules—several of which play key roles in energy conversion processes such as photosynthesis and oxygen transport in blood. Porphyrin compounds are well-suited for extended use as chemical sensors, with properties that include:

- Long-term stability: Chemical stability is an inherent property of aromatic compounds.
- Favorable optical properties: Strong optical absorption and emission is provided by the electronic structures of these compounds.
- Ready preparation: While many porphyrins are commercially available, these compounds are readily prepared and can be modified, allowing "tuning" of chemical or optical properties.

The laboratory leak-detection simulation was carried out using a 12 mm diameter methane gas pipe equipped with a leak valve. The optical fiber was installed along the pipe in a chamber that was filled with sand. Leak detection tests were then carried out in both dry and saturated conditions. Results of tests simulating localized leak events are shown in Fig. 1.11.

Measurements were done by illuminating the embedded sensor compound fiber with a 2000 Hz pulsed 400 nm wave length light emitting diode. The fluorescence signal is transmitted through the fiber and measured by a fast detector for emission duration measurement. When the leak valve is turned on, the corresponding

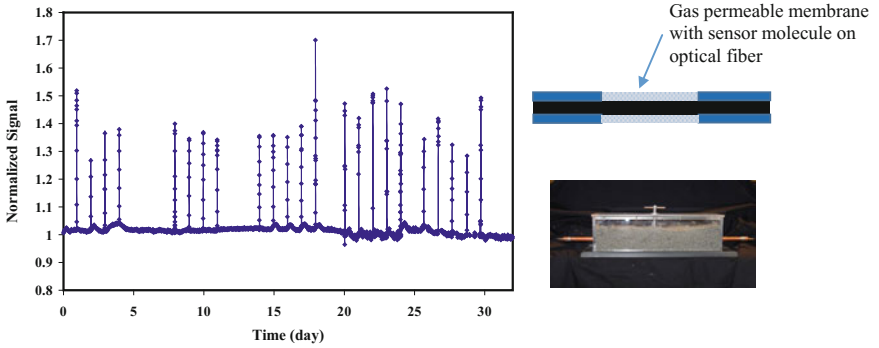

Fig. 1.11 (Right) 1 mm diameter fiber sensor with gas permeable cladding, runs along the embedded gas pipe, also shown, gas leak valve, (Left) Response of the fiber optic oxygen sensor used for methane gas leak detection, monitoring daily induced leak events over one month (except weekends and holidays). The life time emission signal increases with decreasing oxygen level

reduction of oxygen concentration leads to the increased emission of the oxygen sensor molecule. In this case the emission is a phosphorescent red light (650 nm wave length). A detailed description of basic principles and experimental procedures are described in Chap. 13.

Sensing of OH Ions for Application to Hydrated Materials Such as Concrete

There are number of applications where highly caustic environments need to monitored, for example, mapping the distribution of concentration of OH ions in concrete. Cement based materials like concrete have high alkaline pore fluids (approximately pH 13). pH plays a key role in the properties of both fresh and hardened concrete. Therefore, the measurement of internal pH levels is essential for the design, health assessment, and remedial measures of concrete structures.

Classically, distribution of pH level on concrete surfaces is detected with Phenolphthalein as the pH indicator. This indicator is used to distinguish if areas of pH are either above or below pH 10. In a typical test, a phenolphthalein solution is sprayed onto a fractured surface of concrete materials. If the pH is above pH 10, the surface will have a magenta color, and when the pH falls below 10, it becomes colorless, indicating carbonation of the cement (Fig. 1.12). New approaches have been introduced for mapping pH levels between pH 11 and pH 13.5. Chapter 6 describes the development of the sensor molecules, and Chap. 16 describes the application.

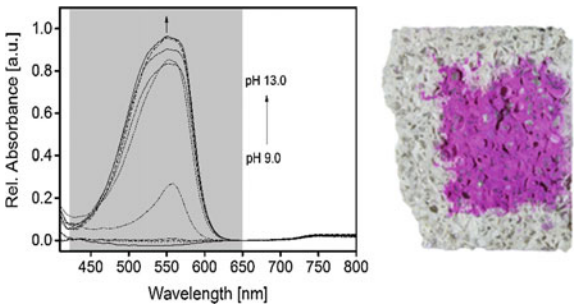

Fig. 1.12 (Right) color change of phenolphthalein on a 2" x 2" cross section of concrete after fracture, showing central areas with pH level higher than pH 10 (in magenta) versus areas lower than pH 10, (Left) corresponding absorption spectra of the phenolphthalein for high and low pH concrete

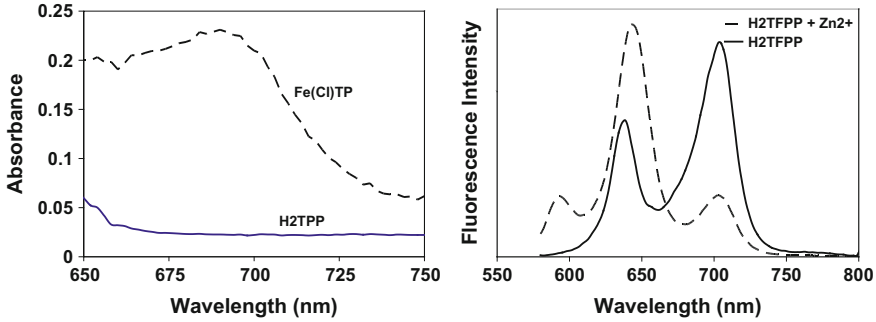

Fig. 1.13 (Left) Absorption spectra of tetraphenylporpyrin (TPP), before and after exposure to iron chloride at room temperature. The life time emission signal increases with decreasing oxygen level. (Right) Fluorescence emission spectra of free-base porphyrin (H2TFPP) before and after adding zinc chloride at room temperature

Sensing of Metal Ions for Measurement of Dissolution by Corrosion

Technologies currently available for detection of corrosion often rely on the corrosion of the probe itself. Nonetheless, there are opportunities in sensing the products of oxidation. Porphyrin molecules form complexes with a number of metals, such as iron and zinc (Fig. 1.13). These indicators can be used for the detection of dissolution of the base metal structure such as steel, as well as for galvanized coatings such as zinc. We have relied on the vast knowledge available on porphyrin chemistry (Gouterman et al. 1989; Khalil 2004; Gouterman et al. 2004) to support our goal of developing metal corrosion sensors.

Both iron and steel undergo an electrochemical process in the presence of water and oxygen. Rust is a mixture of iron oxide mixtures such as FeO, Fe_2O_3, Fe_3O_4 and Fe (OH), (Bentur et al. 1997). The absorption properties of metal porphyrin complexes depend on the particular metal, its oxidation state, and electronic structure. Chelation of porphyrins with iron ions produces a number of iron porphyrin complexes with distinct absorption spectra (Kadish et al. 2000). For example, the absorption spectrum of ferric iron complexed with tetraphenylporphyrin (TPP) has well-defined absorption bands that can be used as a diagnostic tool (for further detail see Chap. 21, Fig. 21.2).

In applications where a metal is covered by zinc or zinc-rich coatings, zinc porphyrins can be used to directly monitor the dissolution of zinc. In contrast to iron porphyrins, zinc porphyrins are fluorescent. The optical fiber adapted for this use would be made with cladding that incorporates free-based tetraphenylporphyrin. As the local chemistry changes and dissolution products of zinc metal reach the fiber, optical spectroscopy along the fiber indicates formation of a zinc porphyrin complex. This is accomplished as the product of newly formed Zn^{2+} cations migrate into the cladding and form ZnTFPP. The result is a fluorescence shift accompanied by a red (640 nm) fluorescence band (Chap. 21, Fig. 21.3).

1.3 Conclusion

The development of optical fiber chemical-sensor technologies represent new opportunities for research in civil infrastructure and environmental health monitoring. It is expected that these technologies will provide assets to the civil engineering community in the way that optical fibers have for endoscopy and remote chemical analysis in medicine or full field imaging in the material sciences and astronomy. In the following chapters we will demonstrate applications of in situ and remote sensing for monitoring the infrastructure and the environment. The objective in the forthcoming chapters is demonstration of the technology and tools for information based infrastructure asset management. In all cases optical metrology is shown to serve as a powerful tool for sampling the environment, its physical state and its chemical composition.

References

Alsubaie, A., Alutaibi, K., & Marti, J. (2016). Resilience assessment of interdependent critical infrastructure. In *10th International Conference on Critical Information Infrastructures Security, CRITIS 2015, October 5, 2015–October 7, 2015* (pp. 43–55). Berlin: Springer.

ASCE. (2009). *2009 Report Card for America's Infrastructure*. America's Infrastructure Advisory Council, ASCE.

Barton, F. (2003). Theory and principles of near infrared spectroscopy. *Spectroscopy Europe, (March)* (pp. 4–6).

Baumann, T., Haaszio, S., & Niessner, R. (2000). Applications of a laser-induced fluorescence spectroscopy sensor in aquatic systems. *Water Research, 34*(4), 1318–1326.

Bentur, A., Diamond, S., & Berke, N. (1997). *Steel corrosion in concrete: Fundamentals and civil engineering practice.* Taylor & Francis.

Böhni, H. (2005). *Corrosion in reinforced concrete structures*. Cambridge: Woodhead Publishing.

Burgess, L. W. (1992). Optical waveguides for chemical sensing. In *22nd International Conference on Environmental Systems, July 13, 1992–July 16, 1992.* SAE International.

Czarnecki, L., & Woyciechowski, P. (2013). Prediction of the reinforced concrete structure durability under the risk of carbonation and chloride aggression. *Bulletin of the Polish Academy of Sciences: Technical Sciences, 61*(1), 173–181.

D'agostino, G., Bologna, S., Fioriti, V., Casalicchio, E., Brasca, L., & Ciapessoni, E. (2010). Methodologies for interdependency assessment. In *5th International Conference on Critical Infrastructure, September 20–22, 2010* (pp. 1–7). Institute of Electrical and Electronics Engineers.

DOT. (2016). *Protecting our infrastructure of pipelines and enhancing safety act of 2016.*

Elster, J. L., Greene, J. A., Jones, M. E., Bailey, T. A., Lenahan, S. M., Velander, W. H., et al. (1999, February). Optical-fiber-based chemical sensors for detection of corrosion precursors and by-products.

Feng, M. Q. (1994). An optical fiber sensor for measurement of dynamic structural response. *Journal of Intelligent Material Systems and Structures, 5*(6), 847–853.

Ge, Z., Brown, C. W., Sun, L., & Yang, S. C. (1993). Fiber-optic pH sensor based on evanescent wave absorption spectroscopy. *Analytical Chemistry, 65*(17), 2335–2338.

George, S. (2016-last update, April). Pipeline safety bill puts new focus on aging gas infrastructure. Available: EDF http://blogs.edf.org/energyexchange/2016/04/01/pipeline-safety-bill-puts-new-focus-on-aging-gas-infrastructure/, February 2017.

Ghandehari, M., Aghamohamadnia, M., Dobler, G., Karpf, A., Buckland, K., Qian, J., & Koonin, S. (2017). Mapping refrigerant gases in the New York City Skyline. *NATURE Scientific Report.*

Gouterman, M., Callis, J., Dalton, L., Khalil, G., Mébarki, Y., Cooper, K. R., et al. (2004). Dual luminophor pressure-sensitive paint: III. Application to automotive model testing. *Measurement Science & Technology, 15*(10), 1986–1994.

Gouterman, M., Hall, R. J., Khalil, G. E., Martin, P. C., Shankland, E. G., & Cerny, R. L. (1989). Tetrakis (pentafluorophenyl) porpholactone. *Journal of the American Chemical Society, 111* (10), 3702–3707.

Grant, A., Davies, A. M. C., & Bilverstone, T. (1989). Simultaneous determination of sodium hydroxide, sodium carbonate and sodium chloride concentrations in aqueous solutions by near-infrared spectrometry. *Analyst, 114*(7), 819–822.

Higazy, M., de Vries, M. J., Abdel-Ghaffar, A. M., Claus, R. O., Masri, S. F., & Agbabian, M. S. (1994). Experimental study of embedded fiber-optic strain gauges in concrete structures. *Journal of Engineering Mechanics, 120*(8), 1696–1717.

Hutchison, D., Kanade, T., & Kittler, J. (2012). *Critical infrastructure protection: Information infrastructure models, analysis, and defense*. Berlin/Heidelberg: Springer.

Jackson, D. (2017-last update). Cost of corrosion annually in the US Over $1.1 Trillion in 2016. Available: www.g2mtlabs.com/corrosion/cost-of-corrosion/.

Kadish, K., Smith, K., & Guilard, R., (Eds.). (2000). *The porphyrin handbook.* Elsevier.

Khalil, G. (2004). Dual-luminophor pressure-sensitive paint I. Ratio of reference to sensor giving a small temperature dependency. *Sensors and Actuators B: Chemical, 97*(1), 13–21.

Khalil, G. E., Gouterman, M. P., & Green, E. (1989). *Method for measuring oxygen concentration.* Google Patents.

Lakowicz, J. R. (2010). *Principles of fluorescence spectroscopy* (3th ed., corr. at 4. print). New York, NY: Springer.

Laursen, P., Mergelas, B., Passaro, P., & Atherton, D. (2007). Inline assessment of transmission pipelines in the oil and gas and water sectors. *Pipelines*, 1–7.

Liu, G., Zhang, P., Xile, Y., & Aibin, M. (2015). In situ monitoring of early cement hydration by X-ray computed tomography. *Materials Research Innovations, 19,* 776–778.

Malvar, L. J., Cline, G. D., Rollings, R., Sherman, T. W., Greene, J., & Burke, D. (2002). Alkali-Silica reaction mitigation: State of the art and recommendations. *Materials Journal, 99* (5), 480–489.

Martin, P. A. (2002). Near-infrared diode laser spectroscopy in chemical process and environmental air monitoring. *Chemical Society Reviews, 31*(4), 21.

Milori, D., Galeti, H., Martin-Neto, L., Dieckow, J., Gonzalez-Perez, M., Bayer, C., et al. (2005). Organic matter study of whole soil samples using laser-induced fluorescence spectroscopy. *Soil Science Society of America Journal, 70*(1), 57.

Minsker, B., Baldwin, L., Crittenden, J., Kabbes, K., Karamouz, M., Lansey, K., et al. (2015). Progress and recommendations for advancing performance-based sustainable and resilient infrastructure design. *Journal of Water Resources Planning and Management, 141*(12).

Montemor, M. F., Alves, J. H., Simoes, A. M., Fernandes, J. C. S., Lourenco, Z., Costa, A. J. S., et al. (2006). Multiprobe chloride sensor for in situ monitoring of reinforced concrete structures. *Cement & Concrete Composites, 28*(3), 233–236.

Mostafavi, A., Abraham, D., & Delaurentis, D. (2014). Ex-ante policy analysis in civil infrastructure systems. *Journal of Computing in Civil Engineering, 28*(5).

NACE Intl., FHWA, Koch, G. H., & CC Technology Laboratories. (2002). *Corrosion cost and preventive strategies in the United States.* Turner-Fairbank Highway Research Center.

Norris, J. (1989). Current status and prospects for the use of optical fibres in chemical analysis. *A review. Analyst, 114*(11), 1359–1372.

Parfomak, P. W. (2013). *Keeping America's pipelines safe and secure: Key issues for congress.* Federation of American Scientists.

Poupard, O., Aït-Mokhtar, A., & Dumargue, P. (2004). Corrosion by chlorides in reinforced concrete: Determination of chloride concentration threshold by impedance spectroscopy. *Cement and Concrete Research, 34*(6), 991–1000.

Sarida, S., Helvaciolu-Yiit, D., Ozcan, M., Avcu, E., & Kizilta, G. (2016). Micro-computerized tomography analysis of cement voids and pull-out strength of glass fiber posts luted with self-adhesive and glass-ionomer cements in the root canal. *Journal of Adhesion Science and Technology, 30*(14), 1585–1595.

Seitz, W. R., & Sepaniak, M. J. (1988). Chemical sensors based on immobilized indicators and fiber optics. *C R C Critical Reviews in Analytical Chemistry, 19*(2), 135–173.

Settle, F. (1997). *Handbook of instrumental techniques for analytical chemistry*. Englewood Cliffs: Yourdon Press.

Sidelev, A., & Ghandehari, M. (2017). Quantitative assessment of subsurface oxidation in coated materials. *Journal of Performance of Constructed Facilities, 31*(5).

Siesler, H. W. (2006). *Near infrared spectroscopy.* (1th ed., 3. repr. edn). Weinheim: Wiley-VCH.

Sweet, I. R., Khalil, G., Wallen, A. R., Steedman, M., Schenkman, K. A., Reems, J. A., et al. (2002). Continuous measurement of oxygen consumption by pancreatic islets. *Diabetes Technology & Therapeutics, 4*(5), 661–672.

Torres-Luque, M., Bastidas-Arteaga, E., Schoefs, F., Sanchez-Silva, M., & Osma, J. F. (2014). Non-destructive methods for measuring chloride ingress into concrete: State-of-the-art and future challenges. *Construction and Building Materials, 68,* 68–81.

Wang, X., & Wolfbeis, O. S. (2013). Fiber-optic chemical sensors and biosensors (2008–2012). *Analytical Chemistry, 85*(2), 487.

Wang, X., & Wolfbeis, O. S. (2014). Optical methods for sensing and imaging oxygen: Materials, spectroscopies and applications. *Chemical Society Reviews, 43*(10), 3666–3761.

Wlodarczyk, M. T., Vickers, D. J., & Kozaitis, S. P. (1987). Evanescent field spectroscopy with optical fibers for chemical sensing. *Cambridge Symposium Fiber/LASE 1986, 18–26 AUGUST 1986, SPIE.* (pp. 192–197).

Wolfbeis, O. (2000). Fiber-optic chemical sensors and biosensors. *Analytical Chemistry, 72*(12), 81.

Wolfbeis, O. S. (2005). Materials for fluorescence-based optical chemical sensors. *Journal of Materials Chemistry, 15*(27–28), 2657–2669.

Zhang, B., Chen, J., & Jiao, M. (2015). Determination of chloride salt solution by NIR spectroscopy. *Guang Pu Xue Yu Guang Pu Fen Xi/Spectroscopy and Spectral Analysis, 35*(7), 1840–1843.

Zimmerman, R. (2004). Decision-making and the vulnerability of interdependent critical infrastructure. In *2004 IEEE International Conference on Systems, Man and Cybernetics, SMC 2004, October 10, 2004–October 13, 2004* (pp. 4059–4063). Institute of Electrical and Electronics Engineers Inc.

Chapter 2
Optical Waveguides

Masoud Ghandehari

Abstract Optical-fiber sensors have two distinct roles in sensing. Firstly, they enable the registration of opto-mechanical and opto-chemical interactions under investigation. The second role is to serve as a channel of communication for remote sensing. This is particularly useful in subsurface or hazardous environments. Optical fibers can efficiently transmit light in wavelengths ranging from the higher range of Ultraviolet radiation to Near-Infrared wavelengths. Developments in optical waveguides and components in microelectronics and communications, such as those utilized in long-distance communication or short distance applications for vehicles and local area networks, have also led to advances in research and development for the sensing community. When combined with advances made in molecular probes for analytical chemistry and biology, optical waveguides have made significant contributions to sensing in both the physical and chemical domains.

2.1 Introduction

Phenomenology of physical and chemical processes in materials using electromagnetic (EM) energy can be distinguished by analyzing the interaction of EM energy and the target analyte. Strategies for *recognition* of a target analyte involve the interpretation of either the intrinsic optical response of the materials or the optical response of sensor molecules that are used as indicators. Additionally, there are differences in the *transduction* strategies, which is how the signal is obtained or recorded. Chapter 1 provides examples of *recognition strategies*; followed by numerous examples in the book for intrinsic sensing for detection of moisture, liquid hydrocarbons, and dissolved chlorides, as well as extrinsic sensing for detection of pH, dissolved oxygen and metal ions. In all cases there are two broad categories for transduction, one using optical waveguides, and other by full field

M. Ghandehari (✉)
New York University, Six Metrotech Center, Brooklyn, NY 11201, USA
e-mail: masoud@nyu.edu

M. Ghandehari, *Optical Phenomenology and Applications*,
Smart Sensors, Measurement and Instrumentation 28,
https://doi.org/10.1007/978-3-319-70715-0_2

imaging. This Chapter introduces optical waveguides, specifically optical fibers, as used in the application domains described in this book.

2.1.1 Optical Waveguides

Optical waveguides have become the information highways of the high speed communication where digitally coded information is transmitted by light pulses through wave guides, including optical fibers (Fresi et al. 2017; Kanno 2017). In telecommunication the fiber cables are made so they are minimally influenced by the external environment. However, in sensing applications the fiber and its components are altered so the transmitted light is modulated, either by the physical or the chemical environment it encounters (Hassanzadeh et al. 2014; Yuan et al. 2004; Kumari et al. 2014; Dai et al. 2010; Stephens et al. 2010; Fernando et al. 2002; Willsch et al. 2011; Sabri et al. 2013).

Optical fibers are conventionally made with a core and cladding with lower refractive index. This index difference confines the propagating light within the fiber core by "total internal reflection" (Burgess 1992). More recently, hollow core or hollow cladding and photonic crystal fibers are manufactured (Yinian et al. 2002). Figure 2.1 (left) shows a side profile of a conventional 600 micron silica core diameter fiber where a portion of the polymeric cladding and jacket is removed. A schematic of the cross section of that fiber is shown in Fig. 2.1 (center), Fiber core materials are typically glass, but can also be polymeric in short distance applications. The cladding materials can also be either glass or polymer depending on the required travel distance. These fibers transmit Visible and Near-Infrared light with some difference in transmissivity depending on the geometrical and materials specification, features that need to be considered in both telecom and sensing applications. For example, in the case of polymeric cladding fibers, low OH cladding materials are suitable for Near-Infrared sensing while high OH cladding materials have better transmission for high UV and low Visible range sensing. Hollow core fibers are used for short distance sensing Mid-Infrared application and

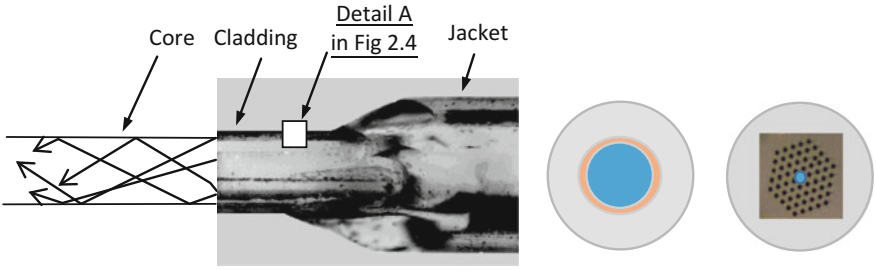

Fig. 2.1 Optical wave guides, (Left and Center) conventional optical fiber, (Right) Photonic Crystal Fiber

photonic crystal fibers (Fig. 2.1, Right) are used for communication and sensing applications.

2.2 Sensing of Physical Parameters

Common applications in sensing physical parameters such as strain are either based on interferometric principles or take advantage of selective scattering induced by periodic alternations to the refractive index of the fiber.

2.2.1 Interferometric Sensors

Interferometry typically involves use of two separate light signals from the same source in which a light beam is split and coupled into two separate fibers. One fiber is attached to a structure while the other is left free. In strain sensing for example, the length of the attached fiber will change, resulting in an increase on the transmitted optical path. The phase shift between the waves will lead to a periodic variation of light intensity, which, when re-combined correspond to the strain in the fiber attached to the structure (Udd and Spillman 2011; Ezekiel et al. 1982; Fernando et al. 2002).

Interferometric measurement is also used for a more compact sensor known as the Fabry-Perot sensor (Higazy et al. 1994; Habel and Hillemeier 1995; Habel and Hofmann 1994). The sensor is made by a capillary tube containing two cleaved optical fibers facing each other, with a small air gap between them. When light is launched into one of the fibers, a back-reflected interference signal is obtained from the reflections of the incoming light on the glass-to-air and air-to-glass interfaces, respectively. The resulting interference fringes are subsequently used to infer changes in the air gap spacing, and the corresponding strain (or displacement) (Fig. 2.2).

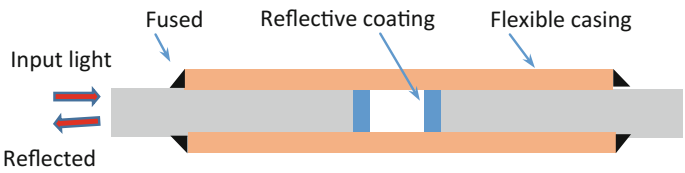

Fig. 2.2 Optical fiber Fabry-Perot sensor

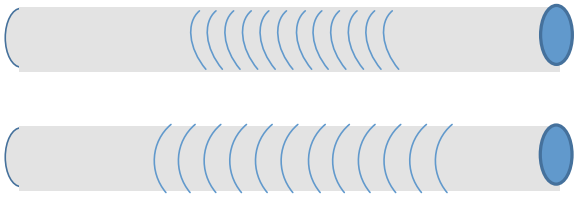

Fig. 2.3 Fiber Bragg grating etched on the fiber, shown when the fiber is stretched versus in original state

2.2.2 Fiber Bragg Gratings

A Bragg grating is a periodic variation of refractive index intentionally applied, commonly by holography, at some point along the length of the fiber where sensing is to take place (Hill et al. 1993; Meltz et al. 1989; Poumellec 1995). The working principle of the Bragg grating sensor is shown in Fig. 2.3. When a broadband or tunable signal passes through the optical fiber, the wavelength corresponding to the period of index variation will be preferentially reflected. Common applications of Bragg sensors are for strain or temperature sensing, where the resulting change in the spacing between the grating leads to a peak shift in the reflected wavelength. Chapter 15 demonstrates the application of long period Bragg grating on photonic crystal fiber for high sensitivity gas sensing.

2.3 Sensing of Chemical Parameters

Optical fibers can also be made to sample the chemical composition of the environment in which they are embedded (Qazi et al. 2012; Pospíšilová et al. 2015; Wang et al. 2014; Calcerrada et al. 2015). They can be functionalized with sensing compounds that are permeable for either gaseous or liquid/ionic species. The sensing compound may have embedded sensor molecules or simply host the analyte for intrinsic sensing.

Figure 2.4 shows schematic of the optical surface waves known as evanescent waves. This transduction mechanism, which resembles a distributed optical antenna, allows for sampling the environment in a distributed fashion along the fiber. The length of the sensing region in the evanescent field sensor is prescribed by the designer. For example, for better representation of concentrations of diffused species, the sensing length can be made on the order of the heterogeneity of the sample space. It can also be made sensitive at fiber tips for point sampling.

A cross-section of a typical custom-designed optical fiber is shown in Fig. 2.4. Light is guided through the core of the fiber by total internal reflection at the interface of the core with the cladding. The total internal reflection generates an extended electromagnetic field, otherwise known as the evanescent field, which penetrates the cladding and travels along the fiber just outside of the core/cladding interface.

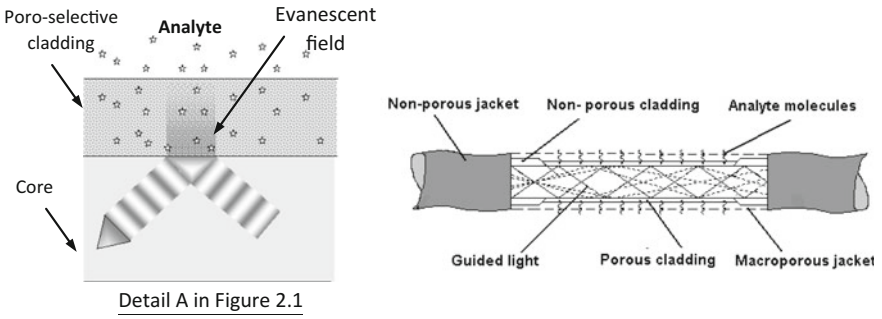

Fig. 2.4 The evanescent wave travels along the fiber cladding at the interface with the fiber core. This surface wave interacts with the analyte in the cladding pore space, and signals the presence of target species by corresponding signal modulations

Unlike the optical fibers used in telecommunications, where the evanescent fields does not interact with the external environment, the cladding can be modified in order to serve as a zone of interaction between the light and the analyte. In other words, the modified optical fibers are designed so the spectral features of the light traveling within the fiber are modulated by the media it encounters within a permeable cladding (Fig. 2.4) (Sequeira et al. 2016). The same sensor compound can also be applied to the distal end of the fiber as a point sensor.

2.3.1 Fiber Materials

Below are the choices among the commonly available fibers.

- **Single mode fibers** are not an option because the number of modes in the fiber is wavelength dependent, while our applications required scanning over a broad region of the electromagnetic spectrum.
- **Silica/silica fibers** (having silica core and silica cladding) have the lowest level of attenuation. However, in the case of evanescent field sensing, the silica cladding is relatively difficult to remove—chemical removal of cladding using hydrofluoric acid is possible, but poses some safety concerns. Moreover, the acid used for cladding removal may also damage the fiber core.
- **Plastic clad silica core (PCS)** fibers have higher attenuation compared to silica/silica fibers, but the polymer cladding can be easily removed mechanically. The excess cladding is subsequently dissolved using organic solvents such as acetone.
- **Polymer optical fibers (POF)** would be a good choice for a durable sensing probe (Sequeira et al. 2016). It should be noted however that their application will be limited to Visible and short NIR ranges. Recent developments are resulting in plastic optical fiber with NIR transmission up to 1500 nm. These include polymers such as Cytop™ (Asahi Glass Co., Ltd., Tokyo, Japan), Zeonex (Zeon Corporation, Tokyo, Japan).

2.3.2 Sensing Compound

Sensing compounds are used to serve as a mediator between the light traveling in the fiber and the external environment which is to be sampled. The gas or liquid permeable compound may contain sensor molecules or it may simply serve as the host for intrinsic sensing of the analyte. The compound may be placed at the fiber tip for point sensing (Fig. 2.5), or it may be a replacement cladding for evanescent field sensing. Fibers used in telecommunications are produced so that light inside the fiber cannot interact with the external environment. However, for chemical sensing, specialty porous cladding materials become the zone of interaction, where light is modulated by the media it encounters. The sensing compound should exhibit certain properties:

1. It should permeable to the target analyte, hydrophilic for ionic species, lipophilic for liquid hydrocarbons, or only gas permeable for gas sensing
2. Good ability to form films or good ability to be molded
3. Good adherence to the surface fiber substrate
4. Good optical transparency

Further discussion on the preparation of the sensing compounds are provided in various chapters targeting a range of sensing applications involving liquids or gases.

2.3.3 Detectors and Light Sources

For the Near-Infrared region of the spectrum the most widely used source is the tungsten-halogen lamp. The tungsten halogen lamps are large-area, incoherent, sources. i.e., there is no fixed-phase relationship between the photons emitted by the light source.

From the point of view of detection, the applications presented in this book are based either on measurement of absorption (Chaps. 6, 7, 8, 9 and 10) or fluorescence. In the latter case it is done either by the measurement of monotonic

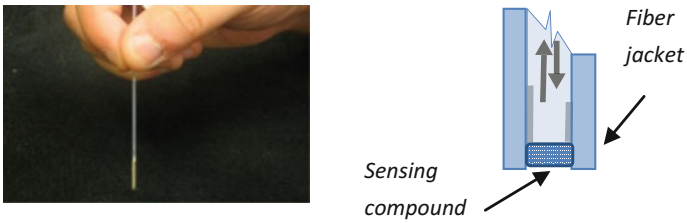

Fig. 2.5 (Left) Optical-fiber high-pH sensing probe, showing scale of probe. (Right) Schematic of probe showing fiber core, cladding, jacket, and sensing compound at tip

fluorescence intensity (Chap. 21), or fluorescence emission lifetime (Chap. 13). Intensity spectra can be done using bench type Fourier Transform spectrometers which are typically housed in large enclosures, smaller portable spectrometers (the size of a calculator) are also available. These units are grating-based and use linear array detectors. In contrast to sensing spectral intensities which are steady state measurements, measurement of fluorescence lifetime (duration), which typically takes place on the order of microseconds, requires fast broad band detectors. Chapter 13 covers the application of fluorescence lifetime measurement for sensing concentrations of dissolved oxygen.

2.4 Conclusion

Optical waveguides in sensing serve a unique role, both as host for sensor compounds and information carriers. Advances in long distance communication, and applications in local area networks, have led to advanced materials for optical sensing. This chapter highlights the mechanisms by which the sensing compound can be developed and integrated with optical fibers, either for sensing at one point or along the length of the optical fiber. Discussion on choices of the optical fiber material is given along with information on light sources and detectors.

References

Burgess, L. W. (1992). Optical waveguides for chemical sensing. In *22nd International Conference on Environmental Systems, July 13–16, 1992*. 1992, SAE International.

Calcerrada, M., Garcia-Ruiz, C., & Gonzalez-Herraez, M. (2015). Chemical and biochemical sensing applications of microstructured optical fiber-based systems. *Laser and Photonics Reviews, 9*(6), 604–627.

Dai, X., Mihailov, S. J., & Blanchetiere, C. (2010). Optical evanescent field waveguide Bragg grating pressure sensor. *Optical Engineering, 49*(2).

Ezekiel, S., & Arditty, H. J. (1982). Fiber-Optic Rotation Sensors and Related Technologies. *First International Conference MIT, Nov 9–11, 1981*.1982, Springer-Verlag.

Fernando, G. F., Webb, D. J., & Ferdinand, P. (2002). Optical-fiber sensors. *MRS Bulletin, 27*(5), 359–361.

Fresi, F., Imran, M., Malacarne, A., Meloni, G., Sorianello, V., Forestieri, E., et al. (2017). Advances in optical technologies and techniques for high capacity communications. *Journal of Optical Communications and Networking, 9*(4), C64.

Habel, W. R., & Hillemeier, B. (1995). Results in monitoring and assessment of damages in large steel and concrete structures by means of fiber optic sensors. *Smart Structures and Materials, 26 Feb–3 Mar, 1995*. 1995 SPIE.

Habel, W.R. & Hofmann, D. (1994). Strain measurements in reinforced concrete walls during the hydration reaction by means of embedded fibre interferometers. *Smart Structures and Materials: Second European Conference, 12–14 October, 1994*. 1994 SPIE.

Hassanzadeh, A., & Azami, D. (2014). Waveguide evanescent field fluorescence microscopy: Theoretical investigation of optical pressure on a cell. *Journal of Nanophotonics, 8*(1).

Higazy, M., de Vries, M. J., Abdel-Ghaffar, A. M., Claus, R. O., Masri, S. F., & Agbabian, M. S. (1994). Experimental study of embedded fiber-optic strain gauges in concrete structures. *Journal of Engineering Mechanics, 120*(8), 1696–1717.

Hill, K. O., Malo, B., Bilodeau, F., Johnson, D. C., & Albert, J. (1993). Bragg gratings fabricated in monomode photosensitive optical fiber by UV exposure through a phase mask. *Applied Physics Letters, 62*(10), 1035.

Kanno, A. (2017). Millimeter- and terahertz-wave over fiber technologies for high-speed communication and non-telecom applications. In *Photonics West OPTO Conference on Broadband Access Communication Technologies XI, January 31–February 1, 2017*. 2017, SPIE, Optical Instrumentation Engineers.

Kumari, B., Barh, A., Varshney, R. K., & Pal, B. P. (2014). Mid-IR evanescent field gas sensor based on silicon-on-nitride slot waveguide. In *12th International Conference on Fiber Optics and Photonics, Photonics, December 13–16, 2014*. 2014, Optical Society of America (OSA).

Meltz, G., Morey, W. W., & Glenn, W. H. (1989). Formation of Bragg gratings in optical fibers by a transverse holographic method. *Optics Letters, 14*(15), 823–825.

Pospíšilová, M., Kuncová, G., & Trögl, J. (2015). Fiber-optic chemical sensors and fiber-optic bio-sensors. *Sensors, 15*(10), 25208–25259.

Poumellec, B. (1995). UV induced densification during Bragg grating inscription in Ge: SiO_2 preforms: Interferometric microscopy investigations. *Optical Materials, 4*(2–3), 404–409.

Qazi, H. H., Mohammad, A. B. B., & Akram, M. (2012). Recent progress in optical chemical sensors. *Sensors, 12*(12), 16522–16556.

Sabri, N., Aljunid, S. A., Salim, M. S., Ahmad, R. B., & Kamaruddin, R. (2013). Toward optical sensors: Review and applications. In *2013 International Conference on Science and Engineering in Mathematics, Chemistry and Physics, SciTech, January 24–25, 2013*. 2013, Institute of Physics Publishing.

Sequeira, F., Bilro, L., Rudnitskaya, A., Pesavento, M., Zeni, L., & Cennamo, N. (2016). Optimization of an evanescent field sensor based on D-shaped plastic optical fiber for chemical and biochemical sensing. In *30th Eurosensors Conference, September 4–7, 2016.* 2016, Elsevier Ltd., pp. 810–813.

Stephens, M. D., Yuan, G., Lear, K. L., & Dandy, D. S. (2010). Optical and physical characterization of a local evanescent array coupled biosensor: Use of evanescent field perturbations for multianalyte sensing. *Sensors and Actuators, B: Chemical, 145*(2), 769–774.

Udd, E., & Spillman, W. B. (2011). *Fiber optic sensors: An introduction for engineers and scientists* (2nd ed.). Somerset: Wiley.

Wang, J., Wei, J., Yang, B., Gao, Z., Zhang, L., & Yang, X. (2014). The recent development of fiber-optic chemical sensor. *Guang Pu Xue Yu Guang Pu Fen Xi/Spectroscopy and Spectral Analysis, 34*(8), 2035–2039.

Willsch, R., Ecke, W., & Bartelt, H. (2011). Optical fiber sensor research and industry in Germany: Review and outlook. In *21st International Conference on Optical Fiber Sensors, May 15–19, 2011*. 2011, SPIE, Inc.; CMC Microsystems Corporation; Innovative Economy: National Strategic Reference Framework.

Yinian, Z., Chao, L., & Ping, S. (2002). Photonic crystal fibers and their applications in optical communications and sensors. *Optical Fiber and Planar Waveguide Technology II, October 16, 2002–October 18*, 2002, SPIE, pp. 37–42.

Yuan, G., Stephens, M. D., Dandy, D. S. and Lear, K. L. (2004). Novel local evanescent field detection waveguide multianalyte biosensor. In *Optical Information Systems II, August 4, 2004–August 5*, 2004, SPIE, pp. 140–146.

Chapter 3
Full Field Imaging

Masoud Ghandehari

Abstract Single snapshots or movies are common examples of full field imaging used to represent information across a field, at an instant or over time. Scientific imaging has taken advantage of this modality of data acquisition in order to map the properties of materials or processes in the environment. Examples include X-rays for mapping broken bones and MRI for detection of tumors, or radio assisted detection and ranging (RADAR) imaging for mapping cloud density and precipitation in the atmosphere. This chapter provides a brief introduction to the applications of imaging for materials and environmental health monitoring. Applications discussed include imaging the intrinsic properties of subject of study, such as detection of subsurface corrosion, versus applications involving sensor molecules for extrinsic sensing, such as mapping transport of OH ions in concrete.

3.1 Introduction

Chapter 1 introduced the principles of the interaction of electromagnetic radiation with physical and chemical processes in materials. Distinctions between recognition strategies and transduction strategies were made. Chapter 2 introduced the application of optical waveguides as a transduction option used for remote sensing, either at a point or along the length of the fiber. This chapter introduces and provides an overview of applications of full field imaging as an another transduction approach for remote sensing. Chapter 4 provides detailed discussion of indicators for extrinsic sensing, followed by numerous applications of full field imaging for intrinsic and extrinsic sensing through the book.

M. Ghandehari (✉)
New York University, Six Metrotech Center, Brooklyn, NY 11201, USA
e-mail: masoud@nyu.edu

M. Ghandehari, *Optical Phenomenology and Applications*,
Smart Sensors, Measurement and Instrumentation 28,
https://doi.org/10.1007/978-3-319-70715-0_3

3.1.1 Spectral Range and Resolution

The imaging of materials is commonly carried out in wavelengths ranging from X-ray to Infrared. Applications range from medical imaging of tissue to satellite imaging of the earth's surface and atmosphere. In some applications, useful information is obtained at specific wavelengths. This is often done by selecting a few wavelengths (multispectral), or by obtaining images at hundreds of wavelengths separately (hyperspectral imaging). On the other hand, in some cases energy from all wavelengths can be used, as in broad band imaging.

Figure 3.1 shows examples of applications of broadband and spectroscopic imaging taken from cases covered in this book. In most instances, a two dimensional array of detectors are used to record images. The exception is tomography which is achieved by rotating scans of a solid using beams of X-ray energy.

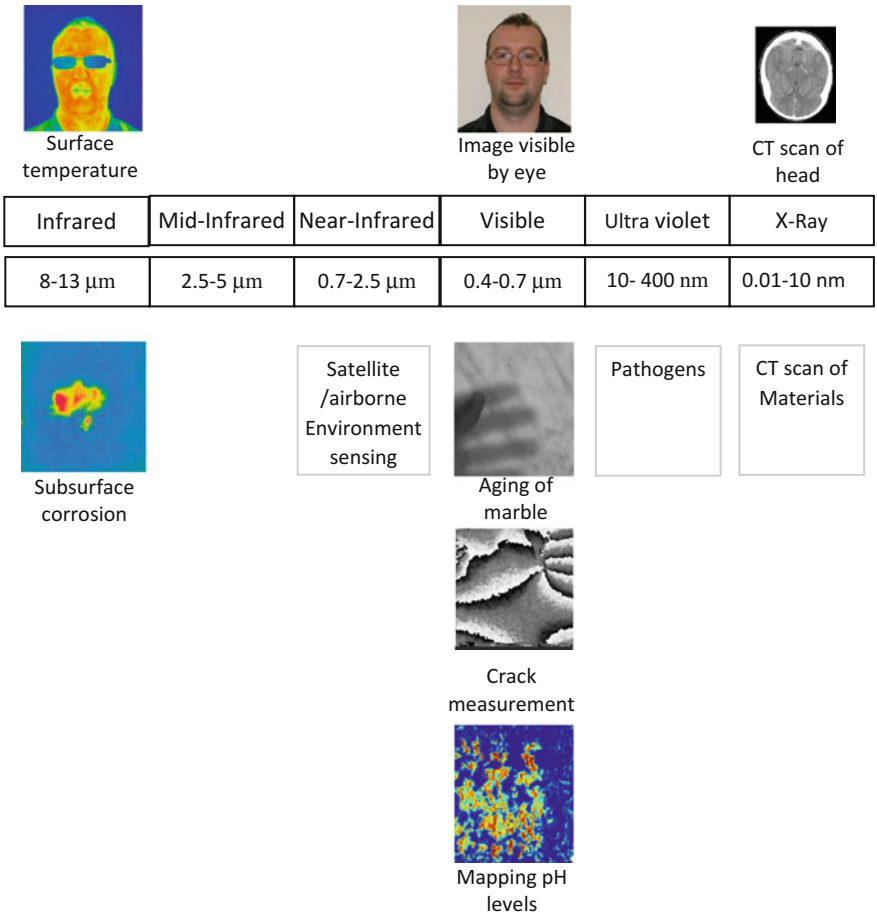

Fig. 3.1 Spectral range and resolution, and potential applications

Imaging of materials in the visible range is mostly done with cameras using silicon detectors. These sensors elements can also be treated and tuned for desired spectral response and sensitivity. For example, arsenic doped silica is sensitive to Long Infrared wavelengths, while doping materials can result in sensitivity to Ultraviolet radiation. Short Wave Near-Infrared, up to 1200 nm (SNIR) and Near-Infrared 1200–2500 are made of Indium Gallium Arsenide (InGaAs), while Mid-Infrared (MIR) detectors are made with Mercury Cadmium Telluride (MerCat). NIR, MIR, and IR detectors are more expensive, therefore those cameras are costlier than cameras with silicon based detectors and often provide lower resolution. Infrared cameras can also be measured with a 2D arrangement of micro scale temperature sensors known as micro bolometers. Chapter 20 demonstrates the application of thermal imaging using cameras with these detectors for subsurface corrosion monitoring.

3.1.2 Broad Band Imaging

Radiance (radiation intensity) is usually a function of the wavelength. For example, the image shown in Fig. 3.2, when seen in color, is a map of distribution of different colors (radiation in the visible wavelengths) the broad band version of the same image can be obtained by adding the intensity of all wavelengths at each pixel and presented in grey scale as shown on the left side of Fig. 3.2.

3.1.3 Multi or Hyperspectral Imaging

Often times, it is important to obtain spatial distribution of radiance at different wavelengths, particularly for chemical analysis. This is done either by multispectral cameras that will capture a few distinct wavelengths or in the case of hyperspectral cameras hundreds of wavelengths (Geladi and Grahn 2007; Herold et al. 2004; Bradley et al. 2011; Wu and Sun 2013; Dobler et al. 2015; Puckrin et al. 2009). The concept is shown in Fig. 3.3 demonstrating the application of hyperspectral imaging where the outskirts of Reno Nevada were imaged at 300 distinct bands ranging from 400 nm to 2400 nm. The grey scale on images shown in the figure represent the intensity of reflectance for a window of approximately 5 nm.

Fig. 3.2 Broad band imaging; grey (Left) versus panchromatic (Right, in a color image)

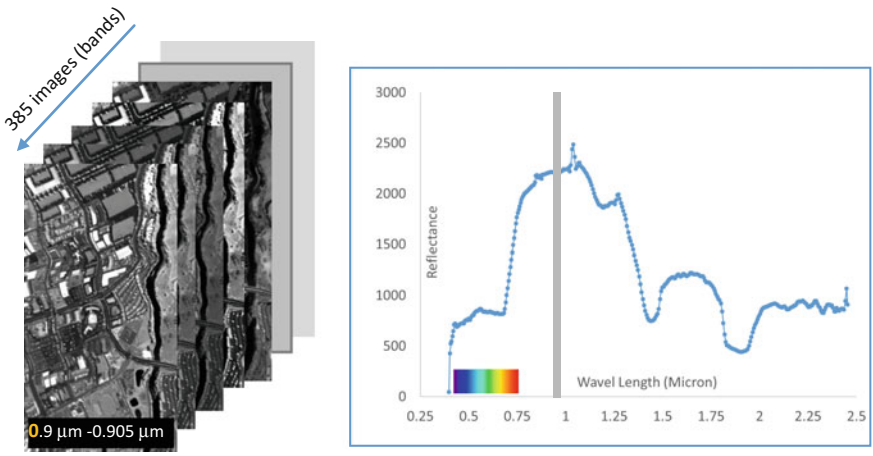

Fig. 3.3 (Left) Hyperspectral images of suburbs of Reno, Nevada, USA. (Right) spectrum of reflectance radiance, pointing to the visible range and the location of the Short Wave Near-Infrared 5 nm wide band image at 0.9 µm

3.2 Applications in Infrared Imaging

All bodies at temperatures above absolute zero (273 °K) emit energy (Fig. 3.4). This energy is strongly correlated to the surface temperature and surface properties, including emissivity (Çengel et al. 2007; Çengel et al. 1995). Infrared thermography is a non-contact technique where the surface temperature of an object is mapped either in broadband or in multi or hyperspectral mode (Fig. 3.5). The term

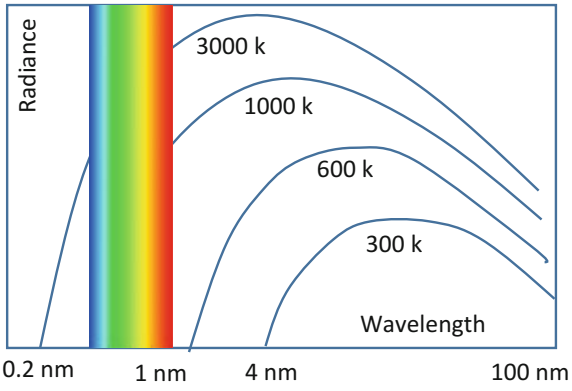

Fig. 3.4 Black body radiation as function of temperature, showing that ambient temperatures, 250–300 k are not visible by eye while super hot objects (greater than 1000 k) emit visible radiation

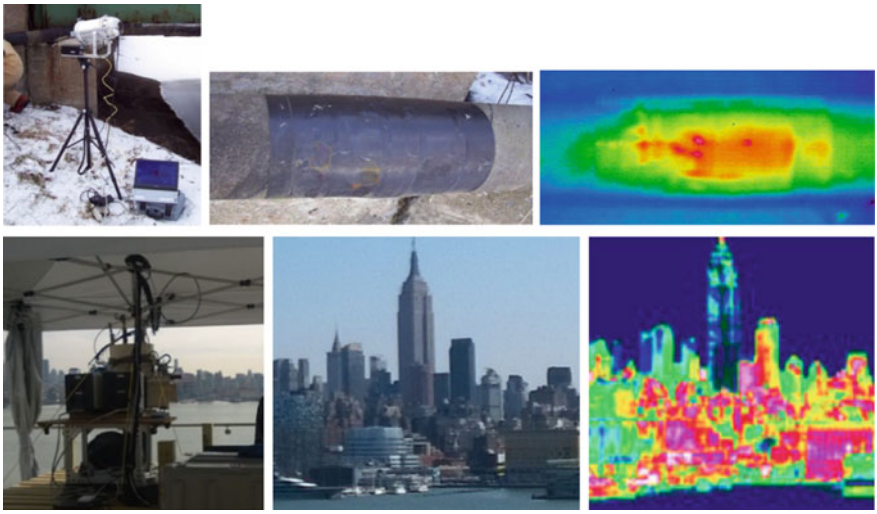

Fig. 3.5 Top (from Left to Right) broad band Infrared camera and head source used for active thermography, visible image, broad band (~8–13 μm thermal image). Bottom (from Left to Right) hyperspectral Infrared imager (~8–13 μm) at 0.04 μm spectral resolution, visible image, thermal image 1 at 11–11.04 μm. Notice the cool water and sky and warm building facades

thermography or thermal imaging is widely used for non-contact infrared thermal imaging (Maldague 2001; Hellier 2001). Surface temperature can be calculated using the measured radiance and surface emissivity. These are usually shown as a color coded (or gray scale) image or an isotherm plot.

Infrared cameras are devices that detect Infrared radiation mostly in Mid or Long Wave Infrared radiation, 3000–5000 nm for hotter temperature applications), and 8000–13,000 nm for ambient temperatures, respectively. Infrared camera detectors are either cooled or un-cooled sensors, where the cooled sensors provide superior sensitivity. Compared to visible cameras, Infrared cameras are costlier, mostly due to IR lenses and detector elements.

Thermal imaging can be done in a passive and active mode. The passive thermography takes advantage of naturally occurring spatial or temporal fluctuation of surface temperatures, while active thermography uses heat flow amplification techniques, where the surface is actively heated using an external heat source (Fig. 3.5). Active Infrared thermography techniques use pulses of heat of prescribed duration, designed as function of the features targeted for detection.

3.3 Applications of Imaging in the Visible Range

3.3.1 Selective Absorption

One of the most common mechanisms of sensing is selective absorption of electromagnetic radiation (EM), one that applies to literally the entire range of the EM radiation from X-ray to radar (Chap. 1, Fig. 1.2). When considering EM radiation in the visible range, we see objects according to the wavelengths not absorbed by the object. For example, we see an object as blue because it absorbs yellow and red. The absorption spectra of that object in the visible range (from 390 to 700 nm), would show broad peaks. The same occurs in non-visible wavelengths, such as the X-ray, which is absorbed by high density matter. This is why bones are distinguished. (Lee 2017). Chapter 16 show how absorption spectroscopy is used for mapping variations of high pH level on fractured surfaces of concrete. In that case band pass filters are used to collect a range of wavelengths in two different regions of the visible spectra (Khalil et al. 2010). The total intensity of measured radiance passing through these filters is then divided by each other as the parameter to relate to pH level (Fig. 3.6). Chapter 21 shows the application of a similar concept in absorption imaging for iron oxides.

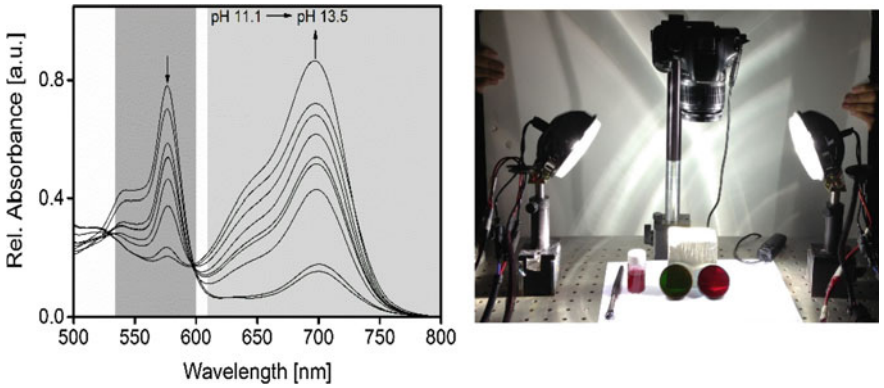

Fig. 3.6 Absorption spectroscopy for high pH imaging: (Left) change of the two absorption peaks of the sensor molecule as function of pH changing from pH 11 to pH 13.5. (Right) apparatus for ratiometric imaging, showing the concrete sample, two band-pass filters selected to match the two peaks, camera, and white light source

3.3.2 Imaging Fluorescence

Rather than using the absorption properties of materials, one can use the fluorescent properties of that material when available. For example, the intrinsic fluorescent characteristics of waterborne bacteria (Chap. 11), or the fluorescence of sensor molecules (flourophore) applied to the target (for extrinsic sensing). For fluorescence to take place, the flourophore needs to be excited by an electromagnetic input (Lavrova et al. 2014). Typically, fluorescence occurs at a wavelength higher than the excitation wavelength. A common example is the black-light poster. It is called black-light because the paint on the poster is excited by ultraviolet energy (425 nm, not visible to the human eye), which is present but not visible in the sky even at night. The fluorescence in black-light posters occurs at higher wavelengths (typically 450 nm), which corresponds to the color blue. Chapter 21 shows examples of fluorescent imaging for detection of metal oxides.

3.3.3 Interferometric Imaging

Rather than using spectroscopic properties of the material or indicators, there are number of approaches that take advantage of interference of coherent light (Ghandehari et al. 1999). An example is phase measurement speckle interferometry for mapping strain localization in brittle materials (Fig. 3.7). Chapters 17 and 18 provides further detail on the application of this approach for mapping crack propagation in concrete, including crack length and crack opening displacement.

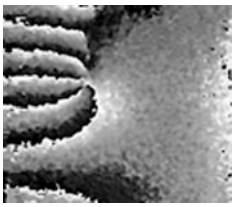

Fig. 3.7 Interference phase pattern, on surface of a 4″ × 4 cm concrete specimen during crack propagation showing crack tip. Each fringe corresponds to 45 μm lateral displacement. The calculated crack mouth opening displacement or this load stage is approximately 1.2 μm

3.4 Conclusion

Imaging technology for the analysis of physical and chemical properties and processes in materials was introduced, distinguishing the intrinsic and extrinsic optical properties. Applications include: mapping subsurface oxidation of metals under protective coatings by broad band imaging of infrared radiation, hyperspectral imaging of surface thermal radiation, multi spectral imaging of surface absorption in the visible range using sensor molecules for mapping high pH level in concrete, and mapping oxidation of metals by fluorescence imaging. Sections II through IV of this book will expand on imaging for materials health monitoring.

References

Bradley, E. S., Leifer, I., Roberts, D. A., Dennison, P., & Washburn, L. (2011). Detection of marine methane emissions with AVIRIS band ratios. *Geophysical Research Letters, 38*(10).

Carson, J. K., Lovatt, S. J., Tanner, D. J., & Cleland, A. C. (2005). Thermal conductivity bounds for isotropic, porous materials. *International Journal of Heat and Mass Transfer, 48*(11), 2150–2158.

Çengel, Y. A., & Boles, M. A. (1995). Thermodynamics: An engineering approach, second edition. *Applied Mechanics Reviews, 48*(5), pp. B66.

Çengel, Y. A., & Klein, S. A. (2007). Heat and mass transfer. 3rd edn. Boston [u.a.]: McGraw-Hill.

Dobler, G., Ghandehari, M., Koonin, S. E., Nazari, R., Patrinos, A., Sharma, M. S. et al. (2015). Dynamics of the urban lightscape. *Information Systems.*

Geladi, P., & Grahn, H. (2007). *Techniques and applications of hyperspectral image analysis*. Chichester: Wiley.

Ghandehari, M., Krishnaswamy, S., & Shah, S. (1999). Technique for evaluating kinematics between rebar and concrete. *Journal of Engineering Mechanics, 125*(2), 234–241.

Hellier, C. J. (2001). *Handbook of nondestructive evaluation.* New York [u.a.]: McGraw-Hill.

Herold, M., Roberts, D. A., Gardner, M. E., & Dennison, P. E. (2004). Spectrometry for urban area remote sensing—Development and analysis of a spectral library from 350 to 2400 nm. *Remote Sensing of Environment, 91*(3), 304–319.

Khalil, G. E., Daddario, P., Lau, K. S. F., Imtiaz, S., King, M., Gouterman, M., et al. (2010). Meso-Tetraarylporpholactones as high pH sensors. *The Analyst, 135*(8), 2125.

Lavrova, O. Y., Mityagina, M. I., & Bocharova, T. Y. (2014). Manifestation of ship wakes in satellite images in periods of intense algae bloom, 2014, *Baltic International Symposium, 27–29 May 2014, Tallinn, Estonia:* IEEE, 2014. pp. 1–6. (in print).

Lee, M. (2017). *X-ray diffraction for materials research* (1st ed.). Boca Raton: Apple Academic Press.

Maldague, X. P. V. (2001). *Theory and practice of infrared technology for nondestructive testing.* New York [u.a.]: Wiley.

Puckrin, E., Turcotte, C. S., Lahaie, P., Dubé, D., Lagueux, P., Farley, V., et al. (Sept, 2009). Airborne measurements in the infrared using FTIR-based imaging hyperspectral sensors. *Whispers 2009. August 26–28, 2009, Grenoble, France:* SPIE. (in print).

Vollmer, M., & Möllmann, K. (2010). *Infrared thermal imaging*. Weinheim: Wiley-VCH.

Wu, D., & Sun, D. (2013). Advanced applications of hyperspectral imaging technology for food quality and safety analysis and assessment: A review—Part I: Fundamentals. *Innovative Food Science & Emerging Technologies, 19,* 1–14.

Chapter 4
Molecular Probes

Gamal Khalil, Christian Brückner and Masoud Ghandehari

Abstract Molecular probes, also referred to as chemosensors, are molecules capable of transforming chemical information, such as the presence or concentration of a specific target species, into an analytically useful, identifiable signal. These signals are commonly either electrical or optical. This chapter is an introduction to molecular probes and the respective optical signatures used for chemical sensing. Features reviewed include the categories of chemo-optical response including absorbance or fluorescence, as well as methods for calibration.

4.1 Introduction

Early work in advanced chemical sensing was based on research in the medical field, built on the functioning of naturally occurring chemical receptors in the body. Well known examples include human senses such a taste or smell, which were used as models for the development of chemical sensor molecules. Also known as molecular probes, these innovations were used in applications ranging from measurement of blood oxygen to mapping the diffusion of ions into cell membranes.

Infrastructure and environmental sensing applications of chemosensors is relatively recent. Nevertheless, chemosensors have demonstrated potential in a wide variety of applications in materials health monitoring and environmental sensing. A chemosensor is a molecule capable of transforming chemical information—such

G. Khalil
Department of Aeronautics & Astronautics, University of Washington,
Box 352250, Seattle, WA 98195, USA
e-mail: gekhalil@gmail.com

C. Brückner
Department of Chemistry, University of Connecticut, Storrs, CT 06269, USA
e-mail: c.bruckner@uconn.edu

M. Ghandehari (✉)
New York University, Six Metrotech Center, Brooklyn, NY 11201, USA
e-mail: masoud@nyu.edu

M. Ghandehari, *Optical Phenomenology and Applications*,
Smart Sensors, Measurement and Instrumentation 28,
https://doi.org/10.1007/978-3-319-70715-0_4

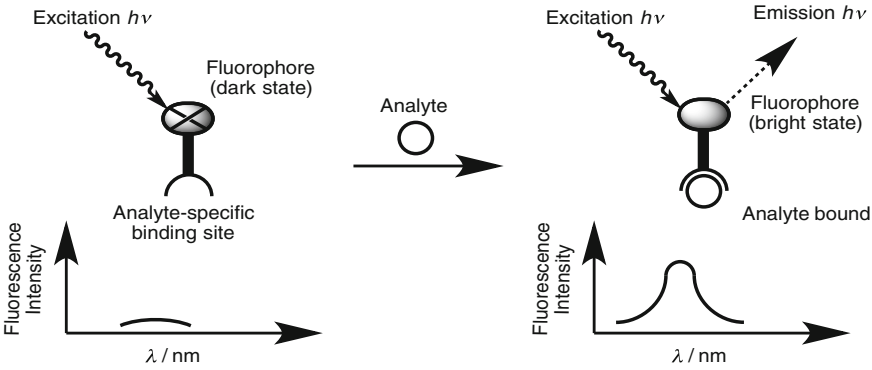

Fig. 4.1 Schematic representation of switch-on-type fluorescent molecular chemosensor. Adapted from (Lim et al. 2005)

as the concentration of a target specie—into an analytically useful signal (Czarnik 1994; Czarnik et al. 1999; McDonagh et al. 2008; Kutz 2012; Valeur and Leray 2000; Faizi et al. 2016). A chemosensor comprises a chemical recognition site, and a signal transduction domain that is triggered upon interaction with the analyte species (Fig. 4.1).

Returning to the example of chemoreceptors for taste, the area of tongue with taste buds are the receptors. There is also a signal transduction to the brain, which in this case is akin to an electric current. When the transduction is optical, the signal domain can be a chromophore (changing color) or a fluorophore (emitting light), both triggered by chemicals in the environment. The corresponding signal is registered by a photo-detector or a two dimensional array of detectors, forming an image. We will look at the different types of chemical probes and ways the signal is triggered; fluorescence versus absorption etc., followed by methods used to calibrate and measure the signal.

4.1.1 Triggering the Signal

When the chemical species or analyte binds with the receptor, a signal is triggered by the binding and how it can be used is multifold. In the case of a fluorophore, it can switch the fluorescence on or off, (Fig. 4.1). The change in the signal intensity can be measured, or the fluorophore can be excited and the emission duration (lifetime) can be measured. In the case of a chromophore it may result in shift in the color, typical in the UV-Visible spectrum. Switch on fluorophores are often (but not always) more selective, as they are related to a specific analyte recognition event rather than quenching which can take place by multiple components. An example of a switch on sensor can be found in freebase Porphyrin used for detecting Zinc ions (Chap. 21); an example of a switch off sensor is Platinum Porphyrin used for

accurate sensing of dissolved oxygen. Comparing fluorescence-based versus absorption sensor, the former is inherently more sensitive since the signal can be measured against darkness, which enables the detection of weak signals.

The specificity and sensitivity of the sensing action is primarily determined by the specificity and binding constant of the analyte with the binding site. Covalent and non-covalent interactions are equally suitable, as long as the formation of the analyte to chemosensor sites form reversibly at a time scale faster than the anticipated changes to analyte under investigation. Irreversible chemosensors can only record the presence or absence of an analyte, and perhaps the highest concentration encountered. But once triggered, they cannot record the absence of the analyte. Such irreversible sensors are being referred to as chemodosimeters (Kaur et al. 2012).

4.2 Ratiometric Measurement of Chemosensor Signals

In general, the preferred criteria for choosing suitable reference and sensor molecules are: photo-stability and brightness (extinction coefficient × emission quantum yield), similar excitation bandwidths combined with distinctly different emission wavelengths of the chemosensor and the reference, and similar formulation properties. In addition, the reference sensor molecule should possess minimal analyte dependency and be compensatory for the temperature dependency of the sensor molecule.

Three wavelengths are the minimum number of wavelengths required for both methods. More wavelengths can be used to potentially increase the accuracy by using the method of principal component decomposition (Jolliffe 2010). In fact, depending on the overlapping of emission and absorption, it may be necessary to use more wavelengths either, in excitation or in detection, to accurately determine the concentration of an analyte.

The signal from the chemosensor indicates the presence of the analyte. Nonetheless, the signal strength can only be directly related to a specific analyte concentration if some specific conditions are met. For example, in absorption-based measurement, these include: the condition that the chemosensor concentration is known, a calibration curve is determined, the opacity of the solution remains constant throughout the measurement, and no interfering chromophores are present. Similarly, the $\lambda_{emission}$ signal derived from a fluorescent chemosensor indicates the presence of an analyte, but a relative $\lambda_{emission}$ increase can reasonably be correlated with an increase of the analyte concentration only if the concentration of the sensor molecules remains constant; that is if the fluorescence quantum yield ϕ of the sensor remains unchanged upon analyte binding or in the presence of other solution components. However, these conditions are rarely met. For instance, the ϕ of most fluorophores is generally solvent-dependent, the concentration of the sensor may change through bleaching events, the light source intensity may fluctuate, and the medium to be probed may be non-homogenous. In fact, infrastructure health monitoring applications frequently deal with non-homogenous materials. Also, the

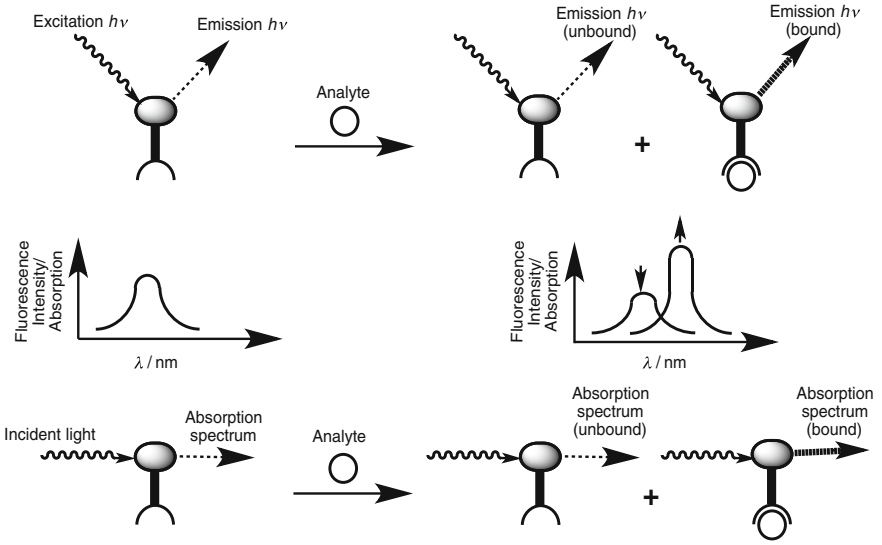

Fig. 4.2 Schematic representation of a ratiometric fluorescence (Top scheme) and ratiometric absorption spectrum-based (Bottom scheme) chemosensor. Adapted from Lim et al. (2005)

concentration of the chemosensor may vary as a function of the sensing layer thickness. These sorts of circumstances require a ratiometric sensor, the principle of which is depicted in Fig. 4.2. Further refined ratiometric measurement methods are detailed below.

The usefulness of a ratiometric measurement of chemical signals is that it is internally calibrated and the measurement of the analyte is independent of the concentration of sensor molecules. A fluorescent chemosensor responds upon binding to an analyte with a shift in its $\lambda_{max-emission}$ which may or may not be concomitant with an increase in $\lambda_{emission}$. Likewise, a UV-Vis-based probe shows a λ shift in its absorption spectrum upon binding (with or without a change in its extinction coefficients ε). An example for the application of a ratiometric absorption-based chemosensing method is presented in Chaps. 6 and 16. In either case, the λ_{max} shift should be large enough to clearly distinguish the λ_{max} of the co-existing analyte-free and analyte-bound versions of the sensor. Detecting both wavelengths will then allow the determination of the ratio of the $\lambda_{emission}$ of the analyte-free to analyte-bound species. Together with the known binding constant of the sensor or using empirical calibrations, an unknown analyte concentration can be derived (Lakowicz 2010). Assuming identical solvent influences on the ϕ for the analyte-free and analyte-bound species, a ratiometric signal is internally calibrated and the measurement becomes sensor concentration independent. Furthermore, neither light source fluctuations nor photo bleaching effects will impact the signal ratio of bound to unbound sensor. In general, when using ratiometric methods, concentration measurement requires that the analyte concentration be in the same

order of magnitude as the binding constant of the sensor for that analyte. If the concentration is much too high, there will not be enough binding sites to respond to the full range of concentration. On the other hand, if the analyte concentration is too low, no appreciable amount of analyte is bound to the sensor and the sensor will provide insignificant response (Lakowicz 2010).

Other fluorescence spectroscopic methods for measuring an analyte make use of an internal referencing system (Lakowicz 2010; Khalil 2004; Gouterman et al. 2004; Köse et al. 2005; Stich et al. 2010). The methods are designed to correct for many problems that exist with intensity measurements. Internal reference methods avoid several problems that arise with luminescent intensity measurement, such as light source changes, changes of the index of refraction of the medium probed, optical geometry variations and fluctuations in sample thickness and dye concentration. The referencing methods in most cases are designed for two sensor molecules in the chemosensor formulation, A and B, and using three distinct wavelengths of light, λ_1, λ_2, and λ_3. Two configurations can be described. In the first, two exciting wavelengths of light and one detecting wavelength are used. In another configuration, one exciting wavelength and two detecting wavelengths of light are used. In principle three distinct relationships between the species A and B can be described producing six distinct internal referencing methods.

One of these methods is the 'yardstick approach' that utilizes one excitation wavelength and two emission bands (wavelengths), whereby one dye component is chosen such that its emission is affected by the variable X while the other component remains constant under the experimental conditions. The latter component thus provides a standard against which the analyte-sensitive emission can be calibrated. Considering, for example, an oxygen sensing method using two emitting dyes A, a silicon complex of octaethylporphyrin (SiOEP), and B, a platinum complex of octaethylporphyrin (PtOEP). PtOEP is affected by varying oxygen concentration—the presence of oxygen leads to an increasing quenching of its fluorescence, while 'the yardstick dye' SiOEP is not affected (Fig. 4.3). Both dyes absorb λ_1^{ex} = 400 nm. SiOEP emits at λ_2^{em} = 570 nm and PtOEP at λ_3^{em} = 650 nm. Commonly the ratio $I(\lambda_3^{em})/I(\lambda_2^{em})$ is used as measure of analyte X. The emission

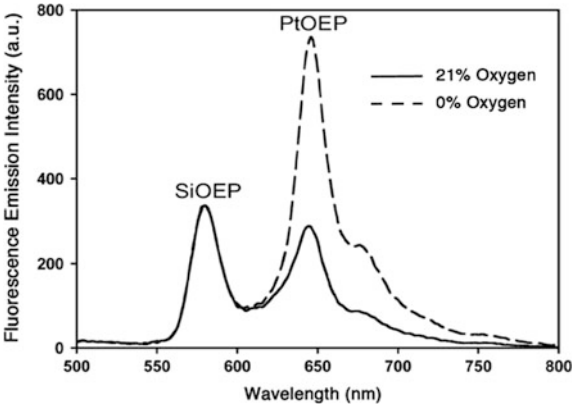

Fig. 4.3 Oxygen partial pressure dependence of the relative intensity of the emission spectra of PtOEP and SiOEP; λ_1^{ex} = 400 nm

λ_3^{em} of PtOEP decreases as a function of oxygen while the emission λ_2^{em} of SiOEP is not affected. A review of the application of metalloporphyrins for optical sensing of oxygen highlighting the above distinctions can be found in the work by Amao and Okura (2009).

4.3 Molecular Origin of the Optical Shifts/Fluorescence on/off Responses

Regardless of the sensing methodologies detailed above, there are a number of different molecular mechanisms by which a chromophore can change its color, or change its fluorescence quantum yield. We will review those that may be most prominent in the applications covered in the following chapters.

4.3.1 Reversible and Irreversible Analyte-Induced Change in Molecular Structure

A chemosensor can change its optical properties based on the presence/absence of an analyte. For example, fluorone-based sensor molecules (such as fluorescein, rhodamine, rose bengal, erythrosine (Red No. 3), eosine, and their derivatives) rely on an intramolecular cyclization reaction, converting a colorless/non-fluorescent spiro-form to a broadly π-conjugated and thus strongly colored/fluorescent form (Fig. 4.4). In the simplest case, this conversion is pH-dependent, giving rise to a halochromic sensor. Substituents on the framework structure can modulate the color of the sensor molecule, the position of equilibrium, and how it may be influenced by other analytes. Similar cyclization reactions are the origin of the color changes observed in phenolphthalein, thymol blue, and derivatives.

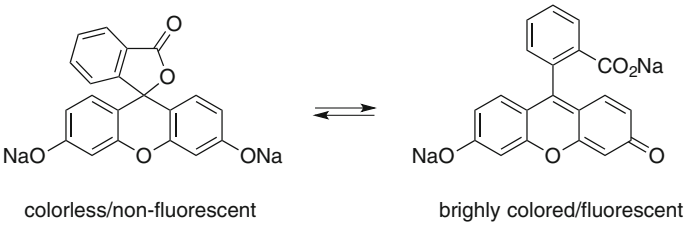

Fig. 4.4 Cyclization/ring-opening equilibrium in the widely used fluorone-based dyes responsible for the pH-dependent color change

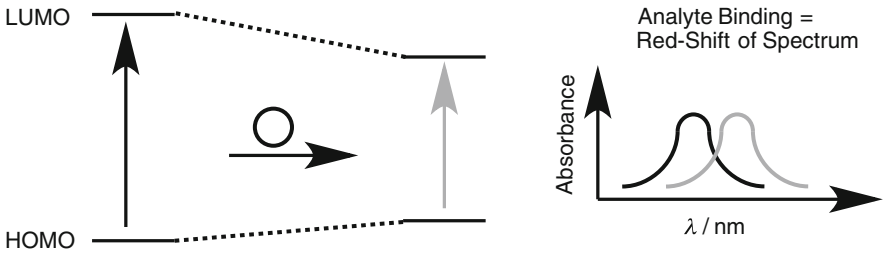

Fig. 4.5 Schematic representation of the molecular mechanism of an absorption spectrum red-shift upon analyte binding

4.3.2 Spectrophotometric Sensing

If an analyte binds reversibly or irreversibly to a chromophore, its UV-vis spectrum changes in a predictable manner. This includes the case where the binding of the analyte changes the electronic structure such that its frontier orbitals (e.g. HOMO π and LUMO π* orbitals typically involved in the electronic transitions responsible for visible color) are more closely spaced, the transition requires less energy and the corresponding absorption band is red-shifted (Fig. 4.5). Inversely, a widening of the frontier orbital gap will lead to a blue-shift of the corresponding band.

4.3.3 Fluorescence Sensing

The fluorescence (or, more broadly, the luminescence = fluorescence and phosphorescence) of a sensor can be switched on, and switched off, the spectrum can be shifted, or its lifetime changed. There are many different mechanisms by which these events can occur. We will review here only a number of mechanisms that are of proven or of likely relevance to applications covered in the following chapters. We refer to reviewed papers for a more comprehensive listing of possible mechanisms (Lakowicz 2010; Hassanzadeh and Azami 2014).

4.3.4 Fluorescence Turn-off Sensing—Paramagnetic Analytes

Luminescence quenching is a process by which the intensity of a luminescent species decreases due to several different interactions, one of them being the interaction with a paramagnetic species. The observation between the emitted light intensity and collision quenching dates back to 1919 by Stern and Volmer (Lakowicz 2010; Stern and Volmer 1919), and is therefore frequently referred to as

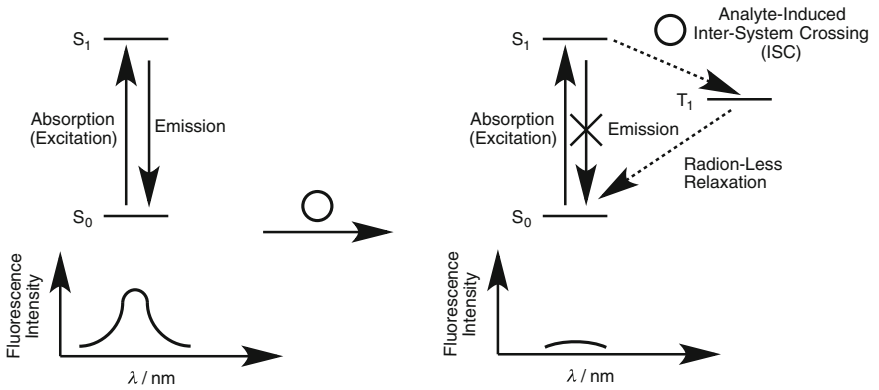

Fig. 4.6 Schematic representation of the paramagnetic contact fluorescence quenching mechanism

Stern-Volmer quenching. The quenching process results from a collisional encounter between the emitting species and the analyte. As this interaction is inherently analyte concentration-dependent, this mechanism has produced several practical chemosensing applications.

The interactions of a fluorescent sensor with a paramagnetic species leading to a fluorescence quenching is shown in Fig. 4.6. The excited singlet S_1 state of the fluorophore is responsible for the fluorescence emission. It generally relaxes rapidly back to the ground S_0 state (lifetimes in the 10^{-9} to 10^{-6} s time frame). The relaxation into an excited triplet state (T_1) is unlikely (i.e. slow) because it is quantum-mechanically spin-forbidden. However, a collision with a paramagnetic species can mediate a very efficient (i.e. fast relative to the S_1 lifetime) inter-system crossing into the T_1 state. Relaxation from this state (also spin-forbidden) is slow and often proceeds along radiation-less pathways. Thus, the interaction of the fluorophore with a paramagnetic analyte leads to an analyte concentration-dependent fluorescence quenching. Application example of this approach incudes sensing Oxygen, Nitric Oxide, and Heavy metals.

4.3.5 Fluorescence Turn-on Sensing—Photo-Induced Electron Transfer (PET) Mechanism

Because a single electron from the chromophore was promoted upon excitation from a doubly occupied highest occupied ground state orbital (the S_0 state) to a higher orbital, the exited (S_1 state) molecule possesses an electron hole in formerly highest occupied orbital. Orbitals on nearby entities (such as lone pairs of amine-type substituents on the chromophore) of the correct energy level can donate an electron into the hole (Fig. 4.7). Thus, the fluorescence of the chromophore is

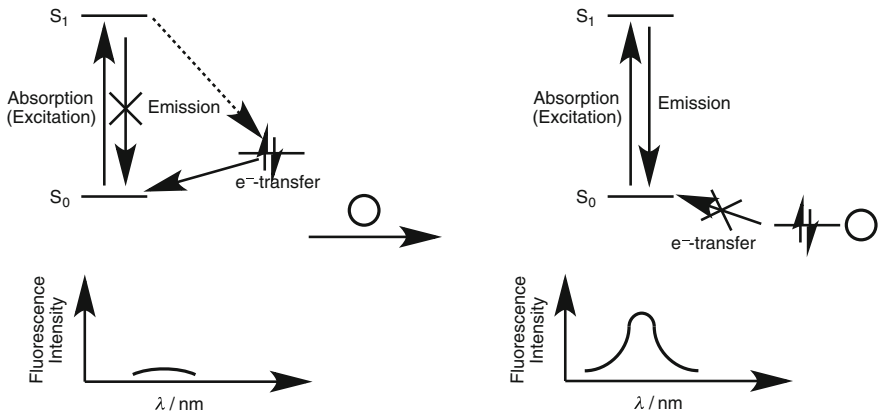

Fig. 4.7 Schematic representation of the molecular mechanism of the photo-induced electron transfer (PET) mechanism of a fluorescence switch-on chemosensor

quenched because the excited state electron now returns through a radiation-less process to replace the electron on the entity, rather than through an emissive pathway to fill the hole. This process is referred to a photo-induced electron transfer (PET) mechanism. If an analyte, such as a metal cation, coordinates to, for example, the lone pair responsible for the fluorescence quenching, it lowers its energy. If this lowering is sufficient to bring the energy level of the lone pair to below the energy level of the hole, it cannot be filling the hole, and the fluorescence of the chromophore is restored. Thus, if the interaction of the analyte with the lone pair is specific for the analyte, the fluorescence intensity of the chromophore is a direct measure of the analyte concentration.

4.3.6 Luminescence Turn-off Sensing—Collisional Quenching by Triplet Oxygen

A special case of a collisional quenching is taking place in many popular oxygen sensors (Fig. 4.8). The luminescent dye is chosen for its property to undergo a very efficient intersystem crossing (ISC) to its triplet state T_1, from where it efficiently emits light upon relaxation (phosphorescence). Sensor molecules carrying heavy atoms, such as palladium and platinum porphyrin, possess a strong spin-orbit coupling of the dye electrons with the heavy atom electrons, thus making these otherwise 'disallowed' processes highly allowed by maintaining the overall orbital spin momentum.

Oxygen in its ground state is a triplet diradical molecule, designated triplet oxygen ($^3O_2$). It can undergo an efficient spin and energy exchange with a triplet dye molecule to recover the dye ground state molecule and (the highly reactive)

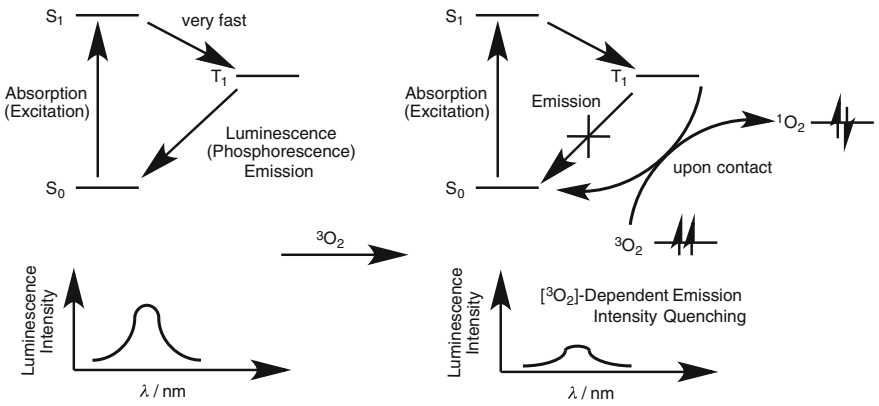

Fig. 4.8 Schematic representation of the Stern-Volmer quenching of an excited state triplet sensor

singlet oxygen ($^1O_2$). The more often this radiation-less process takes place, the greater the luminescence of the dye quenched.

The Stern-Volmer relation quantitatively generally describes the luminescence of a molecular dye in the presence of a quenching species (Stern and Volmer 1919). It states that the intensity of the luminescence is inversely proportional to the concentration of quencher:

$$\frac{I_o}{I} = \frac{\tau_o}{\tau} = 1 + K_{sv}[Q] \tag{4.1}$$

Here I_o (τ_o) is intensity (lifetime) in the absence of quencher, I (τ) is the intensity (lifetime) in the presence of quencher, K_{sv} is the Stern-Volmer constant, and [Q] is the concentration of quencher. Ideally, plots of I_o/I versus [Q] are linear. An extensive range of quenchers can be measured by the luminescence quenching method. The quenchers list includes but is not limited to: amines, halogens, halogenated organic compounds, transition metal ions, nitrogen dioxide and molecular oxygen.

The collisional quenching by oxygen is particularly well studied and has found applications in many fields (McDonagh et al. 2008; Amao and Okura 2009; Wang and Wolfbeis 2013). The Stern-Volmer relation of the luminescence quenching by oxygen partial pressure is:

$$\frac{I_o}{I_{o_2}} = 1 + K_{sv}P_{o_2}[Q] \tag{4.2}$$

Here I_0 is luminescence intensity in the absence of oxygen, I_{O2} is luminescence intensity in the presence of oxygen, K_{SV} is the Stern-Volmer constant and P_{O2} is the local oxygen partial pressure. Oxygen concentration can be determined by monitoring either the luminescence intensity or the decay rate. The process is freely reversible, fast and highly quantitative.

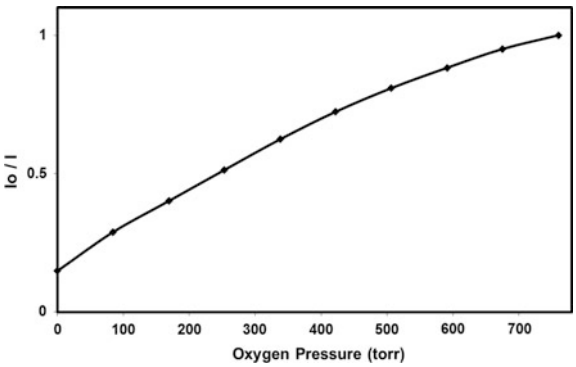

Fig. 4.9 Stern-Volmer plot (oxygen pressure-dependent quenching of the luminescence intensity expressed as I_0/I) of a platinum porphyrin dye embedded in a polymer film

Several known luminescent dye molecules, such as platinum and palladium complexes of porphyrins can be used as an oxygen sensitive molecule (Gouterman et al. 2004). The sensor molecule is commonly embedded in a polymer matrix that allows for oxygen diffusion. Figure 4.9 shows the quenching response of platinum porphyrin film intensity plotted as I_0/I versus oxygen pressure in the Stern-Volmer format. Optical oxygen sensors have found extensive applications in a wide variety of fields, including industrial process control, medical monitoring, agriculture, and environmental sensing. In recent years a number of commercial instruments are currently being offered in the marketplace for measuring dissolved oxygen (Wang and Wolfbeis 2013, 2014).

4.3.7 Fluorescence Resonance Transfer (FRET) Mechanism of Chemosensing

The excited state of an emitter (of a higher S_1 energy level) can be transmitted through space to an emitter of lower S_1 energy level. Therefore, while donor sensor molecule 1 is excited, the emission of acceptor molecule 2 is observed. However, this Förster resonance energy transfer (FRET) is strongly distance-dependent; it takes place only when the two dyes are 10–100 Å apart. This distance dependency can be utilized for a chemosensor (Fig. 4.10). Little to no energy transfer takes place in a situation where the two molecules are far apart, either because both are freely in solution (at low concentrations) or because they are covalently linked by a sufficiently long tether. Using an excitation wavelength that is specific for dye 1, only the emission of dye 1 is observed. The chemosensor is constructed such that the analyte brings the two dyes into close proximity, making a FRET process possible. Thus, exciting the sensor molecule 1, the appearance of the emission of molecule 2 is observed. Provided that the interaction that brings the two together is

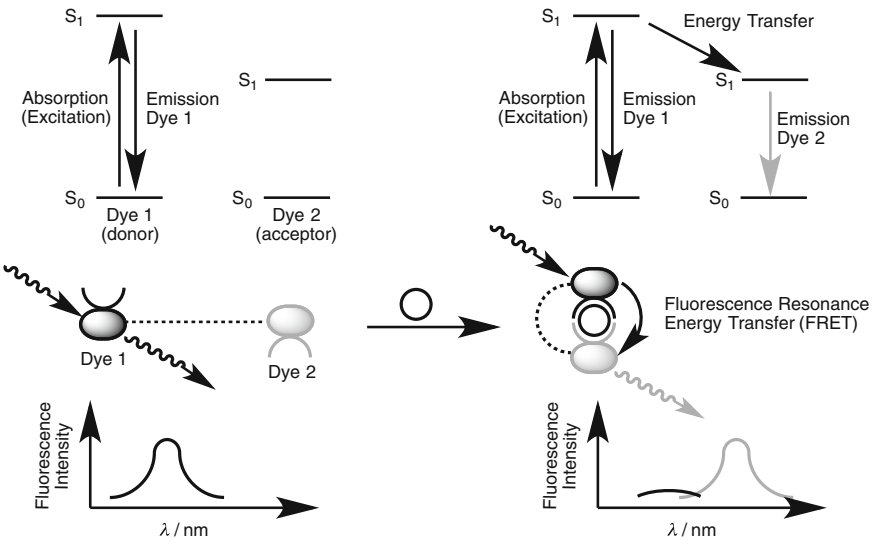

Fig. 4.10 Schematic representation of the molecular mechanism of FRET-based chemosensing

specific for the analyte and generates a single aggregate species, the fluorescence intensity of molecule 2 indicates the presence and concentration of the analyte. Application examples include sensing Metal ions; K^+, Na^+, Mg^{2+}, Ca^{2+}, Fe^{2+}, Fe^{3+}, Al^{3+}, Zn^{2+}, and Hg^{2+}.

4.3.8 Lifetime Measurement Methods

Luminescence measurements are widely used for chemical sensing and imaging applications. Most of the measurement systems are intensity based, where the sample is illuminated by a light source and then simultaneously detected or imaged. Intensity based measurement requires a calibration process to determine the Stern-Volmer constants; it is also highly dependent on the excitation intensity, sample concentration, geometrical orientation and system stability. Measuring the decay rate rather than the intensity produces a more robust sensor whereby several problems that are arise with intensity measurement are avoided. Lifetime measurement methods are known to be independent of illumination intensity changes, tolerate concentration variation, are insensitive to photo bleaching of the indicator, eliminate the need for a reference sensor and have a simpler calibration process. The luminescent lifetime of a molecule is an intrinsic parameter that can be determined using methods that proceed either in the time-domain or in the frequency-domain. Conventional time-domain methods excite the luminophor using a short pulse of light and the lifetime is determined from the time-dependent

intensity of the sample. Conventional frequency-domain measurements excite the sample with sinusoidally modulated light at a known frequency. The luminescence emitted is intensity modulated at the same frequency, but with a phase delay. The lifetime can be determined from both the depth of modulation and the phase delay of the emitted radiation as a function of frequency (Demas 1983; McGraw et al. 2008). In a noise-free system the time and frequency domain methods of lifetime determination produce similar results. Luminescence lifetime imaging is becoming an effective tool for studying environmental applications. Several imaging methods have been developed over the last few years that use different technologies and cover wide ranges of lifetimes (Stich et al. 2010; Wang and Wolfbeis 2014). Luminescence lifetime maps can provide insights into the surroundings of the emitting species, producing 2D images of the local temperature, carbon dioxide, pH and oxygen concentration.

4.4 Conclusion

In preparation for the upcoming sections on applications, this chapter introduced basic concepts associated with sensing with chemical probes. These concepts include applications to extrinsic sensing and calibration. Respective forthcoming applications include subsurface monitoring of dissolved oxygen, sensing neutral and high pH levels, and detection of metal ions.

References

Amao, Y., & Okura, I. (2009). Optical oxygen sensor devices using metalloporphyrins. *Journal of Porphyrins and Phthalocyanines, 13*(11), 1111–1122.

Czarnik, A. W., & Yoon, J. (1999). Chemosensors: Synthetic receptors in analytical sensing applications. In D. N. Reinhoudt (Ed.), *Perspectives in supramolecular chemistry*. Chichester, UK: Wiley, Ltd., pp. 177–191.

Czarnik, A. W. (1994). Chemical communication in water using fluorescent chemosensors. *Accounts of Chemical Research, 27*(10), 302–308.

Demas, J. N. (1983). *Excited state lifetime measurements*. London: Academic Press.

Faizi, M. S. H., Gupta, S., Mohan, K. V., Jain, V. K., & Sen, P. (2016). Highly selective visual detection of Fe3+ at ppm level. *Sensors and Actuators B: Chemical, 222,* 15–20.

Gouterman, M., Callis, J., Dalton, L., Khalil, G., Mébarki, Y., Cooper, K. R., et al. (2004). Dual luminophor pressure-sensitive paint: III. Application to automotive model testing. *Measurement Science & Technology, 15*(10), 1986–1994.

Hassanzadeh, A., & Azami, D. (2014). Waveguide evanescent field fluorescence microscopy: Theoretical investigation of optical pressure on a cell. *Journal of Nanophotonics, 8*(1).

Jolliffe, I. T. (2010). *Principal component analysis.* 2nd edn., Softcover version of original hardcover 2002 edn. New York [u.a.]: Springer.

Kaur, K., Saini, R., Kumar, A., Luxami, V., Kaur, N., Singh, P., et al. (2012). Chemodosimeters: An approach for detection and estimation of biologically and medically relevant metal ions, anions and thiols. *Coordination Chemistry Reviews, 256*(17–18), 1992.

Khalil, G. (2004). Dual-luminophor pressure-sensitive paint I. Ratio of reference to sensor giving a small temperature dependency. *Sensors and Actuators B: Chemical, 97*(1), 13–21.

Köse, M. E., Carroll, B. F., & Schanze, K. S. (2005). Preparation and spectroscopic properties of multiluminophore luminescent oxygen and temperature sensor films. *Langmuir: The ACS journal of surfaces and colloids, 21*(20), 9121–9129.

Kutz, M. (2012). *Handbook of environmental degradation of materials.* 2nd edn. Amsterdam [u.a.]: Elsevier, Wiiliam Andrew.

Lakowicz, J. R. (2010). *Principles of fluorescence spectroscopy.* 3rd edn. (corr. at 4. print.) New York, NY: Springer.

Lim, N. C., Freake, H. C., Brückner, C., et al. (2005). Illuminating Zinc in Biological Systems. *Chemistry: A European Journal, 11*, 38–49.

McDonagh, C., Burke, C. S., & Maccraith, B. D. (2008). Optical chemical sensors. *Chemical Reviews, 108*(2), 400–422.

McGraw, C., Khalil, G., & Callis, J. (2008). Comparison of time and frequency domain methods for luminescence lifetime measurements. *Journal of Physical Chemistry, 112*(21), 8079–8084.

Stern, O., & Volmer, M. (1919). Über die Abklingzeit der Fluoreszenz. *Physik, 20*(183).

Stich, M. I. J., Fischer, L. H., & Wolfbeis, O. S. (2010). ChemInform abstract: Multiple fluorescent chemical sensing and imaging. *ChemInform, 41*(46), pp. no.

Valeur, B., & Leray, I. (2000). Design principles of fluorescent molecular sensors for cation recognition. *Coordination Chemistry Reviews, 205*(1), 3–40.

Wang, X., & Wolfbeis, O. S. (2014). Optical methods for sensing and imaging oxygen: Materials, spectroscopies and applications. *Chemical Society Reviews, 43*(10), 3666–3761.

Wang, X., & Wolfbeis, O. S. (2013). Fiber-optic chemical sensors and biosensors (2008–2012). *Analytical Chemistry, 85*(2), 487.

Part II
Remote Sensing: Ionic Species and Chemical Signatures

Chapter 5
Remote Sensing of Near Neutral pH Levels

Masoud Ghandehari and Cristian S. Vimer

Abstract Fiber optic pH sensors, based on evanescent-wave spectroscopy, are demonstrated for short length distributed chemical sensing in civil infrastructure applications. The fiber sensor was made by removing portions of the poly (-methyl methacrylate) (PMMA) cladding of a plastic clad silica (PCS) optical fiber. The cladding was subsequently replaced with a thin film of PMMA doped with a pH sensitive dye (Methyl Red, Thymolphtalein, Thymol Blue). The change in the pH of the analyte is detected by sending light through the fiber while measuring the absorption spectrum of the embedded sensor molecule.

5.1 Introduction

The opportunity for nondestructive monitoring of civil infrastructure materials from within for early detection of the factors responsible for premature aging is available through the use of optical fibers. This technology applies both for monitoring new structures and for the retrofit installations applied to existing structures. Understanding the internal chemical state of the materials can provide the information needed to assess the long-term effectiveness of material use and design practices; plan for timely protective and remedial action, and provide advance warning for risk of failure and design modification.

In this chapter we present fiber optic evanescent field spectroscopy for in situ monitoring of pH levels in civil infrastructure materials. The fiber optic chemical sensors (FOCS) are produced by removing the plastic clad silica polymer from a typical fiber and replacing it with polymethyl methacrylate, (PMMA) doped with pH sensitive chromoionophores. The chromoionophores used include Methyl Red,

M. Ghandehari (✉)
New York University, Six Metrotech Center, Brooklyn, NY 11201, USA
e-mail: masoud@nyu.edu

C. S. Vimer
Madsen Consulting Engineering, 175 Varick St #803, New York, NY 10014, USA
e-mail: cvimer@gmail.com

M. Ghandehari, *Optical Phenomenology and Applications*,
Smart Sensors, Measurement and Instrumentation 28,
https://doi.org/10.1007/978-3-319-70715-0_5

Thymol Blue, and Thymolphtalein for pH in acidic, neutral and basic environments, respectively. The evanescent wave used selectively excites the indicator molecules within the fiber cladding at the fiber core interface in order to sample the aqueous media surrounding the fiber. The application of these sensors in situ provides information on pH levels within and around civil infrastructure and can be used to inform remediation strategies.

We know that concrete structures are frequently subject to the phenomena known as leaching, sulfate attack, carbonation, and corrosion of reinforcing bars (Mindess et al. 2003). It is also well known that the ingress of certain chemicals species such as chloride, carbon dioxide, sulfates, acids and bases cause accelerated degradation of civil infrastructure materials. A high concentration of hydrogen ions can accelerate the leaching of calcium hydroxide; and calcium silica hydrate may also be attacked in highly acidic environments. Sulfuric and carbonic acids (and any acid that can form soluble calcium salts) can also react with calcium hydroxide in concrete. Moreover, it is evident that strongly alkaline environments, like the interior of concrete, promote the formation of a thin layer of oxide that protects the steel reinforcing bars against corrosion. This passive film is stable in high pH ($\sim$11.5) levels but is destroyed by an increase in acidity as the pH levels of the concrete surrounding the rebar decrease.

Chemically induced degradation is also an issue for the more recently developed polymer concrete (PC) and fiber reinforced polymer composites (FRP) when they are used as structural materials. The degradation of polymers used in demanding conditions is dependent on the macromolecular polymer structure and its chemical environment. Most polymers used in construction contain additives and stabilizers which improve the resistance of the polymers to degradation. However, these additives can be susceptible to leaching or to chemical attack, thereby, leaving the plastic material unprotected. Hydrolytic degradation is a common form of aging of polymers. Hydrolysis occurs when positively charged hydrogen ions (H^+) in acidic media, or negatively charged hydrogen ions (OH^-) in alkaline media, attack the ester linkage, breaking the polyester chain. This reduces the polymer chain length and alters its molecular weight distribution, ultimately impacting its strength.

The fiber optic chemical sensors (FOCS) presented here are based on the evanescent-wave spectroscopic technique (Egami et al. 1996; Stewart et al. 1997; Ghandehari and Vimer 2002; Ge et al. 1993; Zaatar et al. 2000; Gupta and Ratnanjali 2001; Conzen et al. 1993). This work follows that of other reports in civil engineering (Fuhr et al. 1995, 1998; Ghandehari and Vimer 2003; Xi et al. 1995), and other disciplines (Krause et al. 1999a, b; Kosch et al. 1998; Lin 2000). The aim of this application of fiber optical sensors is the development of robust, long lasting sensing devices for application in harsh civil environments for detection of moisture, pH, chlorides, and oxidation processes.

Successful developments in methods for monitoring pH levels or pH dependent processes in structural materials include potentio-metric measurements using embedded micro sensors (Mansfeld et al. 1991; Srinivasan et al. 2000) and electrochemical impedance spectroscopy (EIS) (Tamura et al. 1997). Similar developments in other fields include: the manufacturing of pH-sensitive films of sol-gel

or polymers doped with various fluorescent or absorptive pH-sensitive dyes (Safavi and Abdollahi 1998; Arregui et al. 2002); the use of electro-active polymers, such as polyaniline or Nafion, to develop pH-sensitive films (Farooque et al. 1999; Misra et al. 2002); the creation of fiber optics pH sensors using fluorescent dyes immobilized in polymeric membranes at the tip of optical fibers (Zhang et al. 1996); the development of a pH-sensitive nano-tip array-imaging sensor using fluorescence images transmitted through a fiber-optic bundle (Liu et al. 2000); the development of optical fibers with pH-dependent swelling hydro gel cladding materials (Michie et al. 1995); and the development of pH-sensitive fluorophores time of flight measurement (Elliott et al. 1999).

5.2 Theory

5.2.1 *Evanescent Wave Theory*

Step index fibers were used in these experiments. The number of possible modes (Fig. 5.1) guided through the fiber increases with increasing fiber core diameter and decreasing wavelength. This is expressed as:

$$N_m = 0.5\left[\frac{(\pi D \cdot NA)}{\lambda}\right]^2 \tag{5.1}$$

where N_m is the number of modes, D is the core diameter, NA is the numerical aperture of the fiber, and λ is the wavelength.

The numerical aperture (NA) of the fiber, which is function of the index of refraction of the core and cladding, determines the maximum solid angle at which a beam can be launched.

$$NA = \sin(\alpha/2) = (n_1^2 - n_2^2)^{0.5} \tag{5.2}$$

where α is the acceptance angle, n_1 is the refractive index of the core, and n_2 is the refractive index of the cladding.

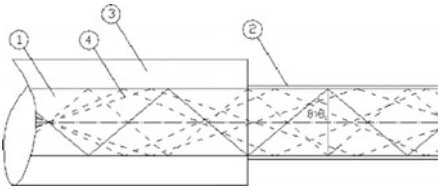

Fig. 5.1 Optical fiber with cladding removed—schematic. Schematic shows (1) fiber core, (2) original cladding, (3) buffer, (4) typical propagation modes

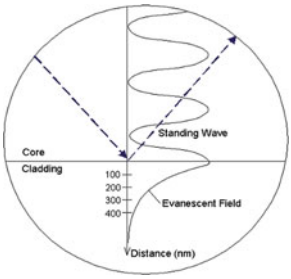

Fig. 5.2 Schematic of the standing wave and the evanescent field at the boundary of core and cladding. The numbers show is the penetration depth in nanometers (nm)

A 600 μm core step-index multimode fiber, with a numerical aperture of 0.48 is described. At 543 nm wavelength, 1,388,209 distinct modes can propagate through the fiber core. The energy guided through the core by total internal reflection also generates a surface-specific, electromagnetic disturbance at the interface between the two dielectric media (the core and the cladding). There is a standing wave at every point of interface incidence. This harmonic wave, which penetrates the cladding over a small distance, is called the *evanescent field* (Fig. 5.2), and it can be described by the exponential decay

$$E = E_0 \cdot \exp(-z/d_p) \tag{5.3}$$

where z is the distance normal to the interface and E_0 is the wave amplitude at z = 0. The penetration depth is:

$$dp = \lambda/(n_1 \cdot 2)\left[\sin^2 - \left(\frac{n_2}{n_1}\right)^2\right]^{0.5} \tag{5.4}$$

where λ is the wavelength of the light traveling through the fiber core, n_1 and n_2 are the refractive indices of the core and the cladding, respectively, and θ is the incidence angle between the propagation vector and the normal to the boundary interface.

5.2.2 Principle of pH Detection

Light as an electromagnetic radiation has the energy defined as:

$$E = \hbar v \tag{5.5}$$

where ħ is the Planck's constant, and ν is the frequency of the wave. Light is transmitted by Photons and is represented by its energy ħν. When a light wave

encounters a particle, or molecule, it can either be scattered (a change in direction) or absorbed (a transfer of energy). Absorption occurs when the energy of the photon corresponds to the difference between energy levels in the molecules encountered. Absorption of the energy from the photon elevates the molecule to an excited state. Chromoionophores are indicator molecules that, in the presence of specific ions (H^+, Ca^{2+}, Cl^-, K^+, etc.) exhibit a change in color, i.e., a change in the absorption spectrum. Absorption is wavelength specific intensity attenuation of energy as it passes through a medium. Beer-Lambert Law describes the relationship between the intensities of light before and after interaction with a chromoionophore:

$$I = I_0 10^{-\varepsilon dc} \quad or \quad \log(I/I_0) = -\varepsilon dc \tag{5.6}$$

where I_0 = initial intensity, I = final intensity, ε = molar extinction coefficient, d = thickness, c = molar concentration.

Absorption (A) is:

$$A = -\log(I/I_0) = \varepsilon dc \tag{5.7}$$

In other words, the molar extinction coefficient (ε) is defined as the absorption (A) of 1 M of pure chromoionophore under standard conditions.

Chromoionophores exhibit unique absorption spectra with specific wavelength of maximum absorption (λ_{max}) in the absence of the specific ions, and also unique spectra in the presence of those ions. The indicators used for the sensors presented here are pH sensitive, non-fluorescent chromoionophores. Depending on the hydrogen ions concentration in the environment, the interaction between the dye molecules and the hydrogen ions in the target analyte causes a dipole change in the indicator and is apparent as changes in the absorption spectrum.

In our work, the factory fiber cladding is removed and PMMA is used as the host matrix for the chromoionophore forming the new cladding. Optimally the new cladding must have the following characteristics:

- Good adhesion to the fiber core (silica or polymer)
- Permeability to water-born analytes
- Good bond to the dye molecules
- Refractive index lower than that of the fiber core in order to satisfy the total internal reflection condition.

Investigating PMMA for this application we found that its adhesion to the fiber core is excellent and its refractive index is well matched. This polymer is commonly used as cladding material for Polymer Clad Silica (PCS) fibers. The polymer resins used for our application must be hydrophilic but water insoluble. Polymers such as polyethylene or Teflon are water insoluble, but they are hydrophobic, and for that reason, they are inappropriate for this application. PMMA is insoluble in water, yet hydrophilic. The permeability of H_2O in PMMA is moderate (5.2 g cm/cm^2 h), allowing the solution to penetrate through and to reach the core/cladding interface.

5.3 Experimental Work

5.3.1 Sensor Cladding Preparation

The cladding is prepared in the following proportions: 800 mg PMMA with molecular weight 996,000, 1 mg indicator, and 100 cm 1, 4 Dioxane. The indicators used are Methyl Red, Thymol Blue, and Thymolphtalein (all chemicals from Sigma-Aldrich Inc., Milwaukee, WI). The prepared polymer solutions are used for:

1. Performing initial solution phase transmission spectroscopic studies
2. Coating optical fibers.

The optical fiber used is plastic clad silica (PCS) fiber, (3M fiber from Thorlabs Inc., Newton, N.J.), with the core diameter 600 μm, cladding 15 μm, and buffer layer thickness 205 μm. Pieces of the fiber 200 mm long are cut, the ends are polished using lapping films, and the original polymer buffer and cladding are mechanically removed (using a surgical blade) over a length of 65 mm. A solution of sulfuric acid and dichromate of potassium is used for complete removal of the original polymer cladding followed by distilled water rinse. The fibers are dip coated at a rate of approximately 1 cm/h. It is then cured at 80 °C for 30 min. The thickness of the new cladding is maintained at approximately 10 μm.

5.3.2 Apparatus

Preliminary spectroscopy tests are performed on the solution phase of the new cladding polymer mixed with the chromoionophores. The solution is placed in a cuvette and its transmission spectrum is compared with the spectrum of a reference clear PMMA solution (800 mg PMMA: 100 cm^3 1, 4 Dioxane, without indicator). A scanning spectrophotometer was used for the comparison.

The apparatus setup used for the optical fiber experiments is shown in Figs. 5.3 and 5.4. A 100 W quartz tungsten halogen (QTH) lamp is used as the white light source (Thermo-Oriel Inc., Stratford. CT). The beam is sent into a Cornerstone monochromator (Thermo-Oriel Inc., Stratford. CT); operation of the monochromator is controlled through a GPIB board (National Instruments, Austin, TX) by a Lab View based software. The white light is scanned using the monochromator and then sent into a fiber optic patch cord (3 M 400 microns core fiber patch cords with SMA connectors (Thorlabs Inc., Newton, NJ), using an SMA connected collimation package for the 0.48 numerical aperture of the fiber. The fiber is passed through a beaker containing the analyte and it is connected at each end to patch cords by tubular connectors treated with index-matching liquid (Norland Products, Inc., Cranbury, NJ). Measurements of the light intensity are made using a photodiode (Thorlabs Inc., Newton, NJ).

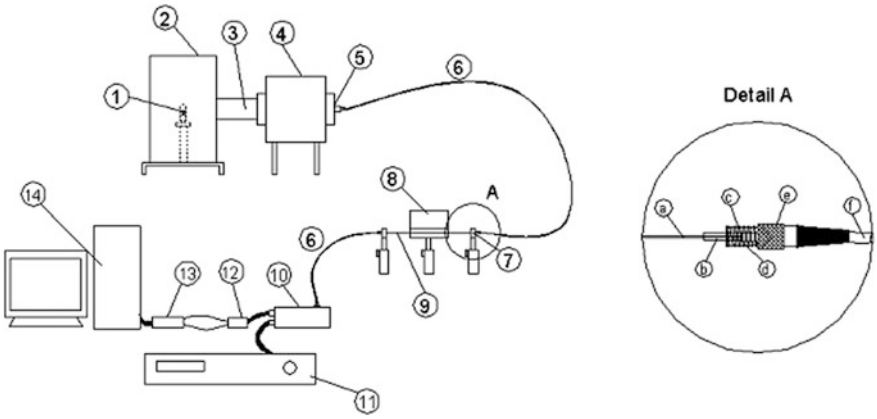

Fig. 5.3 Schematic of the experimental setup. Detail A: Special Fixture for the Test Fiber

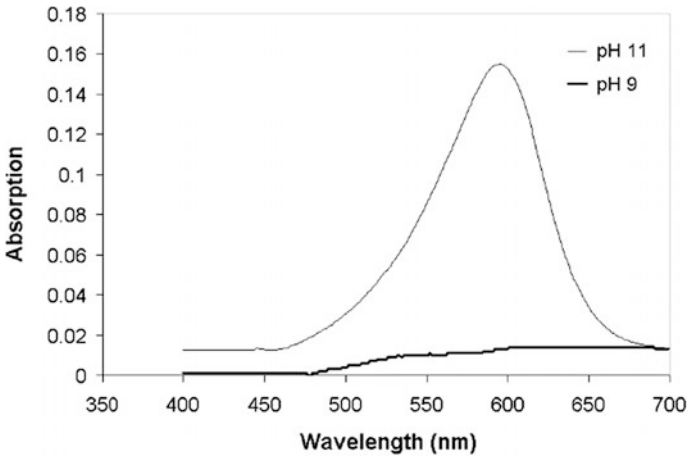

Fig. 5.4 Absorption Spectra of the PMMA solution containing Thymolphtalein at pH 9 and pH 11

The numbered components in Fig. 5.3 are listed as follows:

(1) QTH Lamp
(2) Lamp housing
(3) Lens assembly
(4) Monochromator
(5) Collimation Package for SMA connectors
(6) Fiber optic patch cords with SMA connectors
(7) Special connector for the test fiber

(8) Plastic beaker with analyte
(9) Test fiber
(10) Photomultiplier tube
(11) High voltage power supply
(12) Preamplifier
(13) Data acquisition
(14) Computer with LabView software for data logging.

The components shown in Detail A are labeled as follows:

(a) Test fiber
(b) Special pipe drilled for the exact size of the test fiber
(c) Drop of index-matching liquid
(d) SMA to SMA mating sleeve
(e) SMA connector
(f) Fiber optic patch cord.

5.4 Results and Discussion

5.4.1 Transmission Absorption Spectra of Doped Polymer Solutions in Cuvette

The transmission absorption spectra of the doped polymer solutions show that at this stage of preparation, the sensor material exhibit the anticipated response with changes in pH exposure. The absorption spectra of a blank cuvette were used as reference for all cuvette experiments.

The solution containing Thymolphtalein had practically no absorption below pH 9, but exhibited strong absorption when pH changed from pH 9 to pH 11. Above pH 11 the absorption spectrum was unchanged and stable (Fig. 5.4). The solution is colorless under pH 9, and blue over pH 11.

5.4.2 Absorption Spectra of the Fiber Optic Sensors

Using the setup shown in Fig. 5.3, tests are performed on fibers with a portion of the cladding replaced with PMMA doped with Methyl Red and Thymolphtalein. The spectra through the fiber are measured at various pH levels using the unclad fiber as reference baseline. Results are shown in Figs. 5.5 and 5.6.

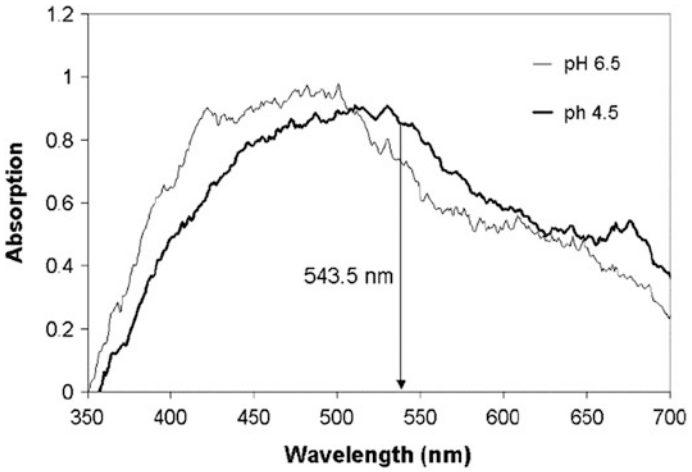

Fig. 5.5 Absorption spectra of the fiber with the cladding replaced with Methyl Red—doped PMMA film, at pH 4.5 and pH 6.5. The arrow shows the wavelength chosen for the diode laser

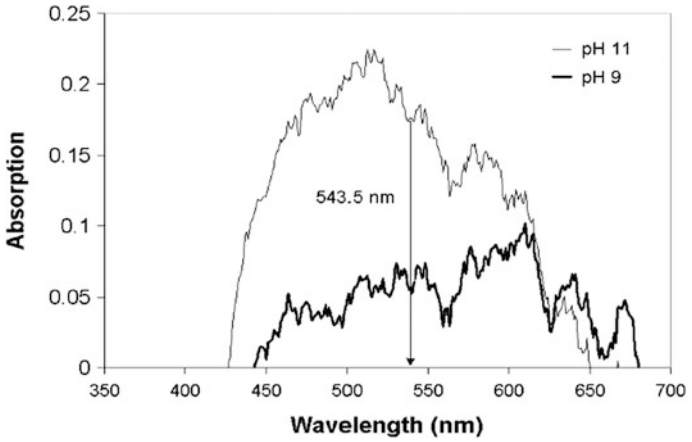

Fig. 5.6 Absorption spectra of the fiber with the cladding replaced with Thymolphtalein—doped PMMA film, at pH 9 and pH 11. The arrow shows the wavelength chosen for the diode laser

5.5 Conclusion

Evanescent wave, optical fiber sensing was tested for nondestructive detection of near neutral pH levels; a chemical parameter that is pertinent to the degradation of non cementious civil infrastructure. Evanescent field sensors are useful for short length distributed detection of pH ranging from the acidic to basic, near neutral levels. PMMA appears to work relatively well as host for physical binding of

chromoionophores. Response time of the sensor is controlled by the permeability coefficient of the host polymer cladding. The sensor tested has slow response time, hence the polymeric coating needs to be reformulated. However, it should be noted that the proposed application does not require rapid response time given that the respective degradation process are in a time scale of months to years.

References

Arregui, F. J., Otano, M., Fernandez-Valdivielso, C., & Matias, I. R. (2002). An experimental study about the utilization of Liquicoat® solutions for the fabrication of pH optical fiber sensors. *Sensors and Actuators: B. Chemical, 87*(2), 289–295.

Conzen, J. P., Burck, J., & Ache, H. J. (1993). Characterization of a fiber-optic evanescent wave absorbance sensor for nonpolar organic compounds. *Applied Spectroscopy, 47*(6), 753–763.

Egami, C., Takeda, K., Isai, M., & Ogita, M. (1996). Evanescent-wave spectroscopic fiber optic pH sensor. *Optics Communications, 122*(4), 122–126.

Elliott, N. J., Wallace, P. A., Uttamlal, M., Smith, S., & Campbell, M. (1999). Quasi-distributed pH sensor. *Fiber Optic Sensor Technology and Applications*, SPIE, Photonics East, 1999.

Farooque, A. M., Al-Amoudi, A., & Numata, K. (1999). Degradation study of cellulose triacetate hollow fine-fiber SWRO membranes. *Desalination, 123*(2), 165–171.

Fuhr, P. L., Ambrose, T. P., Huston, D. R., & Mcpadden, A. P. (1995). Fiber optic corrosion sensing for bridges and roadway surfaces. *Smart Structures and Materials 1995: Smart Systems for Bridges, Structures, and Highways*, SPIE

Fuhr, P. L., Huston, D. R., & Maccraith, B. (1998). Embedded fiber optic sensors for bridge deck chloride penetration measurement. *Optical Engineering, 37*(4), 1221.

Ge, Z., Brown, C. W., Sun, L., & Yang, S. C. (1993). Fiber-optic pH sensor based on evanescent wave absorption spectroscopy. *Analytical Chemistry, 65*(17), 2335–2338.

Ghandehari, M., & Vimer, C. (2003). Moisture sensing in structural materials using near-infrared evanescent field spectroscopy. In: F. Chang (Ed.), *Structural health monitoring 2003 : From diagnosis & prognostics to structural health management; proceedings of the 4th international workshop on structural health monitoring.* Lancaster, Pa: DEStech Publications.

Ghandehari, M., & Vimer, C. S. (2002). Fiber optic evanescent field sensors for pH monitoring in civil infrastructure. *Nondestructive Evaluation and Health Monitoring of Aerospace Materials and Civil Infrastructures*, Proc. SPIE 4704, June 18, 2002.

Gupta, B. D., & Ratnanjali, (2001). A novel probe for a fiber optic humidity sensor. *Sensors and Actuators B: Chemical, 80*(2), 132–135.

Kosch, U., Klimant, I., Werner, T., & Wolfbeis, O. S. (1998). Strategies to design pH optodes with luminescence decay times in the microsecond time regime. *Analytical Chemistry, 70*(18), 3892–3897.

Krause, C., Werner, T., Huber, C., & Wolfbeis, O. (1999a). Emulsion-based fluorosensors for potassium featuring improved stability and signal change. *Analytical Chemistry, 71*(23), 5304–5308.

Krause, C., Werner, T., Huber, C., & Wolfbeis, O. S. (1999b). pH-insensitive ion selective optode: A coextraction-based sensor for potassium ions. *Analytical Chemistry, 71*(8), 1544–1548.

Lin, J. (2000). Recent development and applications of optical and fiber-optic pH sensors. *Trends in Analytical Chemistry, 19*(9), 541–552.

Liu, Y., Dam, T. H., & Pantano, P. (2000). A pH-sensitive nanotip array imaging sensor. *Analytica Chimica Acta, 419*(2), 215–225.

Mansfeld, F., Shih, H., Postyn, A., Devinny, J., Islander, R., & Chen, C. L. (1991). Corrosion monitoring and control in concrete sewer pipes. *Corrosion, 47*(5), 369.

Michie, W. C., Culshaw, B., Mckenzie, I., Konstantakism, Graham N. B., Moran, C., et al. (1995). Distributed sensor for water and pH measurements using fiber optics and swellable polymeric systems. *Optics Letters, 20*(1), 103–105.

Mindess, S., Young, F. J., & Darwin, D. (2003). *Concrete* (2nd ed.). Upper Saddle River, NJ: Pearson.

Misra, V., Mishra, H., Joshi, H. C., & Pant, T. C. (2002). An optical pH sensor based on excitation energy transfer in Nafion® film. *Sensors and Actuators: B. Chemical, 82*(2–3), 133–141.

Safavi, A., & Abdollahi, H. (1998). Optical sensor for high pH values. *Analytica Chimica Acta, 367*(1), 167–173.

Srinivasan, R., Phillips, T. E., Bargeron, C. B., Carlson, M. A., Schemm, E. R., & Saffarian, H. M. (2000). Embedded micro-sensor for monitoring pH in concrete structures. *Smart Structures and Materials 2000: Smart Systems for Bridges, Structures, and Highways*. SPIE, 20 April 2000.

Stewart, G., Jin, W., & Culshaw, B. (1997). Prospects for fibre-optic evanescent-field gas sensors using absorption in the near-infrared. *Sensors and Actuators: B. Chemical, 38*(1), 42–47.

Tamura, F., Akao, N., Hara, N., & Sugimoto, K. (1997). Development of EIS capacitor pH sensor for highly corrosive environment. *Zairyo-to-Kankyo, 46*(4), 243–250.

Xi, H., Shieh, C., Grossman, B., Doi, S., Cosentino, P., & Erbland, P. (1995). Fiber-optic chloride sensor development. *Journal of Geotechnical Engineering, 121*(8), 610–617.

Zaatar, Y., Zaouk, D., Bechara, J., Khoury, A., Llinaress, C., & Charles, J. (2000). Fabrication and characterization of an evanescent wave fiber optic sensor for air pollution control. *Materials Science and Engineering B, 74*(1), 296–298.

Zhang, S. F., Wickramasinghe, Y. A. B. D., & Rolfe, P. (1996). Investigation of an optical fibre pH sensor with the membrane based on phospholipid copolymer. *Biosensors and Bioelectronics, 11*(1), 11–16.

Chapter 6
Optical Sensing of High pH Levels

Christian Brückner, Gamal Khalil and Masoud Ghandehari

Abstract Porphyrins, or more generally, porphyrinoids, have played a big role as chromophores in sensing applications. This is due to the intense absorption they exhibit over a wide section of the UV-vis spectrum, their large fluorescence yields, high chemical stability, and the multiple options for functionalization. Therefore, porphyrinoids and their metal complexes have been used as optical chemosensors for a range of analytes. This chapter provides some details on the characteristic of these indicators for sensing high pH levels, including options for tuning and matrix immobilization.

6.1 Introduction

The measurement of the pH value is a key parameter in essentially all processes in the environment that involve aqueous solutions, whether in chemistry, engineering or biomedicine. The use of glass electrodes for measuring pH (or related electrochemical measurements) is widely favoured for their simplicity, rapid response and wide dynamic range. However, for applications for which the pH range of interest lies deep in the alkaline region, the performance of glass electrodes deteriorates—the so-called 'alkaline error' sets in. This error is, in part, due to the chemical instability of glass at high pH values, rendering these electrodes particularly unsuitable for longer duration monitoring applications in highly alkaline environments. Alternatively, many dyes,

C. Brückner
Department of Chemistry, University of Connecticut, Storrs, CT 06269, USA
e-mail: c.bruckner@uconn.edu

G. Khalil
Department of Aeronautics and Astronautics, University of Washington,
Box 352250, Seattle, WA 98195, USA
e-mail: gekhalil@gmail.com

M. Ghandehari (✉)
New York University, Six Metrotech Center, Brooklyn, NY 11201, USA
e-mail: masoud@nyu.edu

M. Ghandehari, *Optical Phenomenology and Applications*,
Smart Sensors, Measurement and Instrumentation 28,
https://doi.org/10.1007/978-3-319-70715-0_6

e.g. litmus, phenolphthalein, or phenol red, change their color in response to a change in pH (Bühlmann et al. 1998). This forms the basis for the widespread use of optical pH measurements in research and industry. While UV-vis absorption-based pH measurements are the most common, fluorescent pH indicators have also proven effective (Nguyen et al. 2014).

To quantitatively measure the pH of a solution using dyes, it is essential to match the indicator's pK_a to the expected pH range. Most pH dyes are suitable for the sensing of slightly basic, neutral to acidic pH values, with a dynamic range commonly spanning 1–3 pH units, as dictated by the pK_a/pK_b of the indicator. Only relatively few indicator dyes for high pH values (>pH 10) have been reported (Werner and Wolfbeis 1993; Safavi and Abdollahi 1998; Koncki and Wolfbeis 1998; Derinkuyu et al. 2007; Safavi and Banazadeh 2007; Safavi and Sadeghi 2007; Ensafi and Kazemzadeh 1999; Dong et al. 2008; Nguyen et al. 2014). Included among them are the indigo carmine dye (blue up to pH 11.4—yellow at pH 13) and the titan yellow, a triazene dye (yellow up to pH 12—red at pH 13). Both dyes operate by deprotonation of an NH functionality at high pH values (Fig. 6.1). This paucity of sensors is, in part, because the highly caustic environment of aqueous solutions with high pH values presents a particularly challenging environment for the sensor molecules.

A highly practical optical sensor should be chemically robust, possess intense colors or high emission yields and a significant spectral separation between the absorption or emission spectra corresponding to the low and high pH environment. The presence of two strong bands that are diagnostic for the neutral and charged states of the dyes, and a wide spectral separation allows for a particularly practical ratiometric method of measurement (Chitarra et al. 2000). However, only a small subsection of the known high pH sensors fulfill these requirements (Dong et al. 2008; Koncki and Wolfbeis 1998). The ideal optical pH sensor also needs to exhibit a rapid (relative to the time scale of the changes to be measured) chromic response upon change of pH (Werner and Wolfbeis 1993; Safavi and Abdollahi 1998; Niu et al. 2005).

In part, as a response to the unsuitability of the glass pH electrodes in the high pH regime, optical fiber-based sensors measuring changes in pH by monitoring the response in the absorbance, reflectance, fluorescence and refractive indices have been developed. In general, optical fiber sensors offer practical advantages, such as not requiring a reference element, having the potential for miniaturization, low cost

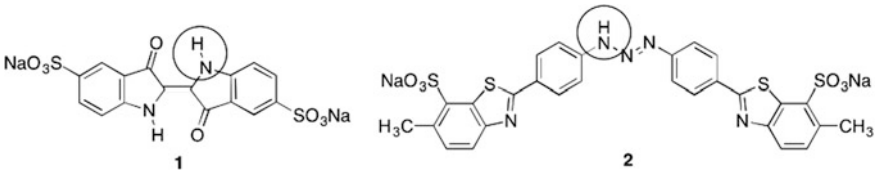

Fig. 6.1 Structures of two representative non-porphyrin-based high pH halochromic sensors. Highlighted are the protons that are lost at high pH conditions

and ease of long distance signal transmission (Cusano et al. 2008). The realization of optical, high pH sensing fiber sensors (optodes) requires a high pH sensing dye that can be affixed to the end of the optical fiber (Nguyen et al. 2014). In this chapter, we will summarize the findings about a relatively new class of high pH indicator dyes, the porpholactones. These synthetic porphyrin-derived dyes have demonstrated reversible spectral red-shifts as a function of pH, are highly chemically stable, and have a dynamic range between pH 11 and pH 13.5. This range can be somewhat adjusted by chemical derivatization and the choice of a carrier matrix. These dyes are also characterized by very high extinction coefficients and chemical robustness. We will detail the properties that define these dyes, including their ability to be incorporated into optodes and that recommend them for high pH sensing applications in infrastructure diagnostics. The specific application of the porpholactones to map the pH of solid cementitious materials is presented in Chap. 16.

6.2 Porphyrinoids as Halochromic Sensors

Porphyrins or, more generally, porphyrinoids such as corrole or expanded porphyrins, have figured prominently as chromophores in sensing applications (Czarnik and Yoon 1999). This is because of their deep colors (high extinction coefficients) over a wide section of the UV-vis spectral range, their generally large fluorescence yields, high chemical stability, and the multiple options to functionalize them. Consequently, porphyrinoids and their metal complexes have been used as optical chemosensors for a range of analytes (Bakker et al. 1997; Yu et al. 2013; Bühlmann et al. 1998; Worlinsky et al. 2014), including their use as halochromic (variation of colour with pH) sensors (Yuan et al. 1993; Blair et al. 1993; Igarashi et al. 1994; Papkovsky et al. 1997; Delmarre et al. 1999; Gulino et al. 2005; Niu et al. 2005; Li et al. 2006; Worlinsky et al. 2013, 2015; Khalil et al. 2010; Liu et al. 2017).

There are several modes of action along which a porphyrinoid can exhibit a halochromic response. On one hand, the inherent basicity of the inner imine (–N=) nitrogen of free-base (non-metallated) porphyrinoids makes them natural choices as low pH sensors (Igarashi et al. 1994; Li et al. 2006; Niu et al. 2005; Blair et al. 1993; Gulino et al. 2005).

On the other hand, the relatively high acidity of the pyrrole (NH) nitrogens of some electron-poor free base porphyrin derivatives also allows them to act as base sensors (Fig. 6.2). It is known that an inner NH group is readily deprotonated with strong bases (Woller and Dimagno 1997; Terazono and Dolphin 2003; Mahammed et al. 2003). Conformational effects strongly modulate the acidity/basicity of the porphyrinoid N and NH moieties (Mahammed et al. 2003; Ou et al. 2007; Thyagarajan et al. 2010; Brückner et al. 2006). These porphyrinic materials operate as halochromic sensors by tracking the change of their optical properties upon protonation/deprotonation.

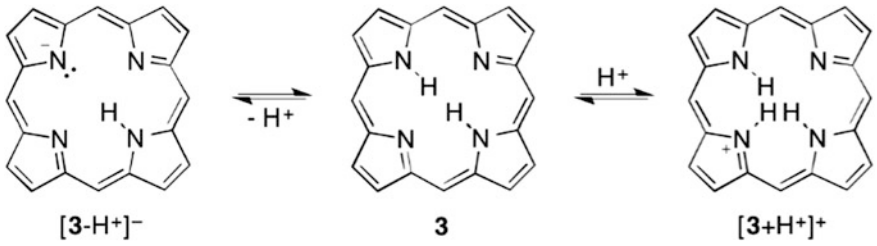

Fig. 6.2 Ability of diprotic, dibasic, free base porphyrinoids to act as sensors for acids and bases

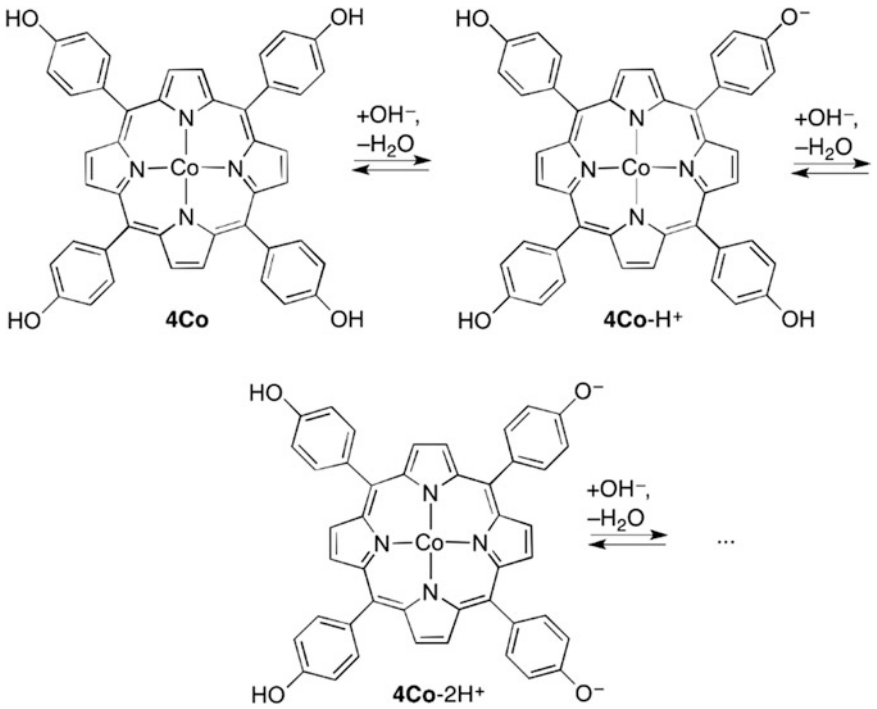

Fig. 6.3 Structures of halochromic porphyrin sensor **4Co**, and its mechanism of pH sensing

Base sensor *meso*-4-hydroxyphenylporphyrin cobalt complex **4Co** carries four base-sensitive substituents (phenol groups) at the porphyrin periphery that are all in electronic interaction with the porphyrin chromophore and, therefore, also with each other (Fig. 6.3). Because of this coupling, this tetraprotic sensor shows four sequential deprotonation events that are reflected in a change of the UV-vis spectrum of the porphyrin. The inner nitrogens are blocked from participation in pH-dependent events by the presence of the coordinated cobalt ion.

Manufactured into a fiber optic sensors, **4Co** showed an unusually broad linear response in the range from pH 8–12 (Blair et al. 1993). This tracking of a [OH^-]-dependent deprotonation of the sensor dye is the most typical mode of operation for base-sensitive dyes, albeit this typically involves only monoprotic dyes. Alternatively, the nucleophilicity of the hydroxide ion can also be utilized to elicit a halochromic response on suitably derivatized porphyrinoids. The class of porpholactones described below are such derivatives (Khalil et al. 2010; Worlinsky et al. 2013, 2015; Liu et al. 2017).

6.3 Porpholactones as High pH Sensors

6.3.1 Synthesis of Porpholactones

In 1984 it was recognized that the oxidation of certain ß-substituted porphyrins **6** can lead to the loss of one ß-carbon and formation of porpholactone (Fig. 6.4; Crossley and King 1984). Thus, one peripheral C=C double bond of a porphyrin was formally replaced by a lactone (–O(C=O)–) moiety. Since the original discovery, multiple simple and high-yielding single and multi step reaction pathways toward porpholactones have become known, incorporating a range of *meso*-aryl substituents (Gouterman et al. 1989; Brückner et al. 2012; Yu et al. 2012). Multiple metal complexes of the porpholactones were also described (Gouterman et al. 1989; Brückner et al. 2012; Ke et al. 2014; Liang et al. 2012; Lv et al. 2012). Of particular importance here are the platinum complexes of the *meso*-pentafluoro-phenyl-substituted porpholactone $\mathbf{5^FPt}$ (Khalil et al. 2002; Khalil 2004).

Irrespective of the replacement of a C=C bond by a lactone moiety, the optical properties of free base porpholactones remain very porphyrin-like (Gouterman et al. 1989; Brückner et al. 2012). Porpholactone platinum complexes have found applications as O_2-sensitive phosphorescent component of pressure sensitive paints, allowing the imaging of

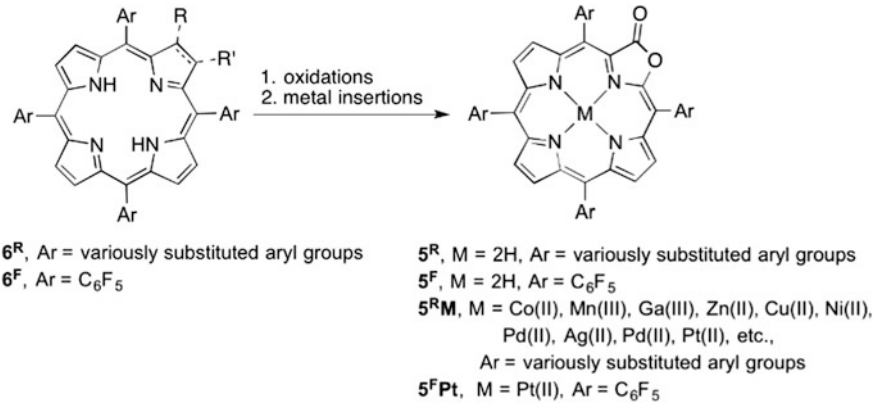

Fig. 6.4 Synthesis of porpholactone by oxidation of the corresponding porphyrin

air flow around objects (Gouterman et al. 2004; Khalil 2004; Zelelow 2003). Free base porpholactone thiono derivatives were also shown to be selective chemodosimeters for hypochloride (OCl^-) (Yu et al. 2013). However, their halochromic response profiles and sensing mechanisms are particularly remarkable and useful (Khalil et al. 2010; Worlinsky et al. 2013, 2015; Liu et al. 2017).

6.3.2 *Colorimetric Base Sensing Using Porpholactones in Organic Solvents*

The UV-vis spectra of free base (**6**, **6^F**) and the Pt(II) complexes of porpholactones (**6Pt**, **6^{F}Pt**) in organic solvents exhibit the spectral shapes and high extinction coefficients typical of porphyrins (**5^F**) and metalloporphyrins (**5^{F}Pt**) (Fig. 6.5; Gouterman 1978).

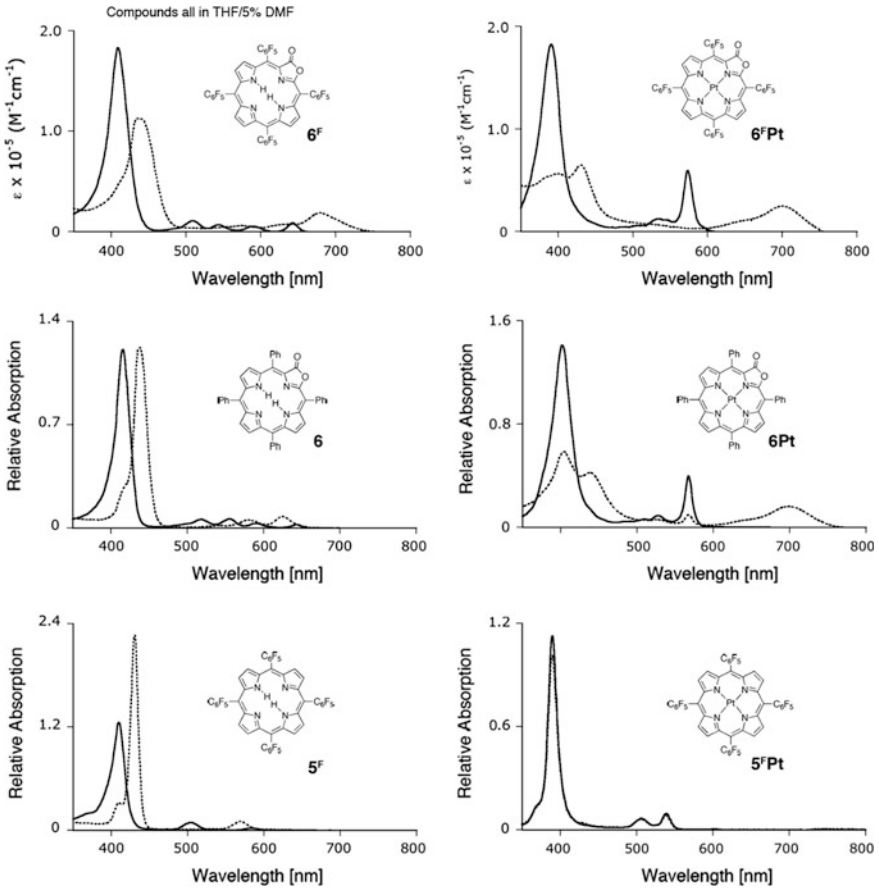

Fig. 6.5 UV-vis spectra (3 mL THF + 5% DMF, 25 °C) of compounds indicated ([Porphyrin] in the range of 10^{-6} M) before (solid trace) and after (dotted trace) addition of stoichiometric excess of NaOMe/MeOH (50 μL 1.0 M NaOMe in MeOH). Adapted from Khalil (2010)

The addition of strong bases (such as NaOMe, $^{i}Pr_4NOH$) to the purple solutions of free base and Pt(II) complexes of porpholactones turns them green. Weaker bases such as pyridine or ammonia elicit no spectral changes. The base-induced shifts are also observed in other metal complexes of the porpholactones (e.g., the Ni(II), Zn(II) and Pd(II) complexes, see below). No change is observed for the non-fluorinated Pt(II) porphyrin complex **5Pt**.

The significant changes of the UV-vis spectra of the porphyrinoids upon base addition can be differentiated into two classes: The longest wavelength band is either red-shifted (for $\mathbf{6^F}$, $\mathbf{6^FPt}$, and **6Pt**) or blue-shifted (for $\mathbf{5^F}$ and **6**). The changes in both classes are reversible upon addition of acid and independent of the choice of strong base used (OH^-, MeO^-).

The wide (>100 nm) spectral separation of the longest wavelengths of absorbance (λ_{max}) band of the parent compound and its base-induced species exhibited by the porpholactone Pt(II) complexes **6Pt** and $\mathbf{6^FPt}$ are particularly appealing for a ratiometric protocol of base sensing. A larger proportion of the electron-poor complex $\mathbf{6^FPt}$ reacted under identical base conditions to form a longer wavelength-absorbing species than the non-fluorinated analogue **6Pt**, making it therefore a more sensitive base sensor.

6.3.3 *Mechanistic Considerations*

The mechanism of action can be derived by comparison of the spectral response of the compounds shown in Fig. 6.5 and was confirmed using a range of other spectroscopic and analytical techniques (Khalil et al. 2010). It is known that an inner NH group of electron-poor free base porphyrins is readily deprotonated with strong bases (Woller and Dimagno 1997; Terazono and Dolphin 2003). The expected spectral changes upon deprotonation of an NH group are demonstrated by porphyrin $\mathbf{5^F}$ and porpholactone **6** (e.g., blue-shift of the λ_{max} band). The control compound, Pt(II) complex $\mathbf{5^FPt}$, contains no NH functionality and thus exhibits no optical changes under the same base conditions.

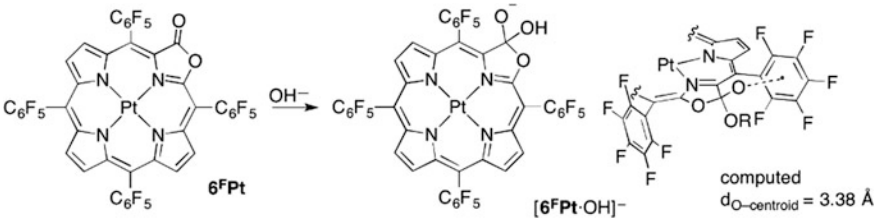

Fig. 6.6 Nucleophilic attack of OH^- onto $\mathbf{6^FPt}$, highlighting the change in hybridization of the lactone carbonyl and the proximity of the orthoester anion charge to the positively polarized center of the flanking pentafluorophenyl group

Notably, free base fluorinated porpholactone **6**$^{\mathbf{F}}$ shows a different response than **5**$^{\mathbf{F}}$ (or **6**)–a distinct red-shift of the λ_{max} band, that is similar to that of the two Pt(II) porpholactones **6Pt** and **6**$^{\mathbf{F}}$**Pt**. Thus, the presence of the lactone moiety coupled with the presence of the electron-withdrawing pentafluorophenyl groups and/or the Pt(II) ion is necessary for such a response. These findings are suggestive of a nucleophilic attack of the hydroxide (or methoxide) onto the lactone moiety (Fig. 6.6), forming an orthoester anion structure (Khalil et al. 2010).

The change of sp^2-hybridization of the lactone carbonyl group upon nucleophilic addition of OH^-/MeO^- to an sp^3-center with the concomitant build-up of an anionic charge at the benzylic position readily rationalizes the observed bathochromic shifts. Precedent cases for both effects are known (McCarthy et al. 2003, 2005; Akhigbe et al. 2009). Molecular modeling of the anionic species suggested a distance of ~3.4 Å of the anionic oxygen to the center of the adjacent pentafluorophenyl group, allowing for a stabilizing anion-π-interaction to occur (Schottel et al. 2008). Because of the rigid porphyrinic ring structure that prevents any ring-opening, no ring-opened forms are expected to contribute to the base species.

6.3.4 Tuning the Halochromic Sensing Range

Considering the mechanism of action of the porpholactone-based high pH sensor dyes, a modulation of the nucleophilicity of the lactone moiety will result in a tuning of its dynamic sensing range. An increase of the nucleophilicity will move the range toward lower pH values, and vice versa. The porpholactone structure offers three obvious positions for modulation: the central metal, the *meso*-aryl groups, and the porpholactone chromophore. In a series of experiments, all three positions were varied (Fig. 6.7) and their apparent pK_{OH} values of the sensors determined (Worlinsky et al. 2013).

As expected, the variation of the *meso*-aryl group from phenyl ($-C_6H_5$) to penta-fluorophenyl ($-C_6F_5$) had a large effect, shifting the pK_{OH} values for each comparable pair by 1–2 log units to lower values. The influence of the metal was

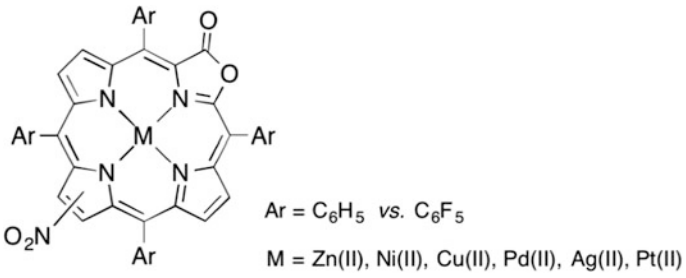

Fig. 6.7 Series of derivatives prepared to study the influence of the central metal, the *meso*-aryl group, and β-nitration on the dynamic halochromic sensing range of the high pH sensors by titration in aqueous solutions in the presence of Cremophore® (Worlinsky 2013)

comparably small, generally within ~0.4 log units. Considering all metals tested were divalent, this may simply be a reflection of their similar charge densities. Correspondingly, later work showed that the use of trivalent metals [such as Ga (III)] shifted the sensing range significantly to lower pH ranges (Worlinsky et al. 2014). The nitration of the β-position had a large but varied effect (between 0.5 and 1.6 log unit increase in base sensitivity). However, the titrations were less well-defined, presumably because of the lack of regioselectivity in the introduction of the nitro group. Thus, the titrations were performed with a mixture of two compounds that each possess slightly different response profiles, leading to a wash-out of the observed titration curve. Most important, however, the work identified the cheaper and easier to prepare zinc, copper and silver complexes of $\mathbf{6^F}$ as excellent alternatives to $\mathbf{6^FPt}$. A fourth option of modulating the sensing range is offered by varying the sensor matrix (Worlinsky et al. 2015).

6.3.5 Chromophore Stability

One of the major factors for the practical utility of a sensor is its chemical stability toward oxidations or solvolytic processes, both of which may be accelerated at high pH values. Pentafluorophenyl-substituted chromophores, including porpholactones, have distinguished themselves in unrelated work through much greater photo-stability than the corresponding tetraphenyl- or even pentafluorophenyl-porphyrins. This increased stability was attributed to the electron-withdrawing effects of the *meso*-aryl group (Gouterman et al. 2004; Khalil 2004; Zelelow 2003). Moreover, porpholactones are already oxidation products of porphyrins. Thus, pentafluorophenyl-substituted porpholactones are expected to be particularly stable toward further oxidative degradation. Indeed, irradiation of a film containing $\mathbf{6^FPt}$ over 60 min in aerobic conditions reduced the absorbance intensity by less than 3%. However, a regular porphyrin or chlorin exposed to the same conditions, might be degraded by as much as 30%. $\mathbf{6^FPt}$- and $\mathbf{6^FGaCl}$-based optodes were stable over months and could be reused repeatedly without any degradation in performance (Worlinsky et al. 2014).

6.3.6 Base Sensing with Porpholactones in Aqueous Solutions: Addition of Surfactants

Porphyrins and porpholactones of the type $\mathbf{5/5^F}$ or $\mathbf{6/6^F}$ are not water-soluble. However, a solution of these compounds in DMF containing Cremophor EL® (a synthetic, nonionic polyethoxylated castor oil-based surfactant), can be diluted with water to form stable emulsions that allow their pH titrations in an aqueous environment (over a limited period of time as Cremophore is also getting hydrolyzed under high pH conditions, slowly reducing the pH of the solution as shown in

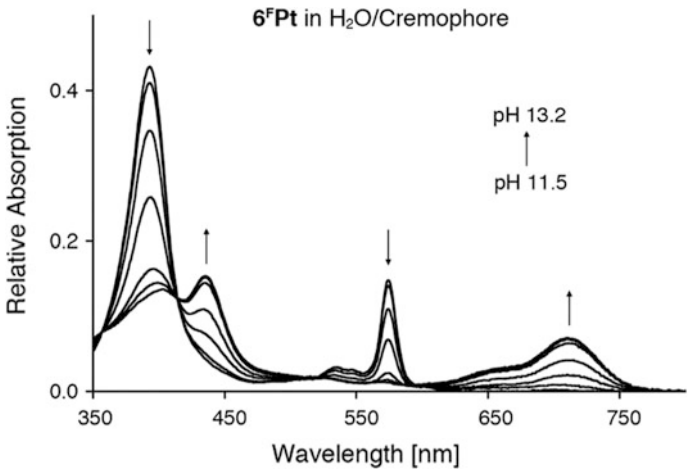

Fig. 6.8 UV-vis titration of $\mathbf{6^{F}Pt}$ (2.4×10^{-6} M in 3 mL water + 5% Cremophor EL® + 5% DMF, 25 °C) with 0.1–5 M NaOH solutions to the pH values indicated. Adapted from (Khalil 2010)

Fig. 6.8). The base titration of $\mathbf{6^{F}}$ shows an approximately 50-fold increase of absorbance at 708 nm in the pH range from 11.5 to 13.2 characteristic for the hydroxide adduct, and a corresponding reduction of the peaks characterizing the neutral species, with sharp isosbestic points. A distinct hysteresis of the UV-vis/fluorescence response to the down and upwards changing pH was noted, indicative for a slower rate of the reverse reaction of the nucleophile addition to the lactone. An effective pK_{OH} value of 12.6 can be computed for this indicator. However, since the physical basis for the operation of the indicator is not based on its Brønsted acidity but on the susceptibility of its lactone carbonyl group toward nucleophilic attack, this value is difficult to compare to the classic pK_a of most other pH sensors.

6.3.7 Base Sensing with Porpholactones in Aqueous Solutions: Water-Soluble Porpholactone Derivatives

The use of surfactants is becoming obsolete with freely water-soluble porpholactone derivatives. The *p*-F atoms of the pentafluorophenyl groups are susceptible to a nucleophilic aromatic substitution reaction using soft nucleophiles, such as amines and thiols (Battioni et al. 1991; Shaw et al. 1999; Samaroo et al. 2007; Ke et al. 2014; Hewage et al. 2015). Thus, reaction of the porpholactones $\mathbf{6^{F}M}$ with a sufficiently long polyethyleneglycol (PEG) and thiol-terminated chain generates porpholactones carrying four PEG chains (Fig. 6.9; Worlinsky et al. 2014, 2015). With PEGs chains of an average molecular weight of 1000 Da, freely water-soluble

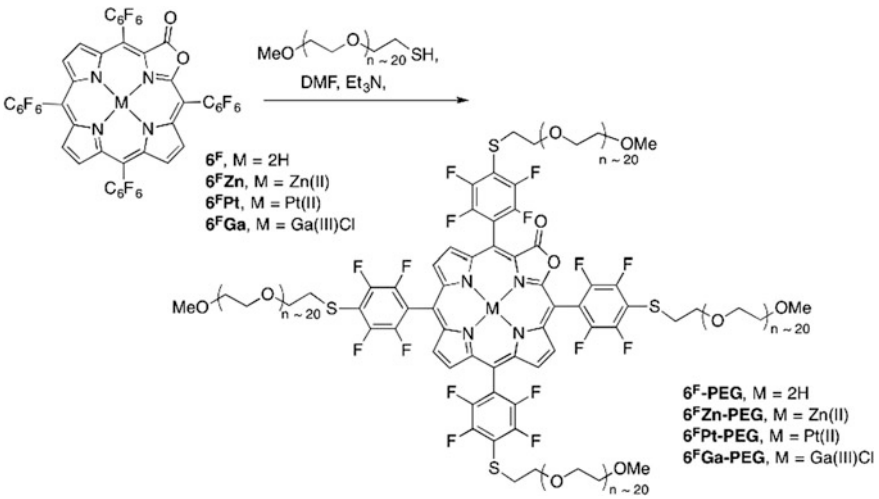

Fig. 6.9 Formation of the water-soluble porpholactones by PEGylation (Worlinsky 2015)

derivatives could be obtained. Much shorter PEG chains were found to be unsuitable to generate freely water-soluble porphyrins.

The optical properties of these derivatives in water (Fig. 6.10) are essentially unchanged from their non-water-soluble derivatives in organic solvents or water in the presence of a surfactant (Figs. 6.5 and 6.8). Their water-solubility allows their titration in aqueous solution and the determination of their pK_{OH} values. The titration of **6^FPt-PEG** shows sharp isosbestic points and a titration curve corresponding to a monobasic event, with a midpoint (pK_{OH}) of 11.2. This value is significantly lower than that determined for the same sensor in water in the presence of the surfactant Cremophore® (Khalil et al. 2010). The shift of the effective dynamic range of the sensor in the presence of the surfactant was attributed to the micellar structure of the surfactant solution that is bundling the sensor in the micelles. This leads to a greater electrostatic repulsions of the anionic form of the sensor when compared to their freely soluble forms, therefore requiring higher base concentrations to achieve the same degree of reaction with hydroxide.

The zinc complex **6^FZn-PEG** possessed a similar pK_{OH} (as shown in Fig. 10.9) than the corresponding platinum complex, highlighting the minor effect of the central metal if the charge of the metal remains unaltered (here, +2 in both cases; see also above discussion of the modulation of the sensing range). If, however, a higher charged metal ion is coordinated to the porpholactone, as the +3 metal Ga (III) in **6^FGa-PEG**, this significantly increases the nucleophilicity of the sensor and thus lowers its pK_{OH} value to 9.3 (Worlinsky et al. 2015).

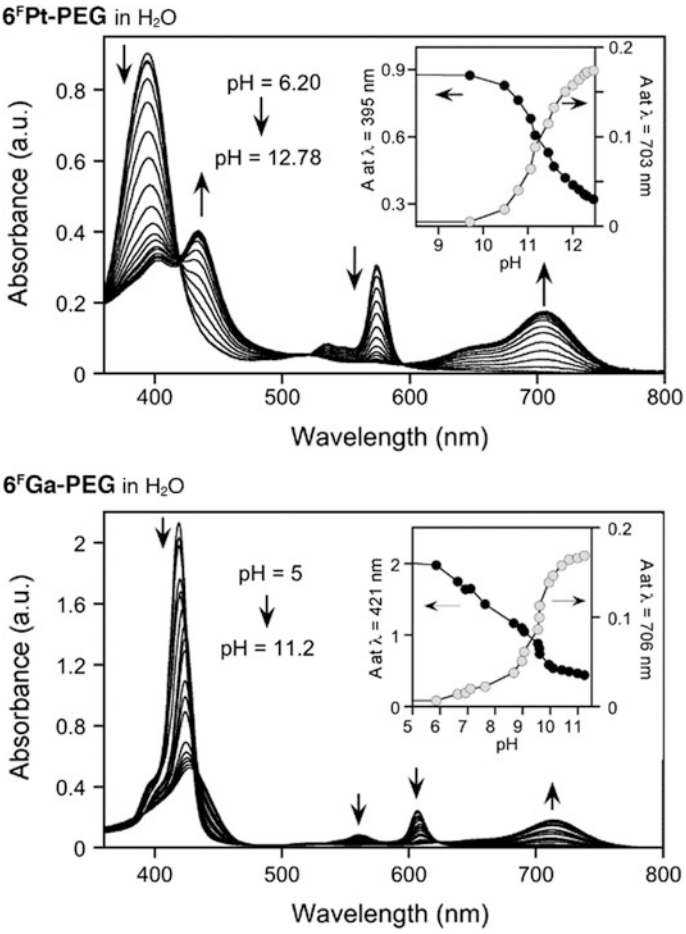

Fig. 6.10 UV-vis spectra of the species indicated upon titrations with base. Inserts: titration curves at the wavelength indicated. *Conditions:* porphyrinoid ($\sim 10^{-6}$ M) in 3 mL H_2O at ambient T, titrated with 0.1–5 M NaOH solutions to the pH values recorded. The equilibrium was established upon the completion of the mixing. Dilution factors <3%. Adapted from Worlinsky (2015)

6.3.8 *Aqueous Base Sensing Porpholactone Holochromic Sensors Embedded in Polymer Matrixes*

Embedding the sensor dye into a polymer allows the construction of optodes and optical fiber-based sensors (Korostynska et al. 2007; Nguyen et al. 2014). The feasibility of embedding sensor **6^FPt** into a polymer for use as a high pH optode was demonstrated by dissolving it into an ion-permeable poly(methyl-metha-crylate)/methy-lene-bis-acryl-amide-methacryl-amido-propyl trimethyl-ammonium

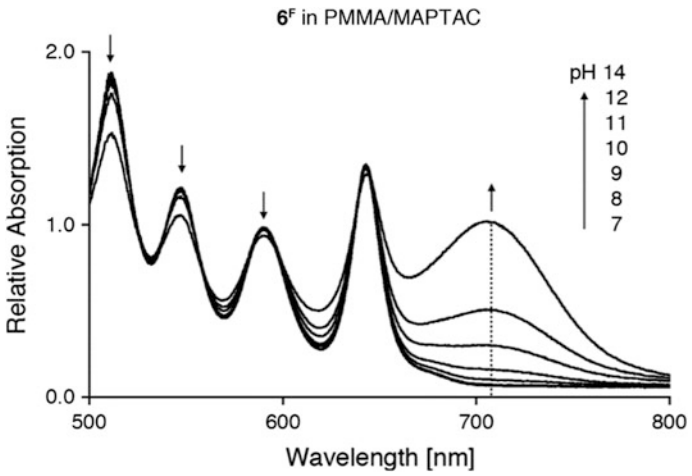

Fig. 6.11 UV-vis of $\mathbf{6}^{\mathbf{F}}$ embedded in a spin-coated layer of PMMA/MAPTAC on a polycarbonate sheet and immersed in pH buffers indicated. Measurements after 5 min equilibration time at 25 °C. Adapted from Khalil (2010)

chloride co-polymer (PMMA/MAPTAC) film that was then spin-coated and dried onto a polycarbonate sheet (Fig. 6.11). This polymer was chosen as its refractive index matches that of the fiber optical core of the optical fiber intended for the fabrication of the optodes, its mechanical robustness, and its previous application in pH sensing (Hara et al. 2009). Immersed into basic pH buffer solutions, it showed the emergence of the base-form of the sensor (indicated by the increase of the band at 710 nm) from pH values of 10 upwards, with significant changes between pH 12 and 14. Not all chromophores present in the polymer matrix are, however, converted to the base form, likely as a function of the film thickness and slow OH^- permeability. Noticeable is also a slight decrease in the apparent pK_{OH} value of the sensor when compared to solution state data (Figs. 6.5 and 6.8), an effect that could be attributed to the polymer matrix as the embedding of other pH dyes in the same matrix led to comparable shifts (Khalil et al. 2010).

A sensor bead of $\mathbf{6}^{\mathbf{F}}\mathbf{Pt}$, embedded in a PMMA/MAPTAC copolymer and mixed with alumina particles for better light reflectance, was attached to the end of an optical Y-configured optical fiber (sensor bead at one end of the fiber, then Y-junction with one end going to the light source and the other end going to the spectrometer). This optode is suitable for pH sensing (Khalil et al. 2010).

The single wavelength response (at 710 nm) of this pH optode to a pH change from pH 7–13, and then back to pH 9 in two steps is shown in Fig. 6.12. The initial steep pH gradient elicits the expected response (intensity increase of the band at 710 nm) and reaches the near-maximum absorbance (equilibrium) value within 30 min. Again, this relatively slow response is a function of the (thickness) of the polymer matrix as the nucleophilic addition reaction in solution is completed upon mixing of the reagents (see above). In this configuration, the optode is only suitable

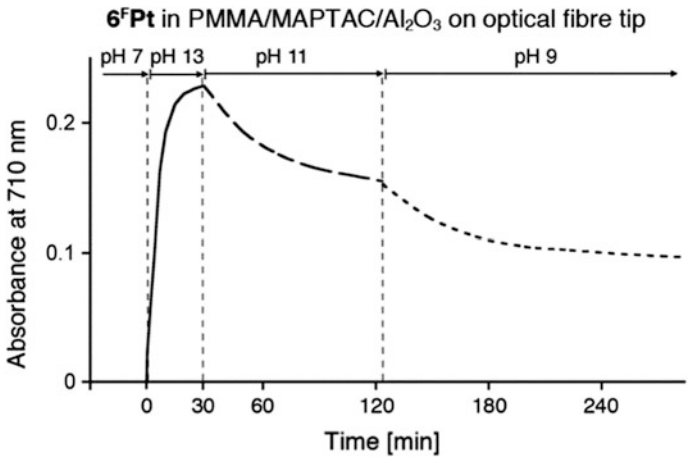

Fig. 6.12 History plot of $\mathbf{T^{F}PLPt}$ embedded in a 25% PMMA/MAPTAC copolymer bead containing alumina particles attached to the tip of an optical fiber submersed in the pH buffers indicated, at 25 °C. Adapted from Khalil (2010)

Fig. 6.13 Chemical structure of Nafion®

$$[(CF_2\text{-}CF_2)_m\text{-}CF(O(CF_2\text{-}CF(CF_3))_p\text{-}OCF_2\text{-}CF_2\text{-}SO_3H)\text{-}CF_2]_n$$

m = 5-13.5
n = ~1000
p = 1-3

for the monitoring of slow processes. This optode proved to be very robust against interference by the complex and high ionic strength aqueous medium represented by a high pH (pH $\sim$ 13) Portland cement slurry that was also allowed to harden around the sensor bead. The optical response differences to buffer solution data were minimal (Khalil et al. 2010).

Nafion®, a sulfonated tetrafluoroethylene based fluoropolymer-copolymer (Fig. 6.13) and polytetrafluoroethylene (PTFE)/Nafion® sandwiches are materials of high chemical, thermal and mechanical stability, and optical transparency. Nafion® membranes were reported as a carrier for a number of optical chemosensors (Misra et al. 2002; Castriciano et al. 2010; Sendhil et al. 2005). On account of the presence of the sulfonate groups, they are hydrophilic with a high ion conductivity. Solutions of this polymer (in water/dimethylformamide) can be cast into very thin films. These properties make Nafion® an attractive matrix material for high pH-sensing membranes.

The incorporation of the water-soluble metalloporpholactones $\mathbf{6^{F}Pt\text{-}PEG}$ and $\mathbf{6^{F}Ga\text{-}PEG}$ into the Nafion® layer of PTFE/Nafion® sandwiches was accomplished and their efficacy as cyanide (Worlinsky et al. 2014) and high pH sensors (Worlinsky et al. 2015) was demonstrated (Fig. 6.14).

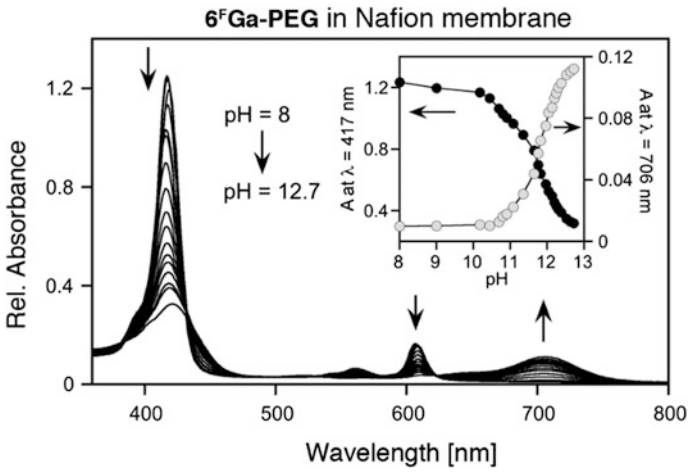

Fig. 6.14 UV-vis titration of **6^{F}Ga-PEG** in Nafion® membrane: ~10 μmol **6^{F}Ga-PEG**/cm^2; membrane suspended in aqueous solution at ambient T, titrated with 0.1–5 M NaOH solution to the pH values recorded. 20 min time to allow for achievement of equilibrium between titration points. Insert: titration curves at the wavelength indicated. Adapted from Worlinsky (2015)

The UV-vis spectra of the membranes (Fig. 6.14) show the presence of the porphyrinoids, with only minor solvatochromic shifts or spectra broadening, compared to the spectra of the corresponding porpholactones in water (Fig. 6.10; Worlinsky et al. 2015). This indicates that the sensors were freely dissolved, not significantly stacked, or in an environment that otherwise changed their optical properties (Worlinsky et al. 2015). Exposure of the Nafion® film containing the sensor dyes to high pH solutions yielded qualitatively the same response as the solution data, notably the appearance of the diagnostic new base band (Figs. 6.10 and 6.14). However, two major quantitative differences can be made out: Firstly, the response of the sensor in the membrane is diffusion-limited and therefore much slower than in solution state. The equilibrium state was reached after ~20 min. Thus, even at the thickness of the membrane of only 0.025 mm (1–2 mil), it presents a significant diffusional barrier. Secondly, and most importantly, sensor **6^{F}Ga-PEG$_{1000}$** in free solution is at pH 11 already quantitatively converted to its base-form, but embedded in the Nafion® membrane it is much less sensitive to base, with a pK_{OH} of only 11.8 (9.3 in solution). Such a shift to higher [OH^-] values for the Nafion®-embedded sensors was also observed for the other metalloporpholactones. Evidently, the anionic Nafion® polymer poses a significant electrostatic barrier for hydroxide anions.

Thus the use of a Nafion® polymer matrix trades response time for chemical stability (Fig. 6.15). Alternating high pH and buffer solutions show that the halochromic response of Nafion®-embedded **6^{F}Ga-PEG$_{1000}$** is reversible; the maintenance of the signal strength shows the durability of the sensor membrane (Worlinsky et al. 2015). The small variations of the sensor were attributed to slight

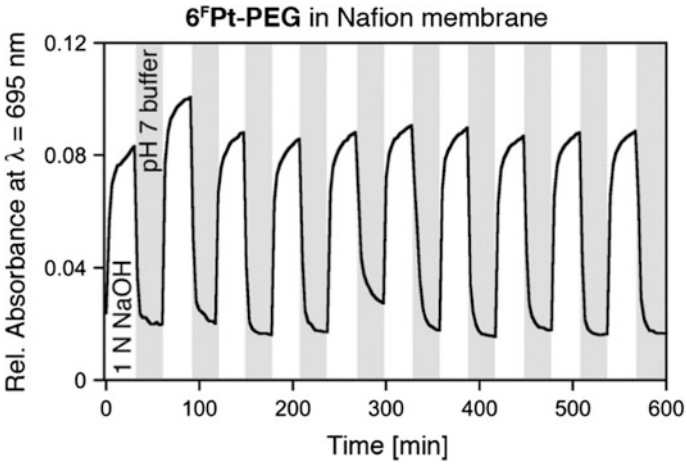

Fig. 6.15 UV-vis signal of the **6^{F}Pt-PEG** in Nafion® membrane upon repeated exposure to 1 M NaOH for 30 min, followed by pH 7 buffer for 30 min each. Adapted from Worlinsky (2015)

positional changes of the soft membrane in the light beam. Importantly, no degradation or leaching of the dye was observed. Upon exposure to high hydroxide conditions, ~80% of the signal height is achieved within 3 min, but the reverse reaction is much faster (~30 s), supporting the electrostatic argument brought forward to explain the slow diffusion of hydroxide into the anionic Nafion® framework.

6.4 Conclusion

Porpholactones and their metal derivatives are suitable as high pH sensors possessing a dynamic range in an unusual high pH range. They operate by a nucleophilic attack by OH^- (or MeO^-, and presumably other alkoxides) onto the lactone carbonyl mechanism. This mechanism changes the optical properties of the porpholactone drastically upon hydroxide attack, leading to the appearance of new peaks in their high extinction coefficient UV-vis spectra that are more than 100 nm apart from the parent porpholactone spectra. This spectral property allows for a highly useful ratiometric sensing method. The pH dynamic sensing range can be modulated to fall into the range between 9 and 13 by variation of the central metals, variation of the aryl groups, modification of the β-positions, or by embedding the sensor dye into different matrix materials. The use of the *meso*-pentafluorophenyl-based porpholactones endows the sensor dyes with a number of particularly favourable chemical and physical properties: excellent solubility in organic solvents, high chemical stability, and the ability to modify the pentaflurophenyl groups to generate water-soluble derivatives. Organic solvent and

water-soluble derivatives could be embedded into polymeric matrixes for the realization of optodes.

The fundamental work toward the synthesis and modification of a wide range of porpholactones has advanced to the point that they are now readily available from a number of simple starting materials; in fact, they are also commercially available. As their principle efficacy as halochromic sensors was also shown, we predict their continued utilization in the field of material sciences and diagnostic infrastructure applications.

References

Akhigbe, J., Ryppa, C., Zeller, M., & Brückner, C. (2009). Oxazolochlorins. 2. Intramolecular Cannizzaro reaction of *meso*-tetraphenylsecochlorin bisaldehyde. *The Journal of Organic Chemistry, 74*(14), 4927–4933.

Bakker, E., Bühlmann, P., & Pretsch, E. (1997). Carrier-based ion-selective electrodes and bulk optodes. 1. General characteristics. *Chemical Reviews, 97*(8), 3083–3132.

Battioni, P., Brigaud, O., Desvaux, H., Mansuy, D., & Traylor, T. G. (1991). Preparation of functionalized polyhalogenated tetraaryl-porphyrins by selective substitution of the *p*-fluorines of *meso*-tetra-(pentafluorophenyl)porphyrins. *Tetrahedron Letters, 32*(25), 2893–2896.

Blair, T. L., Allen, J. R., Daunert, S., & Bachas, L. G. (1993). Potentiometric and fiber optic sensors for pH based on an electropolymerized cobalt porphyrin. *Analytical Chemistry, 65*(15), 2155–2158.

Brückner, C., Foss, P. C. D., Sullivan, J. O., Pelto, R., Zeller, M., Birge, R. R., et al. (2006). Origin of the bathochromically shifted optical spectra of *meso*-tetrathien-2′- and 3′-ylporphyrins as compared to *meso*-tetraphenylporphyrin. *Physical Chemistry Chemical Physics, 8*(20), 2402–2412.

Brückner, C., Ogikubo, J., McCarthy, J. R., Akhigbe, J., Hyland, M. A., Daddario, P., et al. (2012). Oxazolochlorins. 6. *meso*-Arylporpholactones and their reduction products. *The Journal of Organic Chemistry, 77*(15), 6480–6494.

Bühlmann, P., Pretsch, E., & Bakker, E. (1998). Carrier-based ion-selective electrodes and bulk optodes. 2. Ionophores for potentiometric and optical sensors. *Chemical Reviews, 98*(4), 1593–1688.

Castriciano, M. A., Carbone, A., Saccà, A., Donato, M. G., Micali, N., Romeo, A., et al. (2010). Optical and sensing features of $TPPS_4$ J-aggregates embedded in Nafion® membranes: Influence of casting solvents. *Journal of Materials Chemistry, 2*(14), 2882–2886.

Chitarra, L. G., Breeuwer, P., van den Bulk, R. W., & Abee, T. (2000). Rapid fluorescence assessment of intracellular pH as a viability indicator of *Clavibacter michiganensis* subsp. *michiganensis*. *Journal of Applied Microbiology, 88*(5), 809–816.

Crossley, M. J., & King, L. G. (1984). Novel heterocyclic systems from selective oxidation at the β-pyrrolic position of porphyrins. *Journal of the Chemical Society, Chemical Communications, 14,* 920–922.

Cusano, A., Cutolo, A., & Giordano, M. (2008). Editorial [Hot topic: Fiber optic chemical and biological sensors: Perspectives and challenges approaching the nano-era]. *Current Analytical Chemistry, 4*(4), 271–402.

Czarnik, A. W., & Yoon, J. (1999). Chemosensors: Synthetic receptors in analytical sensing applications. In: D. N. Reinhoudt (Ed.), *Perspectives in supramolecular chemistry* (pp. 177–191). Chichester, UK: Wiley.

Delmarre, D., Méallet-Renault, R., Bied-Charreton, C., & Pasternack, R. F. (1999). Incorporation of water-soluble porphyrins in sol–gel matrices and application to pH sensing. *Analytica Chimica Acta, 401*(1), 125–128.

Derinkuyu, S., Ertekin, K., Oter, O., Denizalti, S., & Cetinkaya, E. (2007). Fiber optic pH sensing with long wavelength excitable Schiff bases in the pH range of 7.0–12.0. *Analytica Chimica Acta, 588*(1), 42–49.

Dong, S., Luo, M., Peng, G., & Cheng, W. (2008). Broad range pH sensor based on sol–gel entrapped indicators on fibre optic. *Sensors and Actuators: B. Chemical, 129*(1), 94–98.

Ensafi, A. A., & Kazemzadeh, A. (1999). Optical pH sensor based on chemical modification of polymer film. *Microchemical Journal, 63*(3), 381–388.

Gouterman, M. (1978). Optical spectra and electronic structure of porphyrins and related ring. In: D. Dolphin (Ed.), *The Porphyrins,* Vol. 3 (pp. 1–165). New York: Academic Press.

Gouterman, M., Callis, J., Dalton, L., Khalil, G., Mébarki, Y., Cooper, K. R., et al. (2004). Dual luminophor pressure-sensitive paint III. Application to automotive model testing. *Measurement Science and Technology, 15*(10), 1986–1994.

Gouterman, M., Hall, R. J., Khalil, G. E., Martin, P. C., Shankland, E. G., & Cerny, R. L. (1989). Tetrakis(pentafluorophenyl)porpholactone. *Journal of the American Chemical Society, 111* (10), 3702–3707.

Gulino, A., Mineo, P., Bazzano, S., Vitalini, D., & Fragalà, I. (2005). Optical pH meter by means of a porphyrin monolayer covalently assembled on a molecularly engineered silica surface. *Chemistry of Materials, 17*(16), 4043–4045.

Hara, N., Ohashi, H., Ito, T., & Yamaguchi, T. (2009). Reverse response of an ion-recognition polyampholyte to specific ion signals at different pHs. *Macromolecules, 42*(4), 980–986.

Hewage, N., Yang, B., Agrios, A. G., & Brückner, C. (2015). Introduction of carboxylic ester and acid functionalities to *meso*-tetrakis(pentafluorophenyl)porphyrin and their limited electronic effects on the chromophore. *Dyes and Pigments, 121,* 159–169.

Igarashi, S., Kuwae, K., & Yotsuyanagi, T. (1994). Optical pH sensor of electrostatically immobilized porphyrin on the surface of sulfonated-polystyrene. *Analytical Sciences, 10*(5), 821–822.

Ke, X., Yang, B., Cheng, X., Chan, S. L., & Zhang, J. (2014). Ytterbium(III) porpholactones: β-Lactonization of porphyrin ligands enhances sensitization efficiency of lanthanide near-infrared luminescence. *Chemistry-A European Journal, 20*(15), 4324–4333.

Khalil, G. (2004). Dual-luminophor pressure-sensitive paint I. Ratio of reference to sensor giving a small temperature dependency. *Sensors and Actuators B: Chemical, 97*(1), 13–21.

Khalil, G. E., Daddario, P., Lau, K. S. F., Imtiaz, S., King, M., Gouterman, M., et al. (2010). Oxazolochlorins. 3. *meso*-Tetraarylporpholactones as high pH sensors. *The Analyst, 135*(8), 4505–4508.

Khalil, G., Gouterman, M., Ching, S., Costin, C., Coyle, L., Gouin, S., et al. (2002). Synthesis and spectroscopic characterization of Ni, Zn, Pd and Pt tetra(pentafluorophenyl)porpholactone with comparisons to Mg, Zn, Y, Pd and Pt metal complexes of tetra(pentafluorophenyl)porphine. *Journal of Porphyrins and Phthalocyanines, 6*(2), 135–145.

Koncki, R., & Wolfbeis, O. S. (1998). Composite films of Prussian blue and *N*-substituted polypyrroles: Fabrication and application to optical determination of pH. *Analytical Chemistry, 70*(13), 2544–2550.

Korostynska, O., Arshak, K., Gill, E. I., & Arshak, A. (2007). Review on state-of-the-art in polymer based pH sensors. *Sensors, 7*(12), 3027–3042.

Li, C., Zhang, X., Han, Z., Åkermark, B., Sun, L., Shen, G., et al. (2006). A wide pH range optical sensing system based on a sol-gel encapsulated amino-functionalised corrole. *Analyst, 131*(3), 388–393.

Liang, L., Lv, H., Yu, Y., Wang, P., & Zhang, J. (2012). Iron(III) tetrakis(pentafluorophenyl)-porpholactone catalyzes nitrogen atom transfer to C=C and C–H bonds with organic azides. *Dalton Transactions, 41*(5), 1457–1460.

Liu, E., Ghandehari, M., Brückner, C., Khalil, G., Worlinsky, J., Jin, W., et al. (2017). Mapping high pH levels in hydrated calcium silicates. *Cement and Concrete Research, 95,* 232–239.

Lv, H., Yang, B., Jing, J., Yu, Y., Zhang, J., & Zhang, J. (2012). Dual facet of gold(III) in the reactions of gold(III) and porphyrins. *Dalton Transactions, 41*(11), 3116–3118.

Mahammed, A., Weaver, J. J., Gray, H. B., Abdelas, M., & Gross, Z. (2003). How acidic are corroles and why? *Tetrahedron Letters, 44*(10), 2077–2079.

McCarthy, J. R., Melfi, P. J., Capetta, S. H., & Brückner, C. (2003). Use of Ag(II) as a removable template in porphyrin chemistry: Diol cleavage products of [*meso*-tetraphenyl-2,3-*cis*-diolchlorinato]silver(II). *Tetrahedron, 59*(46), 9137–9146.

McCarthy, J. R., Perez, J. M., Brückner, C., & Weissleder, R. (2005). Polymeric nanoparticle preparation that eradicates tumors. *Nano Letters, 5*(12), 2552–2556.

Misra, V., Mishra, H., Joshi, H. C., & Pant, T. C. (2002). An optical pH sensor based on excitation energy transfer in Nafion® film. *Sensors and Actuators: B. Chemical, 82*(2–3), 133–141.

Nguyen, T. H., Venugopala, T., Chen, S., Sun, T., Grattan, K. T. V., Taylor, S. E., et al. (2014). Fluorescence based fibre optic pH sensor for the pH 10–13 range suitable for corrosion monitoring in concrete structures. *Sensors and Actuators B: Chemical, 191,* 498–507.

Niu, C., Gui, X., Zeng, G., & Yuan, X. (2005). A ratiometric fluorescence sensor with broad dynamic range based on two pH-sensitive fluorophores. *Analyst, 13*(11), 1551–1556.

Ou, Z., Shen, J., Shao, J., Wenbo, E., Gałezowski, M., Gryko, D. T., et al. (2007). Protonated free-base corroles: Acidity, electrochemistry, and spectroelectrochemistry of $[(Cor)H_4]^+$, $[(Cor)H_5]^{2+}$, and $[(Cor)H_6]^{3+}$. *Inorganic Chemistry, 46*(7), 2775–2786.

Papkovsky, D. B., Ovchinnikov, A. N., Ponomarev, G. V., & Korpela, T. (1997). Complexes of the phosphorescent porphyrin dyes with hydrophilic carriers: Optical properties and sensing applications. *Analytical Letters, 30*(4), 699–716.

Safavi, A., & Abdollahi, H. (1998). Optical sensor for high pH values. *Analytica Chimica Acta, 367*(1), 167–173.

Safavi, A., & Banazadeh, A. R. (2007). Dynamic method as a simple approach for wide range pH measurements using optodes. *Analytica Chimica Acta, 583*(2), 326–331.

Safavi, A., & Sadeghi, M. (2007). Development of an optode membrane for high pH values. *Spectrochimica Acta Part A: Molecular and Biomolecular Spectroscopy, 66*(3), 575–577.

Samaroo, D., Vinodu, M., Chen, X., & Drain, C. M. (2007). *meso*-Tetra(pentafluorophenyl)porphyrin as an efficient platform for combinatorial synthesis and the selection of new photodynamic therapeutics using a cancer cell line. *Journal of Combinatorial Chemistry, 9*(6), 998–1011.

Schottel, B. L., Chifotides, H. T., & Dunbar, K. R. (2008). Anion-π interactions. *Chemical Society Reviews, 37*(1), 68–83.

Sendhil, K., Vijayan, C., & Kothiyal, M. P. (2005). Nonlinear optical properties of a porphyrin derivative incorporated in Nafion polymer. *Optical Materials, 27*(10), 1606–1609.

Shaw, S. J., Edwards, C., & Boyle, R. W. (1999). Regioselective synthesis of multifunctionalised porphyrins-coupling of mono-(pentafluorophenyl)porphyrins to electrophiles. *Tetrahedron Letters, 40*(42), 7585–7586.

Terazono, Y., & Dolphin, D. (2003). Synthesis of the hemin of β-tetrakis(trifluoromethyl)-*meso*-tetraphenylporphyrin and its evaluation as a P-450 mimic. *Inorganica Chimica Acta, 346,* 261–264.

Thyagarajan, S., Leiding, T., Arsköld, S. P., Cheprakov, A. V., & Vinogradov, S. A. (2010). Highly non-planar dendritic porphyrin for pH sensing: Observation of porphyrin monocation. *Inorganic Chemistry, 49*(21), 9909–9920.

Werner, T., & Wolfbeis, O. S. (1993). Optical sensor for the pH 10–13 range using a new support material. *Fresenius' Journal of Analytical Chemistry, 346*(6–9), 564–568.

Woller, E. K., & Dimagno, S. G. (1997). 2,3,7,8,12,13,17,18-Octafluoro-5,10,15,20-tetraarylporphyrins and their zinc complexes: First spectroscopic, electrochemical, and structural characterization of a perfluorinated tetraarylmetalloporphyrin. *The Journal of Organic Chemistry, 62*(6), 1588–1593.

Worlinsky, J. L., Halepas, S., & Brückner, C. (2014). PEGylated *meso*-arylporpholactone metal complexes as optical cyanide sensors in water. *Organic & Biomolecular Chemistry, 12*(23), 3991–4001.

Worlinsky, J. L., Halepas, S., Ghandehari, M., Khalil, G., & Brückner, C. (2015). High pH sensing with water-soluble porpholactone derivatives and their incorporation into a Nafion® optode membrane. *The Analyst, 140*(1), 190–196.

Worlinsky, J. L., Zarate, G., Zeller, M., Ghandehari, M., Khalil, G., & Brückner, C. (2013). Oxazolochlorins 11: Tuning the dynamic high pH sensing range of [*meso*-tetraarylporpholactonato] M(II) complexes by variation of the central metal ion, the aryl substituents, and introduction of a β-nitro group. *Journal of Porphyrins and Phthalocyanines, 17*(08), 836–849.

Yu, Y., Czepukojc, B., Jacob, C., Jiang, Y., Zeller, M., Brückner, C., et al. (2013). Porphothionolactones: Synthesis, structure, physical, and chemical properties of a chemodosimeter for hypochlorite. *Organic & Biomolecular Chemistry, 11*(28), 4613–4621.

Yu, Y., Lv, H., Ke, X., Yang, B., & Zhang, J. (2012). Ruthenium-catalyzed oxidation of the porphyrin β, β′-pyrrolic ring: A general and efficient approach to porpholactones. *Advanced Synthesis & Catalysis, 354*(18), 3509–3516.

Yuan, R., Chai, Y., Shen, G., & Yu, R. (1993). Chemically modified electrode based on poly[tetra (4-aminophenyl)porphyrin] as a pH sensor. *Talanta, 40*(8), 1255–1259.

Zelelow, B. (2003). Dual luminophor pressure sensitive paint II. Lifetime based measurement of pressure and temperature. *Sensors and Actuators B: Chemical, 96*(1–2), 304–314.

Chapter 7
Sensing of Dissolved Chlorides Using Intrinsic Signals

Masoud Ghandehari, Cristian S. Vimer and Peter Spellane

Abstract The dissolution of a "structure breaking reagent" such as NaCl results in reduction of hydrogen bonds between water molecules and a corresponding change in the absorption of electromagnetic energy at specific absorption bands (Chap. 1). This change in energy absorption is proportional to the amount of salt dissolved in water. Sodium and Calcium Chlorides are among the strongest structure-breaking reagents, a quality which is used in deicing agents. As part of a program investigating the use of optical spectroscopy for applications to the subsurface monitoring of infrastructure materials, a study was carried out involving analysis of the Near-Infrared (NIR) spectra of EM radiation when interacting with aqueous solutions containing dissolved Sodium Chloride (NaCl). This chapter described results of sensitivity and calibration procedures for in situ intrinsic sensing of dissolved Chlorides.

7.1 Introduction

Using optical waveguides, laboratory experiments were carried out with Chloride concentrations ranging from 0.5 to 5 weight percent (equivalent to 0.085–0.85 M Chloride solutions). The Near-Infrared absorption spectra of the solutions were studied simultaneously with the effect of alkalinity and temperature on the absorption spectra. Results of experiments are presented and a technique for calibration is proposed. This study highlights the intrinsic optical characteristic of aqueous solu-

M. Ghandehari (✉)
New York University, Six Metrotech Center, Brooklyn, NY 11201, USA
e-mail: masoud@nyu.edu

C. S. Vimer
Madsen Consulting Engineering, 175 Varick St #803, New York, NY 10014, USA
e-mail: cvimer@gmail.com

P. Spellane
Chemistry Department, New York City College of Technology (CUNY),
Brooklyn, NY 11201, USA
e-mail: pspellane@citytech.cuny.edu

M. Ghandehari, *Optical Phenomenology and Applications*,
Smart Sensors, Measurement and Instrumentation 28,
https://doi.org/10.1007/978-3-319-70715-0_7

tions as a reagent free approach for long-term and continuous monitoring of the subsurface environment with applications including soil and concrete infrastructure.

There are several scenarios where in situ and long term monitoring of subsurface dissolved Chloride ions is necessary and valuable. Examples include ground water monitoring, particularly near bodies of salty water (Mortl et al. 2006; Charette and Allen 2006; Liu et al. 2006; Furby et al. 2010; Arslan and Demir 2013; Wood and Harrington 2015), and health monitoring of cement based infrastructure (Jin et al. 2017; Yu et al. 2007; Chen et al. 2012; Sookoomjariyapong et al. 2011; Darmawan 2010; Bae et al. 2014; Nie et al. 2016). The application to ground water salinity as a result of salt intrusion is intuitive, while the presence of salinity in concrete infrastructure is equally significant. Sources of Chlorides that impact the degradation of infrastructure include exposure to coastal environments and deicing salts.

The role of Chloride ions in iron corrosion is widely recognized and documented, however it is not completely understood. The most accepted theory states that, when the Chloride ion concentration surpasses a certain threshold value, ferrous Chloride, or a ferrous Chloride complex, forms on the steel surface, replacing the protective oxide. In the absence of the protective oxide, iron tends to turn into its more thermodynamically unstable state through a corrosion process.

In most cases, pitting corrosion of reinforced and/or prestressed steel in concrete is a result of exposure to Chlorides. Pitting corrosion is localized and it can occur very rapidly. Chloride ions attack the passivity of steel, resulting in accelerated corrosion even without a decrease in pH levels (Alonso, et al. 2002; Angst et al. 2009). This also applies to general oxidation of steel reinforcements when adequate moisture is present (Moreno et al. 2004; Assouli et al. 2005; Hansson and Sorensen 1990; Holden et al. 1983; Mehta et al. 1992; Dhir et al. 1993; Saremi and Mahallati 2002; Darmawan 2010).

Numerous investigations have been carried out using electrochemical tests (potentiodynamic polarization tests, polarization resistance measurements, half-cell potential tests etc.) in simulated concrete pore solutions aiming to determine a universal critical Chloride concentration for pitting initiation. However, the Chloride threshold depends on several variables including the pH value of the surrounding concrete, the water content, the proportion of water-soluble Chloride, and the temperature. Values reported by different researchers show a wide range of results (Li and Sagues 2001; Ann and Song 2007; Bertolini et al. 1996; Moreno et al. 2004). We expect that a robust sensor for long term monitoring of dissolved Chlorides, in conjunction with electrochemical measures such as corrosion potential, can significantly contribute to advancing the understanding of the effect of Chlorides on durability of reinforced concrete structures. This chapter is focused on the evaluation of sensitivity and calibration of optical fiber Chloride probes.

7.2 Intrinsic Sensing of Dissolved Chlorides

High sensitivity measurement of Chlorides is typically carried out using indicator based sensing (Chalk and Tyson 1998; Fuhr et al. 1996; Laferriere et al. 2008). In the case of long term in situ application, there are issues with long term calibration

and durability of indicator based approaches. The research presented in this chapter aims at overcoming some of these limitations by considering indicator free sensing.

For alternative approaches to intrinsic sensing of Chlorides, the reader is referred to literature on using Nuclear Magnetic Resonance (NMR), (Yun et al. 2004), microwave/radar (Al-Mattarneh 2016; Bois et al. 2001; Hugenschmidt and Loser 2008), X-Ray fluorescence measurement, (Kanada et al. 2006; Moradillo et al. 2017; Proverbio and Carassiti 1997) laser breakdown spectroscopy (Wilsch et al. 2005) or impedance spectroscopy, (Jain and Neithalath 2011; Poupard et al. 2004) and amperometric methods (Trnkova et al. 2008).

Chapter 1 introduced a brief overview of molecular spectroscopy for intrinsic sensing of water, including the role of Chloride Ions and their effect on the water hydrogen bonds, and how that mechanism can be used for sensing. Chapters 8 and 9 will describe the application of Near-Infrared (NIR) Spectroscopy for in situ monitoring of moisture in cement based material, and in soil respectively. Chapter 10 presents the application for cure monitoring in hydraulic cement. This chapter focuses on the calibration of changes in the NIR signal of water in the presence of NaCl. Results of experiments present how this recognition mechanism can be activated for in situ sampling in porous media using embedded optical fibers.

7.2.1 *Effect of Chlorides on Molecular Vibration of Water*

Increases in ionic concentration, temperature or pressure, breaks up the hydrogen bonding network causing changes in the molecular vibrations (Chap. 1). For example, when a salt such as NaCl is dissolved in water, it causes measurable modifications in the spectral signature of the Electromagnetic (EM) radiation interacting with that water (Fig. 7.1). This is evident in both the Mid-IR and the Near-IR regions. This offers the utility as a reagent free approach for detection of Chlorides.

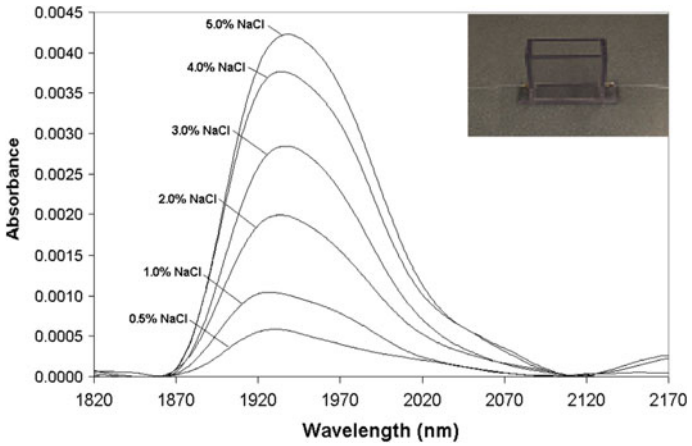

Fig. 7.1 Absorption spectra of water soluble sodium chloride measured by the optical fiber probe with sensing length of 10.5 cm

7.2.2 Experimental Setup and Procedure

In order to test the utility of using optical fiber evanescent field spectroscopy (Chap. 2, Fig. 2.4) for intrinsic sensing of Chlorides in aqueous media, experiments were carried out. The optical fiber probes used in the experiments described below were made using step-index multimode low OH plastic clad silica (PCS) fibers. The original fibers were manufactured by Thorlabs Inc., (Newton, NJ), with a 600-μm core diameter, 630 μm cladding diameter and 1030 μm buffer diameter. Portions of the buffer and cladding were removed and replaced with porous materials. The fiber ends were polished using lapping films and were fitted with SMA type connectors. The fibers were placed in a Plexiglas container (Fig. 7.1) which would contain the aqueous solutions with various concentrations of Sodium Chloride.

One meter portions of the fiber were cut; the buffer and cladding of fiber were removed in the middle region over a length of 10 cm in preparation for the application of the new porous cladding layer using cellulose. The highly polarized OH groups in cellulose have the unique ability to form strong hydrogen bonds with adjacent cellulose chains, making the cellulose rigid and strong while tunable for desired porosity. In order to plasticize and cast cellulose on a fiber, the polymer chains must be fluid. This is achieved, for example, through replacing the cellulose OH groups with either acetyl groups, known as cellulose acetate, or nitro groups known as cellulose nitrate (Safavi and Abdollahi 1998). Cellulose acetate derives from cellulose through a reaction with acetic acid and acetic anhydride in the presence of sulfuric acid. Through this process, cellulose can be prepared in a liquid phase for casting claddings with desired thickness and porosity.

The analysis was done by connecting the optical fiber probes to a Shimadzu Prestige-21-NIR spectrometer (Shimadzu America/Shimadzu Scientific Instruments, Inc. USA, Columbia, MD). This is a lab instrument, but similar analysis can be done with handheld NIR spectrometers. The fiber connection was made through ports manufactured by Harrick Scientific Corporation, (Ossining, NY). Data processing and post-processing were performed using the Shimadzu IR-Solutions software. The Near-Infrared spectra of water is measured by the evanescent field, similar to that shown in Chap. 1 (Fig. 1.4) (Falco et al. 1986; Ghandehari and Vimer 2003, 2006; Ghandehari et al. 2012; Kodl 2004; Leung et al. 2008). The aqueous samples were also placed in between two glass slides with 400 nm gap and tested in transmission mode for comparison with the evanescent field mode.

Using the absorption spectra of water as the baseline, three sets of experiments were conducted. The first set of experiments evaluated the effect of concentration of water-soluble Sodium Chloride on the Near-Infrared activity of water. The second and third sets of experiments evaluated the effect of pH level and the effect of temperature, respectively. The latter two were done in order to develop the protocol for calibration.

For the Chloride tests, Near-Infrared absorption spectra of solutions of distilled water with dissolved Sodium Chloride at increasing concentrations: from 0.5–5.0% by weight were measured (Fig. 7.1). The effect of temperature fluctuations was

measured by recording the spectra of distilled water (with the baseline reading at 5 °C) at temperatures of 7, 20, 40, 60 and 80 °C. Temperature changes had a larger effect on the readings than changes in pH, calling for a temperature calibration method described below.

To determine the effect of changes in pH, the absorption spectra of solutions containing potassium hydroxide (KOH) at various concentrations were tested (Fig. 7.3), including 0.1 M (0.56% by weight, corresponding to pH13), 0.2 M (1.12%, pH13.3), 0.4 M (2.24%, pH13.6) and 1 M (5.6%, pH14). The effect of pH at values below pH13 on the absorption spectra was negligible therefore it is not reported. All tests were performed using the 10 cm length of modified fiber length for evanescent field sensing.

The absorption spectra and the second derivative transforms (of absorption vs. wavelength) were smoothed for 80 values using the Savitzky-Golay algorithm (Savitzky and Golay 1964). The algorithm is based on performing a least squares linear regression fit of a polynomial of degree k over at least k + 1 data points. A multipoint baseline correction has been applied to all the spectra.

7.3 Results

7.3.1 Measurements of NaCl Concentration Changes Using the Fiber Optic Probe

The hydrogen bond between the water molecules has the effect of inhibiting molecular vibrations. The process of the dissolution of NaCl by water is accompanied by breaks of hydrogen bonds between water molecules. This corresponds to an increase in the absorbed electromagnetic energy at specific bands, for example those centered at 1450 and 1928 nm. As expected, according to Beers law, the energy absorption is proportional to the amount of salt dissolved in water. The corresponding absorption spectra are shown in Fig. 7.1 The second derivative transform (not shown) can also help remove baseline shifts and increases the spectral resolution (Grant et al. 1989). These tests were carried out using a fiber optic evanescent field probe with a 10 cm sensing region exposed to aqueous NaCl solutions with concentrations varying from 0 to 5% w/v (0.085–0.85 M NaCl solutions). The reference signal was obtained using the same sensor in distilled water.

7.3.2 Effect of Temperature

Temperature has a somewhat similar effect on the hydrogen bonds of the water molecule. An increase in temperature results in a decrease in the number of hydrogen bonds and a corresponding increase in covalent O–H bonds. This leads to a shift of the absorption peak to higher frequencies (shorter wavelengths), but with

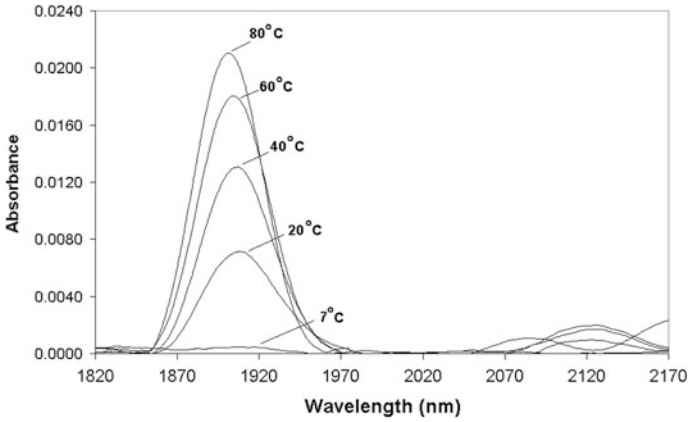

Fig. 7.2 Absorption spectra (with water at 5 °C as reference) of the fiber optics probe immersed in solutions with temperatures 7, 20, 40, 60 and 80 °C, respectively

peak values different from the ones observed in case of NaCl concentration changes. Figure 7.2 shows the temperature dependent changes in the absorption spectra measured with the fiber optics probe in distilled water for changes in temperature up to 75 °C, using the spectrum measured for distilled water at 5 °C as reference. The corresponding second derivative transform (not shown) can further highlight the effect of temperature compared to the effects of NaCl.

7.3.3 Effect of pH Level

Highly alkaline solutions, such as those containing NaOH or KOH, may also affect the hydrogen bonds and the water absorption spectrum. Figure 7.3 shows the changes in the absorption spectra as measured using the fiber optics probe immersed in solutions containing 0.1, 0.2, 0.4 and 1 M KOH per liter of water corresponding to pH levels of 13.0, 13.3, 13.6, and 14.0, respectively. Distilled water was used as the background for these measurements. The corresponding second derivative transform not shown will further reveal differences between the effects of NaCl and hydroxides on the water spectrum.

7.3.4 Eliminating the Effects of Changes in Temperature and pH

In order to eliminate the effect of temperature changes, the absorbance at the second derivative isosbestic value of 1968 nm may be used. The absorbance second

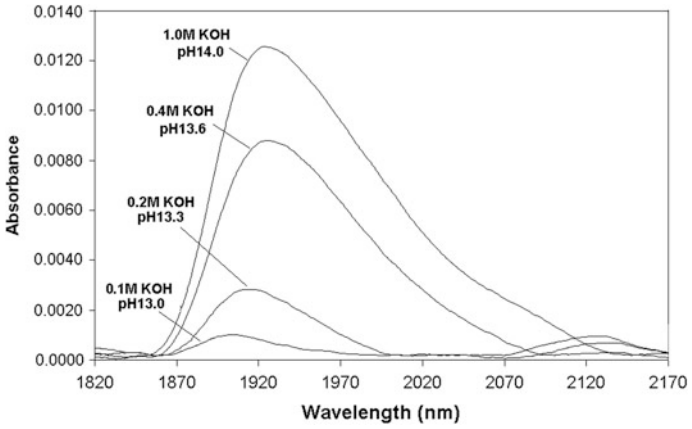

Fig. 7.3 Effect of pH on the absorption. Absorption spectra (with pure water as reference) of the fiber optics probe immersed in solutions containing 0.1, 0.2, 0.4 and 1 M KOH per liter of water, corresponding to pH levels of 13.0, 13.3, 13.6, and 14.0, respectively

derivative plot at 1968 nm increases almost linearly with increasing NaCl concentrations, while it is virtually unchanged with changes in temperature. Effect of pH variation above pH13 can be calibrated for in a similar manner. Here a second derivative transforms for NaCl concentrations versus changes in pH at 1901 nm can be used. Calibration for the effects of temperature and pH level can be accounted for by ratio of peaks in absorption intensity as well as the second derivative of absorption intensity as shown in Figs. 7.4, 7.5 and 7.6.

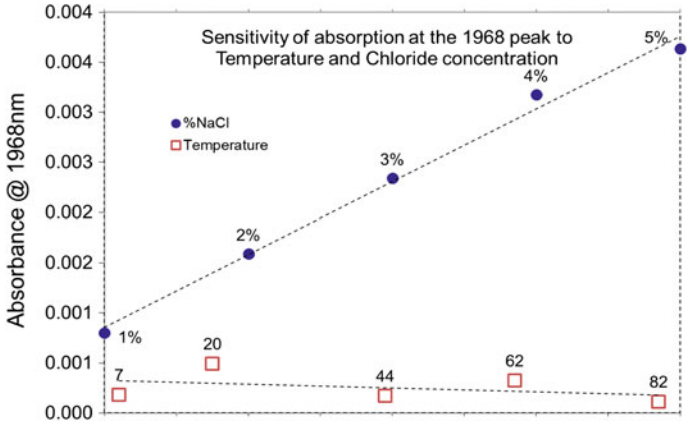

Fig. 7.4 Single wavelength calibration for chloride concentration at 1968 nm, practically invariant to temperature (°C)

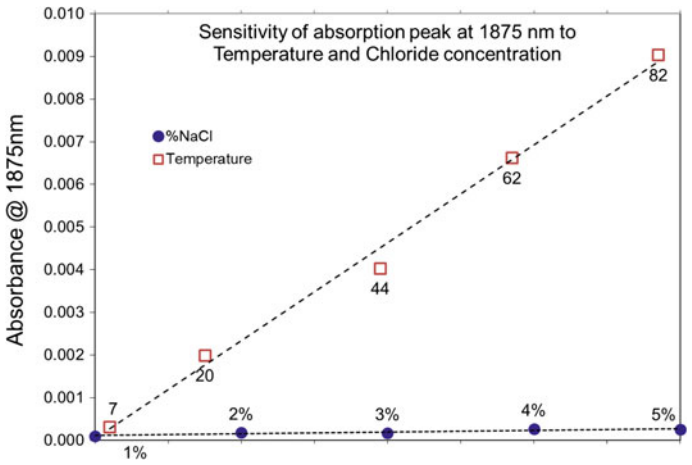

Fig. 7.5 Single wavelength calibration for temperature (°C) at 1875 nm, practically invariant to chloride concentration

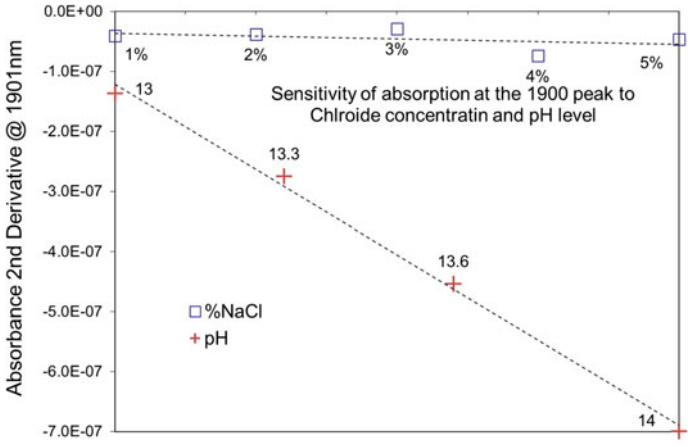

Fig. 7.6 Single wavelength calibrating for pH level using 2nd derivative transform of absorbance at 1901 nm, practically invariant to Chloride concentration

7.4 Conclusion

Sensing of Chlorides in analytical chemistry, food industry and in biological assays is often done using reagents (Zenki and Iwadou 2002). Typical reagent molecules for Chlorides (poly-aromatic hydrocarbons or heterocycles) are either absorption sensors that change color, or are emitters. Those compounds have high sensitivity but are known to exhibit limitations with long term stability due to degradation,

therefore not ideal for extended duration applications in harsh environments. For this reason, we are reporting a reagent free recognition strategy using the intrinsic optical characteristic of soluble Chlorides. The results of the experiments discussed above indicate that using this type of sensor, it is possible to measure moderate concentrations of Chlorides in concrete, in the range where the Chloride ion threshold for initiating pitting corrosion has been reported in literature. The lower limit of detection can easily be increased by increasing the path length (Beer's law). It is also shown that the effect of pH is insignificant and that the effect of temperature can be compensated for by using calibration.

References

Al-Mattarneh, H. (2016). Determination of chloride content in concrete using near- and far-field microwave non-destructive methods. *Corrosion Science, 105,* 133–140.

Alonso, C., Castellote, M., & Andrade, C. (2002). Chloride threshold dependence of pitting potential of reinforcements. *Electrochimica Acta, 47*(21), 3469–3481.

Angst, U., Elsener, B., Larsen, C. K., & Vennesland, Ø. (2009). Critical chloride content in reinforced concrete—A review. *Cement and Concrete Research, 39*(12), 1122–1138.

Ann, K. Y., & Song, H. (2007). Chloride threshold level for corrosion of steel in concrete. *Corrosion Science, 49*(11), 4113–4133.

Arslan, H., & Demir, Y. (2013). Impacts of seawater intrusion on soil salinity and alkalinity in Bafra Plain, Turkey. *Environmental monitoring and assessment, 185*(2), 1027–1040.

Assouli, B., Simescu, F., Debicki, G., & Idrissi, H. (2005). Detection and identification of concrete cracking during corrosion of reinforced concrete by acoustic emission coupled to the electrochemical techniques. *NDT and E International, 38*(8), 682–689.

Bae, J. Y., Shin, K. J., Hyun, J. H., Jang, Y. I., & Kim, Y. Y. (2014). Chloride resistance of concrete with marine blended cement using corrosion resistant mineral admixture. In *2013 3rd International Conference on Civil Engineering and Building Materials, CEBM 2013, December 7–8, 2013.* Trans Tech Publications Ltd., pp. 23–26.

Bertolini, L., Bolzoni, F., Pastore, T., & Pedeferri, P. (1996). Behaviour of stainless steel in simulated concrete pore solution. *British Corrosion Journal, 31*(3), 218–222.

Bois, K. J., Benally, A. D., & Zoughi, R. (2001). Near-field microwave non-invasive determination of NaCl in mortar. *IEE Proceedings-Science, Measurement and Technology, 148*(4), 178.

Chalk, S. J., & Tyson, J. F. (1998). Determination of chloride by flow injection spectrophotometry with membrane reagent introduction. *Analytica Chimica Acta, 366*(1), 147–153.

Charette, M. A., & Allen, M. C. (2006). Precision ground water sampling in coastal aquifers using a direct-push, shielded-screen well-point system. *Ground Water Monitoring and Remediation, 26*(2), 87–93.

Chen, X., Tang, M., & Ma, K. (2012). Underground concrete structure exposure to sulfate and chloride invading environment. *Zhongnan Daxue Xuebao (Ziran Kexue Ban)/Journal of Central South University (Science and Technology),* **43**(7), 2803–2812.

Darmawan, M. S. (2010). Pitting corrosion model for reinforced concrete structures in a chloride environment. *Magazine of Concrete Research, 62*(2), 91–101.

Dhir, R. K., Jones, M. R., & McCarthy, M. J. (1993). Quantifying chloride-induced corrosion from half-cell potential. *Cement and Concrete Research, 23*(6), 1443–1454.

Falco, L., Berthou, H., Cochet, F., Scheja, B., & Parriaux, O. (1986). Temperature sensor using single mode fiber evanescent field absorption. In *Fiber Optic Sensors. Conference Presented at*

the 2nd International Technical Symposium on Optical and Electro-Optical Applied Science and Engineering, 25–27 November, 1985. SPIE, pp. 114–119.

Fuhr, P. L., Huston, D. R., Mcpadden, A. P., & Cauley, R. F. (1996). Embedded chloride detectors for roadways and bridges. In *Smart Structures and Materials 1996: Smart Systems for Bridges, Structures, and Highways, February 28–29, 1996*. Society of Photo-Optical Instrumentation Engineers, pp. 229–237.

Furby, S., Caccetta, P., & Wallace, J. (2010). Salinity monitoring in Western Australia using remotely sensed and other spatial data. *Journal of Environmental Quality, 39*(1), 16–25.

Ghandehari, M., & Vimer, C. (2003). Moisture sensing in structural materials using near-infrared evanescent field spectroscopy. In F. Chang (Ed.), *Structural health monitoring 2003: From diagnosis & prognostics to structural health management; Proceedings of the 4th international workshop on structural health monitoring*. Lancaster, Pa: DEStech Publications.

Ghandehari, M., & Vimer, C. (2006). In-situ monitoring of moisture in pavement materials. In A. GUERMES, (Ed.), *Structural health monitoring: Proceeding of the third European conference, July 5–7 2006*. Granada, Spain: Transportation Research Board.

Ghandehari, M., Vimer, C. S., Ioannou, I., Sidelev, A., Jin, W., & Spellane, P. (2012). In-situ measurement of liquid phase moisture in cement mortar. *NDT and E International, 45*(1), 162.

Grant, A., Davies, A. M. C., & Bilverstone, T. (1989). Simultaneous determination of sodium hydroxide, sodium carbonate and sodium chloride concentrations in aqueous solutions by near-infrared spectrometry. *Analyst, 114*(7), 819–822.

Hansson, C. M., & Sorensen, B. (1990). Threshold concentration of chloride in concrete for the initiation of reinforcement corrosion. *ASTM Special Technical Publication, 1065,* 3–16.

Holden, W. R., Page, C. L., & Short, N. R. (1983). The influence of chlorides and sulphates on durability. *Corrosion of reinforcement in concrete construction, 13-15 June 1983*. Society of Chemical Industry, pp. 143-150.

Hugenschmidt, J., & Loser, R. (2008). Detection of chlorides and moisture in concrete structures with ground penetrating radar. *Materials and Structures, 41*(4), 785–792.

Jain, J., & Neithalath, N. (2011). Electrical impedance analysis based quantification of microstructural changes in concretes due to non-steady state chloride migration. *Materials Chemistry and Physics, 129*(1–2), 569–579.

Jin, M., Jiang, L., Lu, M., & Bai, S. (2017). Monitoring chloride ion penetration in concrete structure based on the conductivity of graphene/cement composite. *Construction and Building Materials, 136,* 394–404.

Kanada, H., Ishikawa, Y., & Uomoto, T. (2006). On-site elemental analysis of concrete by portable energy dispersive X-ray fluorescence analyzer. In *10th East Asia-Pacific Conference on Structural Engineering and Construction, EASEC 2010, August 3–5, 2006*. School of Engineering and Technology, pp. 279–284.

Kodl, G. (2004). A new optical waveguide pressure sensor using evanescent field, 2004, IEEE, pp. 1946 Vol. 2.

Laferriere, F., Inaudi, D., Kronenberg, P., & Smith, I. F. C. (2008). A new system for early chloride detection in concrete. *Smart Materials and Structures,* **17**(4).

Leung, C. K. Y., Wan, K. T., & Chen, L. (2008). A novel optical fiber sensor for steel corrosion in concrete structures. *Sensors, 8*(3), 1960–1976.

Li, L., & Sagues, A. A. (2001). Chloride corrosion threshold of reinforcing steel in alkaline solutions–open-circuit immersion tests. *Corrosion, 57*(1), 19.

Liu, G., Widger, R. A., & Jin, Y. C. (2006). Trend analysis of road salt impacts on groundwater salinity at a long-term monitoring site. In *2006 Annual Conference of the Transportation Association of Canada: Transportation Without Boundaries, TAC/ATC, September 17 – 20, 2006.* Transportation Association of Canada (TAC).

Mehta, P. K., Scheissl, P., & Raupach, M. (1992). Performance and durability of concrete systems. In *9th International Congress on the Chemistry of Cement, November 1992, Delhi, India*. National Council for Cement and Building Materials, pp. 571–605.

Moradillo, M. K., Sudbrink, B., Hu, Q., Aboustait, M., Tabb, B., Ley, M. T. et al. (2017). Using micro X-ray fluorescence to image chloride profiles in concrete. *Cement and Concrete Research,* 92, 128–141.

Moreno, M., Morris, W., Alvarez, M. G., & Duffo, G. S. (2004). Corrosion of reinforcing steel in simulated concrete pore solutions effect of carbonation and chloride content. *Corrosion Science, 46*(11), 2681–2699.

Mortl, A. E., Munoz-Carpena, R., Li, Y. C. (2006). Hydroperiod and soil water salinity in the baldcypress floodplains of the loxahatchee river. In *International Conference on Hydrology and Management of Forested Wetlands, April 8 – 12, 2006.* American Society of Agricultural and Biological Engineers, pp. 395–402.

Nie, M., Huang, H., Dai, Y., Li, W., Jiang, P., Yang, W. (2016). Experiment on chloride ion content of concrete structure in coastal salt-fog area. In *International Symposium on Materials Application and Engineering, SMAE 2016, August 20 – 21, 2016.* EDP Sciences.

Poupard, O., Aït-Mokhtar, A., & Dumargue, P. (2004). Corrosion by chlorides in reinforced concrete: Determination of chloride concentration threshold by impedance spectroscopy. *Cement and Concrete Research, 34*(6), 991–1000.

Proverbio, E., & Carassiti, F. (1997). Evaluation of chloride content in concrete by X-ray fluorescence. *Cement and Concrete Research, 27*(8), 1213–1223.

Safavi, A., & Abdollahi, H. (1998). Optical sensor for high pH values. *Analytica Chimica Acta, 367*(1), 167–173.

Saremi, M., & Mahallati, E. (2002). A study on chloride-induced depassivation of mild steel in simulated concrete pore solution. *Cement and Concrete Research, 32*(12), 1915–1921.

Savitzky, A., & Golay, M. J. E. (1964). Smoothing and differentiation of data by amplified least squares procedures. *Analytical Chemistry, 36,* 1627–1639.

Sookoomjariyapong, C., Vongchavalitkul, S., & Sayamipuk, S. (2011). Risk assessment of reinforced concrete structure attacked by chloride, In *2011 1st International Conference on High Performance Structures and Materials Engineering, ICHPSM 2011, May 5–6, 2011.* Trans Tech Publications, pp. 734–739.

Trnkova, L., Adam, V., Hubalek, J., Babula, P., & Kizek, R. (2008). Amperometric sensor for detection of chloride ions. *Sensors, 8*(9), 5619–5636.

Wilsch, G., Weritz, F., Schaurich, D., & Wiggenhauser, H. (2005). Determination of chloride content in concrete structures with laser-induced breakdown spectroscopy. *Construction and Building Materials, 19*(10), 724–730.

Wood, C., & Harrington, G. A. (2015). Influence of seasonal variations in sea level on the salinity regime of a coastal groundwater-fed wetland. *Groundwater, 53*(1), 90–98.

Yu, H., Hartt, W. H., & Virmani, Y. P. (2007). Effects of reinforcement and coarse aggregates on chloride ingress into concrete and time-to-corrosion: Part I—Spatial chloride distribution and implications. *Corrosion, 63*(9), 843–849.

Yun, H., Patton, M. E., Garrett, J. H., Fedder, G. K., Frederick, K. M., Hsu, J., et al. (2004). Detection of free chloride in concrete by NMR. *Cement and Concrete Research, 34*(3), 379–390.

Zenki, M., & Iwadou, Y. (2002). Repetitive determination of chloride using the circulation of the reagent solution in closed flow-through system. *Talanta, 58*(6), 1055–1061.

Part III
In Situ Analysis of Transport Processes in Porous Media

Chapter 8
In Situ Analysis of Moisture in Cement Based Materials

Masoud Ghandehari, Cristian S. Vimer, Ioannis Ioannou, Alexey Sidelev and Peter Spellane

Abstract An approach for the evaluation of moisture transport in porous media is introduced and demonstrated through measurement of capillary absorption and evaporative drying in cement mortar. The sensing method is based on the application of Near-Infrared spectroscopy, where the internal environment of the cement mortar is monitored by measurement the absorption peaks of the water molecule using light traveling through an optical fiber. The fibers were altered by replacing a short length of the fiber cladding with a porous membrane, allowing the propagating light to interact with the water in the surrounding pore space, registering the respective moisture content.

8.1 Introduction

The durability of cementitious materials is a critical issue for engineers (Dyer 2014; Ansari 2000) and everyone who relies on a safe and healthy infrastructure. The service life of these materials depends to a great extent on their water transport

M. Ghandehari (✉)
New York University, Six Metrotech Center, Brooklyn, NY 11201, USA
e-mail: masoud@nyu.edu

C. S. Vimer
Madsen Consulting Engineering, 175 Varick St #803, New York, NY 10014, USA
e-mail: cvimer@gmail.com

I. Ioannou
School of Engineering, University of Cyprus, Nicosia, Cyprus
e-mail: ioannis@ucy.ac.cy

A. Sidelev
Parsons, 100 Broadway, New York, NY 10005, USA
e-mail: a.sidelev@gmail.com

P. Spellane
Chemistry Department, New York City College of Technology (CUNY), Brooklyn, NY 11201, USA
e-mail: pspellane@citytech.cuny.edu

M. Ghandehari, *Optical Phenomenology and Applications*,
Smart Sensors, Measurement and Instrumentation 28,
https://doi.org/10.1007/978-3-319-70715-0_8

properties. Cementitious materials are porous and permeable and therefore absorb and transmit water more or less freely (Hall and Hoff 2011; Youngs et al. 1994). According to their composition, these materials respond to moisture around them by absorbing water as vapor or liquid, redistributing it, and under drying conditions breathing it back into the air (Hall and Yau 1987; Hanzic and Ilic 2003; Henkensiefken et al. 2009; Martys 1995; Grasley et al. 2006).

The transport of moisture in cementitious materials can influence it's performance and durability (Claisse 2014), including physical processes such as freeze thaw action, or it can facilitate chemical processes such as akali-silica reaction (Poukhonto 2003). Water moving inside the porous material can also carry unwanted chemical species such as soluble sulphates. It is known that sulphates react with tricalcium aluminate (C3A) present in cement, leading to the formation of calcium sulphate and calcium sulphoaluminate. These products have a greater volume than the compounds they replace and lead to the expansion and break-up of the material. In addition to sulphate attack, the serious problems of reactive aggregates (i.e. alkali-silica reactions) also depend on the presence of water (Hobbs 2001). In fact, alkali-silica reactions are accelerated by alternate wetting and drying caused by a cycle of rain and moisture evaporation in dry conditions (FHWA 2017). Furthermore, cementitious materials, as indeed any other porous material, are susceptible to damage from freeze-thaw cycles (Hobbs 2001). Freeze-thaw damage is, in turn, directly related to the amount of water present in the pore structure of these materials.

The pore space of cementitious materials is seldom fully saturated; its degree of saturation depends on several factors such as previous exposure to moisture and the relative humidity of the surrounding environment. At the same time, mass transport into any porous material depends on several factors, namely pore size distribution, connectivity and tortuosity. For cementitious materials, these factors depend on the composition of the material, the processes of cement hydration, interfaces with aggregates, and the influence of admixtures. The complexity of the microstructure and the various means for transport of moisture through the porous matrix of cementitious materials make the theoretical study of transport in these materials quite challenging (Martys 1995; Martys and Hagedorn 2002; Crank 1976; Hoff et al. 1979; Hall and Yau 1987; Hall and Hoff 2011).

The detailed simulation of this transport phenomena, subject to varying conditions of external environment and internal saturation levels, is challenging because of the difficulty of modeling fluid flow in random pore geometries, and the proper consideration of the interfacial boundary conditions. Although numerical methods, such as the lattice Boltzmann or Sharp Front Models (Hoff and Hall 2009), provide a means for numerical modeling of such complex fluid and mass transport processes, further comparisons between simulation and experimental observations are crucial, not only to validate these simulation methods, but to further their development. This article presents our work in the experimental evaluation of moisture transport in cement mortars. Results of the relative moisture content shown, point to

the opportunity of implementing optical fibers for laboratory or field monitoring of moisture content in porous substances including cement based materials.

8.1.1 Moisture Measurement

There are several existing methods for measuring moisture in concrete and cement mortars. The most widely used technique is the gravimetric sorptivity method (Hall and Yau 1987). This method is applicable for laboratory use and it can provide direct information on the quantity but not the distribution of moisture within a given specimen. Methods such as nuclear magnetic resonance (NMR), gamma ray, X-ray or neutron radiography (NR), microwave spectroscopy (transmission, reflection or resonance), penetrating radar (GPR like), and electrochemical impedance spectroscopy (EIS) can be used to provide time resolved information about the dynamics of moisture transport (Gummerson et al. 1981; Kumaran and Bomberg 1985; Hanzic and Ilic 2003; Hansen and Hansen 2002; Sun et al. 2017; Laurens et al. 2005). These techniques have provided valuable fundamental insight through laboratory studies (Pavlík et al. 2006; Okamura 2000; Prado 2001; de J. Cano-Barrita et al. 2009; Boguszynska et al. 2005; Kanematsu et al. 2009; Zhang et al. 2011; Roels and Carmeliet 2006; da Rocha et al. 2001; Henkensiefken et al. 2009). However, the majority of these techniques are complex or not suitable for long term field monitoring. Furthermore, in addition to requiring presence of a strong magnetic field, the NMR signal in concrete is weak, while gamma or X-rays cannot give satisfactory results when moisture content is low and/or when the sample is thick. Radar penetrating methods can be used for moisture measurement in cured concrete, however, they have limited penetration depth (Laurens et al. 2005). Surface measurements utilizing microwaves also has depth limitations (Pavlík et al. 2003) or require access from both sides of the object (Okamura 2000).

8.2 Optical Diagnostics

In this study we used optical fibers for probing the internal environment of cement mortars' moisture content. This method of distributed sensing employs attenuated total reflection through the fiber, where the light propagating along the length of an optical fiber is attenuated by the environment immediately adjacent to the fiber. This attenuation is selective according to the chemical species present and can be used for sensing. Below is a brief summary of detection technique; further detail of Near-Infrared absorption spectroscopy is introduced in Chap. 1, followed by description of the evanescent field in optical waveguides in Chap. 4, and how the evanescent field is used for sensing applications. Further detail may also be found in the references (Ghandehari and Khalil 2005; Ghandehari and Vimer 2004; Cheng et al. 2008).

8.2.1 Recognition Mechanism

When electromagnetic energy interacts with matter its selectively absorbed as function of wavelength. The absorbance A shown in Eq. 8.1, also know as Beer's law:

$$A = \varepsilon bc \tag{8.1}$$

where absorbance A has no units, ε is the molar absorptivity of the material, b is the interaction path length of interaction of light with the analyte, and c is the molar concentration of analyte in the sample space.

EM radiation is selectively absorbed (in resonance) according the modes of vibration of the molecules it interacts with. For example, in water the modes of vibration correspond to stretching of the OH (symmetric stretch ν1), bending of the OH bond (ν2), and anti-symmetric OH stretch (ν3). The fundamental vibration modes are in resonance with Mid-Infrared radiation at 3048, 6079, and 2865 nm wavelengths, respectively.

However, most optical fibers do not transmit Mid-Infrared energy and consequently measurement of Mid-IR absorptions are not practical. However, overtones of the fundamental vibration which occur in the Near-Infrared region (NIR) of the electromagnetic (EM) spectrum can be transmitted through optical fibers. The Near-Infrared region of the EM spectrum occurs between 750 nm and 2500 nm. Near-Infrared spectroscopy can be used for qualitative identification of many materials and chemicals including water. Near-Infrared spectroscopy is particularly useful for in situ as they can be used to effectively transmit Near-Infrared energy to samples. For the water molecule in the liquid phase, the Near-Infrared absorption bands theoretically occur at 1947 nm (ν2 + ν3), 1477 nm (ν1 + ν3), 995 nm (2ν1 + ν3), and 750 nm (3ν1 + ν3). A typical Near-Infrared spectrum of water from 1000 to 2200 nm is shown in Fig. 8.1. This spectrum was obtained using the same setup as that used for detection of moisture in cement mortar. We will be using the larger peak for the moisture ingress analysis.

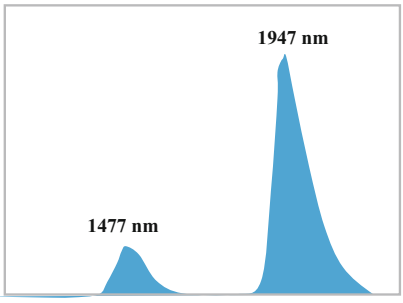

Fig. 8.1 Absorption spectrum of deionized water transduced by the evanescent field penetrating the porous cladding along the fiber probe

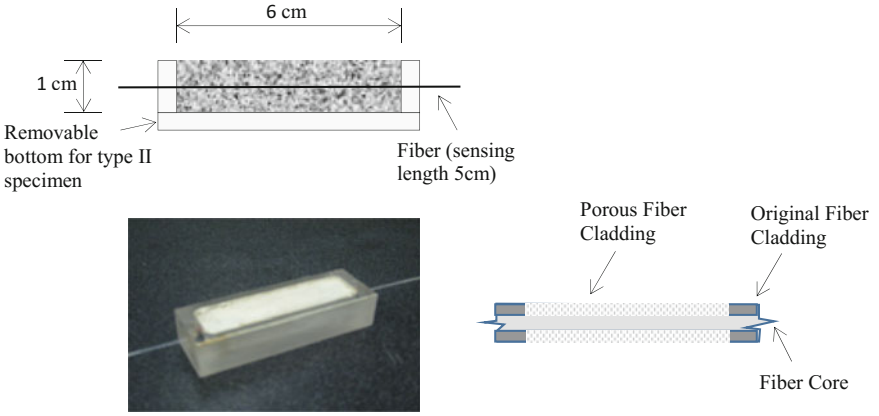

Fig. 8.2 Test specimens and fiber sensor

8.2.2 Transduction

In optical fibers used for communications, the optical signal is carried by the principle of Total Internal Reflection (TIR). In this application the fibers are designed so that the energy traveling inside the fiber does not interact with the outside environment. However, when the fiber cladding is replaced with a porous material, the fiber can be used as a sensor utilizing what is known as the evanescent field. This is the portion of the guided energy that penetrates the cladding. In telecom fibers the evanescent field is isolated from the outside environment. When replaced with alternative materials (Fig. 8.2), the evanescent field can be used to sense the environment in the immediate vicinity of the fiber. The evanescent field functions as a distributed antenna along the fiber. This can be used as an analytic approach for material characterization. For example a polymer can be applied to an optical fiber as cladding, simply to use the attenuated total internal reflection for spectroscopic characterization of the polymer. Alternatively, the cladding can be made porous to the surrounding for environmental sensing (Mijović and Andjelić 1995; Johnson et al. 2000; Ghandehari and Vimer 2004).

8.3 Experimental Setup

Here we introduce a method for in situ measurement of moisture transport. Tests on capillary absorption and moisture drying were carried out using cement mortar specimens. Two different boundary conditions were tested: the first specimen with a single surface exposed, the second specimen with two surfaces exposed when the bottom of the mold was removed, (Fig. 8.2). The results of relative moisture content were recorded at prescribed time intervals.

8.3.1 Sensor

Multimode plastic clad silica (PCS) optical fibers with a core diameter of 400 μm were used. One-meter-long pieces of the fiber were cut and fiber couplers were attached at both ends. The buffer and cladding of the fibers were removed over a length of 5 cm at the middle of the fiber and a new porous cladding was cast. The fiber and connections were purchased from Thorlabs Inc. Newton, NJ. The porous cladding is approximately 100 μm thick and is made of a specialty Poly Methyl Methacrylate. Potential interaction of this polymer with the alkaline cement would result in optical activity in the mid 1600 nm region (corresponding to CH bonds). This effect will not interfere with moisture information derived from OH bond vibrations in the 1900 nm region.

8.3.2 Specimens and Testing

Fibers were placed through the Plexiglas molds at mid height, as shown in Fig. 8.2; Portland cement Type I mortar was cast with 0.6 water to cement (w/c) ratio and 0.3 cement to sand ratio. The specimens were then cured by wrapping in wet cloth and sealed in plastic bags for 4 weeks at ambient room conditions (average relative humidity RH 60%; average temperature 25 °C). After curing, the samples were submerged in water for 5 days, then removed and tested while monitoring the drying out. The mortar specimens were then dried at 50 °C for 7 days and tested for capillary absorption. The closed boundaries were made of Plexiglas sealed with silicon at seams. For the absorption tests, the specimens were placed on supporting rods in order to allow free access of the water to the inflow surface.

The fibers were connected to a Shimadzu Prestige-21 IR-NIR spectrometer using a fiber-port. Data acquisition was carried out using the Shimadzu IR-Solutions 1.10 software. The energy absorption spectra were smoothed using the Savitzky-Golay algorithm (Savitzky and Golay 1964). The smoothing algorithm uses a least squares linear regression fit of a polynomial of degree K over at least K + 1 data points. For the reported experiments, K = 25 was used. This smoothing eliminates the high frequency noise and minimally impacts the peak absorption values used for calculation of moisture absorption.

8.4 Results and Discussion

The fibers were first tested in water for functionality prior to casting the mortar. The spectra shown in Fig. 8.1 represent the energy absorption spectra of de-ionized water over the NIR wavelength range from 1000 to 2200 nm. The OH vibration near 1947 nm is greater than the corresponding signal at 1477. Therefore, for the remainder of the study and for analysis of moisture content in mortar, only the 1947 nm region was used.

8.4.1 Drying

After curing, the samples were submerged in water for 5 days, then placed in ambient conditions (average relative humidity RH 60%; average temperature 25 °C) and monitored for relative moisture content at the fiber level. Figure 8.3 shows the variation in energy absorption at the level of the fiber for the specimen with top surface exposed. Figure 8.4 provides the same information for the specimen with both top and bottom surfaces exposed. The reported wavelength range of 1840–2140 nm represents the entire strong NIR water absorption band caused by the ν2 + ν3 fundamental vibration mode.

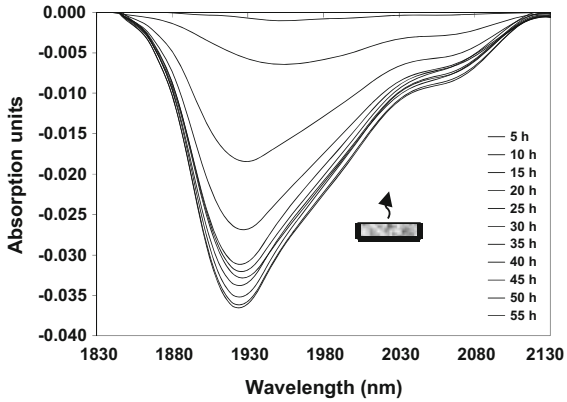

Fig. 8.3 Optical energy absorption spectra for moisture desorption test (relative to 5-day saturation level) on specimens with top side exposed only. (Time values in the legend correspond in order of absorption peak values plotted)

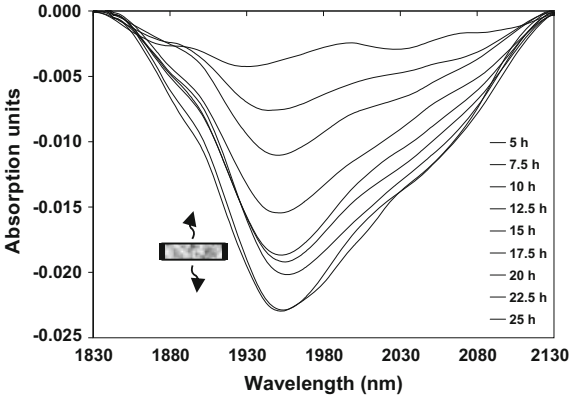

Fig. 8.4 Energy absorption spectra for moisture desorption (relative to 5-day saturation level) on specimens with top and bottom sides exposed. (Time values in the legend correspond in order of absorption peak values plotted)

The reference/background spectrum used was that associated with the 5 day cured condition, just before the start of test. Therefore, the plotted negative absorbed energy level is indicative of a lower number of water molecules present at the fiber level. A direct relationship between moisture content and optical absorption is used and peak optical absorption values are normalized to that measured at steady state. Steady state conditions are defined as time when little or no change in the optical absorption spectra versus consecutive acquisition cycles is observed. Result of test on capillary desorption (Figs. 8.3 and 8.4) and absorption (Figs. 8.5 and 8.6) are summarized in Fig. 8.7. Steady state moisture content was obtained at approximately 50 h for the one side exposed specimen and 25 h for the two sides exposed specimen.

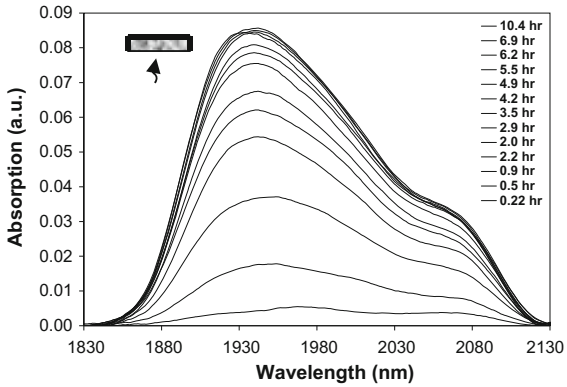

Fig. 8.5 Energy absorption spectra for capillary absorption (relative to 7-day oven dried conditions) into specimens with bottom side exposed only. (Time values in the legend correspond in order of absorption peak values plotted)

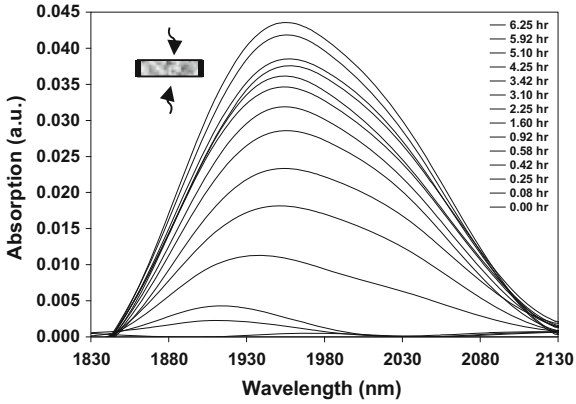

Fig. 8.6 Energy absorption spectra for capillary absorption (relative to 7-day oven dried conditions) into specimens with top and bottom sides exposed. (Time values in the legend correspond in order of absorption peak values plotted)

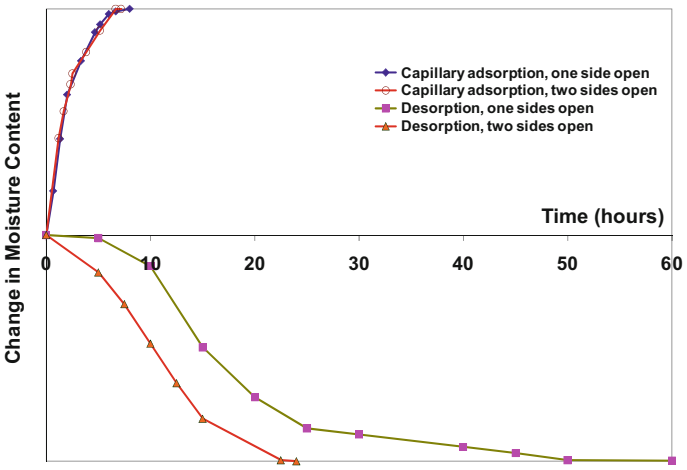

Fig. 8.7 Comparative summary of change in moisture content derived from peak optical absorption values shown in Figs. 8.3, 8.4, 8.5 and 8.6

8.4.2 Capillary Absorption

Following the same test procedure described above, the mortar specimens were placed in an oven at 50 °C for 7 days. They were then used for testing for capillary absorption of water. Figure 8.5 shows the variation in moisture at the level of the fiber for the specimen having only the bottom surface exposed to water. Figure 8.6 provides the same information for the specimen submerged in water to 5 mm above its top surface. As shown in the plot, first signs of moisture at the fiber level appeared at 0.08 and 0.22 h for the double and single sided tests, respectively. Steady state moisture content (i.e. capillary equilibrium) was obtained at approximately 8 h for single sided exposure and 6.7 h for double sided exposure conditions.

8.4.3 Discussion

Figure 8.7 summarizes the test results. It is constructed using the peak values of optical absorption plotted in Figs. 8.3, 8.4, 8.5 and 8.6. A direct relationship between moisture content and optical absorption peak is assumed, where the peak optical absorption values are normalized to that measured at steady state conditions. This assumes a linear relationship between change in optical absorption and change in moisture content.

Drying: The results vividly confirm the theory (Hall and Hoff 2011) which states that drying of porous materials under constant environmental conditions occurs in two distinct stages, often called the constant period (Stage I), and the falling period (Stage II). Stage I drying is independent of capillary processes inside the material. Instead, it depends on external conditions (temperature, RH and air speed). Stage II drying; on the other hand, depends wholly on the capillary properties of the material. Figure 8.7 shows that, for the first 8–10 h (Stage I), the mortar specimen having both sides exposed is drying at approximately double the rate than the specimen with the single exposed side. This is entirely reasonable since Stage I drying is considered to be in action during this period of time. Hence, by having both sides exposed, the specimen dries quicker since water evaporates from a surface area which is double in size than the equivalent drying surface area of the specimen with the single exposed side. For the remaining time, both specimens are drying at almost the same rate. We ascribe this to Stage II drying behavior. Since both specimens were cast in a similar way, capillary processes inside them are expected to be identical. Hence, the drying rates during Stage II are not expected to differ. This is confirmed by the similar shapes of the drying curves at later stages, as shown in Fig. 8.7.

Adsorption: The capillary adsorption results can be explained in terms of the theory of air trapping (Hall and Hoff 2011; Ioannou et al. 2003). In contrast capillary absorption into systems that have unsealed boundary surfaces from which air may escape, it is invariably assumed that the air that is driven forward by the advancing wet front is displaced easily without generating significant internal pressure gradients. In the case of adsorption into a sample that is sealed on all faces except the inflow surface, the displaced air driven ahead of the wetting front is trapped by the sealed end face (Hall and Hoff 2011; Youngs et al. 1994). As the wetting front advances, the volume occupied by the air within the sample decreases and the pressure of the displaced air rises. The advancing wet front experiences increasing resistance as it compresses the air ahead of it and eventually imbibition ceases when the increase in air pressure equals the wetting front capillary pressure. This has been demonstrated experimentally by Ioannou et al. (2003) who used the equilibrium pressure of the displaced air to estimate the wetting front capillary pressure of a porous fired clay brick. A similar effect takes place when a sample is absorbing a liquid from two opposite sides simultaneously. In this case, air is trapped in between the two wetting fronts. During our experiments, no bubbles were seen escaping from the sample having both sides exposed to absorption. This confirms that all air was compressed by the pincer action of the two wetting fronts approaching from opposite sides. Since both samples were cast in a similar way, one could assume that they both have the same porosity (hence the same volume of air). Entrapment of this volume of air either behind the sealed end face or in between the two wetting fronts, as water is absorbed into the specimens, leads to capillary equilibrium at approximately the same time for both samples.

8.5 Conclusion

Tests on the application of Near-Infrared spectroscopy for monitoring moisture transport in cement mortar were carried out. The results indicate that:

(1) Optical fibers are an effective means for in situ analysis of aqueous species in porous construction materials. They minimally disturb the analysis environment and therefore closely reflect features of the bulk environment. Furthermore, they do not contain metallic components and are not prone to corrosion.
(2) The evanescent field of the optical energy is capable of distributed transduction of information about the internal variations of moisture content in porous structures. This is particularly important for heterogeneous materials like cement mortars and concrete where point measurement may not provide a true representative measure.
(3) Capillary absorption and drying by evaporation tests on mortar samples indicate that the proposed method can be used to reveal internal variations of moisture content as a function of time and boundary condition in porous construction materials.

References

Ansari, F. (2000). *Condition monitoring of materials and structures*. Reston, Va: American Society of Civil Engineers.

Boguszynska, J., Brown, M. C. A., Mcdonald, P. J., Mitchell, J., Mulheron, M., Tritt-Goc, J., et al. (2005). Magnetic resonance studies of cement based materials in inhomogeneous magnetic fields. *Cement and Concrete Research, 35*(10), 2033–2040.

Cheng, K. C., Yoon, S., Kostarelos, K., Ghandehari, M., & Vimer, C. (2008). *Near-Infrared spectroscopy for in-situ monitoring of geoenvironment*.

Claisse, P. A. (2014). *Transport properties of concrete: Measurements and applications*. Cambridge: Woodhead Publishing.

Crank, J. (1976). *The mathematics of diffusion* (2nd ed., Repr. edn.). Oxford: Clarendon Pr.

Da Rocha, M. C., Da Silva, L. M., Appoloni, C. R., Portezan Filho, O., Lopes, F., Melquíades, F. L., et al. (2001). Moisture profile measurements of concrete samples in vertical water flow by gamma ray transmission method. *Radiation Physics and Chemistry, 61*(3), 567–569.

De J. Cano-Barrita, P. F., Marble, A. E., Balcom, B. J., García, J. C., Masthikin, I. V., Thomas, M. D. A., et al. (2009). Embedded NMR sensors to monitor evaporable water loss caused by hydration and drying in portland cement mortar. *Cement and Concrete Research, 39*(4), 324–328.

Dyer, T. (2014). *Concrete durability* (1st ed.). London: Crc Press.

FHWA. (2017-last update). ASR reference center. Available: https://www.fhwa.dot.gov/pavement/concrete/asr/referencecfm.

Ghandehari, M., & Khalil, G. (2005). Materials health management by in-situ chemical analysis. *ASNT Journal of Materials Evaluation, 63*(7).

Ghandehari, M., & Vimer, C. S. (2004). In-situ monitoring of pH level with fiber optic evanescent field spectroscopy. *NDT and E International, 37*(8), 611–616.

Grasley, Z., Lange, D., & D'ambrosia, M. (2006). Internal relative humidity and drying stress gradients in concrete. *Materials and Structures, 39*(9), 901–909.

Gummerson, R. J., Hall, C., & Hoff, W. D. (1981). Water movement in porous building materials—III. A sorptivity test procedure for chemical injection damp proofing. *Building and Environment, 16*(3), 193–199.

Hall, C., & Hoff, W. D. (2011). *Water transport in brick, stone and concrete* (2ed.). London [u.a.]: Taylor & Francis.

Hall, C., & Yau, M. H. (1987). Water movement in porous building materials—IX. The water absorption and sorptivity of concretes. *Building and Environment, 22*(1), 77–82.

Hansen, E. J., & Hansen, M. H. (2002). TDR measurement of moisture content in aerated concrete. In *6th symposium on building physics in The Nordic Countries, June 17–19, 2002* (pp. 381–388). Norwegian University of Science and Technology.

Hanzic, L., & Ilic, R. (2003). Relationship between liquid sorptivity and capillarity in concrete. *Cement and Concrete Research, 33*, 1385–1388.

Henkensiefken, R., Castro, J., Bentz, D., Nantung, T., & Weiss, J. (2009). Water absorption in internally cured mortar made with water-filled lightweight aggregate. *Cement and Concrete Research, 39*(10), 883–892.

Hobbs, D. W. (2001). Concrete deterioration: Causes, diagnosis and minimizing risk. *International Materials Reviews, 46*(3), 117–144.

Hoff, W. D., & Hall, C. (2009). *Water transport in brick, stone and concrete.* (2nd ed.). Baton Rouge: CRC Press.

Hoff, W. D., Hall, C., Hawkes, R., Holland, G. N., Moore, W. S., & Gummerson, R. J. (1979). Unsaturated water flow within porous materials observed by NMR imaging. *Nature, 281* (5726), 56–57.

Ioannou, I., Hall, C., Wilson, M. A., Hoff, W. D., & Carter, M. A. (2003). Direct measurement of the wetting front capillary pressure in a clay brick ceramic. *Journal of Physics. D. Applied Physics, 36*(24), 3176–3182.

Johnson, F. J., Cross, W. M., Boyles, D. A., & Kellar, J. J. (2000). "Complete" system monitoring of polymer matrix composites. *Composites: Part A, 31*(9), 959–968.

Kanematsu, M., Maruyama, I., Noguchi, T., Iikura, H., & Tsuchiya, N. (2009). Quantification of water penetration into concrete through cracks by neutron radiography. *Nuclear Inst. and Methods in Physics Research, A, 605*(1), 154–158.

Kumaran, M. K., & Bomberg, M. A. (1985). A gamma-spectrometer for determination of density distribution and moisture distribution in building materials (pp. 485–490). *National Research Council Canada,* NRCC24693.

Laurens, S., Balayssac, J., Rhazi, J., Klysz, G., & Arliguie, G. (2005). Non-destructive evaluation of concrete moisture by GPR: Experimental study and direct modeling. *Materials and Structures, 38*(9), 827–832.

Martys, N. (1995). *Survey of concrete transport properties and their measurement* (Nistir 5592 ed.). Gathersburg Md: National Bureau of Standards.

Martys, N., & Hagedorn, J. (2002). Multiscale modeling of fluid transport in heterogeneous materials using discrete Boltzmann methods. *Materials and Structures, 35*(10), 650–658.

Mijović, J., & Andjelić, S. (1995). In situ real-time monitoring of reactive systems by remote fibre-optic near-infra-red spectroscopy. *Polymer, 36*(19), 3783–3786.

Okamura, S. (2000). Microwave technology for moisture measurement. *Subsurface Sensing Technologies and Applications, 1*(2), 205.

Pavlík, Z., Jiřičková, M., Černý, R., Sobczuk, H., & Suchorab, Z. (2006). Determination of moisture diffusivity using the time domain reflectometry (TDR) method. *Journal of Building Physics, 30*(1), 59–70.

Pavlík, J., Tydlitát, V., Černý, R., Bouška, P., Rovnaníková, P., & Kle, T. (2003). Application of a microwave impulse technique to the measurement of free water content in early hydration stages of cement paste. *Cement and Concrete Research, 33*(1), 93–102.

Poukhonto, L. M. (2003). *Durability of concrete structures and constructions: Silos, bunkers, reservoirs, water towers, retaining walls*. Exton, PA: A.A. Balkema.

Prado, P. J. (2001). NMR hand-held moisture sensor. *Magnetic Resonance Imaging, 19*(3), 505–508.

Roels, S., & Carmeliet, J. (2006). Analysis of moisture flow in porous materials using microfocus x-ray radiography. *International Journal of Heat and Mass Transfer, 49*(25), 4762–4772.

Savitzky, A., & Golay, M. J. E. (1964). Smoothing and differentiation of data by amplified least squares procedures. *Analytical Chemistry, 36,* 1627–1639.

Sun, H., Ren, Z., Memon, S. A., Zhao, D., Zhang, X., Li, D., et al. (2017). Investigating drying behavior of cement mortar through electrochemical impedance spectroscopy analysis. *Construction and Building Materials, 135,* 361.

Youngs, E. C., Leeds-Harrison, P. B., & Garnett, R. S. (1994). Water uptake by aggregates. *European Journal of Soil Science, 45*(2), 127–134.

Zhang, P., Wittmann, F. H., Zhao, T., Lehmann, E. H., & Vontobel, P. (2011). Neutron radiography, a powerful method to determine time-dependent moisture distributions in concrete. *Nuclear Engineering and Design, 241*(12), 4758–4766.

Chapter 9
Subsurface Monitoring of Water in Soil

Masoud Ghandehari, Konstantinos Kostarelos and Christian S. Vimer

Abstract This chapter demonstrates the usefulness of Near-Infrared optical fiber analysis for sensing moisture migration in soil. As a result of a series of experiments and laboratory testing a number of sensing probes have been developed that are comprised of optical fibers using the evanescent field as the signal transduction mechanism. The movement of water through dry sand was simulated in the laboratory and the sensors were used in situ to measure the variation of soil moisture in real time.

9.1 Introduction

Soil moisture monitoring has long been critical to variety of water resource applications including agriculture. There has been considerable effort made toward development of tools for in situ monitoring of subsurface soil moisture and other non-aqueous species. Excellent reviews of methods for moisture analysis can be found in the literature (Zazueta and Xin 1994; Walker et al. 2004; Pignatti et al. 2014; Culligan et al. 2005; Kun et al. 2015; Ochsner et al. 2013; Charbeneau 2000; DOE 2001; EPA 2005; McCulloch et al. 1995). Among the various technologies for detection of moisture content, electrochemical methods have been the most popular. These include hygrometric sensors based on electrical resistance, capacitance, piezoelectric sorption, dew point, and psychometric measurements. Electrochemical

M. Ghandehari (✉)
New York University, Six Metrotech Center, Brooklyn, NY 11201, USA
e-mail: masoud@nyu.edu

K. Kostarelos
College of Engineering, University of Houston, 5000 Gulf Freeway, Houston, TX 77204, USA
e-mail: kkostarelos@uh.edu

C. Vimer
Madsen Consulting Engineering, 175 Varick St #803, New York, NY 10014, USA
e-mail: cvimer@gmail.com

M. Ghandehari, *Optical Phenomenology and Applications*,
Smart Sensors, Measurement and Instrumentation 28,
https://doi.org/10.1007/978-3-319-70715-0_9

probes are well established and accurate but exhibit limited durability for long-term use in harsh environments (Zazueta and Xin 1994).

In parallel, full field remote sensing technologies for soil surface analysis have been implemented for large surface analysis (Famiglietti et al. 2008). Recent techniques include wireless CMOS sensors (Morais et al. 2004) and microwave radiometry (Narayan et al. 2004). Examples of products include those developed by Sandia National Laboratories (SNL) that permit real–time, continuous measurement of moisture. The system is a time domain reflectometry (TDR) sensor and is based on analyzing the velocities of an electromagnetic wave that is passed along the waveguides (SNL 1995). The velocity depends on the dielectric constants of soil and moisture.

Optical sensors have some unique uses for moisture detection, including long-term durability. Wlodarczyk and colleagues developed an evanescent field, fiber optic sensor for water vapors, using a fiber with the cladding removed and exposed to relative humidity (RH), where the reduction in the signal of a single LED source was measured and correlated with RH levels (Wlodarczyk et al. 1987). Sandia National Laboratories also engineered a sensor that permits real–time, continuous measurement of moisture (Ho et al. 2001). The fiber optic RH sensor mentioned above quantifies capillary pore pressure in dry soils. The sensor is made of porous polymer sensing material located between the tips of two standard optical fibers. When water vapor reacts with the sensing material, the optical characteristics of that material are affected. This fiber optic RH sensor is calibrated to measure relative humidity and pore pressure (Ho et al. 2001). Other developments in remote monitoring for moisture include down–hole logging systems developed by Sandia National Laboratories and supplied by Troxler Labs (Williams et al. 1996). These incorporate a neutron source made of radioactive americium/beryllium (10 mCi) and a detector for hydrogen atoms where probes are winched through tubes which have been preinstalled under the waste sites. The process is capable of making accurate measurements but the radioactive source must be handled carefully.

The technique presented in this paper is based on using functional hydrophilic polymeric cladding materials on the surface of the optical fiber core. Similar to the hydrocarbon detection strategy in Chap. 12, Near-Infrared absorption bands of water are used for detection of moisture and its content. The most significant advantage of NIR spectroscopy is the elimination of indicators, improving the probe durability. Light interaction through hydrophilic membranes is a robust approach for sampling the harsh subsurface environment.

9.2 Optical Spectroscopy

9.2.1 Optical Fiber Probe and the Evanescent Field

In an optical fiber, light travels within the fiber core by Total Internal Reflection (TIR) from the core–cladding interface (Fig. 9.1). However, a small portion of the light

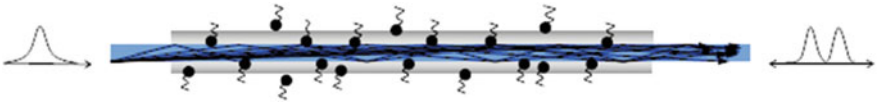

Fig. 9.1 Schematic of the principle of evanescent field spectroscopy

penetrates the cladding and travels as a surface wave on the outside of the interface. This guided energy is called the *evanescent field*. In telecommunication, the evanescent field is isolated from the outside environment. However, for sensing, the optical fiber may be coated with porous polymeric membranes (Ghandehari and Vimer 2004) allowing interaction. In effect, the evanescent field enables the optical energy traveling within the fiber core to sample the media that has penetrated the porous cladding. For aqueous species, a water friendly polymer such as cellulose may be used; for hydrocarbons, a variety of lipophilic polymers such as olefin copolymer can be used.

9.2.2 Absorption Spectroscopy

When electromagnetic radiation travels through a substance, the energy is absorbed or transmitted. This phenomenon is a function of the frequency and the structure of the molecules encountered. Such absorption spectra are often used for characterization or sensing of materials. For example, the frequency of the absorbed radiation relates to the material's characteristic energy levels according to Planck's law:

$$E_{final} - E_{initial} = E = hc/\lambda \tag{9.1}$$

where E is energy, h is the Planck's constant, c is the speed of light in the specific media, and λ is the wavelength of the light beam. Absorption spectroscopy can be defined as the measurement and analysis of electromagnetic radiation absorbed by atoms, molecules or other chemical entities. In microwave spectroscopy, the absorption is accompanied by a transition from one rotational energy level of a molecule to another. In Infrared spectroscopy, the transition is from one vibrational energy level of a molecule to another. In Ultraviolet–Visible (electronic absorption) spectroscopy, transition levels relate to valence electrons in the molecule. In general, absorption is defined by the Beer–Lambert Law as:

$$A(\lambda) = \varepsilon bc(\lambda) \tag{9.2}$$

Therefore, absorption depends on the concentration of absorbing species "c", the path length of interaction "b", as well as the specific molar absorptivity "ε" of the species. The fact that absorptivity is wavelength dependent is reflected in the shape of the absorption spectra. The relationship shown in Eq. 9.2 can be written in a different form:

$$A(l) = -\log(I(l)/I_0(l)) \tag{9.3}$$

where I_0 is the intensity of the energy before the interaction with the analyte of interest and I is the intensity after the interaction. A plot of the absorption "A" versus wavelength is called the absorption spectra. Larger values in the y axis indicate greater absorption.

In the work presented in this paper, Near-Infrared molecular vibration spectroscopy is carried out, where the absorbing volume is comprised of the depth of the evanescent field times the cladding circumference times the contact length of fiber. Databases containing the Infrared spectra of many molecules are available. This information has been traditionally documented in the Mid-Infrared region (2.5–25 m) of the electromagnetic spectra. Analyses are often carried out using bench–top instruments. However, recent advances and availability of optical devices and wave guides in the Near-Infrared region (NIR) offer new opportunities for in situ Near-Infrared spectroscopy.

9.3 Near-Infrared Signatures

The Near-Infrared region of the electromagnetic spectrum (1.2–2.5 m) contains overtones (higher frequency modes) of the fundamental Mid-Infrared modes of vibrations. Since each material is a unique combination of atoms, no two compounds produce the exact same Near-Infrared signature. Therefore, Near-Infrared (NIR) spectroscopy can be an affordable means for the identification of materials or chemical species. NIR absorption bands are broad, so that the need for high–resolution instruments is not required. However, the absorption intensity is dramatically reduced in intensity, posing certain limitations for detecting low concentrations of contaminants compared to Mid-Infrared spectroscopy. Nevertheless, in situ, Near-Infrared analysis promises to be a low cost and convenient tool for initial screening and analysis of numerous substances in the subsurface environment and, most importantly, for long–term, real–time monitoring.

As an example, the water molecule has N = 3 atoms resulting in $3N-6 = 3$ fundamental vibration modes. These vibration modes which take place in the Mid-Infrared region (MIR) of the EM spectrum consist of (1) symmetric OH stretch, (2) anti–symmetric OH stretch, and (3) OH bending mode (Fig. 9.2). In liquid water, wavelengths associated with these vibrations are 3106, 2903, and 6079 nm, respectively. Overtones of these vibration modes appear in the Near-Infrared region of the EM spectra. Important absorption bands of water in this region appear at approximately 1935 nm ($\nu_2 + \nu_3$), 1435 nm ($\nu_1 + \nu_3$), 980 nm ($2\nu_1 + \nu_3$), and 745 nm ($3\nu_1 + \nu_3$). The absorption band of water at 1935 nm is used in the following experiments.

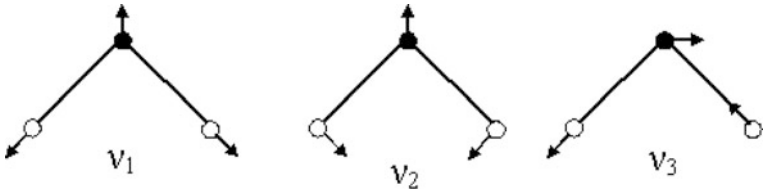

Fig. 9.2 Vibration modes of water molecule: ν1 (symmetric OH stretch), ν2 (OH bending), and ν3 (anti–symmetric OH stretching)

9.4 Experimental Work

An experimental program was planned to assess whether the proposed NIR spectroscopic technique provides adequate selectivity among typical contaminants. Additionally, experiments were carried out to demonstrate the validity of the technique by comparison with certain known models of transport of the contaminant in dry and saturated soil. Six experiments were conducted:

(1) Transport of water through dry sand in a panel subject to a constant flow (Fig. 9.3a);
(2) Capillary moisture transport through dry sand in a column (Fig. 9.3b).

Experimental Setup
Experiments 1, 2 and 3 were carried out using a table top spectrometer (Shimadzu Prestige-21 IR-NIR spectrometer) and experiments 4, 5 and 6 were carried out using a portable spectrometer (Ocean optics NIR256). The experiment was done using a Plexiglas chamber (Fig. 9.3). NIR light is launched from the spectrometer through a fiber optic patch chord and into the embedded sensing probe. The light reflects back from a fiber tip reflector through the probe and into the spectrometer. In this configuration the light interacts twice with the sample along the sensing length. The optical fiber probes were developed using step-index multimode low OH plastic clad silica (PCS) fibers (Thor Labs Inc., Newton, NJ) with 600 μm core diameter, 630 μm cladding diameter and 1030 μm buffer diameter. One meter portions of the

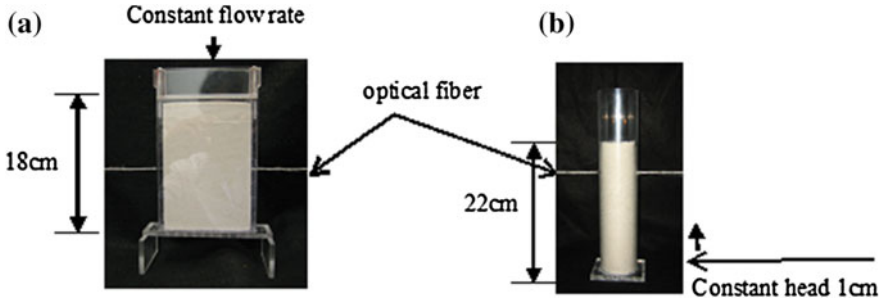

Fig. 9.3 Test chambers: panel specimen **(a)**, column specimen **(b)**

fiber were cut; the buffer and cladding were removed in the middle region over a length of 10 cm using a surgical blade and acetone. The fiber ends were polished using lapping films and the ends were fitted with SMA type connectors. The optical fiber probes were illuminated by a Tungsten Halogen light source connected to the portable Ocean Optics Near-Infrared spectrometer operated through a laptop. The operative wavelength of the spectrometer ranges from approximately 1250–2150 nm with resolution of approximately 4 nm using a 256 element array of Indium Gallium Arsenide (InGaAs) detector elements. This resolution is adequate for the relative wide NIR absorption bands of water and hydrocarbons.

9.4.1 Transport of Water Through Dry Sand

The purpose of this experiment was to validate the proof of the concept that the sensor could detect changes in soil moisture. Federal fine sand (U.S. Silica) was placed into a Plexiglas® container 18 cm x 12 cm x 1 cm by raining the sand through a series of screens to achieve an even rain intensity over the cross sectional area, while vibrating the container to settle the grains. Gradation of this sand is shown in Fig. 9.4. The fiber optic probe was placed at mid–height of the chamber prior to filling with sand. The optical fiber probe was connected to the portable NIR spectrometer for real time data collection.

A constant flow of 2.5 ml/min water was provided by an electric pump distributed through a line source at the top of the cell simulating one dimensional, gravity–driven flow. A reference intensity spectrum (1250–2150 nm) was recorded in a dry state followed by intensity spectra of various wet states at 30 s intervals. The absorption spectra were calculated using Eq. 9.3. The spectra are smoothed for

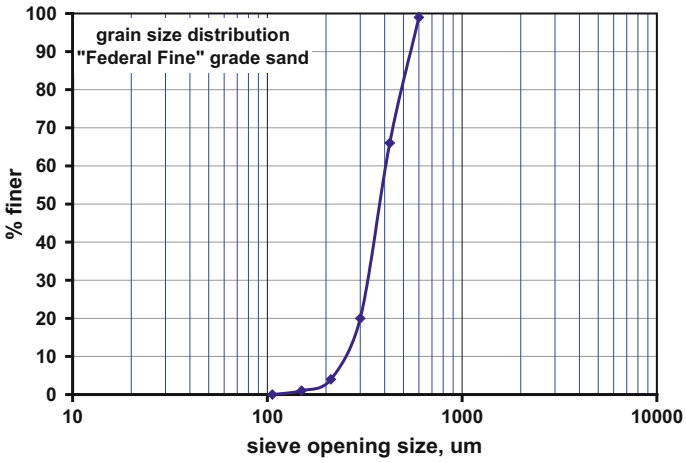

Fig. 9.4 Sand gradation

50 values using the Savitzky–Golay algorithm (Savitzky and Golay 1964). The algorithm averages the points in a data set but first multiplies each point by a weighting factor. The factors which are derived from second and third degree polynomials give the most emphasis to the center point of the data set, and progressively less emphasis to the points further out. Distortion of peak apexes is minimized with this algorithm. In order to eliminate the "bending" or "falling down" of the measured spectra caused by light scattering, a multipoint baseline correction is applied to all spectra.

Figure 9.5 shows the dominant NIR absorption band of water (1850–2150 nm) with distinct increase in the absorption value versus time as the water reaches the sensing region. The lower degree of NIR absorption measured initially (0, 0.5 min, etc.) correspond to low water saturations. The intensity increased up to 0.009 absorption units (a.u.) reaching steady state within 15.5 min, which is indicative of a greater degree of water contact with the probe or an increasing water saturation. We assume that the steady state value represents 100% *effective* saturation. The changes in the peak absorption intensity (at 1935 nm wavelength) were plotted versus time in Fig. 9.6. These changes in absorption are caused by the increased degree of water contact with the probe, *i.e.*, increased water saturation. The observed behavior is consistent with known models for water imbibition, where dry soil will increase from 0% saturation until it reaches a certain value. It should be noted that this value may not reach *true* 100% saturation because some soil pores may be inaccessible or contain trapped air (Charbeneau 2000; Gupta 2001). This value represents an effective fully–saturated soil. The line in Fig. 9.6 is a trend line, the sensitivity at lower moisture contents may be limited.

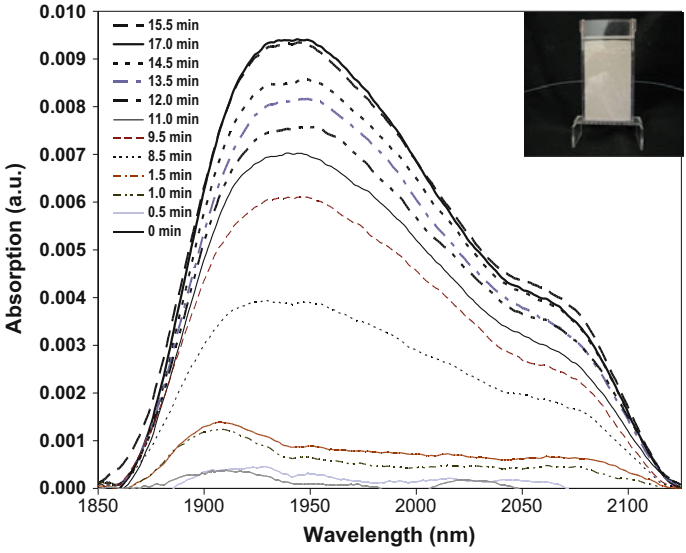

Fig. 9.5 Absorption spectra versus time for constant flow rate experiment

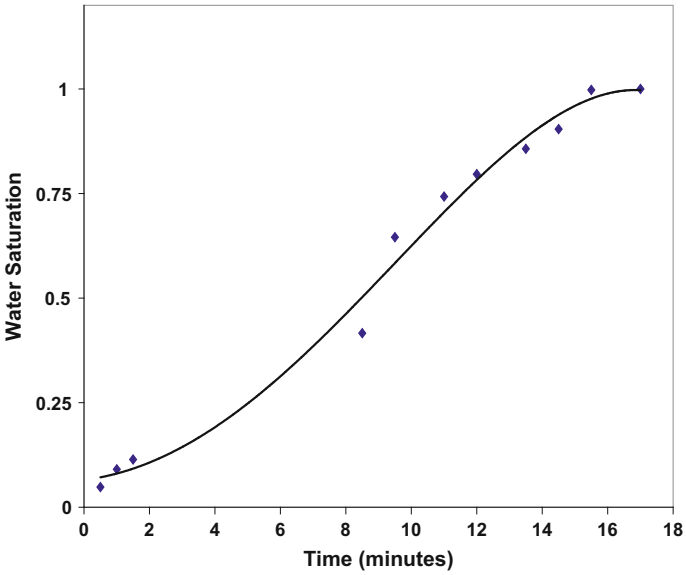

Fig. 9.6 Water saturation for constant flow rate experiment based on absorption peak measured at 1935 nm (solid line is trend line of data points)

9.4.1.1 Experiment: Capillary Moisture Transport Through Dry Sand

The second set of experiments was carried out to determine whether the sensor could be used to measure the degree of soil moisture. This experiment also differed from the first in that a sensor response (NIR absorption) corresponding to 100% water saturation was made and not assumed. In addition, water was allowed to flow from the bottom upward (due to capillarity) within a 5 cm diameter Plexiglas column packed with dry sand. The fiber optic probe was placed at a height of 17 cm and the column was filled with dry Federal fine grade sand, as used in the first experiment. The test chamber is shown in Fig. 9.3b. This test included a pump to maintain constant one centimeter water level at the bottom of the column. The data was acquired using dry sand as the initial condition. Once water was allowed to enter the bottom of the packed column, the sensor response due to changes in water saturation was measured in terms of the NIR absorption spectra of water (centered at approximately 1935 nm) as shown in Fig. 9.7. Absorption intensity reached a steady value of 0.0045 a.u. at approximately 72 min. The results shown in Fig. 9.7 correspond to the changes in water saturation due to the capillary rise of water within sand and the steady value corresponds to equilibrium saturation. This value reflects the partially saturated condition of the soil.

In order to quantify the degree of water saturation, the head was raised to 18 cm and spectra corresponding to 100% water saturation were evaluated (Fig. 9.7). We know that the soil will be 100% saturated at the location of the water table, thus

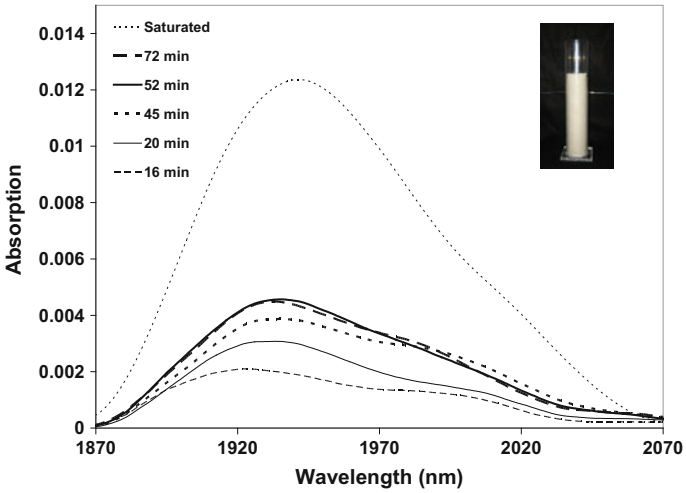

Fig. 9.7 Absorption spectra versus time for 1 cm constant head experiment

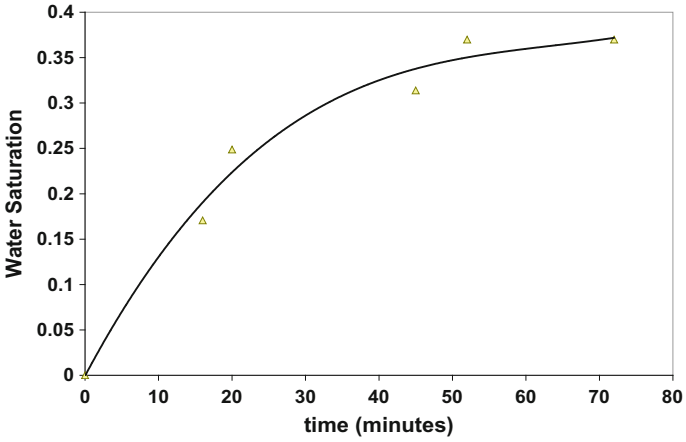

Fig. 9.8 Water saturation for constant head experiment, based on absorption peak measured at 1935 nm, (solid line is trend line of data points)

raising the water level above the fiber optic sensor, hence providing a fully–saturated state. The response of 0.012 a.u. for the 1935 nm wavelength was then used to compute the degree of saturation for other absorption intensities as a fraction of the response at 100% saturation. Figure 9.8 shows the moisture saturation changes from dry to a partially saturated condition due to the capillarity at the fiber sensor.

In a separate but analogous column experiment, the degree of water saturation was measured by obtaining grab samples of the soil and comparing the mass before and after drying in an oven. Results indicate 25% water saturation, lower than the

35% value obtained using the sensor. There are several reasons why measurement of saturation of soil samples would be lower than that measured using the sensor. First, the fiber within the soil structure presents an intrusion within the granular packing which will cause the soil pores to become somewhat extended. Furthermore, the fiber/soil interface may not represent a homogenous and undisturbed soil environment. Such interfaces tend to attract moisture and so the fiber may be registering a somewhat higher degree of saturation than the soil pores. Of course, the difference that we experienced between the value of saturation measured by the sensor and that measured gravimetrically may be simply due to a difference in the packing of the two columns or due to the statistical scatter of the experimental result. These issues need to be thoroughly explored in future work. Nonetheless, the results shown here demonstrate a potential of the technology for measurement of moisture within soil.

9.5 Conclusion

Near-Infrared spectroscopy using optical fibers provides an opportunity for in situ monitoring of moisture within porous media. Flow experiments were conducted to test the sensor's response to changes in moisture content. Water saturation levels ranging from 5 to 100% were recorded as the wetting front made contact with the sensor. Capillary transport of water in a column was carried out and water saturation levels ranging from 15 to 100% were measured. The minimum measured value of water saturation was dictated by the sampling speed, so the reported 15% is not an indication of the minimum detection limit.

References

Charbeneau, R. J. (2000). *Groundwater hydraulics and pollutant transport*. Upper Saddle River, NJ: Prentice Hall.

Culligan, P. J., Ivanov, V., & Germaine, J. T. (2005). Sorptivity and liquid infiltration into dry soil. *Advances in Water Resources, 28*(10), 1010–1020.

DOE. (2001). *Internal reflection sensor for the cone penetrometer DOE/EM-0611*. Washington, DC: DOE Office of Environmental Management.

EPA. (2005). Road map to understanding innovative technology options for brownfields investigation and cleanup. Washington DC: EPA.

Famiglietti, J. S., Rodell, M., Jackson, T. J., Ryu, D., & Berg, A. A. (2008). Field observations of soil moisture variability across scales. *Water Resources Research Journal, 44*(1), N/A.

Ghandehari, M., & Vimer, C. S. (2004). In-situ monitoring of pH level with fiber optic evanescent field spectroscopy. *NDT and E International, 37*(8), 611–616.

Gupta, R. S. (2001). *Hydrology and hydraulic systems* (2nd ed.). Prospect Heights, Ill: Waveland Press.

Ho, C. K., Itamura, M. T., Kelley, M. J., & Hughes, R. C. (2001). *Review of chemical sensors for in situ monitoring of volatile contaminants.* Sandia National Laboratories.

Kun, X., Sheng, Q., Zhang, X., Li, P., & Chen, S. (2015). Design and calibration of the unilateral sensitive soil moisture sensor. *IEEE Sensors Journal, 15*(8), 4587–4594.

Mcculloch, M., Fadeff, S. K., Mong, G. M., Riley, R. G., Sklarew, D. S., Thomas, B. L., et al. (1995). The U.S. Department of Energy (DOE) sampling and analytical chemistry guide: DOE methods for evaluating environmental and waste management samples. *International Journal of Environmental Analytical Chemistry, 60*(2–4), 289–293.

Morais, R., Valente, A., Couto, C., & Correia, J. H. (2004). A wireless RF CMOS mixed-signal interface for soil moisture measurements. *Sensors and Actuators, A: Physical, 115*(2), 376–384.

Narayan, U., Lakshmi, V., & Njoku, E. G. (2004). Retrieval of soil moisture from passive and active L/S band sensor (PALS) observations during the soil moisture experiment in 2002 (SMEX02). *Remote Sensing of Environment, 92*(4), 483–496.

Ochsner, T. E., Cosh, M. H., Cuenca, R. H., Dorigo, W. A., Draper, C. S., Hagimoto, Y., et al. (2013). State of the art in large-scale soil moisture monitoring. *Soil Science Society of America Journal, 77*(6), 1888–1932.

Pignatti, S., Simoniello, T., Sterk, G., & De Jong, S. M. (2014). Sensing techniques for soil characterization and monitoring. *European Journal of Soil Science, 65*(6), 840–841.

Savitzky, A., & Golay, M. J. E. (1964). Smoothing and differentiation of data by amplified least squares procedures. *Analytical Chemistry, 36,* 1627–1639.

Sandia National Laboratories. (1995-last update). Fiber optic relative humidity and TDR sensors for the cone penetrometer. Available: http://www.cpeo.org/techtree/ttdescript/fiorhtdr.htm, March, 2017.

Walker, J. P., Willgoose, G. R., & Kalma, J. D. (2004). In situ measurement of soil moisture: A comparison of techniques. *Journal of Hydrology, 293*(1), 85–99.

Williams, C., Burford, T., & Allen, C. A. (1996). *Technology integration report: Environmental restoration technologies department*. Albuquerque, NM: Sandia National Laboratories.

Wlodarczyk, M. T., Vickers, D. J., & Kozaitis, S. P. (1987). *Evanescent field spectroscopy with optical fibers for chemical sensing,* Cambridge Symposium Fiber/LASE, 18–26 August 1986, SPIE, pp. 192–197.

Zazueta, F. S., & Xin, J. (1994). *Soil moisture sensors.* Gainesville, FL: University Of Florida.

Chapter 10
Sensing Hygrothermal Processes in Calcium Silicate Hydrates

Masoud Ghandehari, Alexey Sidelev, Engui Liu, Christian Brückner and Gamal Khalil

Abstract Two parameters are used to assess the maturity of fresh hydraulic cement during the curing process: temperature and water content. This chapter describes the preparation and the application of two optical fiber sensors for simultaneous measurement of temperature and moisture. The temperature sensor utilizes Europium beta diketonates, a luminescent complex with an emission signal that provides temperature data. The moisture sensor utilizes the intrinsic optical properties of the water molecule used for the quantitative measurement of the liquid phase moisture content. These probes were tested in fresh cement paste during the curing processes.

10.1 Introduction

Cement hydration is a multi-staged and multi-component chemical reaction, which effects physical properties of concrete such as strength and durability. Cement hydration is a reaction between hydraulic cement and water (Newman 2003), where

M. Ghandehari (✉)
New York University, Six Metrotech Center, Brooklyn, NY 11201, USA
e-mail: masoud@nyu.edu

A. Sidelev
Parsons, 100 Broadway, New York, NY 10005, USA
e-mail: a.sidelev@gmail.com

E. Liu
New York University Abu Dhabi, PO Box 129188, Abu Dhabi, UAE
e-mail: engui.liu@nyu.edu

C. Brückner
Department of Chemistry, University of Connecticut, Storrs, CT 06269, USA
e-mail: c.bruckner@uconn.edu

G. Khalil
Department of Aeronautics & Astronautics, University of Washington,
Box 352250, Seattle, WA 98195, USA
e-mail: gekhalil@gmail.com

M. Ghandehari, *Optical Phenomenology and Applications*,
Smart Sensors, Measurement and Instrumentation 28,
https://doi.org/10.1007/978-3-319-70715-0_10

the water is consumed and the corresponding reaction between water and the constitutions of cement (calcium, silica, alumina) results in release of energy as heat. The rate of water consumption and heat release, as well as conditions of the environment, influence the dynamic equilibrium during the hydration and curing reactions (Malhotra 2004). It is therefore important to track the hydration process, and, in some cases, actively control the hydration reaction in order to guarantee the required properties of the hardened concrete (McCall 2011; Dyer 2014).

While water is essential for formation and synthesis of constituents of a concrete mix; excessive amounts of water also create multiple issues, both in the short and long-term (Poukhonto 2003). Temperature also plays key role in curing, for example elevated temperatures increase hydration rate, but when it occurs non-uniformly, thermal stress results in cracking. This type of cracking is particularly pronounced in high-volume concrete/mass structures, where concrete placement is continuous and cooling of the cast concrete is challenging. Even in smaller castings, the heat generated may be enough to create a thermal gradient and cracking (McCall 2011). In addition to thermal stress, the high temperature during the hydration process leads to delayed ettringite formation (DEF) (Day 1992; Acquaye 2006; Barbarulo et al. 2005) which causes cracking over extended timescales. Monitoring of moisture and temperature simultaneously and in situ can insure quality concrete. While there are years of research and application experience in casting, monitoring and curing of concrete (Chotard et al. 2003; Norris et al. 2008; Pavlík et al. 2003), there are still gaps in the understanding of the chemical processes during hydration (Newman 2003; Malhotra 2004).

When considering the application of sensors for in situ monitoring, harsh concrete conditions, such as high pH levels, relatively high temperature and active chemical reactions limit the application of chemo-electric sensors. For these reasons fiber optic (FO) sensors (Yin 2008) have been introduced with a number of utilities for application to concrete including small size and durability (Yin 2008; Yeo et al. 2008; Leung et al. 2015). This chapter describes the application of fiber optic sensor for cure monitoring in concrete by simultaneous measurement of temperature and water content during the hydration process.

10.2 Materials

Sensing of temperature and moisture described in this chapter follow two different detection approaches. The temperature sensor is based on fluorescence spectroscopy while the moisture sensing is by absorbance spectroscopy.

10.2.1 Temperature Sensor

Similar to thermocouples, there are optically active molecules that are sensitive to change in ambient temperature (Amao and Okura 2002; Baleizão et al. 2008;

Venturini et al. 2015; Wang and Wolfbeis 2013; Brübach et al. 2011). We designed the temperature sensor as an optical fiber with temperature sensing compound at the tip. The sensing compound was based on a EuTTA temperature sensor molecule, which exhibits a fluorescent lifetime highly sensitive to temperature. The sensing compound was applied to the fiber tip and cured for 24 h at 80 °C and cooled to room temperature under ambient conditions. A protective aluminum cap was placed over the tip to prevent damage in concrete. The lifetime intensity was measured using a fluorimeter (MFPF-1) manufactured by TauTheta Instruments LLC (Boulder, Colorado). An Ocean Optics UV-VIS splitter was used to connect the temperature sensor to the fluorometer. The fluorometer had a built-in excitation light source. In addition, it had the capability to measure temperatures using thermocouple, which we used as reference. The optical fiber used for temperature sensing was a polymer optical fiber (POF Simplex plastic fiber) from FiberFin. The temperature sensor molecule was Europium (III) thenoyltrifluoroacetonate (EuTTA).

10.2.2 Moisture Sensor

The fiber optic moisture sensor was made as a tip-type sensor, where the sensor compound was a permeable PMMA. The recognition mechanism was based on the measurement of the optical absorption of Near-Infrared energy which is modulated by the moisture in the tip. Chapter 8 describes the recognition mechanism in full detail. The sensing tip was prepared by dipping a polished fiber tip into a PMMA-MAPTAC mixed with titanium dioxide, (TiO_2). The light intensity was checked to verify that enough light was delivered to the spectrometer. The sensing tip was cured for 24 h at 80 °C and cooled to room temperature in a drying chamber.

A Near-Infrared spectrometer (NIR256) manufactured by Ocean Optics, and a NIR LS-1 light source from Ocean Optics were used along with a fiber optic splitter to connect the sensing fiber. The moisture sensor was constructed using BFL37-600 silica fiber from Thorlabs. The MAPTAC-PMMA polymer was obtained from Professor Okamoto, of the Polytechnic University of New York University. Titanium dioxide grade CR-828 was obtained through Aldrich and manufactured by Tronox.

10.2.3 Cement Samples

Cement paste was prepared using Lafarge Type I Portland cement and tap water. The mold was an aluminum can (2.5″ diameter, 6″ tall) that was thermally insulated by a tight fit into a polystyrene cube (6.5″ × 6.5″ × 9″) with a 3″ thick removable cap.

10.3 Methods

10.3.1 Calibration and Monitoring

The moisture sensor was first tested in water and air. Figure 10.1 shows the response of the sensor in absorption and desorption by drying at ambient conditions (25 °C and 60% relative humidity). Figure 10.1 shows the sensor response, obtained by measuring the optical absorbance at the 1928 nm peak versus time. For details see Chap. 8. The sensor response in desorption is considerably faster than the absorption, however this is not very problematic given that curing processes in concrete occur in the desorption stage, and that duration of curing is much longer than the sensor response.

The temperature sensor was calibrated using temperature controlled water baths. The FO sensor signal and thermocouple temperature readings are shown in Fig. 10.2. Close correlation between the FO Temperature sensor signal and the thermocouple readings can be observed.

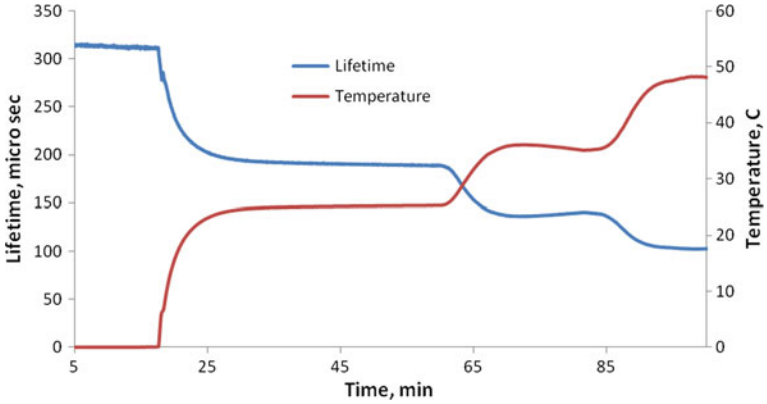

Fig. 10.2 FO temperature sensor signal (showing flourescence lifetime starting from 320 μs) and thermocouple readings response to temperature change

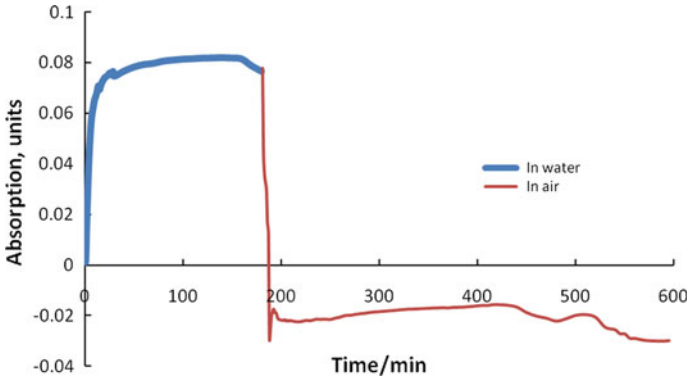

Fig. 10.1 Moisture sensor in water and in air

10.3.2 Curing

The sensors were placed in an empty mold. The cement and water (W/C ratio 0.5) was prepared combined and mixed and for 1 min. The fresh mix was poured into the mold containing the sensors, and covered with a polystyrene cap. The readings from the moisture and temperature sensors were then recorded. Figure 10.3 shows the response of the embedded FO temperature sensor and thermocouple.

Figure 10.4 shows the time response of the FO moisture and FO temperature sensors for 18 h after mixing the cement with water, the moisture sensor signal shown is the ratio of main NIR absorption peak to the absorbing wavelength

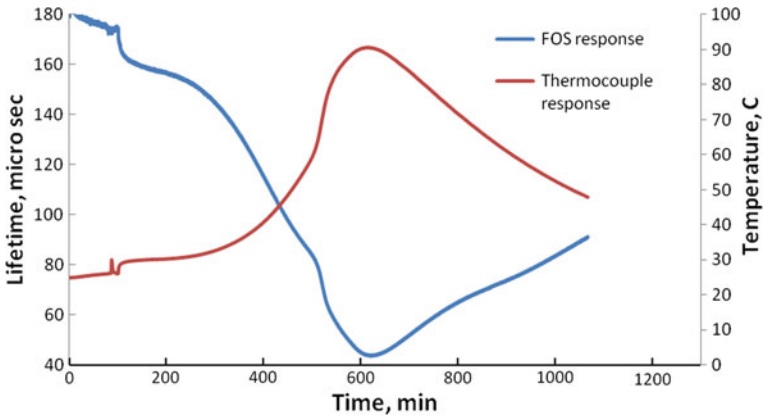

Fig. 10.3 FO temperature sensor signal (starting at 180 μs) and thermal couple temperature readings in curing cement paste

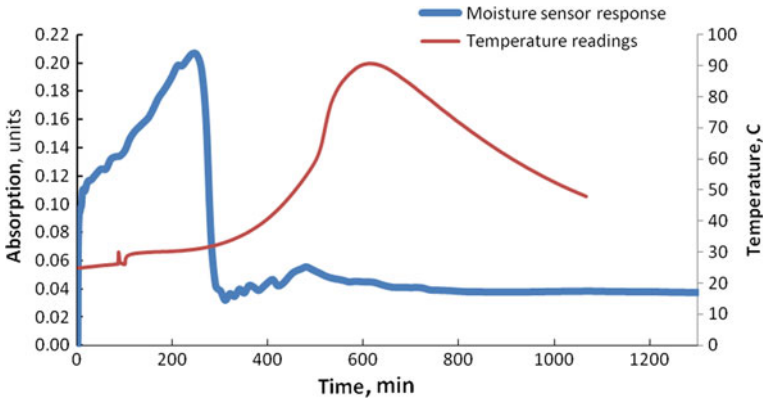

Fig. 10.4 FO moisture sensor signal and thermal couple temperature readings in curing cement paste

(see discussion in Chap. 8). At 4 h a high rate of water consumption is observed lasting approximately 20 min, concurrent with the heat of hydration rapidly releasing up to a peak at 10 h.

10.4 Conclusion

Preparation and application of two fiber optic (FO) sensors for cure monitoring of concrete was demonstrated. These included an FO Temperature sensor based on a temperature sensitive fluorescent compound at the distal end of the fiber. The moisture sensor was based on the measurement of the selective attenuation of the Near-Infrared energy by the water molecule. The application of this dual sensor system was demonstrated while tracking curing of cement paste for the first 15 h of hydration.

References

Acquaye, L. (2006). *Effect of high curing temperatures on the strength, durability and potential of delayed ettringite formation in mass concrete structures*, University of Florida.

Amao, Y., & Okura, I. (2002). Optical molecular thermometer based on the fluorescence of fullerene dispersed in poly(methyl methacrylate) film. *Bulletin of the Chemical Society of Japan, 75*(2), 389–391.

Baleizão, C., Nagl, S., Schäferling, M., Berberan-Santos, M. N., & Wolfbeis, O. S. (2008). Dual fluorescence sensor for trace oxygen and temperature with unmatched range and sensitivity. *Analytical Chemistry, 80*(16), 6449–6457.

Barbarulo, R., Peycelon, H., Prené, S., & Marchand, J. (2005). Delayed ettringite formation symptoms on mortars induced by high temperature due to cement heat of hydration or late thermal cycle. *Cement and Concrete Research, 35*(1), 125–131.

Brübach, J., Kissel, T., Frotscher, M., Euler, M., Albert, B., & Dreizler, A. (2011). A survey of phosphors novel for thermography. *Journal of Luminescence, 131*(4), 559–564.

Chotard, T. J., Smith, A., Boncoeur, M. P., Fargeot, D., & Gault, C. (2003). Characterisation of early stage calcium aluminate cement hydration by combination of non-destructive techniques: acoustic emission and X-ray tomography. *Journal of the European Ceramic Society, 23*(13), 2211–2223.

DAY, R. L. (1992). *Ettringite Formation on the Durability of Concrete.* Skokie, IL: Portland Cement Association.

Dyer, T. (2014). *Concrete durability* (1st ed.). London: CRC Press.

Leung, C. K. Y., Wan, K. T., Inaudi, D., Bao, X., Habel, W., Zhou, Z., et al. (2015). Review: Optical fiber sensors for civil engineering applications. *Materials and Structures, 48*(4), 871–906.

Malhotra, V. M. (2004). *Handbook on nondestructive testing of concrete* (2 ed.). Boca Raton, Fla. [u.a.]: CRC Press.

Mccall, W. C. (2011). The new ACI 301, "Specifications for structural concrete". *Concrete International,* 66.

Newman, J. (2003). *Advanced concrete technology.* Oxford [u.a.]: Elsevier.

Norris, A., Saafi, M., & Romine, P. (2008). Temperature and moisture monitoring in concrete structures using embedded nanotechnology/microelectromechanical systems (MEMS) sensors. *Construction and Building Materials, 22*(2), 111–120.

Pavlík, J., Tydlitát, V., Černý, R., Bouška, P., Rovnaníková, P., & Kle, T. (2003). Application of a microwave impulse technique to the measurement of free water content in early hydration stages of cement paste. *Cement and Concrete Research, 33*(1), 93–102.

Poukhonto, L. M. (2003). *Durability of concrete structures and constructions: silos, bunkers, reservoirs, water towers, retaining walls*. Exton, PA: A. A. Balkema.

Venturini, F., Bürgi, R., Borisov, S. M., & Klimant, I. (2015). Optical temperature sensing using a new thermographic phosphor. *Sensors and Actuators, A: Physical, 233,* 324–329.

Wang, X., & Wolfbeis, O. S. (2013). Fiber-optic chemical sensors and biosensors (2008–2012). *Analytical Chemistry, 85*(2), 487.

Yeo, T. L., Sun, T., & Grattan, K. T. V. (2008). Fibre-optic sensor technologies for humidity and moisture measurement. *Sensors and Actuators, A: Physical, 144*(2), 280–295.

Yin, S. (2008). *Fiber optic sensors* (2nd ed.). Boca Raton, Fla. [u.a.]: CRC Press.

Part IV
Subsurface Detection of Water Contaminants

Chapter 11
Sensing Water-Borne Pathogens by Intrinsic Fluorescence

Hao-Ming Fang, Karina Yew-Hoong Gin, Bavigadda Viswanath, Mircea Petre and Masoud Ghandehari

Abstract We investigated the feasibility of using intrinsic fluorescence of water-borne contaminants as a detection strategy. Four common pathogens, *Escherichia coli*, *Enterococcus faecalis*, *Pseudomonas aeruginosa* and *Salmonella typhimurium*, were cultured under controlled conditions; each sample was then diluted in a buffer solution, and analyzed for intrinsic fluorescence. Despite the findings reported in the literature, the experiments on the above four bacteria revealed very little difference in the emission spectra. Nevertheless, multivariate analysis of the emission data was able to classify the four species.

11.1 Introduction

Infectious water related diseases are a major cause of mortality in countries at all levels of economic development, posing a significant threat to public health (WHO 2012; Lopman et al. 2003; Ashbolt 2004). Most waterborne pathogens are introduced into drinking water by human activities such as urban runoff, leaking

H.-M. Fang · K. Y.-H. Gin · B. Viswanath
Department of Civil and Environmental Engineering, National University of Singapore, 1 Eng. Drive, Singapore 117576, Singapore
e-mail: erifh@nus.edu.sg

K. Y.-H. Gin
e-mail: ceeginyh@nus.edu.sg

B. Viswanath
e-mail: viswanath21@gmail.com

M. Petre
OptoTech Pte Ltd, 101A Upper Cross Street, #11-16 People's Park Centre, Singapore 58358, Singapore
e-mail: mpetre@optotech.com.au

M. Ghandehari (✉)
New York University, Six Metrotech Center, Brooklyn, NY 11201, USA
e-mail: masoud@nyu.edu

M. Ghandehari, *Optical Phenomenology and Applications*,
Smart Sensors, Measurement and Instrumentation 28,
https://doi.org/10.1007/978-3-319-70715-0_11

sewer pipes and waste water discharges. Among these pathogens, bacterial species contribute to a large portion of water-related diseases (WHO 2012).

Rapid identification of the bacterial species in recreational and drinking water will support efforts to identify the sources and distribution of bacterial contamination such that appropriate actions can be taken to protect public health. The conventional identification method based on morphology and biochemical tests involves a large number of reagents, is time-consuming and can take several days. Given population exposure through recreational water use (Oster et al. 2014; McBride et al. 2013; La Rosa et al. 2015) and patterns of drinking water distribution and consumption (Sokolova et al. 2015; Ashbolt 2015; Nabeela et al. 2014; Lavanya and Ravichandran 2013; Lu et al. 2015) there is an urgent need for the development of rapid, sensitive and reliable methods to identify and quantify harmful bacteria in water (Figueras and Borrego 2010; Jung et al. 2014; Tram et al. 2014). Molecular methods, in particular the quantitative polymerase chain reaction (qPCR) method, have been widely used to identify pathogens in water (Girones et al. 2010), such as *Salmonella* (Tambalo et al. 2012), *Campylobacter jejuni* and *Shigella flexneri* (Clark et al. 2011). However, molecular methods require DNA isolation, and the frequent presence of inhibitors in water sample may limit the efficacy of PCR-based methods (Schriewer et al. 2011).

In recent years, reagent-free, rapid methods, such as vibrational spectroscopy (including Fourier transform Infrared (FT-IR) (Nicolaou and Goodacre 2008; Horton et al. 2011), Fourier transform Near-Infrared (FT-NIR) (Rodriguez-Saona et al. 2001), and Raman spectroscopy (Fan et al. 2011), have been applied for detection and identification of bacteria, especially in food samples. While these methods provide high sensitivity, the cost of instrumentation is high, and the bacterial samples have to be pre-treated and coated onto a surface before they can be analyzed.

Live microorganisms contain a variety of intracellular biomolecules, such as tryptophan and other amino acids and coenzymes, etc., that emit photons following their excitation in the Ultraviolet region (Ammor 2007; Ammor et al. 2007; Estes et al. 2003). Previous studies have shown that the fluorescent characteristics of different microorganisms have specific excitation and emission wavelength spectra (Leblanc and Dufour 2002), and thus could be of use in biological detection techniques. It was reported that bifidobacteria species from human gastrointestinal tract were successfully identified at the species level or even subspecies level when combined with intrinsic fluorescence measurement and principal components analysis (PCA) and factorial discriminant analysis (FDA) (Ammor et al. 2007). Sohn et al. (2009) used fluorescence spectroscopy and multivariate analysis for rapid detection and differentiation of pathogenic bacteria in foods, such as *Escherichia coli*, *Salmonella*, and *Campylobacter* (Sohn et al. 2009). They found that the emission spectra from the three bacteria groups were very similar, creating difficulty in classification. We demonstrate below that some distinction is possible by applying principal components analysis (PCA).

In this chapter, we present a laboratory based study designed to detect waterborne bacteria based on their intrinsic fluorescence. The purpose of this study was to identify the optical signatures of the bacteria toward a possible portable

Target Species	Author (Reference)	Fluorescent component	Excitation wavelength (nm)	Emission wavelength (nm)
Escherichia coli	Marose	NADH	350	450
	Roselle	Tryptophan	250-305	345
		Tryptophan	330	400,435
	Seaver	Tryptophan	270,285,300	330
	Sohn	Tryptophan	225,280	335-345
	Giana		410,430	500-550
	Anwer	Tryptophan	280-300	340-380
	Wlodarski	NADH	280,340	330,440
	Bao	Flavins	488	535
Pseudomonas strains	Leriche	AAA+NA	250	280-480
			270	305-400
		NADH	340	397,399,427,449
Pseudomanas fluorescene	Leblanc	Tryptophan	250	334
Pseudomonas aeruginosa	Ju	NAD(P)H	340	460
	Chen	NAD(P)H	340	460
Salmonella	Sohn	Tryptophan residues	225,280	345
Salmonella Enteritidis PT1	Bao	Flavins	488	535
Enterococcus faecalis	Giana		410,430	500-550
Enterobacter aerogenes	Anwer	Tryptophan	280-300	340-380

Fig. 11.1 Excitation-emission wavelength for selected microorganisms

reagentless detection system. The experiments involved two common water fecal indicators, *E. coli* and *Enterococcus faecalis*, and two important waterborne pathogenic bacteria, *Pseudomonas aeruginosa* and *Salmonella typhimurium*, were selected. The study was motivated by review of the literature cited above and summarized in Fig. 11.1, indicating that it may be possible to apply intrinsic fluorescence to discriminate between various microorganisms in water. Our results showed that while intrinsic fluorescence measurement showed very similar emission spectra, multivariate analysis of these bacteria can be used to distinguish them.

11.2 Materials and Methods

11.2.1 Microorganisms Used in this Study

All bacteria used in this study are listed in Table 11.1. Bacteria were cultured in liquid media at 37 °C overnight with shaking (200 rpm). On the second day, a volume of 0.1 ml of culture suspension was transferred to 9.9 ml of fresh medium, and kept at 37 °C for another 3, 5 and 7 h with shaking. For *E. coli*, *E. faecalis, P. aeruginosa*, *Bacillus subtilis* and *Burkholderia pyrrocinia*, Tryptic Soy Broth (TSB) (BD, USA) was used. For *S. typhimurium, Enterococcus durans*, *Streptococcus bovis* and *Arthrobacter woluwensis*, Brain Heart Infusion broth (BHI) (BD, USA) was used. For *Pseudomonas veronii*, Nutrient Broth (BD, USA) was used.

Table 11.1 Bacterial strains used in this study

Bacteria	Strain name	Source	Coding
Escherichia coli	ATCC 700891	ATCC	EC
E. coli	EC1	Lab isolate	EC1
E. coli	EC2	Lab isolate	EC2
E. coli	EC3	Lab isolate	EC3
E. coli	EC4	Lab isolate	EC4
E. coli	EC5	Lab isolate	EC5
E. coli	EC6	Lab isolate	EC6
E. coli	EC7	Lab isolate	EC7
E. coli	EC8	Lab isolate	EC8
E. coli	EC9	Lab isolate	EC9
Enterococcus faecalis	ATCC 29212	ATCC	EF
Salmonella typhimurium	ATCC 14028	ATCC	ST
Pseudomonas aeruginosa	ATCC 27853	ATCC	PA
Enterococcus durans	ED1	Lab isolate	ED
Arthrobacter woluwensis	ATCC 700220	ATCC	AW
Bacillus subtilis	ATCC 6633	ATCC	BS
Burkholderia pyrrocinia	ATCC 15958	ATCC	BP
Pseudomonas veronii	ATCC 700474	ATCC	PV
Streptococcus bovis	ATCC 33317	ATCC	SB

ATCC American Type Culture Collection

11.2.2 Fluorescence Spectrometer

A table top spectrofluorometer (Model RF5301PC, Shimadzu, Japan) was used for fluorescence spectra measurements. It consists of a Xenon lamp (150 W) emitting light continuously from 220 to 900 nm. The instrument was set at 3-D excitation increment mode with 5 nm interval and was used to obtain fluorescent 3-D maps. The excitation and emission slit widths were fixed at 5 nm each. The software Panorama (developed by Avantes, USA) was used to acquire the 3D scanning spectra.

11.2.3 Sample Preparation for Fluorescence Spectra Measurement

Bacterial strains from two plates (3 days and 10 days old, respectively) were cultured in liquid broth overnight at 37 °C or 30 °C with shaking. On the 2nd day morning, the culture was diluted to fresh medium with a dilution ratio of 1:100. Cells were further incubated at 37 °C for 3, 5, or 7 h. The bacterial culture was then centrifuged at 4500 rpm for 10 min. After removal of supernatant, the cell pellet was washed once with phosphate-buffered saline (PBS), and re-suspended in PBS.

The bacterial cell suspension was then diluted to a concentration of OD_{600} 0.05, and further adjusted to 5×10^7 cells/ml. After that, 3 ml of bacterial suspension was loaded in a quartz cuvette (10 mm path length) and the intrinsic fluorescence was measured at room temperature (22–24 °C).

To study whether the physiological status of bacterial cells affect the intrinsic fluorescence, *E. coli* cells were cultured overnight first, and transferred to fresh media on second day for further growth at a ratio of 1:1000. The intrinsic fluorescence was measured at different stages (3 h: late log phage; 6 h: exponential phage; 9 h: late exponential phase; 12 h: stationary phase).

For the environmental bacterial samples, *E. coli* isolates were cultured in Tryptic Soy Agar (TSA) plates overnight. A small amount of a single colony was picked with a sterile inoculation loop, and put into a tube containing 5 ml of sterile PBS solution. After vigorously vortexing for 3 min, the bacterial suspension (OD_{600} is about 0.03–0.1) was used for fluorescence spectra measurement.

To measure the intrinsic fluorescence, 3 ml of bacterial suspension in PBS was put into a 4 ml-quartz cuvette. Samples were measured either in an auto 3D scanning mode or at a set excitation wavelength. For excitation at 225 nm, the emission spectra were collected from 250 to 600 nm. For excitation at 280 nm, the emission spectra were collected from 300 to 600 nm.

11.2.4 Data Processing and Multivariate Analysis

Fluorescence spectra of all bacteria tested were analyzed with Unscrambler software (version 10.x, CAMO Software AS, Oslo, Norway). The spectra were first truncated from wavelengths between 260 and 430 nm, and the reference spectrum corresponding to phosphate buffered saline (PBS) was subtracted from individual spectra. The emission spectra were then normalized by reducing each spectral area to 1. Hierarchical clustering analysis was performed by using complete linkage clustering method (Harz et al. 2005). Partial least squares regression (PLSR) was used for bacterial classification and identification.

11.3 Results

11.3.1 3-D Fluorescence Scans of Microorganisms

The intrinsic fluorescent characteristics of four waterborne bacteria, *E. coli*, *E. faecalis*, *P. aeruginosa* and *S. typhimurium*, were analyzed with a spectrofluorometer (Shimadzu RF5301PC). Bacterial cells were prepared in phosphate-buffered saline, and measured using a 3-D scanning mode to investigate the maximal excitation/emission for each bacteria. The 3D excitation and emissions are shown in Fig. 11.2 together with the measurement scale. Different cells were

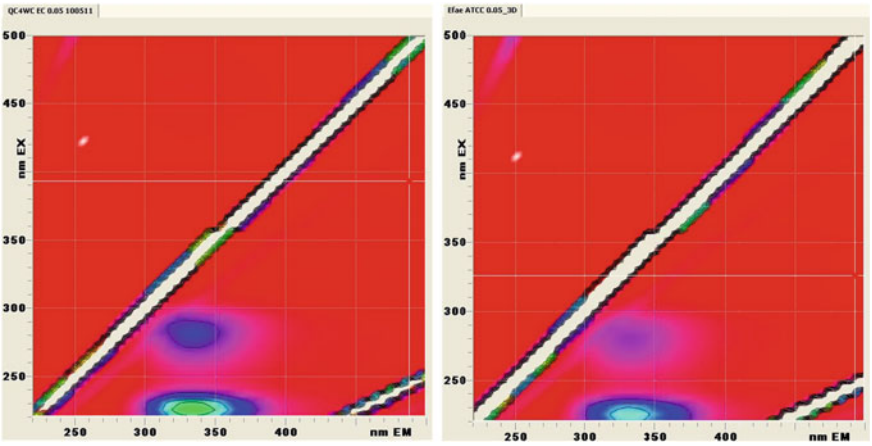

Fig. 11.2 Excitation-emission map: (Left) *E.Coli*, (Right) *E. faecalis*

excited in the wavelength range of 220–600 nm and emission was observed between 220–600 nm at increments of 5 nm. Two main emission peaks were shown. The optimum excitation and emission wavelength combinations were found at (Ex, Em) = (225–229 nm, 334 nm) and (280, 334 nm).

The white lines are due to Rayleigh scattering and represent saturated light intensity. Results suggest that all 4 groups of waterborne bacteria have very similar intrinsic fluorescence patterns. This is due to similar biological nature of bio-molecules which contribute the overall intrinsic fluorescence, e.g., amino acids and nuclei acids (AAA and NA).

11.3.2 2-D Fluorescence Scanning of Four Bacteria

The 2D emission spectra of the four bacteria, i.e., *E. coli*, *E. faecalis*, *S. typhimurium* and *P. aeruginosa*, were studied using log phage cell suspension under an excitation wavelength of 225 nm. As shown in Fig. 11.3, the emission spectra of

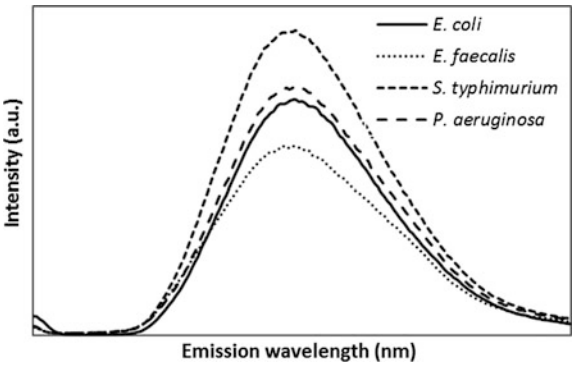

Fig. 11.3 Fluorescence spectra of four bacteria following excitation at 225 nm on dilute suspension (5×10^7 cells/ml)

the four bacteria tested exhibited very similar patterns, although they showed different fluorescence intensity. They all exhibited a peak emission at 334 nm. Despite the minor observable difference in the emission spectra, partial least squares regression (PLS regression) analysis was able to discriminate certain differences.

11.3.3 *Effect of Growth Stage on the Fluorescence Intensity of Bacteria*

To study whether the physiological status of bacterial cells affect the intrinsic fluorescence, the intrinsic fluorescence of *E. coli* cells was measured at different stages, e.g., late log phage, exponential phage, late exponential phase and stationary phase. As shown in Fig. 11.4, exponential and stationary phase cells exhibited higher fluorescence intensity. This may due to the higher cell mass at these stages.

11.3.4 *Evaluation of the Spectra of* E. coli, E. faecalis, S. typhimurium *and* P. aeruginosa

Due to the close spectral similarity between microorganisms, one has to rely on chemometric postprocessing methods to enhance the weak differential signal obtained by measurements (Sohn et al. 2009). In the current study, we use the Unscrambler software to analyze the spectra of different bacteria. The fluorescence emission spectra of the four waterborne bacteria (17 spectra from each bacterium at different growth stages) were normalized for analytical data processing by reducing the area under each spectrum to 1. The area normalized emission spectra corresponding to each class of bacterium is collectively shown in Fig. 11.5. It is clear that the spectra of different bacteria differ slightly around the variables 330 and 370 nm. These changes can be detected by the PLS and cluster analysis.

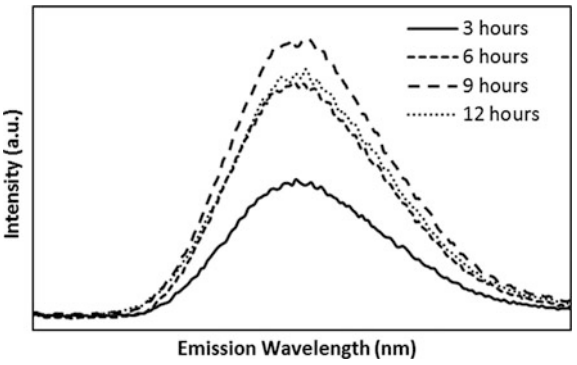

Fig. 11.4 The intrinsic fluorescence spectra of *E. coli* at different growth stage. Overnight culture of *E. coli* was transferred to fresh media (1:1000), and further cultured at 3, 6, 9, and 12 h before fluorescence was measured at a concentration of 10^7 cells/ml

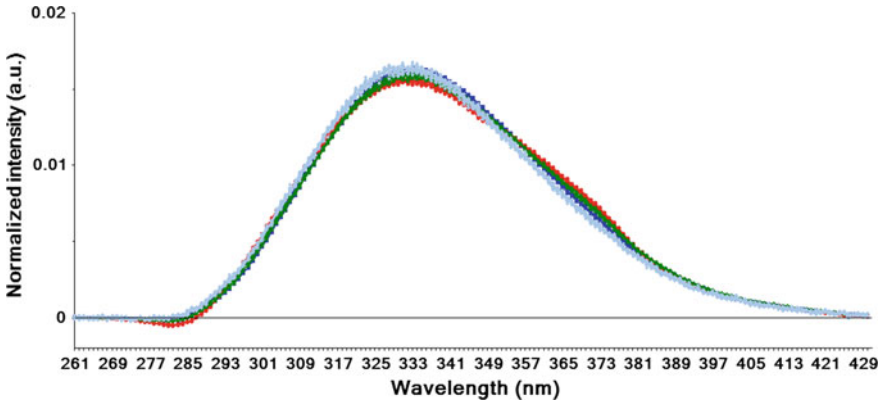

Fig. 11.5 Area normalized fluorescence emission spectra of waterborne bacteria when excited at 225 nm. Concentrations of the samples are 5×10^7 cells/ml. Emission data (260–330 nm) were used for analysis. EC: *E. coli*; EF: *E. faecalis*; PA: *P. aeruginosa*; ST: *S. typhimurium*

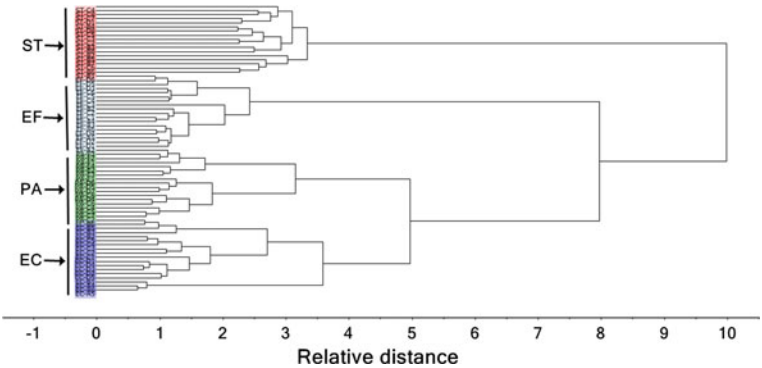

Fig. 11.6 Hierarchical complete-linkage clustering of waterborne bacteria. EC: *E. coli*; EF: *E. faecalis*; PA: *P. aeruginosa*; ST: *S. typhimurium*

Hierarchical clustering analysis was performed by testing with the complete linkage clustering method (Harz et al. 2005). Euclidean distance was used to measure dissimilarity between the individual bacterial species. These species were linked together according to the selected distance measured to form clusters of increasing dissimilarity. Figure 11.6 shows that all *E. coli* samples were very similar to each other and hence formed a cluster. Similarly, other samples from different bacterial species, including *E. faecalis*, *P. aeruginosa* and *S. typhimurium,* formed clusters, respectively. These bacterial clusters were finally linked to each other based on the Euclidean distance between samples or clusters. This tree-like dendrogram clearly shows four clusters corresponding to the four bacteria investigated (Fig. 11.6). Apart from forming clusters, the dendrogram provides no

information on the specific differences between bacterial samples. Therefore, other analytical methods such as PCA or PLS need to be performed to explain clustering (Alexandrakis et al. 2008).

Partial least square discriminant analysis (PLS-DA) is a classification method derived from PLS regression analysis. PLS-DA focuses on the variation between the classes rather than the variation within the class (Olafsdottir et al. 2006). PLSR was performed on area normalized spectral data using NIPALS algorithm in the Unscrambler software. For performing PLSR, a matrix of spectral data obtained from Fig. 11.5 was used. The matrix consists of fluorescence response (intensity points) at different wavelengths as columns (X-variables) and bacterial sample labels as rows. Each class of bacteria was assigned to a category for each of the four bacteria classes that are in the present studies. The reference matrix (Y-variables) is derived from the category variables (class) by assigning a numerical value 0 or 1, as identifiers for different bacterial species. The PLSR model was calculated with full or leave-one-out cross validation (Leblanc and Dufour 2002; Esbensen et al. 2004). This model further validated on some unknown field samples which were not included in the model development.

The PLSR calculation produces two statistical parameters during internal validation (full cross validation) procedure. These parameters are the correlation coefficient squared (R^2) and the root mean square error of prediction (RMSEP). The parameters can be used to evaluate the models performance. The correlation coefficient is defined as the correlation between observed and predicted Y-values. The value of correlation coefficient is between 0 and 1, the higher the value (close to 1) the better the model performance. RMSEP is used to express the expected average error associated with future predictions. The lower the RMSEP the better the accuracy of prediction of the Y-values for new samples.

Figure 11.7 shows the PLS regression score plots for the 4 groups of bacteria. The map defined by principal factors 1 and 2 showed 4 groups corresponding to the four bacteria. For a bacterial species, all the spectra were clustered close to each other, allowing discrimination of the four bacteria. The reproducibility of the method was confirmed by the tight clustering of the replicated sampling. The optimum number of factors is found to be 5 which explain 91% variation in the X and Y matrices. Factor 1 explains 66% and factor 2 explains 22% of variation in X. Explained Y variance along factor 1 and 2 is 32 and 31% respectively. *S. typhimurium* was separated from other bacteria by variables around 325 and 370 nm along factor 1. *E. coli* was separated from other bacteria by variables around 310 and 345 nm along factor 2. It is clear from Fig. 11.7 that there are four clusters corresponding to four bacterial species. These results are a clear indication that PLSR analysis indeed discriminates across different waterborne bacteria.

The score plot obtained from PLS regression is shown in Fig. 11.8. The score plot is constructed from reduced number of variables called factors. These factors are the sample coordinates along the model components. PLS analysis is useful to summarize the variation in X or Y-space.

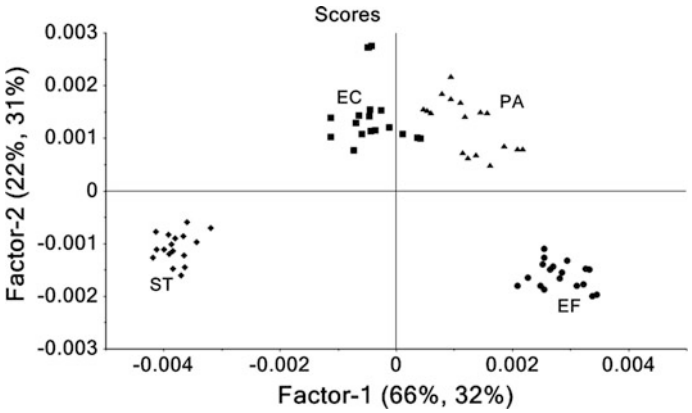

Fig. 11.7 Partial least squares discriminant analysis predictive score plot for four waterborne bacteria when excited at 225 nm. Concentrations of the samples are 5×10^7 cells/ml. Emission data (260–330 nm) were used for analysis. EC: *E. coli*; EF: *E. faecalis*; PA: *P. aeruginosa*; ST: *S. typhimurium*

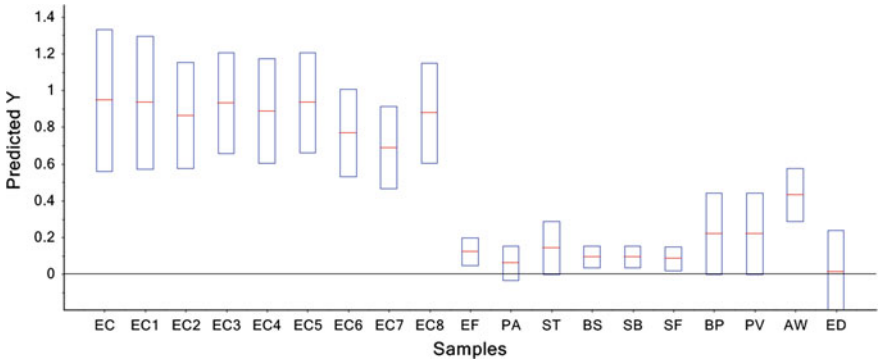

Fig. 11.8 Partial least squares discriminant analysis prediction results for test samples of different bacteria. Noted that values close to 1 indicate their membership to *E. coli* class. EC: *E. coli* type strain ATCC 700891; EC1 to EC9: *E. coli* isolates from surface water; For other coding of bacteria, see Table 11.1

The sensitivity and specificity of this PLS analysis method was also determined. The PLS-DA model could give a calibration model that maximizes the sensitivity and specificity of the training data set (Ammor et al. 2004). Table 11.2 shows the sensitivity and specificity of the bacterial identification using PLSR model. From Fig. 11.8, it is clear that all the samples of *S. typhimurium* and *E. faecalis* and *P. aeruginosa* are located inside their respective groups. Two samples of *E. coli* are nearly overlapping the cluster of *P. aeruginosa* samples; hence sensitivity of *E. coli* is 88%. The specificity of *P. aeruginosa* is 96% because two samples of *E. coli* are

Table 11.2 Sensitivity and specificity of bacterial identification using PLSR analysis

Bacteria	Sensitivity (%)	Specificity (%)
E. coli	88	100
P. aeruginosa	100	96
E. faecalis	100	100
S. typhimurium	100	100

in its cluster. Highest sensitivity and specificity values are found in samples of *E. faecalis* and *S. typhimurium*.

11.3.5 Rapid Identification of Bacterial Samples Isolated from Surface Water

To study whether intrinsic fluorescence spectra can be used for rapid identification of waterborne bacteria, we selected nine *E. coli* strains (EC1 to 9, isolated from surface water) for evaluation. For control, some other bacterial species were included, which include PA, EF, ST, *Bacillus subtilis* (BS), *Streptococcus bovis* (SB), *Shigella flexneri* (SF), *Burkholderia pyrrocinia* (BP), *Pseudomonas veronii* (PV), *Anthrobacter woluwensis* (AW) and *Enterococcus durans* (ED). The fluorescence spectra were obtained by scanning the bacterial suspension prepared directly from colonies. The spectra were then normalized, and applied to the PLSR model to predict the y-value of the unknown samples using their x-data using PLS-DA (Olafsdottir et al. 2006). PLS-DA searches for factors, to maximize the variations in the sample data from the X-matrix that can be used to predict the class from the Y-matrix. In a PLS-DA model, a Y-matrix is generated to assign the samples to the known classes. The Y-matrix values alternate between 0 and 1. For each class y-value was calculated separately. Any new sample was assigned to a particular class if their y-value was above 0.5. Samples which have y-value below 0.5 were not assigned to that class. The prediction result was shown in Fig. 11.8. Values close to 1 indicate their membership to *E. coli* class. It showed that all these *E. coli* isolates were clearly discriminated from other species, suggesting this method could be applied for rapid identification of field bacterial isolates.

11.4 Discussion and Conclusion

We have attempted to use the intrinsic fluorescence of bacteria in order to investigate its optical signature as a viable means for rapid identification of water contamination. Four bacteria, two common water indicators (*E. coli* and *E. faecalis*) and two waterborne pathogens (*S. typhimurium* and *P. aeruginosa*), were chosen for model study. The bacterial intrinsic fluorescence has been shown to discriminate

and identify at the genus, species and subspecies levels (Estes et al. 2003; Ammor et al. 2004; Bhatta et al. 2006). The bacterial aromatic amino acids (AAA) and nucleic acids (NA) are able to generate intrinsic fluorescence when excited at low ultraviolet range, such as 250 nm (Ammor et al. 2007), while NADH and FDA generates intrinsic fluorescence with a maxima emission at 413 and 436 nm, respectively, when excited at 316 and 380 nm (Ammor et al. 2004). In our study, by using a 3-D scanning program it was found that all bacterial strains tested exhibited peak emission intensity at about 334 nm when excited at 225 nm or 280 nm. This was also in agreement with previous finding by other research groups (Sohn et al. 2009) where three pathogenic bacteria in foods, *E. coli*, *Salmonella* and *Campylobacter,* were scanned with fluorescence spectroscopy. From the 2-D fluorescence scanning of the four bacteria, as expected, all four bacteria tested also exhibited very similar spectral pattern when excited at 225 nm.

The bacterial cell wall provides structural integrity to the cell. In Gram-negative bacteria, such as *E. coli*, the cell wall contains a thin peptidoglycan layer adjacent to the cytoplasmic membrane. When the cell wall was removed by treating with lysozyme, the intensity of intrinsic fluorescence was increased, suggested the physical barrier of cell wall has some blocking effect in the emission signal. Our experiment also investigated the effect of growth phase on fluorescence intensity. Results suggested that older cells, such as in late log phase and in stationary phase, exhibited higher fluorescence intensity as compared with younger cells (in lag phase or early log phase). This was possibly due to the high amino acid content in older cells.

Multivariate regression method is widely used in large-scale data mining and predictive modeling. Two multivariate regression exercises, PCA and Partial least squares regression (PLSR), are often used to convert a set of highly correlated variables to a set of independent variables by using linear transformation. It had been reported that when a dependent variable for a regression is specified, the PLSR technique is more efficient than the PCA technique for dimension reduction due to the supervised nature of its algorithm (Maitra and Yan 2004). In this study, PLSR was used for identification and classification of four waterborne bacteria, and for rapid detection of *E. coli* isolates from surface water. These results show that intrinsic fluorescence of bacteria could be a useful technique to investigate the discrimination and the identification of bacteria isolated from surface water at the genus and species level.

The aim of this study was to explore opportunities in reagentless testing for contaminants, while recognizing it may compromise sensitivity. In recent years, efforts have been focused on using spectroscopy technology for rapid and reagentless identification of bacteria. These include Fourier Transform Infrared (FT-IR), Fourier transform Near-Infrared (FT-NIR), Raman and fluorescence spectroscopy. Fluorescence spectroscopy provides advantages compared with other spectroscopic methods.

In the reported study we used a commercial spectrofluorometer to analyze the intrinsic fluorescence of four different groups of waterborne bacteria. The intention

is to be able to replace the bench top system with a similar system for field applications. Results showed that the four microorganisms exhibit similar intrinsic fluorescence at 334 nm when subject to UV excitation at 225 and 280 nm. While it was difficult to discriminate the spectra, through PLS regression analysis, these four bacteria were successfully discriminated and identified by their genus. This method was used for field samples. Results showed that *E. coli* can be differentiated from other waterborne bacteria. It must be added that depending on the bacteria of interest and expected concentration level, real field application would require high level of centrifuge. The fluorescence of other microorganisms in water should also be investigated in the next stages of study.

References

Alexandrakis, D., Downey, G., & Scannell, A. G. M. (2008). Detection and identification of bacteria in an isolated system with near-infrared spectroscopy and multivariate analysis. *Journal of Agricultural and Food Chemistry, 56*(10), 3431–3437.

Ammor, M. (2007). Recent advances in the use of intrinsic fluorescence for bacterial identification and characterization. *Journal of Fluorescence, 17*(5), 455–459.

Ammor, M. S., Delgado, S., Álvarez-Martín, P., Margolles, A., & Mayo, B. (2007). Reagentless identification of human bifidobacteria by intrinsic fluorescence. *Journal of Microbiological Methods, 69*(1), 100–106.

Ammor, S., Yaakoubi, K., Chevallier, I., & Dufour, E. (2004). Identification by fluorescence spectroscopy of lactic acid bacteria isolated from a small-scale facility producing traditional dry sausages. *Journal of Microbiological Methods, 59*(2), 271–281.

Ashbolt, N. J. (2004). Microbial contamination of drinking water and disease outcomes in developing regions. *Toxicology, 198*(1), 229–238.

Ashbolt, N. J. (2015). Microbial contamination of drinking water and human health from community water systems. *Current Environmental Health Reports, 2*(1), 95.

Bhatta, H., Goldys, E., & Learmonth, R. (2006). Use of fluorescence spectroscopy to differentiate yeast and bacterial cells. *Applied Microbiology and Biotechnology, 71*(1), 121–126.

Clark, S. T., Gilbride, K. A., Mehrvar, M., Laursen, A. E., Bostan, V., Pushchak, R., et al. (2011). Evaluation of low-copy genetic targets for waterborne bacterial pathogen detection via qPCR. *Water Research, 45*(11), 3378–3388.

Esbensen, K. H., Guyot, D., Westead, F., & Houmoller, L. P. (2004). *Multivariate data analysis–in practice: An introduction to multivariate data analysis and experimental design*. Oslo, Norway: Camo.

Estes, C., Duncan, A., Wade, B., Lloyd, C., Ellis, W., & Powers, L. (2003). Reagentless detection of microorganisms by intrinsic fluorescence. *Biosensors & Bioelectronics, 18*(5), 511–519.

Fan, C., Hu, Z., Mustapha, A., & Lin, M. (2011). Rapid detection of food- and waterborne bacteria using surface-enhanced raman spectroscopy coupled with silver nanosubstrates. *Applied Microbiology and Biotechnology, 92*(5), 1053–1061.

Figueras, M. J., & Borrego, J. J. (2010). New perspectives in monitoring drinking water microbial quality. *International Journal of Environmental Research and Public Health, 7*(12), 4179–4202.

Girones, R., Ferrús, M. A., Alonso, J. L., Rodriguez-Manzano, J., Calgua, B., De Abreu Corrêa, A., et al. (2010). Molecular detection of pathogens in water—The pros and cons of molecular techniques. *Water Research, 44*(15), 4325–4339.

Harz, M., Rösch, P., Peschke, K., Ronneberger, O., Burkhardt, H., & Popp, J. (2005). Micro-Raman spectroscopic identification of bacterial cells of the genus staphylococcus and dependence on their cultivation conditions. *Analyst, 13*(11), 1543–1550.

Horton, R. B., Duranty, E., Mcconico, M., & Vogt, F. (2011). Fourier transform infrared (Ft-Ir) spectroscopy and improved principal component regression (PCR) for quantification of solid analytes in microalgae and bacteria. *Applied Spectroscopy, 65*(4), 442–453.

Jung, A., Le Cann, P., Roig, B., Thomas, O., Baurès, E., & Thomas, M. (2014). Microbial contamination detection in water resources: Interest of current optical methods, trends and needs in the context of climate change. *International Journal of Environmental Research and Public Health, 11*(4), 4292–4310.

La Rosa, G., Della Libera, S., Petricca, S., Iaconelli, M., Briancesco, R., Paradiso, R., et al. (2015). First detection of papillomaviruses and polyomaviruses in swimming pool waters: Unrecognized recreational water-related pathogens? *Journal of Applied Microbiology, 119* (6), 1683–1691.

Lavanya, V., & Ravichandran, S. (2013). Microbial contamination of drinking water at the source and household storage level in the peri-urban area of southern Chennai and its implication on health India. *Journal of Public Health, 21*(5), 481–488.

Leblanc, L., & Dufour, E. (2002). Monitoring the identity of bacteria using their intrinsic fluorescence. *FEMS Microbiology Letters, 211*(2), 147–153.

Lopman, B. A., Reacher, M. H., Van Duijnhoven, Y., Hanon, F., Brown, D., & Koopmans, M. (2003). Viral gastroenteritis outbreaks in Europe, 1995–2000. *Emerging Infectious Diseases, 9* (1), 90–96.

Lu, J., Struewing, I., Yelton, S., & Ashbolt, N. (2015). Molecular survey of occurrence and quantity of legionella spp., mycobacterium spp., pseudomonas aeruginosa and amoeba hosts in municipal drinking water storage tank sediments. *Journal of Applied Microbiology, 119*(1), 278–288.

Maitra, S., & Yan, J. (2004). Principle component analysis and partial least squares: Two dimension reduction techniques for regression. *Casualty Actuarial Society, 2008 Discussion Paper Program*.

Mcbride, G. B., Stott, R., Miller, W., Bambic, D., & Wuertz, S. (2013). Discharge-based QMRA for estimation of public health risks from exposure to stormwater-borne pathogens in recreational waters in the united states. *Water Research, 47*(14), 5282–5297.

Nabeela, F., Azizullah, A., Bibi, R., Uzma, S., Murad, W., Shakir, S., et al. (2014). Microbial contamination of drinking water in Pakistan—A review. *Environmental Science and Pollution Research, 21*(24), 13929–13942.

Nicolaou, N., & Goodacre, R. (2008). Rapid and quantitative detection of the microbial spoilage in milk using fourier transform infrared spectroscopy and chemometrics. *Analyst, 133*(1), 1424–1431.

Olafsdottir, G., Lauzon, H. L., Martinsdottir, E., & Kristbergsson, K. (2006). Influence of storage temperature on microbial spoilage characteristics of haddock fillets (Melanogrammus aeglefinus) evaluated by multivariate quality prediction. *International Journal of Food Microbiology, 111*(2), 112–125.

Oster, R. J., Wijesinghe, R. U., Haack, S. K., Fogarty, L. R., Tucker, T. R., & Riley, S. C. (2014). Bacterial pathogen gene abundance and relation to recreational water quality at seven great lakes beaches. *Environmental Science and Technology, 48*(24), 14148.

Rodriguez-Saona, L. E., Khambaty, F. M., Fry, F. S., & Calvey, E. M. (2001). Rapid detection and identification of bacterial strains by fourier transform near-infrared spectroscopy. *Journal of Agricultural and Food Chemistry, 49*(2), 574–579.

Schriewer, A., Wehlmann, A., & Wuertz, S. (2011). Improving qPCR efficiency in environmental samples by selective removal of humic acids with DAX-8. *Journal of Microbiological Methods, 85*(1), 16–21.

Sohn, M., Himmelsbach, D. S., Barton, F. E., & Fedorka-Cray, P. J. (2009). Fluorescence spectroscopy for rapid detection and classification of bacterial pathogens. *Applied Spectroscopy, 63*(11), 1251–1255.

Sokolova, E., Petterson, S. R., Dienus, O., Nyström, F., Lindgren, P., & Pettersson, T. J. R. (2015). Microbial risk assessment of drinking water based on hydrodynamic modelling of pathogen concentrations in source water. *The Science of the Total Environment, 526,* 177–186.

Tambalo, D. D., Fremaux, B., Boa, T., & Yost, C. K. (2012). Persistence of host-associated bacteroidales gene markers and their quantitative detection in an urban and agricultural mixed prairie watershed. *Water Research, 46*(9), 2891–2904.

Tram, K., Kanda, P., Salena, B. J., Huan, S., & Li, Y. (2014). Back cover: Translating bacterial detection by DNAzymes into a litmus test (Angew. Chem. Int. Ed. 47/2014). *Angewandte Chemie International Edition,* **53**(47), 12972.

WHO. (2012). *Global analysis and assessment of sanitation and drinking-water (GLAAS): The challenge of extending and sustaining services. Un-water global annual assessment of sanitation & drinking-water.* Geneva: World Health Organization.

Chapter 12
Remote and In Situ Monitoring of Subsurface Liquid Hydrocarbons

Masoud Ghandehari, Konstantinos Kostarelos and Cristian S. Vimer

Abstract The work presented in this chapter is designed to forward the development of an optical probe for the remote monitoring of liquid hydrocarbons. A series of experiments were carried out to differentiate between classes of hydrocarbons and to discriminate between compounds within a class of similar molecular structures. It was observed that unique absorption spectra can be obtained for each hydrocarbon, and this uniqueness can be used to discriminate between hydrocarbons from different families. Results summarize measurements of the Near-Infrared optical absorption of alkanes, aromatics, and chlorinated hydrocarbons. This approach was selected to assess the feasibility of remote in situ measurements using optical waveguides.

12.1 Introduction

Organic compounds known to contaminate the soil are found both in a separate immiscible (non-aqueous) phase and dissolved in groundwater. Investigating the presence and transport of these compounds (known as non-aqueous phase liquids or "NAPLs") in the subsurface environment is time-consuming and difficult because of the inherently slow natural processes at work and our limited ability to detect and monitor these compounds. This chapter describes an approach for in situ long-term detection and continuous monitoring of the subsurface environment containing hydrocarbons.

M. Ghandehari (✉)
New York University, Six Metrotech Center, Brooklyn, NY 11201, USA
e-mail: masoud@nyu.edu

K. Kostarelos
College of Engineering, University of Houston, 5000 Gulf Freeway,
Houston, TX 77204, USA
e-mail: kkostarelos@uh.edu

C. Vimer
Madsen Consulting Engineering, 175 Varick St #803, New York, NY 10014, USA
e-mail: cvimer@gmail.com

M. Ghandehari, *Optical Phenomenology and Applications*,
Smart Sensors, Measurement and Instrumentation 28,
https://doi.org/10.1007/978-3-319-70715-0_12

The proposed sensing technique for monitoring the subsurface geo-environment uses optical fiber, Near-Infrared spectroscopy, where the Near-Infrared energy is selectively absorbed, for example, when encountering hydrocarbons. The method employs robust silica based optical fibers for probing the subsurface environment. The work presented in this chapter is aimed at evaluating the potential of discriminating among classes of organic compounds and, furthermore, the specific compounds within each class, by way of library of NIR spectra of respective substances (Klavarioti et al. 2014).

Target compounds include those typically found at contaminated sites. The NIR spectra of number of pure hydrocarbons (including alkanes, aromatics, and chlorinated hydrocarbons) were measured using a NIR spectrometer and a light source emitting energy from 600 to 2200 nm. There is some information regarding the NIR spectra of certain hydrocarbons, although not comprehensive (Hirschfeld and Zeev-Hed 1981; Workman et al. 1998). This background information will be augmented by a full battery of tests described in this chapter.

12.1.1 Prior Work in Subsurface Contaminant Detection

Considerable effort has been carried out developing tools for in situ monitoring of aqueous and organic species in soil. Reviews of the monitoring techniques described above can be found in the literature (Looney and Falta 2000; Ho and Hughes 2002; Kram et al. 2001; Pospíšilová et al. 2015; Cullum and Angel 1999). These techniques are classified into three broad categories: (1) chromatographic, (2) electrochemical, (3) optical. Each category offers competing qualities such as selectivity, detection limit, robustness, low cost and ease of installation. Below is summary of the existing approaches with a greater emphasis on the optical methods.

1. Chromatographic techniques (Inamuddin and Mohammad 2014; Martins et al. 2015) are accurate but relatively expensive. Currently, portable units are available for gas and liquid phase analysis (Bruker-Daltronics Process Analyzers). These units are primarily used at large sites such as Department of Defense (DOD) and Department of Energy (DOE) facilities. Micro-Chem-Lab technology developed at Sandia National Labs is expected to overcome limitations of size and cost associated with standard chromatographic instruments (Ho et al. 2001).
2. Electrochemical instruments are cost effective but do not discriminate among species. Furthermore, electrical components degrade in the harsh subsurface environment. This prohibits their use for long term in situ applications.
3. Optical techniques are numerous. Laser-induced fluorescence (LIF) geo-probes are available for detection of the presence of polyaromatic hydrocarbon (PAH) contaminants. (Bulatov et al. 1997; Baumann et al. 2000; Pepper et al. 2002; Quinn et al. 2002). LIF is one of the most established techniques for low cost, in situ hydrocarbon monitoring. LIF probes show detection levels ranging from 10 to 100 parts per million (ppm) in soil and 0.5–10 ppm in groundwater. The main drawback of LIF is that it detects compounds that fluoresce, primarily

PAHs, and can suffer natural background fluorescence from humic substances. Another shortcoming of LIF is species discrimination. Researchers at Lawrence Livermore National Laboratory (LLNL) have also implemented special reagents for optical detection of trichloroethylene (TCE). Also, EIC Labs have used changes of refractive index of optical fiber for detection of DNAPL (DOE 2001; Spencer 1999). NASA has developed luminophore doped sol-gels as optical fiber materials, and Pacific Northwest National Lab (PNNL) (Goleen et al. 1996), and others (Long et al. 2011) have achieved colorimetric measurement of volatile organic compounds (VOCs) in water. These technologies offer simplicity of implementation, in situ capability, and cost effectiveness. However, one potential limitation is long-term durability, as techniques that rely on use of reagents often suffer degradation, either by leaching or by photo degradation.

Work presented in this chapter follows prior research in this area including the following:

- Maclean et al. (2003) for the possibility of distributed sensing. They reported using hydrocarbon reactive swelling hydrogel along the fiber surface. The technique provided the benefit of distributed measurement of leaks using optical time domain measurements. However, this technology does not discriminate among species (Maclean et al. 2003).
- Schweizer et al. (1997) have also been working on a distributed sensing fiber optic sensor for monitoring organic pollutants in air and water. The sensor detects hydrocarbons by measuring UV absorption spectra via the evanescent field of silica fibers coated with hydrophobic polymers such as siloxanes and Teflon® (Pospíšilová et al. 2015; Schweizer et al. 1997).
- Using a similar technique but in longer wavelengths, attenuated total internal reflection Mid-Infrared spectroscopy was used by Karlowatz et al. (2004) for simultaneous detection and quantification of benzene, toluene, and xylene isomers. The analytes were enriched into a thin polymer membrane coated onto the surface of an internal reflection wave guide which is exposed to the aqueous sample. Direct detection of analytes permeating into the polymer coating is performed by evanescent field spectroscopy in the Mid-Infrared region (MIR). Limits of detection obtained were lower than 20 ppb (v/v) for all xylene isomers, 45 ppb (v/v) for benzene, and 80 ppb (v/v) for toluene (Karlowatz et al. 2004).
- Roy and Mielczarski (2002) used attenuated total reflection (ATR) probes for detection of hydrocarbons using the MIR of the electromagnetic (EM) spectrum (Beyer et al. 2003; McCue et al. 2006; Mizaikoff et al. 1995; Krska et al. 1993). Evanescent field spectroscopy described in this work is an extension of attenuated total internal reflection (ATR) spectroscopy. This technology has led to development of MIR optical fiber sensors for in situ detection of contaminants. However this technology still has the length and potential durability limitations associated with MIR optical materials (Roy and Mielczarski 2002).
- Conzen et al. (1993) developed evanescent field fiber optics sensors in the NIR region for detection of nonpolar organic compounds by using a silicone-clad quartz glass fiber coiled on a stainless steel/Teflon® support. The silicone cladding acts as a hydrophobic membrane that enriches non polar organic

species. We are building on this work by carrying out detailed spectroscopic analysis for identification of various species (Conzen et al. 1993).

- A fiber optic sensor for volatile organic compounds was developed by Goswami et al. (1999) with long period gratings (LPG) coated with proprietary chemical indicators having strong affinities for VOCs. The sensor relies on the evanescent field interaction of core-guided light with volatile organic compounds surrounding the long period gratings (Goswami et al. 1999).
- NIR optical fiber sensing overcomes some of the limitations mentioned above. Researchers have investigated the use of NIR spectroscopy for the in situ monitoring of the subsurface geo-environment (Ho et al. 2001; Buerck et al. 1999; Conzen et al. 1993; Degrandpre and Burgess 1990; Albuquerque et al. 2005; Raichlin and Katzir 2008; Reboucas et al. 2011). NIR absorption measurements were carried out in order to identify and discriminate hydrocarbons from different classes as well as hydrocarbons from the same class. The study being reported in this chapter furthers that work.

The motivation for the technique presented in this chapter is to lower costs and offer the possibility of in situ, real-time analysis. Applications may include analysis of soil or groundwater during site investigation and waste containment monitoring. We propose an indicator-free recognition strategy in order to develop a more durable probe.

12.2 Near-Infrared Measurements of Hydrocarbons

When excited by electromagnetic energy, most molecules (e.g. containing OH or CH bonds) selectively absorb specific wavelength bands (Fig. 12.1). This is known as the absorbance spectra, a characteristic signature of the molecule. Similar to that

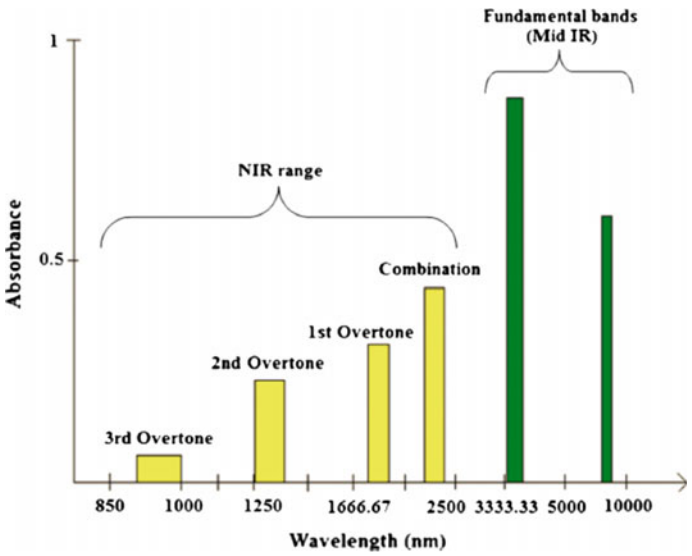

Fig. 12.1 Absorbance bands in the Near and Mid-Infrared regions of the electromagnetic spectrum

shown for water, the Near and Mid-Infrared regions of the electromagnetic spectra are useful for the characterization of hydrocarbons.

Mid-Infrared energy corresponds to the fundamental modes of vibration of hydrocarbons, and Near-Infrared energy corresponds to the overtones (harmonics) of those vibrations. Since each material is a unique combination of molecules, different hydrocarbons produce different Near-Infrared signatures. Therefore, Near-Infrared (NIR) spectroscopy can be a convenient means for the identification of materials or chemical species.

Compared to MIR wavelengths, NIR absorption bands are broad, so high resolution data acquisition instruments are not required. However, the absorption intensity is dramatically reduced, posing certain limitations for detecting low concentrations of contaminants. Nevertheless, in situ, Near-Infrared analysis promises to be a low cost and convenient tool for initial screening and analysis of numerous substances in the subsurface environment and, most importantly, for long-term, real-time monitoring.

For field applications, the question of the distance between the site to the instrument should also be addressed. Near-Infrared energy has good transmissivity through most commercially available low-OH silica fibers, while the transmission of Mid-Infrared energy through fibers is limited to much shorter distances (a few meters in length). Despite the fact that Mid-Infrared wavelengths offer higher sensitivity detection, NIR spectroscopy is more suitable for remote and long distance, geo-environmental sensing applications.

12.2.1 Experiments

This chapter reports on experiments studying the transport of mineral oil through partially saturated sand in a column; and measurement of alkanes (heptane, octane, dodecane), aromatics (benzene, toluene, phenol), and chlorinated hydrocarbons (trichloroethylene or "TCE", dichloromethane) demonstrating the recognition capability by NIR absorption spectra via optical transmission mode.

Experiments were carried out using a portable spectrometer (Ocean optics NIR256). A schematic of the typical experimental setup using the portable spectrometer is shown in Fig. 12.2. NIR light is launched from the spectrometer through a fiber optic patch chord and into the embedded sensing probe. The light reflects back from a fiber tip reflector through the probe and into the spectrometer. In this configuration the light interacts twice with the sample along the sensing length. Similar set up using a mirror instead of the chamber was used for the measurement of the compound absorption spectra (Fig. 12.2 left).

The optical fiber probes were developed using step-index multimode low OH plastic clad silica (PCS) fibers (Thor Labs Inc., Newton, NJ) with 600 nm core

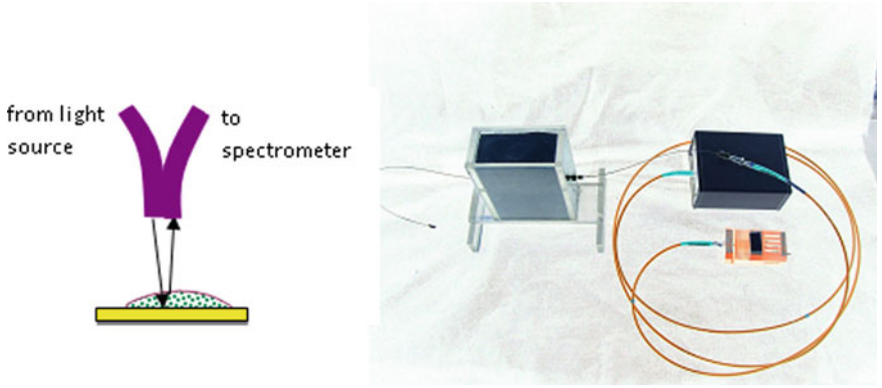

Fig. 12.2 Typical experimental setup: (Right), light source, spectrometer and fiber optic cable delivering light to the sensor in the soil filled chamber, (Left) set up for measurement of absorption spectra of pure compound, using a mirror instead of the chamber

diameter, 630 nm cladding diameter and 1030 nm buffer diameter. One meter portions of the fiber were cut; the buffer and cladding were removed in the middle region over a length of 10 cm using a surgical blade and acetone. The fiber ends were polished using lapping films and the ends were fitted with SMA type connectors. The optical fiber probes were illuminated by a Tungsten Halogen light source connected to the portable Ocean Optics Near-Infrared spectrometer operated through a laptop. The operative wavelength of the spectrometer ranges from approximately 1250 to 2150 nm with resolution of approximately 4 nm using the 256 InGaAs detector elements. This resolution is adequate for the relatively wide NIR absorption bands of water and hydrocarbons.

12.2.2 Monitoring the Transport of Mineral Oil Through Partially Saturated Sand

Mineral oil was used to model a hydrocarbon pollutant. Preliminary tests were performed in order to determine the NIR absorption spectra of mineral oil using an optical fiber probe. Then, an experiment was performed to monitor the transport of mineral oil into partially saturated sand. The experimental setup consisted of a vertically oriented Plexiglas column (Fig. 12.3) packed with 22 cm of dry Federal fine grade sand with a horizontal optical fiber probe located 17 cm from the bottom.

The sand was made wet from the bottom using a water reservoir, maintaining a constant head so that the moisture content (MC) varied from 100% at the bottom to dry at the top. Prior to introducing mineral oil, an intensity spectrum with sand,

35% MC, was collected at the fiber location and stored as the reference value. Mineral oil was then allowed to flow slowly into the column from the top.

Absorption spectra were recorded every 3 min and smoothed for 50 values using the Savitzky-Golay algorithm, similar to moisture experiments reported in Chap. 9. As shown by the absorption spectra in Figs. 12.3 and 12.4, oil had not reached the

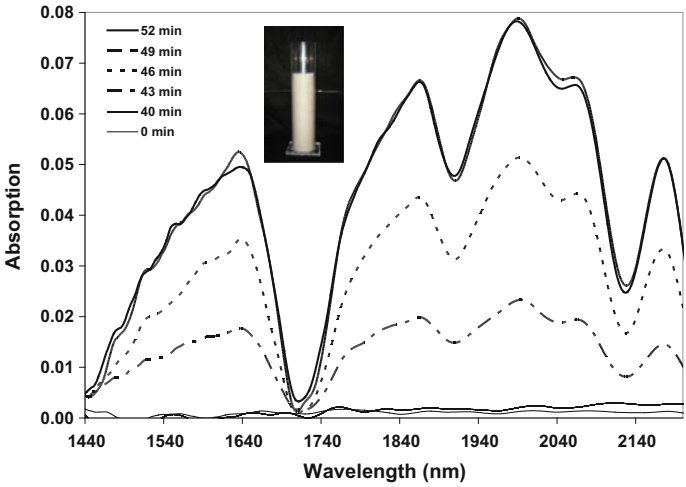

Fig. 12.3 Absorption spectra of mineral oil recorded during constant volume injection of mineral oil in wet sand (MC = 35%)

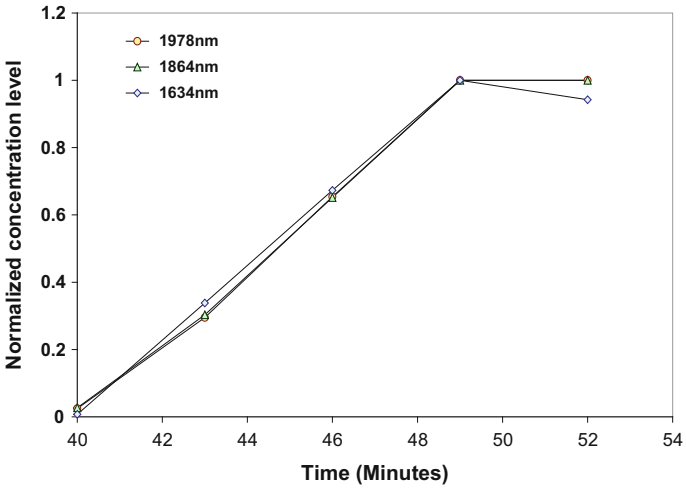

Fig. 12.4 Normalized concentration of oil based on absorption peak measured at 1634, 1854, and 1978 nm

probe region by the 40th minute. This was followed by rapid change in the optical absorption, as shown in the steady-state exposure to mineral oil by approximately the 49th minute.

12.2.3 Experimental Identification of Characteristic NIR Absorption Spectra of Contaminants

The absorption spectra of three classes of pure hydrocarbons were obtained by testing the absorption spectra of each compound (Fig. 12.2 left). These contaminants included alkanes (heptane, octane, dodecane), aromatics (benzene, toluene, phenol), and chlorinated hydrocarbons (trichloroethylene, or TCE and dichloromethane). A similar setup of spectrometer, light source, and optical fiber (Fig. 12.2) was used to obtain the NIR spectra of the liquid hydrocarbons. For these tests, the chamber was not used, however a mirror was used (Fig. 12.2 left) on which a droplet of each pure compound was placed. The light was sent through the droplet and back into the spectrometer. Results are shown in Fig. 12.5a–c for each class of compounds, respectively. Note that the 2nd derivative transformed spectra of compounds within each class are similar to each other, but are distinct from those of other classes. This observation shows that the NIR absorption spectra can be used to identify the class of an unknown compound. More systematic identification of each class, and in some cases certain hydrocarbons within each class, are possible by carrying out regression and principle component analysis. A database of the NIR absorption spectra of a wide range of compounds can be developed following the same procedures which can then be used to identify unknown compounds.

12.3 Conclusion

Application of Near-Infrared (NIR) spectroscopy using optical fibers is an opportunity for in situ subsurface monitoring of hydrocarbon transport. Tests were carried evaluating the NIR absorption spectra of three classes of hydrocarbon showing that the NIR signature represents distinct information for the identification of the hydrocarbons. This includes the compound class at large and for specific compounds within each class. The potential application of optical fibers for in situ monitoring was demonstrated using mineral oil in sand with an embedded optical fiber.

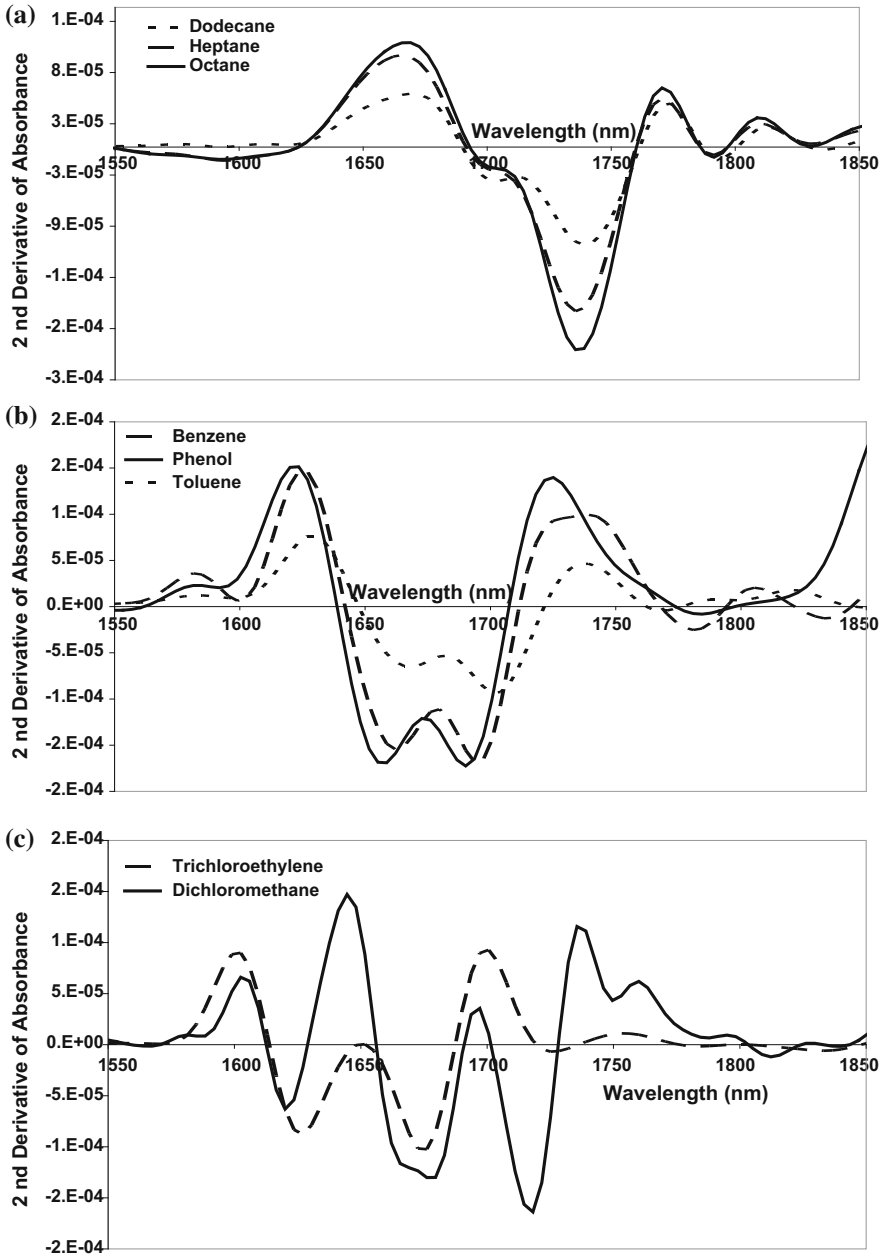

Fig. 12.5 Characteristic Near-Infrared absorption spectra of **a** alkanes; **b** aromatics; and **c** chlorinated hydrocarbons

References

Albuquerque, J. S., Pimentel, F. M., Valdinete, L. S., Raimundo, I. M., Rohwedder, J. R., & Pasquini, C. (2005). Silicone sensing phase for detection of aromatic hydrocarbons in water employing near-infrared spectroscopy. *Analytical Chemistry, 77*(1), 72–77.

Baumann, T., Haaszio, S., & Niessner, R. (2000). Applications of a laser-induced fluorescence spectroscopy sensor in aquatic systems. *Water Research, 34*(4), 1318–1326.

Beyer, T., Hahn, P., Hartwig, S., Konz, W., Scharring, S., Katzir, A., et al. (2003). Mini spectrometer with silver halide sensor fiber for in situ detection of chlorinated hydrocarbons. *Sensors & Actuators: B. Chemical, 90*(1), 319–323.

Buerck, J., Denter, P., Mensch, M., Kraemer, K., & Scholz, M. (1999). Fiber optic NIR evanescent wave absorption sensor systems for in-situ monitoring of hydrocarbon compounds in waste and ground water. In *Environmental Monitoring and Remediation Technologies*. MA: SPIE.

Bulatov, V., Gridin, V. V., Polyak, F., & Schechter, I. (1997). Application of pulsed laser methods to in situ probing of highway originated pollutants. *Analytica Chimica Acta, 343*(1), 93–99.

Conzen, J. P., Burck, J., & Ache, H. J. (1993). Characterization of a fiber-optic evanescent wave absorbance sensor for nonpolar organic compounds. *Applied Spectroscopy, 47*(6), 753–763.

Cullum, B. M., & Angel, S. M. (1999). Development of a fiber optic REMPI probe for environmental contaminants. In *Environmental Monitoring and Remediation Technologies*. MA: SPIE.

Degrandpre, M. D., & Burgess, L. W. (1990). A fiber-optic FT-NIR evanescent field absorbance sensor. *Applied Spectroscopy, 44*(2), 273–279.

DOE. (2001). *Internal reflection sensor for the cone penetrometer DOE/EM-0611*. Washington, DC: DOE Office of Environmental Management.

Goleen, S. C., McCulloch, M., Thomas, B. L., Riley, R. G., Sklarew, D. S., Mong, G. M., et al. (1996). *DOE methods for evaluating environmental and waste management samples*. Richland, WA: US DOE.

Goswami, K., Prohaska, J. D., Menon, A., Mendoza, E. A., & Lieberman, R. A. (1999). Evanescent wave sensor for detecting volatile organic compounds. In *Photonics East*. MA: SPIE.

Hirschfeld, T., & Zeev-Hed, A. (1981). *The Atlas of near infrared spectra*. Philadelphia: Sadtler.

Ho, C. K., & Hughes, R. C. (2002). In-situ chemiresistor sensor package for real-time detection of volatile organic compounds in soil and groundwater. *Sensors, 2*(1), 23–34.

Ho, C. K., Itamura, M. T., Kelley, M. J., & Hughes, R. C. (2001). *Review of chemical sensors for in-situ monitoring of volatile contaminants*. NM: Sandia National Laboratories.

Inamuddin, D., & Mohammad, A. (2014). *Green chromatographic techniques*. DE: Springer.

Karlowatz, M., Kraft, M., & Mizaikoff, B. (2004). Simultaneous quantitative determination of benzene, toluene, and xylenes in water using mid-infrared evanescent field spectroscopy. *Analytical Chemistry, 76*(9), 2643–2648.

Klavarioti, M., Kostarelos, K., Pourjabbar, A., & Ghandehari, M. (2014). In situ sensing of subsurface contamination—Part I: Near-infrared spectral characterization of alkanes, aromatics, and chlorinated hydrocarbons. *Environmental Science and Pollution Research, 21*(9), 5849–5860.

Kram, M. L., Keller, A. A., Rossabi, J., & Everett, L. G. (2001). DNAPL characterization methods and approaches, Part 1: Performance comparisons. *Ground Water Monitoring and Remediation, 21*(4), 109–123.

Krska, R., Taga, K., & Kellner, R. (1993). New IR fiber-optic chemical sensor for in situ measurements of chlorinated hydrocarbons in water. *Applied Spectroscopy, 47*(9), 1484–1487.

Long, J., Xu, J., Yang, Y., Wen, J., & Jia, C. (2011). A colorimetric array of metalloporphyrin derivatives for the detection of volatile organic compounds. *Materials Science and Engineering B, 176*(16), 1271–1276.

Looney, B., & Falta, R. W. (Eds.). (2000). *Vadose zone science and technology solutions.* Columbus, OH: Battelle Press.

Maclean, A., Moran, C., Johnstone, W., Culshaw, B., Marsh, D., & Parker, P. (2003). Detection of hydrocarbon fuel spills using a distributed fibre optic sensor. *Sensors and Actuators, A: Physical, 109*(1), 60–67.

Martins, C. C., Doumer, M. E., Gallice, W. C., Dauner, A. L. L., Cabral, A. C., Cardoso, F. D., et al. (2015). Coupling spectroscopic and chromatographic techniques for evaluation of the depositional history of hydrocarbons in a subtropical estuary. *Environmental Pollution, 205,* 403–414.

McCue, R. P., Walsh, F., Walsh, J. E., & Regan, F. (2006). Modular fibre optic sensor for the detection of hydrocarbons in water. *Sensors & Actuators: B. Chemical, 114*(1), 438–444.

Mizaikoff, B., Taga, K., & Kellner, R. (1995). Infrared fiber optic gas sensor for chlorofluoro-hydrocarbons. *Vibrational Spectroscopy, 8*(2), 103–108.

Pepper, J. W., Wright, A. O., & Kenny, J. E. (2002). In situ measurements of subsurface contaminants with a multi-channel laser-induced fluorescence system. *Spectrochimica Acta Part A: Molecular and Biomolecular Spectroscopy, 58*(2), 317–331.

Pospíšilová, M., Kuncová, G., & Trögl, J. (2015). Fiber-optic chemical sensors and fiber-optic bio-sensors. *Sensors (Basel, Switzerland), 15*(10), 25208–25259.

Quinn, M. F., Alemeddine, O., Al-Awadi, E., Mukhopadhyay, A., Qabazard, A. M., Al-Rasheedi, M., et al. (2002). The application of laser-induced fluorescence techniques for the measurement of hydrocarbons in the groundwater of Kuwait. *Instrumentation Science and Technology, 30* (1), 79–95.

Raichlin, Y., & Katzir, A. (2008). Fiber-optic evanescent wave spectroscopy in the middle infrared. *Applied Spectroscopy, 62*(2), 72A.

Reboucas, M. V., Brandão, D. S., Trindade, A., Pimentel, M. F., & Teixeira, L. S. G. (2011). Chemical composition determination of complex organic-aqueous mixtures of alcohols, acetone, acetonitrile, hydrocarbons and water by near-infrared spectroscopy. *Vibrational Spectroscopy, 55*(2), 172–182.

Roy, G., & Mielczarski, J. A. (2002). Infrared detection of chlorinated hydrocarbons in water at ppb levels of concentrations. *Water Research, 36*(7), 1902–1908.

Schweizer, G., Latka, I., Lehmann, H., & Willsch, R. (1997). Optical sensing of hydrocarbons in air or in water using UV absorption in the evanescent field of fibers. *Sensors & Actuators: B. Chemical, 38*(1), 150–153.

Spencer, K. (1999-last update). Detection of DNAPLs by Raman Spectroscopy. Available: http://www.eiclabs.com/Raman_Detection_of_DNAPLs.pdf, March 2017.

Workman, J., Jerry, Springsteen, A., & Workman, J., Jr. (1998). *Applied spectroscopy* (1 ed.). US: Academic Press.

Part V
Sensing Gases

Chapter 13
Optical Sensing of Dissolved Oxygen

Masoud Ghandehari, Gamal Khalil, Filip Mlekicki, Alex Sidelev and Mohsen Hossein

Abstract We present the application of Platinum Porphyrin for in situ measurements of dissolved oxygen using optical fibers. The method employs a sensor compound composed of Porphyrin luminescent indicator in a gas permeable substrate. The compound is used along with optical fibers for both illumination and detection of fluorescence lifetime which is calibrated to changes in ambient oxygen concentration.

13.1 Introduction

It is projected that by 2030 $35 billion will be spent on cleaning up 5000 contaminated sites (EPA 2006). Among the dozens of remediation techniques that exist for treating these site conditions, monitored natural attenuation (MNA) is often the preferred method of cleanup. The natural attenuation capacity of a soil and groundwater environment is monitored, tested, and enhanced in order to degrade the entrapped contaminants by natural (physical, chemical, and biological) processes. The success of this technique is based on three basic activities: site

M. Ghandehari (✉)
New York University, Six Metrotech Center, Brooklyn, NY 11201, USA
e-mail: masoud@nyu.edu

M. Hossein
e-mail: mhossein@nyu.edu

G. Khalil
Department of Aeronautics & Astronautics, University of Washington, Box 352250, Seattle, WA 98195, USA
e-mail: gekhalil@gmail.com

F. Mlekicki
Chromosense LLC, One Metrotech Center, Brooklyn, NY 11201, USA
e-mail: filipmlekicki@gmail.com

A. Sidelev
Parsons, 100 Broadway, New York, NY 10005, USA
e-mail: a.sidelev@gmail.com

M. Ghandehari, *Optical Phenomenology and Applications*,
Smart Sensors, Measurement and Instrumentation 28,
https://doi.org/10.1007/978-3-319-70715-0_13

characterization, treatment or enhancement, and the capacity to monitor the parameters of interest in order to determine the overall success of the remediation (Bergman 1968; Baleizão et al. 2008; Eich et al. 2010).

The potential for monitoring innovations in this area comes from the fact that most samples are currently taken through a rather lengthy manual process which uses several pieces of mechanical equipment and observation wells. These analyses are time-consuming and therefore costly, and error-prone due to the physical extraction of samples for analysis. Certain monitoring pain points can be addressed with the development of robust in situ monitoring tools that track parameters common to most MNA projects. These geochemical parameters include pH, oxidation-reduction potential and contaminant concentrations. In the applications involving aerobic bioremediation O_2 is a critical geochemical parameter.

In this chapter we show how coupling the photo-physical properties of Platinum Porphyrin (Eich et al. 2010; Khalil 2004) along with the utility of optical fiber technology can be used to the quantitative assessment of subsurface oxygen in situ. The chemical stability of Porphyrin is an attractive feature of the fluorinated porphyrin compounds for the intended long term applications.

13.2 Sensor Molecules for Sensing Dissolved Oxygen

The luminescence of conjugated organic and metallo-organic molecules is quenched by oxygen (McDonagh et al. 1998), an effect that can be used to monitor oxygen concentration by monitoring either the luminescence intensity or the intensity decay rate. Several molecules are known to be sensitive to oxygen concentration. These sensor molecules are commonly embedded in a hydrophobic polymeric or solgel matrix permeable to oxygen diffusion. Most commercial oxygen sensor molecules in this category are based on luminescence quenching of ruthenium complexes (Wang and Wolfbeis 2016). The most recent commercial development for measurement of dissolved oxygen is based on our porphyrin research (Sweet et al. 2002; Khalil et al. 2005).

13.2.1 Detection Method: Intensities and Lifetimes

The concept of using luminescence changes to monitor oxygen concentration was originally developed with the goal of monitoring the oxygen concentration in blood and other fluids. It was conceived as a tiny volume of oxygen-permeable polymer with a luminescent indicator at the tip of an optical fiber (Klukowska 2004). The lifetime (duration) of emission of the luminescent indicator and the diffusion rate of oxygen in the host (which can be a polymer including solgel) are designed so there is a measurable change in the luminescence level, such that the anticipated oxygen pressure range can be accurately measured. The host matrix functions as a carrier for the

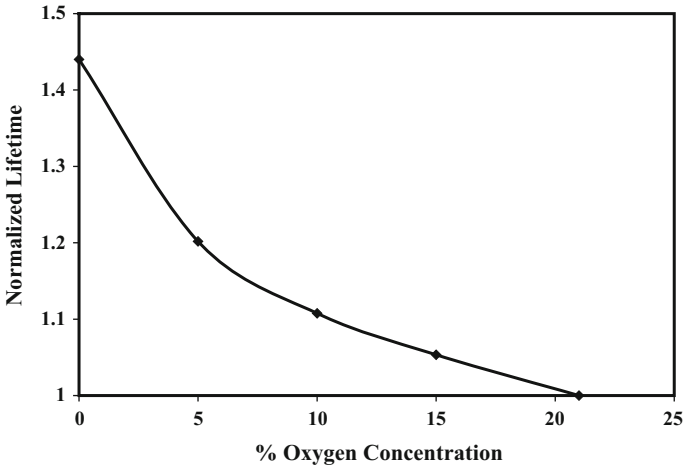

Fig. 13.1 Fluorescence lifetime (normalized versus value at 22% O_2) versus Oxygen concentration

indicator and provides interaction sites for the oxygen sensing. The preferred method for measuring oxygen is based on measuring the fluorescence intensity versus time as it decays. The phosphorescent intensity upon removal of the excitation light source is

$$I(t) = I_0 e - t/\tau \tag{13.1}$$

τ is the phosphorescent lifetime and is the inverse of the overall phosphorescence rate of decay. A calibration curve is generated by plotting the observed τ at known oxygen concentrations. Measured τ values will be used to determine oxygen level (Sweet et al. 2002).

Determinations of quenching based on luminescence rate of decay avoid several problems that arise when determinations are based on intensity measurements, including light source intensity fluctuations, index of refraction shifts, optical geometry variations, variations in film thickness, and sensor molecule concentration due to aging. Lifetime measurement of porphyrins (Fig. 13.1) can be easily accomplished using instruments made with reliable and inexpensive solid-state components. Integration of luminescence energy at three different points along the decay time provides a reliable measurement of luminescence lifetime.

13.2.2 Simultaneous Sensing of Temperature

An independent temperature sensitive sensor molecule will be needed since the luminescence is also function of temperature (Acquaye 2006; Barbarulo et al. 2005; Baleizão et al. 2008; Norris et al. 2008; Venturini et al. 2015; Wang and Wolfbeis 2014, 2016). This is the important for long-term applications where the temperature

will vary. Photo-physical properties of luminescent organic and metallo-organic compounds provide lifetime based systems where an oxygen sensitive and a temperature sensitive sensor molecule may be embedded in the same matrix.

The temperature sensor is a tris(β-diketonate) phenanthroline europium complex, with absorption peaked at 370 nm and sharp emission peak at 615 nm. Lifetime of this compound varies between 350 and 50 μs over the temperature range 5–45 °C, for a derivative of −5.3 μs/°C. The oxygen and the temperature sensors have maximum absorption in the range 370–400 nm (Fig. 13.2) but emission spectra, which do not overlap (Fig. 13.3).

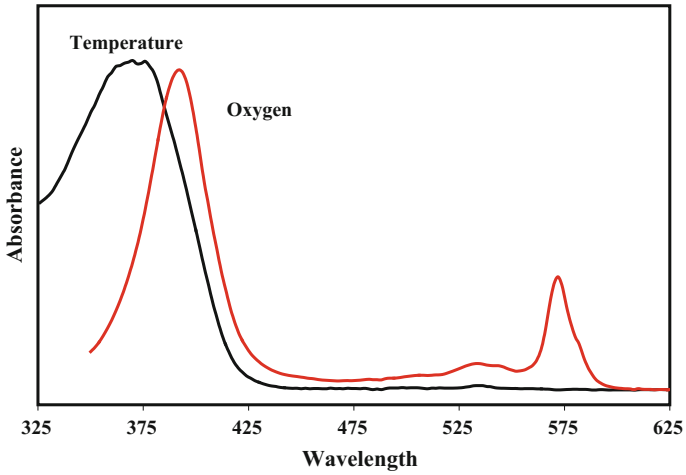

Fig. 13.2 Absorption peaks of the oxygen and temperature sensor molecules

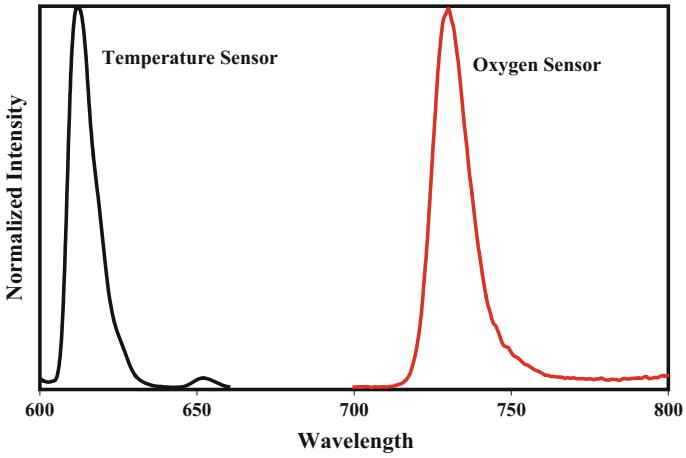

Fig. 13.3 Emissions peaks corresponding to the absorption peaks shown in Fig. 13.2

The example shown here is platinum-tetra (pentafluorophenyl)porpholactone [PtTFPL], recently developed in our labs. This compound has a principal absorption band at 390 nm and a red-shifted phosphorescence at 740 μm. In the flouro-isopropyl-butyl (FIB) polymer PtTFPL has a lifetime flourescence range of 42.7–6.6 μs in going from 0 to 21% oxygen.

13.3 Experimental Results in Dry and Saturated Soil

Experiments were conducted in a chamber (Fig. 13.4) filled with sand which was tested dry and at various level of saturation while the Oxygen concentration was varied. This was achieved by releasing methane from a valve (Fig. 13.4) embedded in the soil. Results of these experiments for the case of wet sand are shown in Fig. 13.5; note the slower rebound to the natural condition is observed. The x-axis

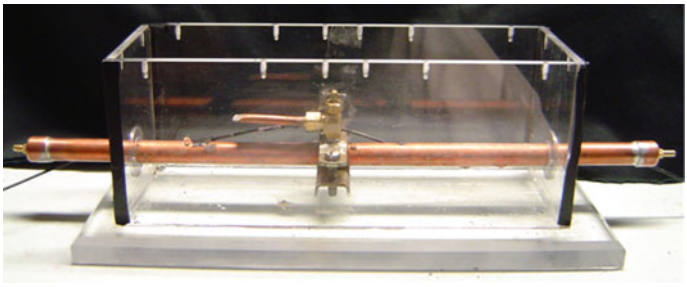

Fig. 13.4 Test chamber showing copper pipe with holes and valve

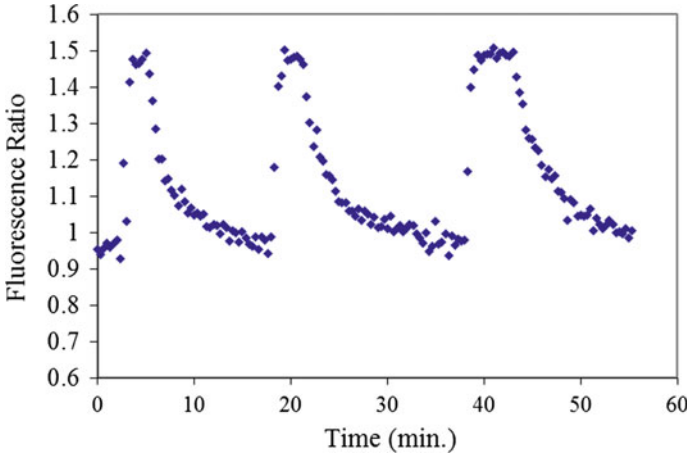

Fig. 13.5 Response to variation of oxygen concentration in wet sand. Vertical axis is the ratio of fluorescence lifetime versus the lifetime before gas was released

is time, and the y-axis is the normalized response of the sensor. The longer relaxation time of the sensor response in wet sand is expected since the moisture in the sand tends to trap gases, making the diffusion rate of gases through liquids much slower than through air.

13.3.1 Choice of Sensor Molecule

The proper choice of the sensing compound, allows one to tune for a desired detection range of dissolved oxygen concentration. Good dynamic range can be achieved by employing sensor molecules with different triplet state lifetimes. For example, a luminescent dye with a long excited state lifetime is suitable for application with high O_2 concentration, as would be the case in sandy soil, while a short-lived luminescent dye is better for lower O_2 concentration, as may be the case in clay. The relationship between sensitivity and the sensor molecule excited state lifetime is shown in Table 13.1.

The luminescence efficiency of porphyrin compounds is typically between 20 and 30%. Variations of the above compounds have demonstrated stability, and are commercially available from several suppliers, including Frontier Scientific (Ogden, UT), Aldrich (Milwaukee, WI) and Molecular Probes (Eugene, OR).

13.3.2 Choice of Host Matrix

In the case of polymeric hosts, the Porphyrin sensor compounds can be immobilized in polymer matrices that form the fiber tip or the cladding for the optical fiber along the length. The host polymer has two functions: (1) to hold the porphyrin indicator close to the optical fiber in order to be excited by the incident energy, either at the tip or by evanescent field energy, and (2) to provide interaction sites for the oxygen. In general, oxygen sensitivity is polymer-dependent; different polymers elicit different response characteristics. Figure 13.6 shows results of a study on the oxygen sensitivity of various host polymers. It is possible to "tune" the sensitivity

Table 13.1 Optical properties of the sensor molecules

Luminescent dye	Lifetime (μs)	Sensitivity	Application
PtTPP	0.124	45	λ_{ex} 510 nm–λ_{em} 650 nm
PdTPP	1.4	20	λ_{ex} 554 nm–λ_{em} 680 nm
PdTFPP	1.8	20	λ_{ex} 540 nm–λ_{em} 650 nm
TaTPP	2.5	45	λ_{ex} 565 nm–λ_{em} 710 nm
HfTPP	10.8	NA	λ_{ex} 540 nm–λ_{em} 650 nm

λ_{ex} Excitation λ_{em} Emission

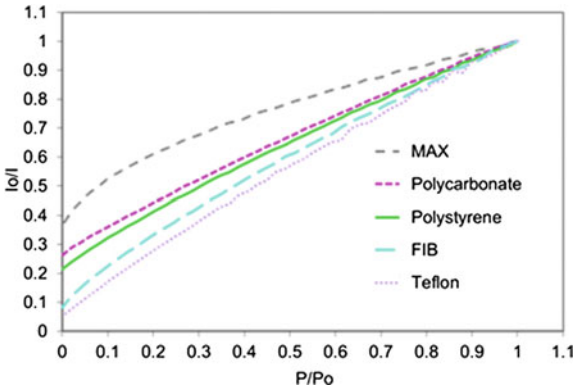

Fig. 13.6 Stern-Volmer oxygen sensitivity in various polymers

for detecting a certain oxygen level by and response time by selecting the appropriate polymer. The sensing compound can therefore be matched with a particular sensor molecule that has an optically emissive triplet state lifetime appropriate to the application.

13.4 Conclusion

This chapter demonstrated the utility of a porphyrin sensor molecule for sensing dissolved oxygen, and a europium complex for temperature sensing and calibration. Both are embedded in the same polymer which is applied to an optical fiber for remote in situ monitoring of subsurface oxygen. The proposed approach has two main desirable features: inherently robust composition of the sensor molecules, and the internal calibration strategy made possible through fluorescence lifetime measurements. Response of the fiber optic oxygen sensor was tested in a chamber filled with sand, testing the sensor response in dry and saturated condition.

References

Acquaye, L. (2006). *Effect of high curing temperatures on the strength, durability and potential of delayed ettringite formation in mass concrete structures*. University of Florida.

Baleizão, C., Nagl, S., Schäferling, M., Berberan-Santos, M. N., & Wolfbeis, O. S. (2008). Dual fluorescence sensor for trace oxygen and temperature with unmatched range and sensitivity. *Analytical Chemistry, 80*(16), 6449–6457.

Barbarulo, R., Peycelon, H., Prené, S., & Marchand, J. (2005). Delayed ettringite formation symptoms on mortars induced by high temperature due to cement heat of hydration or late thermal cycle. *Cement and Concrete Research, 35*(1), 125–131.

Bergman, I. (1968). Rapid-response atmospheric oxygen monitor based on fluorescence quenching. *Nature*, *218*(5139), 396.

Eich, S., Schmälzlin, E., & Löhmannsröben, H. (2010). Distributed fiber optical sensing of molecular oxygen with OTDR. *Photonics Europe*, April 12–16, SPIE, Brussels, Belgium, 2010 Print.

EPA. (2006). Cleaning up the nation's waste sites. *Markets and technology trends 2004 Edition*, 2006 ASI 9218-69, EPA 542-R-04-015.

Khalil, G. (2004). Dual-luminophor pressure-sensitive paint I. Ratio of reference to sensor giving a small temperature dependency. *Sensors and Actuators B: Chemical, 97*(1), 13–21.

Khalil, G. E., Kimura, F., Chin, A., Ghandehari, M., Wan, R., Shinoki, W., et al. (2005). Continuous underground monitoring of gas leaks. *Research in Nondestructive Evaluation, 16* (3), 119–130.

Klukowska, A. (2004). *Switching hybrid polymers with physically and covalently entrapped organic photochromes*. Julius Maximilians Universitat, Wurzburg.

McDonagh, C., Maccraith, B. D., & McEvoy, A. K. (1998). Tailoring of sol-gel films for optical sensing of oxygen in gas and aqueous phase. *Analytical Chemistry, 70*(1), 45–50.

Norris, A., Saafi, M., & Romine, P. (2008). Temperature and moisture monitoring in concrete structures using embedded nanotechnology/microelectromechanical systems (MEMS) sensors. *Construction and Building Materials, 22*(2), 111–120.

Sweet, I. R., Khalil, G., Wallen, A. R., Steedman, M., Schenkman, K. A., Reems, J. A., et al. (2002). Continuous measurement of oxygen consumption by pancreatic islets. *Diabetes Technology & Therapeutics, 4*(5), 661–672.

Venturini, F., Bürgi, R., Borisov, S. M., & Klimant, I. (2015). Optical temperature sensing using a new thermographic phosphor. *Sensors and Actuators, A: Physical, 233,* 324–329.

Wang, X., & Wolfbeis, O. S. (2014). Optical methods for sensing and imaging oxygen: Materials, spectroscopies and applications. *Chemical Society Reviews, 43*(10), 3666–3761.

Wang, X., & Wolfbeis, O. S. (2016). Fiber-optic chemical sensors and biosensors (2013-2015). *Analytical Chemistry, 88*(1), 203.

Chapter 14
Molecular Probes for Detection of Subsurface Methane Leaks

Masoud Ghandehari and Gamal Khalil

Abstract A method for monitoring natural gas leaks was designed based on the highly sensitive measurement of oxygen, which would be displaced in the event of a subsurface volatile gas leak. A fiber optic sensor was made using a gas-permeable polymer cladding, doped with oxygen-responsive porphyrin. The evanescent field at the interface of the core and the cladding was used to detect gas leaks. Tests were carried out using methane gas leaks in a chamber filled with dry and wet sand. Results of sensitivity, response time and reversibility are presented.

14.1 Introduction

The national energy infrastructure is subject to a number of vulnerabilities when it comes to resilience and physical security (Parfomak 2013). The aging of large parts of the energy infrastructure is the largest vulnerability; as an example, in a study conducted by the Gas Research Institute and the U. S. Environmental Protection Agency (EPA) natural gas pipeline compressor stations were found to be the single largest leakage source in the gas industry (EPA and GRI 2016; Mokhatab et al. 2015). Leaking valves account for roughly half the emissions of volatile organic compounds (VOCs) from oil refineries (Committee on Government Reform 1999). The environmental damage, operational hazards and economic loss from this systemic leakage as well as functional disruption due to extreme weather events, political instability or terrorist activities are all sources of significant concern (TRB 2004). No matter the cause, risk of leaks, large and small, exist at all points of the natural gas infrastructure; during extraction, refining processes, transportation, delivery and point of sale. To

M. Ghandehari (✉)
New York University, Six Metrotech Center, Brooklyn, NY 11201, USA
e-mail: masoud@nyu.edu

G. Khalil
Department of Aeronautics & Astronautics, University of Washington,
Box 352250, Seattle, WA 98195, USA
e-mail: gekhalil@gmail.com

M. Ghandehari, *Optical Phenomenology and Applications*,
Smart Sensors, Measurement and Instrumentation 28,
https://doi.org/10.1007/978-3-319-70715-0_14

address these vulnerabilities, the U.S. Department of Energy has developed a comprehensive strategy to assess and mitigate risks (U.S. DOE 2017). Nonetheless, system wide, leaking valves, flanges and connections continue to be significant sources of fugitive gas and volatile chemical emissions in oil extraction, chemical manufacturing, gas production, transmission and distribution.

To begin to quantify and address the environmental impact of fugitive VOCs, the U.S. EPA has developed Leak Detection and Repair (LDAR) regulations. Under the LDAR rules, a leak is typically defined as a release of more than 10,000 ppm of VOCs or other pollutants (EPA 2006). The work of the EPA and the DOE establish the scope of the problem at both the micro and macro levels, and in 2016 the Pipe Safety Bill addressed the scope and complexity of the problem while also taking into account the economic losses and environmental damage caused by pipeline leakage (DOT 2016; George 2016). Nationally, replacement costs of aging pipelines are estimated at $270 billion (U.S. DOE 2017; DOT 2016; George 2016). While there are many detection strategies available, few of them are able to meet cost of use and durability requirements to be practical. Cost effective detection of these methane leaks, particularly when considering the extensive national network of subsurface pipelines, would enable both strategic and ongoing monitoring that mitigates risk and prioritizes infrastructure remediation and environmental protection. (McKain et al. 2015; Murvay and Silea 2012).

14.2 Background

According to estimates, the natural gas pipeline infrastructure spans nearly three million miles, supplying residential and industrial customers around the globe. In the United States alone there are just over 300,000 miles of mainline transmission lines (EIA 2007). With an average of $700 per mile spent each year on maintenance and inspection, approximately $300 million per year is devoted to servicing this existing infrastructure. Moreover, continued infrastructure growth is expected in order to meet the anticipated 50% increase in demand for natural gas over the next 20 years.

Within this infrastructure, the current methods for detecting leaks measure the concentration of VOCs. These methods include catalytic oxidation, flame ionization, infrared absorption, colorimetric testing and photoionization (EPA 2006; ASTM E1003-95 2005; ASTM E515-95 2011; ASTM E1066 2006; ASTM E1002-96 2005). While the sensitivity of these detectors is high, each is limited to detecting only certain types of VOCs. In addition, these detectors are relatively expensive, require constant calibration and skilled operators. Most importantly, many are not suitable for subsurface applications. As an example, in a colorimetric test, a pipeline is filled with air containing a small percentage of ammonia, which changes the hue of a color developer applied over the pipeline in the event of a leak. While this method is very sensitive and low cost, the addition of ammonia requires clean up after testing and is corrosive to vessels containing copper and brass. Similarly, the gold standards for evaluating pipeline integrity, the pressure test and direct assessment for gas or

water pipelines, often require that sections of pipe be taken out of service and excavated during testing, an approach that is both costly and disruptive. As pipeline infrastructure grows there is a demand for monitoring techniques that can be applied in particular to the subsurface environment. The gas leak detection approach we describe utilizes the high sensitivity of the oxygen probe described in Chap. 13. The detection mechanism is by monitoring the change in oxygen levels displaced by volatile gas in the space the leak occurs. Therefore, it is capable of detecting several types of VOC's in the subsurface environment. This approach also benefits from the inherent qualities of durability, immunity to electromagnetic interference etc.

Overall there are two general categories for leak detection: (1) Technologies for periodic inspections or continuous monitoring of indoor leaks which are often carried out using solid state and catalytic sensors. (2) Technologies for remote standoff detection of outdoor leaks from pipelines or larger facilities using technologies based on Near, Mid, or Far-Infrared spectroscopy, either at a point or as an image. '*A survey on gas leak detection and localization techniques*', can be found in this report (Murvay and Silea 2012).

In the presence of methane gas leaks, oxygen levels in the immediate environment decrease. This chapter presents a novel approach which is based on continuously monitoring the oxygen concentrations surrounding a natural gas pipeline; it is a low cost and durable gas-leak detection system. Gas leaks from the pipeline are detected through the associated displacement of oxygen using fiber optic evanescent field spectroscopy via an oxygen-luminescent sensor. The detection system can capture and measure leaks in real time from refineries as well as oil, gas and chemical processing equipment, including flanges, valves, pumps and buried pipelines. For applications requiring monitoring for longer durations, time-of-flight measurements can be implemented to identify the location of a gas leak.

14.3 Method

The sensor described below is an optical fiber coated with oxygen-permeable polymer containing a luminophor sensor molecule that is quenched by oxygen (Chap. 13). When used as a sensor and illuminated by a light source that excites the luminophor, the compound has the ability to detect and quantify small changes in oxygen concentrations in the surrounding environment. In a demonstrative visual experiment shown in Fig. 14.1, a Pd (II) meso-tetra (pentafluorophenyl) porphyrine doped polymeric mesh was used to cover a hole in a pipe containing nitrogen; an inert gas that displaces oxygen. Figure 14.1 shows an image of the leaking hole covered with the mesh, subject to ambient white light (on the right), versus when excited by 400 nm wavelength light, causing it to emit in red on the left (650 nm). The red luminescence intensity and lifetime of the compound depends on the leak rate.

The oxygen-sensitive compound can be deposited on to an optical fiber either on the tip or as part of a gas permeable cladding (Fig. 14.2). In a typical application an optical fiber cable would be placed alongside a natural gas pipeline or in spots

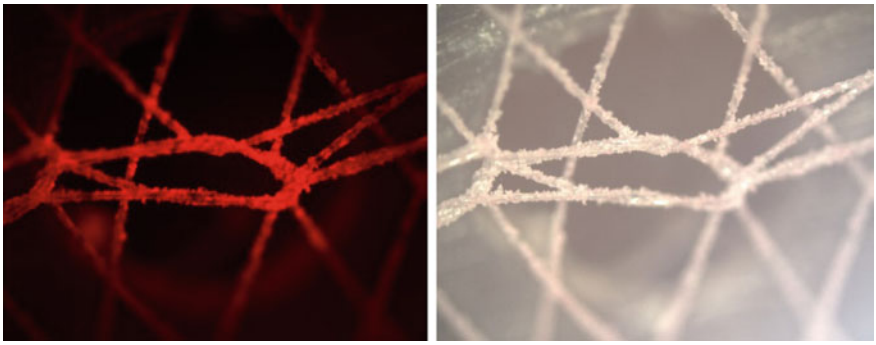

Fig. 14.1 The sensing film covers a 1/16″ hole in a PVC gas pipe. The left image is taken under ambient light and the right image shows the phosphorescence at 650 nm under illumination by 400 nm light. The red light (left) is caused by the depletion of oxygen in the film due to permeated nitrogen gas

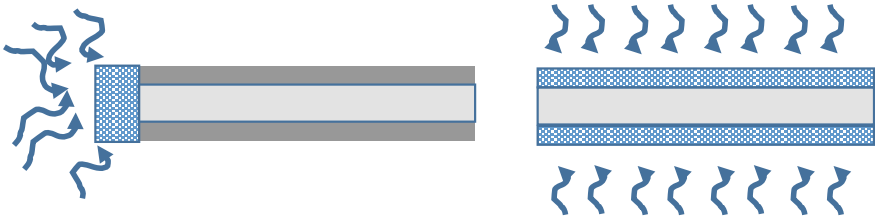

Fig. 14.2 Multimode Optical fiber with (Left) sensing compound at tip, (Right) sensing compound along the length as cladding

where potential leaks may be expected. The environment surrounding the pipeline would contain constant or slowly changing amounts of oxygen, the concentration of which would decrease in the vicinity of a leak due to the displacement by gaseous VOCs.

14.3.1 Oxygen Sensing

The quenching of luminescence by oxygen was first discussed by Stern and Volmer (1919) and Smoluchowski (1906). The concept of using luminescence changes to monitor oxygen concentration was later developed with the goal of monitoring the oxygen concentration in blood and other fluids. It was then conceived as a tiny volume of oxygen-permeable polymer with a luminescent indicator at the tip of an optical fiber (Khalil et al. 1989, 1994). In this study, the functional polymer is used as cladding along a short fiber segment and is excited by the evanescent field (Chap. 5, Fig. 5.2). The level of luminescence is used to measure the concentration

of oxygen over the sensing layer. The lifetime of the luminescent indicator and the diffusion rate of oxygen in the polymer are designed so there is a measurable change in the luminescence level for the anticipated oxygen pressure range to be monitored. The polymer functions as a carrier for the indicator and provides interaction sites for the oxygen sensing. Here the preferred method for measuring oxygen is based on lifetime detection, outlined in Sect. 14.4.

14.3.2 Transduction Through the Optical Fiber

In the case of distributed sensing, light is guided through the core of an optical fiber by internal reflection from the core/cladding interface. This process generates a surface wave (see Chap. 2 and Chap. 5 for the discussion of evanescent wave), which travels along the fiber just outside this interface. While in telecommunications, optical fiber materials are produced so the evanescent field does not interact with the external environment, in this case the fibers are modified so the signal is modulated by the external environment. For example, permeable cladding can serve as the zone of interaction, in which light is effected by the media it encounters. In this application the evanescent field functions as a distributed antenna for interrogating the gaseous environment surrounding the fiber.

14.3.3 Determination of Leak Location Along Fiber Length

For spatially resolved measurements, Optical Time of Flight (OTOF) techniques can be adapted from mature diagnostic approaches developed in fiber optic communications. OTOF techniques have also been used for distributed sensing of physical parameters such as strain and temperature. Typically, short pulses of light are coupled into an optical waveguide, and events such as absorption, fluorescence and scattering are recorded. Time delays between the excitation pulse and specific changes in the forward or backward signal are used for post processing. Such concepts are transferable for leak location identification. Here, the analytical information is derived from the amplitude and temporal characteristics of the luminescence caused by interaction of the input pulse and the analyte (Potyrailo and Hieftje 1998). Alternatively, a bundle of tip sensors can be used with prescribed tip locations.

14.4 Materials and Testing

Oxygen sensor compound: The oxygen sensor was made by first dissolving 1.0037 g of a polycarbonate-silicon copolymer in a minimal amount of dichloromethane ($\sim$3 mL). To this solution, 20-mL of α,α,α-trifluorotoluene (TFT) was

added. Finally, 2.5 mg of PD (II) and Pt (II) meso-tetra(pentafluorophenyl) porphyrin (PtTFPP) were purchased from Frontier Scientific (a.k.a. Porphyrin Products) in Logan, UT, and added to the solution. The solution was mixed until a clear, uniformly pink-orange color was established.

Calibration: The oxygen sensor was calibrated by using known, premixed oxygen/nitrogen mixtures. A number of premixed gases were passed through the test chamber, where the sensor was allowed to equilibrate 5 min for each gas mixture. Figure 14.3 shows the sensitivity of the oxygen sensor at various oxygen concentrations. Results are shown for the sensor compound at the fiber tip, and in another model as cladding. The results are compared with a commercial ambient air gas sensor, not applicable for subsurface applications.

Oxygen detection system: Both the luminescence intensity and the luminescence lifetime (decay rate) can be used as sensor molecule response measures for detecting oxygen levels. However, measuring the luminescence decay rate produces a more robust sensor and avoids several problems that arise with intensity measurements, including light-source intensity fluctuations, index-of-refraction shifts and variations in film thickness or indicator concentration due to aging. Fluorescence decay (life time) measurements of porphyrins can be accomplished easily using reliable and inexpensive solid-state components; and the integration of luminescence energy at three different points along the decay time provides a robust and independent measurement of luminescence lifetime.

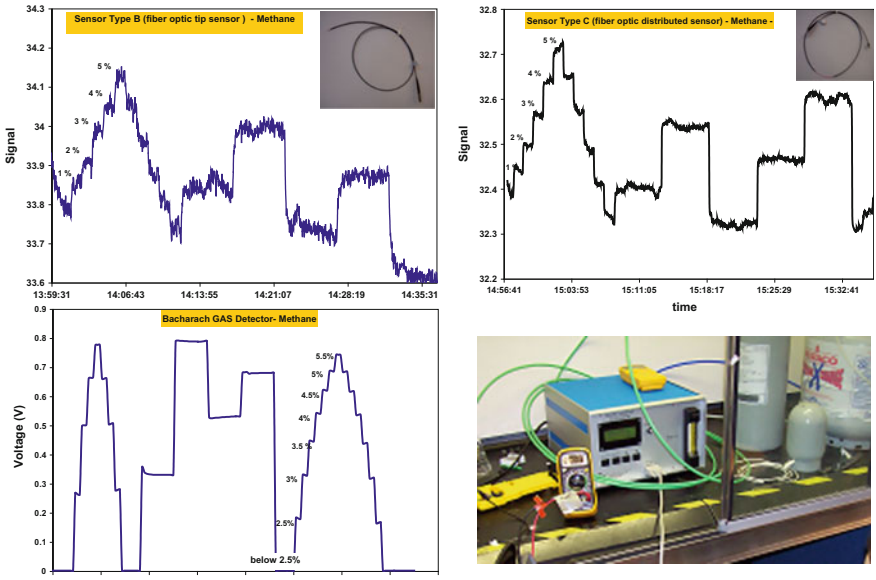

Fig. 14.3 Calibration test results (upper left) tip fiber, (upper right) side sensing fiber, (lower left) commercially available sensor for ambient sensing, (lower right) the set up

In the system, cladding from a polymer-clad silica fiber was stripped along a 4 cm length where the oxygen-sensor compound was applied as a solution. For protection, the Fiber Optic Cable (FOC) was covered with a porous jacket. The oxygen sensor was excited with a pulsed (2000 Hz) 400 nm LED, passed through one end of the FOC. The excited oxygen sensor subsequently emitted a phosphorescent red light (650 nm) that traveled along the FOC to the detector, which was fitted with a 650 nm high pass filter. The characteristic emission decay lifetime of the sensor ranges from 20 to 100 μs. The lifetime of the emission was quantified by comparing the amount of light emitted from 0 to 30 μs after the excitation pulse (Ia) with the light emitted from 30 to 180 μs after the excitation pulse (Ib). The output measurement was the ratio of intensities over these two periods, R = Ib/Ia, which increased with decreasing oxygen concentrations. Previous work has produced results that indicate a limit of detection of 1% O_2 with a 0.01% resolution, and the sensor showed no measurable drift for ~20 h of continuous monitoring at 21% oxygen value (Sweet et al. 2002).

Test chamber for subsurface evaluation: The subsurface tests were conducted on simulated gas leaks inside of a Plexiglas test chamber filled with sand (Fig. 14.4). The chamber was used to evaluate the effectiveness of the proposed leak-detection system for sensing subsurface gas leaks. In order to simulate an operational natural gas pipeline, a copper pipe containing mixtures of methane gas was passed through the longitudinal axis of the chamber. Methane gas leaks were subsequently simulated and controlled through a valve located at mid-length of the pipe. When open, the valve allowed methane gas to leak out of the buried pipe into the surrounding sand. A fiber optic sensor cable was buried alongside the pipe and was made oxygen reactive 4 cm from the location of the leak. A schematic of the experimental set up is shown in Fig. 14.5. Leak events were monitored subject to various chamber environments, including an empty chamber, a sand-filled chamber and a sand-and-water-filled chamber.

Fig. 14.4 Leak-detection test chamber: copper pipe with leak valve passes through the chamber. Fiber optic cable passes along the side of the copper pipe with 4 cm of evanescent field sensing length near the leak location

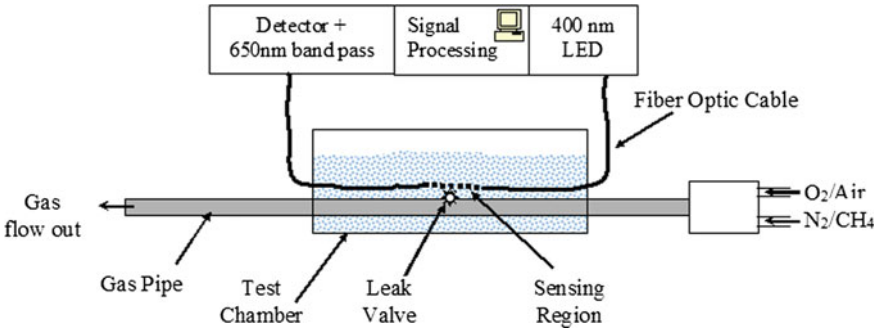

Fig. 14.5 Schematic of leak-detection experiment setup

14.5 Results and Discussion

Several feasibility studies were performed to evaluate the detection system, subject to various simulated environments. First, leaks in an above-ground pipeline were simulated by leaving the test chamber open to the atmosphere. Methane gas was passed through the main pipe at the flow rate of the valve. After 2 min the leak valve was closed, and the sensor was allowed to re-establish a steady baseline. This process was repeated several times to demonstrate the reproducibility of the results. A no-leak, steady-baseline sensor response in ambient environment was then established before the leak valve was opened for 2 min, allowing methane gas to leak through.

Identical experiments were conducted as the chamber was filled with sand and with a mixture of sand and water. Results of these experiments are shown in Fig. 14.6. The x-axis describes the time at which the leaks were induced, and the y-axis is the

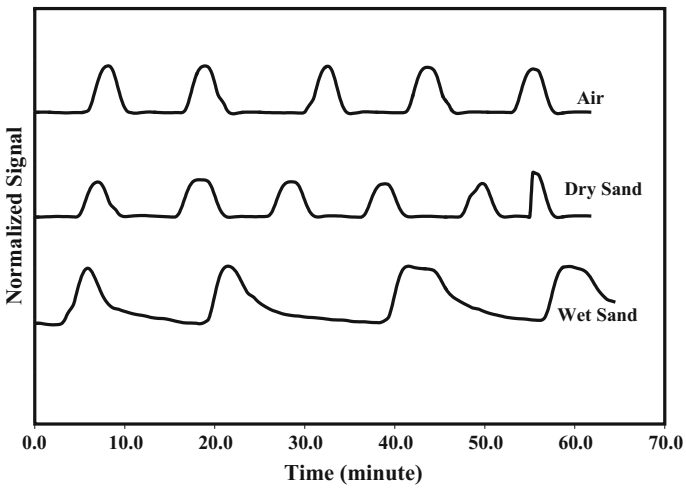

Fig. 14.6 The response of the oxygen sensor to methane gas leaks: the upper graph shows leak detection in air, the middle graph in dry sand, the bottom graph in saturated sand

normalized response of the sensor. The longer relaxation time of the sensor response in wet sand is expected since the moisture in the sand tends to trap gases, making the diffusion rate of gases through liquids much slower than through air.

The long-term performance of the leak-detection system was tested over a period of 30 days. Figure 14.7 shows the results of the continuous monitoring of methane gas leaks introduced in 2-min bursts every 24 h in an empty chamber. The sensor showed no measurable reduction in sensitivity or response time. Figure 14.8 shows the detection of methane gas leaks by the oxygen sensor embedded in saturated sand. The peaks generated in the graph are on the specific days that the system was

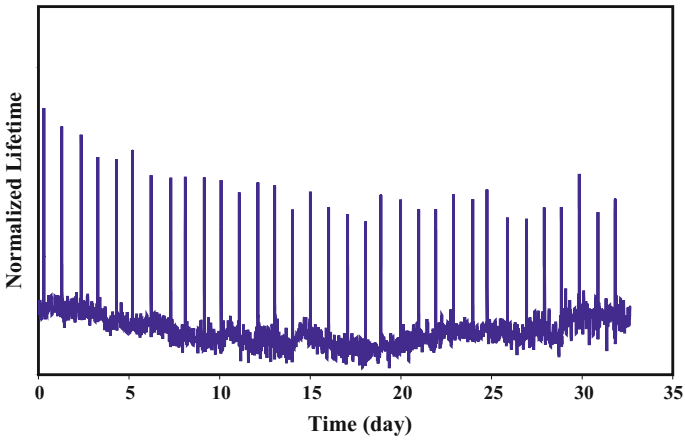

Fig. 14.7 Continuous monitoring of daily leaks in an empty chamber over 33 days

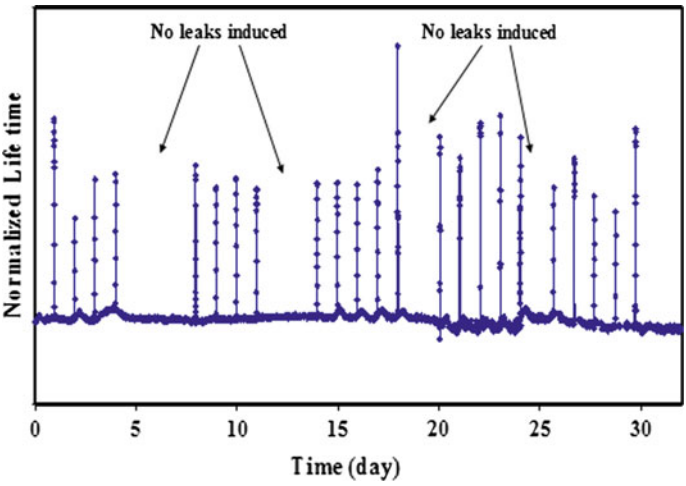

Fig. 14.8 Continuous monitoring of leaks in a chamber filled with saturated sand

subjected to methane leak. Leaks were induced on a daily schedule except on weekends and holidays.

14.6 Conclusion

This chapter introduced the concept of using optical fiber evanescent field measurements of fluorescence lifetime to detect gas leaks in buried pipelines. It further showed that the detection of oxygen concentrations provides an effective means for detecting gaseous leaks of volatile hydrocarbons. The leak sensor uses phosphorescence quenching of specially designed phosphorescent molecules to measure oxygen concentration. The proposed sensor utilizes both stable materials and a robust detection method capable of operating reliably in aggressive environments. Key features of the technology are long-term performance based on well-understood platinum porphyrin chemistry and the capability for distributed sensing using evanescent field spectroscopy.

References

ASTM E1002-96. (2005). *Standard Test Method for Leaks Using Ultrasonics*. West Conshohocken, PA: ASTM International, 1996. www.astm.org.

ASTM E1003-95. (2005). *Standard test method for hydrostatic leak testing*. West Conshohocken, PA: ASTM International, 1995. www.astm.org.

ASTM E1066. (2006). *Standard Test Method for Ammonia Colorimetric Leak Testing*. West Conshohocken, PA: ASTM International, 2006. www.astm.org.

ASTM E515-11. (2011). *Standard Practice for Leaks Using Bubble Emission Techniques*. West Conshohocken, PA: ASTM International, 2011. www.astm.org.

Committee On Government Reform. (1999). *Oil refineries fail to report millions of pounds of harmful emissions.* Washington DC: A Report Prepared for Rep. Henry Waxman, November 10, 1999.

DOT. (2016). *Protecting our infrastructure of pipelines and enhancing safety act of 2016.*

EIA. (2007-last update, June). About U.S. Natural Gas Pipelines—Transporting Natural Gas. Available: https://www.eia.gov/pub/oil_gas/natural_gas/analysis_publications/ngpipeline/index.html.

EPA. (2006). *EPA regulation, 40 CFR 60.482.* Environmental Protection edn.

EPA and GRI. (2016). *Directed inspection and maintenance at gas processing plants and booster stations.* EPA.

George, S. (2016-last update, April). Pipeline safety bill puts new focus on aging gas infrastructure. Available: EDF http://blogs.edf.org/energyexchange/2016/04/01/pipeline-safety-bill-puts-new-focus-on-aging-gas-infrastructure/, February 2017.

Khalil, G. E., Gouterman, M. P., & Green, E. (1989). *Method for measuring oxygen concentration.* Google Patents.

Khalil, G., Yim, J., & Vurek, G. G. (1994). In vivo blood gases: Problems and solutions. *Proceedings of SPIE 2131, Biomedical Fiber Optic Instrumentation*. http://dx.doi.org/10.1117/12.180741, 28 July 1994.

Mckain, K., Down, A., Raciti, S., Budney, J., Hutyra, L. R., Floerchinger, C., et al. (2015). Methane emissions from natural gas infrastructure and use in the urban region of Boston, Massachusetts. *Proceedings of the National Academy of Sciences, 112*(7), 1941–1946.

Mokhatab, S., Poe, W. A., & Mak, J. Y. (2015). *Handbook of natural gas transmission and processing* (3rd ed.). Amsterdam: Gulf Professional Publishing is an imprint of Elsevier.

Murvay, P., & Silea, I. (2012). A survey on gas leak detection and localization techniques. *Journal of Loss Prevention in the Process Industries, 25*(6), 966.

Parfomak, P. W. (2013). *Keeping America's pipelines safe and secure: Key issues for congress.* Federation of American Scientists.

Potyrailo, R. A., & Hieftje, G. M. (1998). Spatially resolved analyte mapping with time-of-flight optical sensors. *Trends in Analytical Chemistry, 17*(10), 593–604.

Stern, O., & Volmer, M. (1919). Über die Abklingzeit der Fluoreszenz. *Physik, 20*(183).

Sweet, I. R., Khalil, G., Wallen, A. R., Steedman, M., Schenkman, K. A., Reems, J. A., et al. (2002). Continuous measurement of oxygen consumption by pancreatic islets. *Diabetes Technology & Therapeutics, 4*(5), 661–672.

TRB. (2004). *Transmission pipelines and land use: A risk-informed approach—Special Report 281.* National Academies.

U.S. DOE. (2017-last update, January). Natural gas infrastructure modernization programs at local distribution companies: Key issues and considerations. Available: https://energy.gov/epsa/downloads/natural-gas-infrastructure-modernization-programs-local-distribution-companies-key, February 2017.

Von Smoluchowski, M. (1906). Zur kinetischen Theorie der Brownschen Molekularbewegung und der Suspensionen. *Annalen der Physik, 326*(14), 756–780. Retrieved from http://onlinelibrary.wiley.com/doi/10.1002/andp.19063261405/abstract.

Chapter 15
High Fidelity Gas Sensing with Photonic Crystal Fibers

Shijie Zheng and Masoud Ghandehari

Abstract This chapter describes the use of photonic crystal fibers treated with long period grating (PCF-LPG) used for gas sensing. We set out to determine the best PCF configuration design for optimal performance. Numerical simulations were carried out to better understand the mode characteristics of a given PCF configuration and role of the Bragg grating in generating the cladding mode for gas sensing. This was used for determination of optimal PCF structure for the cladding mode coupling.

15.1 Introduction

Demand for gas monitoring and applications to environmental protection, defense, civil engineering, and homeland security has resulted in advanced technologies for gas sensing. Many of these innovations are in optical sensing, (Polynkin et al. 2005; Zhou et al. 2003; Birks et al. 2005; Muhammad et al. 1993). Compared to electrochemical phenomena, optical signals have some inherent benefits, including resistance to electromagnetic interference and immunity to combustion and explosion. Optical fiber sensors also provide a means of guiding the light to target areas of interest.

This chapter highlights absorption spectroscopy using optical waveguides. Absorption sensing is based on the absorption signature of gases, where changes of signal at characteristic absorption lines for a particular gas is used for detection (Webber et al. 2001). We will particularly emphasize the application of laser absorption spectroscopy in silica Photonic Crystal Fibers (PCFs) and Long-Period Gratings (LPGs), and their evanescent field (Zheng et al. 2013, Tian et al. 2012a, b).

S. Zheng
Harbin Institute of Technology, Harbin 150090, China
e-mail: zhengshijie@hit.edu.cn

M. Ghandehari (✉)
New York University, Six Metrotech Center, Brooklyn, NY 11201, USA
e-mail: masoud@nyu.edu

M. Ghandehari, *Optical Phenomenology and Applications*,
Smart Sensors, Measurement and Instrumentation 28,
https://doi.org/10.1007/978-3-319-70715-0_15

These technologies offer high sensitivity and selectivity and can be integrated in optical microfluidic devices.

Fiber-optic sensors based on the conventional optical fiber have been utilized for wide range of sensing applications (Boisdé and Harmer 1996), where the interaction of evanescent field of the guided wave with the surrounding environment has been used for sensing. In a conventional fiber, the evanescent wave is an optical field that extends a short distance of $\lambda/3$ from the guiding core to the surrounding low-index cladding. Evanescent field fiber sensors thus require modifications to the fiber cladding making them permeable to the analyte, for example such that a gas or liquid can reach the interaction zone at the core cladding interface. One issue is that the sensing length for these types of sensors are limited to short lengths because of the high attenuation and the susceptibility to damage of the modified fiber. The short length results in limited sensitivity (no better than parts per million, ppm). This has been a challenge when using the evanescent field of conventional optical fibers for sensing.

Innovations in photonic crystal fibers have opened new opportunities in this area (Bise and Trevor 2004; Jensen et al. 2003). The high sensitivity of PCFs is attributed to the strong interaction between the evanescent field of the guided light and the gas sample within air channels in the fiber cladding (hosting the gaseous analyte), practically usable over long optical path (Zheng et al. 2015; Zheng 2015).

15.1.1 Absorption Spectroscopy for Gas Sensing

In recent years, advances in laser absorption spectroscopic technologies have been made, enhancing sensitivity, selectivity, and in situ detection speed of trace gases in the Near-IR (NIR) region of the electromagnetic spectra (Martin 2002; Werle et al. 1998; Weidmann et al. 2004). Laser absorption spectroscopy has been used to achieve gas sensing at trace detection limits on the order of parts per billion (ppb).

As both a waveguide and a vapor/aqueous transmission cell, the PCF has unique advantage compared to its conventional all-solid fiber counterpart (Sazio et al. 2006; Couny et al. 2007), in that it does not require the removal of the fiber cladding. As an evanescent wave sensing device, the guided core mode in the PCF has been utilized for evanescent field-based absorption spectroscopy (Pristinski and Du 2006; He et al. 2011). However, when using solid core PCF, there are two inherent limitations. First, the evanescent field only extends a small distance from the guided core mode to the surrounding PCF cladding mode. Second, the guided core mode is mostly localized in the PCF solid-core. In fact, for the most PCF designs, less than 1% power of the core mode overlaps with the surrounding air channels within the inner-ring in the cladding area (Zhu et al. 2008), thus affording weak interaction with the sample for spectroscopic measurement.

15.1.2 PCF Modes

A well-designed PCF can improve the sensitivity and optical capabilities of the sensing system. One of the key factors is the coupling of the cladding mode with the core mode. There are a few steps, or factors to consider in this case: the mode calculation, the excitation control and cladding signal loss. For a given geometrical structure, modal analysis must be performed to achieve the necessary understanding and control of excitation. It is also useful for determination of low-loss cladding modes at the desired resonance wavelength, either attenuating in the cladding or further recoupling back into the core of the PCF. We have employed two well-established simulation tools for this purpose. These include the multipole method and COMSOL Multiphysics (RF Module) interfaced with MATLAB. These simulations were used to analyze the core and cladding mode coupling, for design of a long period grading to enhance that coupling.

Two types of PCFs, with 4 rings of air-channel in cladding (shown in Fig. 15.1 and 15.2) and 5 rings of air channel in cladding were considered. Those PCFs were commercially available and provided by Yangtze Optical Fiber and Cable Company, China. These products offer an endless single mode operation, a large effective mode field area for power delivery and energy transformation of mode coupling, low loss without nonlinear effects or material damage at high power intensity, symmetrical distribution of cladding mode field, and easy alignment.

Analysis of PCFs indicates that, for a given cladding symmetry, air-channel size, and channel-to-channel separation, the confinement loss of the most likely coupled cladding mode decreases exponentially with the increase of the number of air-channel rings (Fig. 15.2). The confinement losses of cladding modes are also a

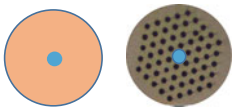

Fig. 15.1 Optical wave guides, (Left) conventional optical fiber, (Right) photonic crystal fiber, with either hollow or solid core

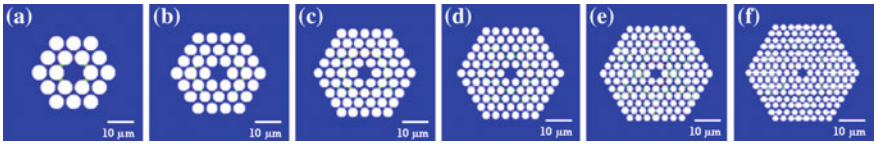

Fig. 15.2 Solid-core PCF with various numbers of air-channel rings: **a** 2 rings of air-channel with mode radius of 19.41 µm and loss of 21,152 dB/m, **b** 3 rings of air-channel with mode radius of 24.66 µm and loss of 864.3 dB/m, **c** 4 rings of air-channel with mode radius of 29.9 µm and loss of 181.6 dB/m, **d** 5 rings of air-channel with mode radius of 35.15 µm and loss of 75.05 dB/m, **e** 6 rings of air-channel with mode radius of 40.4 µm and loss of 48.02 dB/m, and **f** 7 rings of air-channel with mode radius of 45.6 µm and loss of 14.37 dB/m

function of cladding microstructure. Numeral calculations can serve as a guide for prediction and better understanding of the mode characteristics of a given PCF configuration. This is ultimately useful for the design and fabrication of optimal PCF structures for excitation of cladding mode coupling.

15.2 Sensor Head

The evanescent field (EF) in the cladding is absorbed by the characteristic absorption peaks of the gaseous species in air channels. In order to enhance the strength of the evanescence in the cladding, a long period grating (LPG) was inscribed in the PCF coupling of the core modes into the cladding. A reflective silver film was also deposited at the end of the PCF in order to increase the interaction length. The PCF-LPG sensing head is shown in Fig. 15.3. The LPG was inscribed on the PCF core by a CO_2 laser, and the silver coating was applied by vapor deposition. The PCF fiber was a solid core single-mode PCF type-D, with 9.2 μm core, 3.1 μm air-channel, and 126 μm cladding diameters. The grating periodicity was 92 at 430 nm given an LPG with a 40 mm total length.

Figure 15.3 is a schematic of the laser beam propagation through the sensor head. The incoming laser beam is coupled into the cladding mode at the resonance wavelength of the LPG, designed for optimum coupling. The coupled cladding mode travels along the air channels and interacts with the gas. Figures 15.3a–f show the simulation of the laser power at various stages of propagation.

Reflectivity of the silver coating on the fiber facet was also tested using a SMS-28 normal optical fiber and the solid core single-mode PCF (type-B, 5 rings of air-channel with attenuation 1.5 dB/km at 1550 nm; core and air-channel diameters of 8.5 μm, 2.9 μm. All had been deposited with silver on one of their end-facets. The fibers are first cleaved at one end, and then mounted on the sample plate in the e-beam evaporator (AUTO 500 Edwards) and subject to evaporation rate of 0.2 nm/s. The thickness of silver coating is about 50 nm. Figure 15.4 shows SEM images of

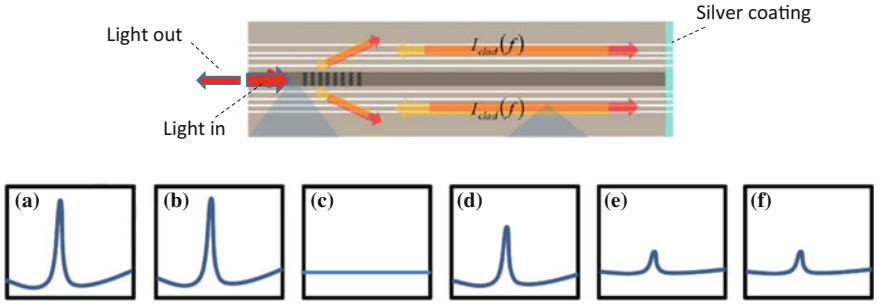

Fig. 15.3 Expected spectra of core mode and the first cladding mode coupling in the sensor head, with a silver mirror at fiber facet: **a** tunable laser entering the PCF; **b** in cladding after LPG; **c** in core after LPG; **d** in cladding before reflection; **e** before recoupling from PCF cladding at LPG; and **f** signal light out of PCF core

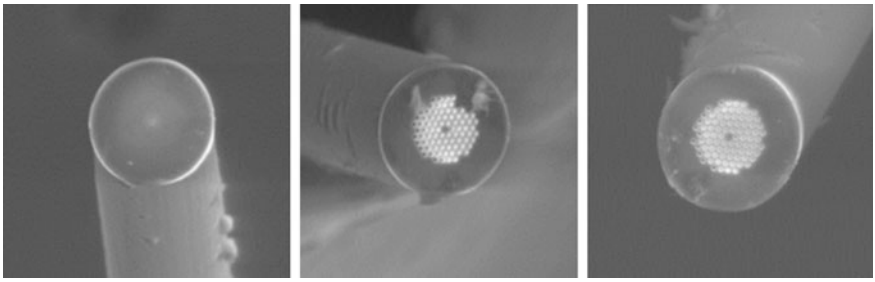

Fig. 15.4 SEM images of cleaved fiber cross-sections 10 mm from the silver coated fiber facets: from left to right, normal fiber, PCF type-B, and PCF type-D

the fibers cleaved 10 mm from the silver coated facets. The reflection parameters of the three types of fibers are 20.09, 73.91, and 28.51%. Different refractivity is attributed to factors including coating thickness, roughness of fiber facet, and coating uniformity as well as splicing losses between PCFs and FC/APC connectors. The main contribution of different refractivity is the fiber facet roughness. The highest reflectivity PCF-LPG sensor head was used for the gas sensing experiments.

15.3 Results and Discussions

Figure 15.5 shows the schematic diagram of the experimental setup for testing the sensor selectivity and concentration limits for various gases. The setup consists of one diode pump laser at wavelength of 980 nm, two optical isolators at wavelengths of 980 and 1550 nm, a 980 nm/1550 nm WDM coupler, an Er-doped fiber with length of 25 m, a 3-port optical circulator, a pigtailed FFP-TF, a polarization controller, an 80–20% 1 × 2 optical coupler, and a sensing head (gas cell), which

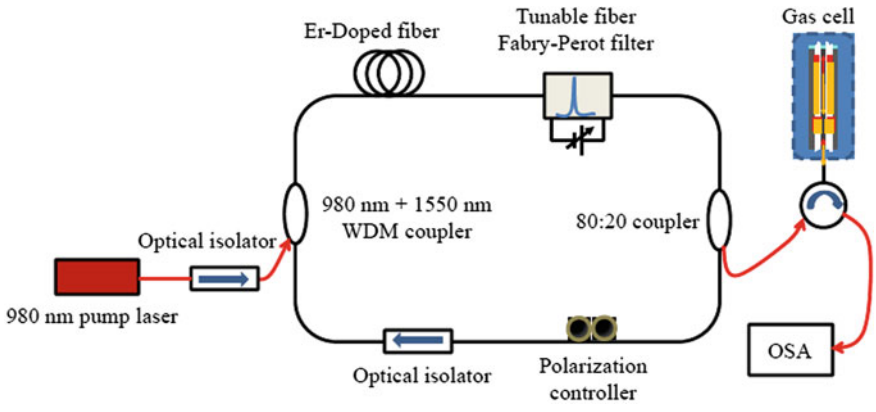

Fig. 15.5 Experimental setup for the absorption spectroscopic ammonia gas sensing

has an effective length of approximately 12 cm. One end of the sensing probe is connected to the optical circulator with the FC/APC connector, which enables the sensing head with the more favorable performance, such as a longer working distance and lower insertion attenuation. In this setup, another end of the sensing head is used as analyte inlet ("sniffing") and as a port for the reentry of the transmitted light upon reflection from the silver reflector at the fiber end.

The performance of the gas sensor is dominantly influenced by the output signal power, tuning range, and sensitivity, which are determined by a number of critical parameters: the ring-cavity attenuation, length of Er-doped fiber, and output coupler ratio. With the use of a compact tunable Er-doped fiber ring laser, this arrangement can be made portable for field evaluation. Note that because the sensing capacity relies on the spectroscopic approach, it is a rather general detection method that is applicable to a broad variety of gases and is, in addition, highly selective due to the specific vibrational-rotational states (*fingerprint*) for each type of gas. The Er-doped fiber is used as the gain medium in the tunable fiber ring laser because its broad gain bandwidth covers absorption lines of many gases permitting multiple gas detection without the need to change the light source.

The sensing device performance parameters which include sensitivity, resolution, and response time for gas diffusion, can be optimized by considering design features including fiber type, cladding mode selected for the recoupling process, mode coupling mechanism by external perturbation, and characteristics of the tunable Er-doped fiber ring laser. The effect of these features can be tested through gas sensing experiments. Highly purified analyte liquid (ammonia, ethanol, and methanol) is put into a small beaker, then moved into the chamber for testing. The concentration of the analyte in gas phase gradually increases as the liquid becomes volatile and evaporates.

Two types of laser sources, diode laser and tunable fiber ring laser were used. Shown in Fig. 15.6a is an optical spectrum of diode laser used for detection of ammonia via overtone transition of NH3 at wavelength around 1548.4 nm by absorption.

The reflected light from PCF-LPG sensor header is about—23.618 dBm ($\sim$4.347 μW), and measured intensity is about—28.255 dBm ($\sim$1.494 μW) when NH3 concentration reaches 165 ppm from 0 ppm in the gas chamber. The rate of power absorption is 65.7% while absorption sensitivity is about 17.3 nW/ppm at linear range of concentration. The relationship between absorption intensity and NH3 concentration is shown in Fig. 15.6b. It can be seen that the absorption intensity decreases linearly with increase of NH3 concentration in the range between 0 and 165 ppm. After concentration is larger than 165 ppm, the NH3 molecules are saturated and condensed on the surface of air channels in PCF cladding. Therefore, the sensing head possesses high sensitivity at low NH3 concentration, but not at higher concentrations.

To verify the selectivity of the proposed sensor, the methanol and methane are used for laser absorption tests at the same condition used for NH3 experiment. Show in Fig. 15.6c and d are the absorption laser intensity versus methanol and

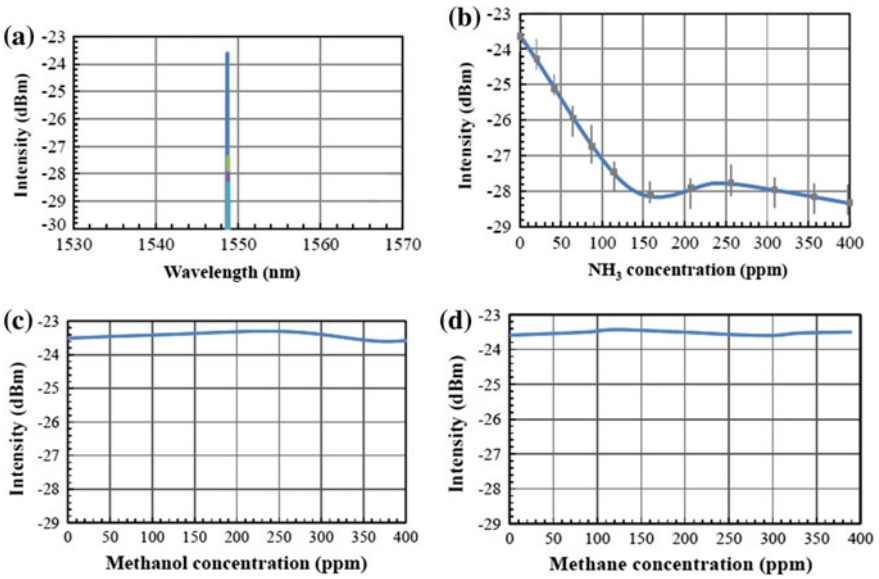

Fig. 15.6 **a** Optical spectrum of diode laser at wavelength of 1548.4 nm, **b** dependence of absorption laser intensity on ammonia concentration, **c** dependence of absorption laser intensity on methanol concentration, and **d** dependence of absorption laser intensity on methane

methane concentration, respectively. There are no laser absorptions at wavelength of 1548.4 nm for the methanol and methane gases.

Tests on ammonia were also carried out using the tunable fiber ring laser. Shown in Fig. 15.7a is an optical spectrum of tunable Er-doped fiber ring laser at wavelength of 1563.6 nm which is one of six harmonic and combination bands at wavelength of NIR range and selected for monitoring of NH3 in atmospheric and combustion applications. The reflected intensity from sensor head without ammonia absorption is about—25.127 dBm (~3.071 μW). As NH3 concentration goes up, the light intensity goes down. The light intensity of—28.238 dBm (~1.5 μW) corresponds to ammonia concentration of 125 ppm, below which the absorption intensity also decreases linearly. In this case, the absorption rate is about 51.2% and the sensitivity is 12.6 nW/ppm, slightly less than the case with the diode laser. The absorption intensity versus ammonia concentration is shown in Fig. 15.7b. Figure 15.7c and b show the relation for methanol and methane concentration at wavelength of 1563.6 nm, respectively. The trend of relationship between absorption intensity and NH3 concentration is almost same for the diode laser source and tunable fiber ring laser source, but the tunable fiber ring laser source has a broad gain bandwidth that covers the absorption lines of many gases, permitting multi-gas detection.

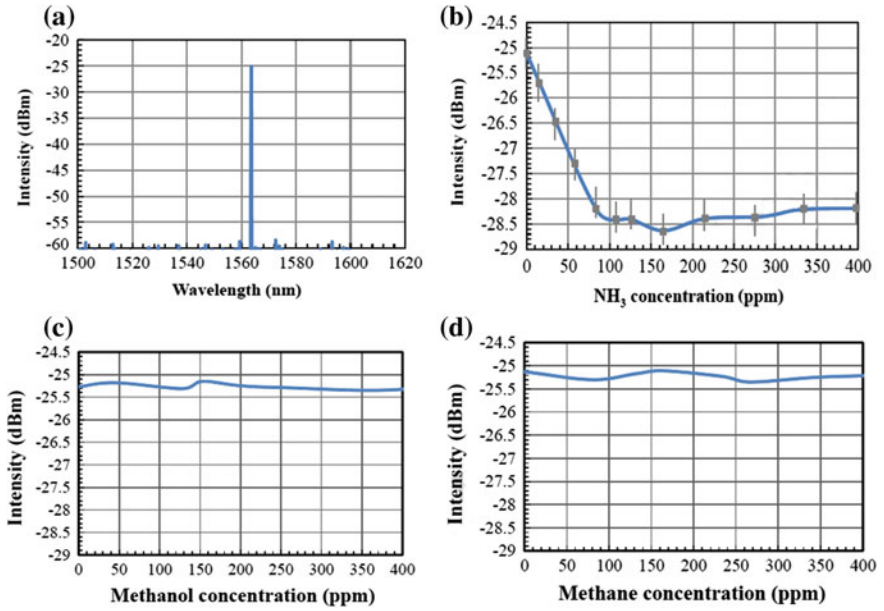

Fig. 15.7 **a** Optical spectrum of tunable fiber ring laser at wavelength of 1563.6 nm and **b** dependence of absorption laser intensity on ammonia concentration, **c** dependence of absorption laser intensity on methanol concentration, and **d** dependence of absorption laser intensity on methane

15.4 Conclusion

Design and testing of Photonic Crystal Fibers with Long Period Grating used as a sensor head for gas detection was described. The sensor head was excited by a tunable Er-doped fiber ring laser to produce an absorption spectroscopic gas sensor sensitive to methanol, methane and ammonia. The Er-doped fiber ring laser can be tuned to a wavelength within the C-band; therefore, the absorption spectra of the transition lines of multiple gases can be monitored. The benefit of this excitation strategy is that during the gas absorption processing only a single tunable laser source is required. Good sensitivity is achieved; for example, for NH3 up to 17.3 nW/ppm with no cross-sensitivity to other gases. The system is not adequately sensitive at high gas concentrations.

References

Birks, T. A., Russell, P. S. J., Couny, F., Knight, J. C., & Benabid, F. (2005). Compact, stable and efficient all-fibre gas cells using hollow-core photonic crystal fibres. *Nature, 434*(7032), 488–491.

Bise, R. T., & Trevor, D. J. (2004). *Surface absorption in microstructured optical fibers, 2004* (pp. 716) IEEE.

Boisdé, G., & Harmer, A. (1996). *Chemical and biochemical sensing with optical fibers and waveguides.* Boston [u.a.]: Artech House.

Couny, F., Benabid, F., & Light, P. S. (2007). Subwatt threshold cw Raman fiber-gas laser based on H2-filled hollow-core photonic crystal fiber. *Physical Review Letters, 99*(14), 143903.

He, Z., Tian, F., Zhu, Y., Lavlinskaia, N., & Du, H. (2011). Long-period gratings in photonic crystal fiber as an optofluidic label-free biosensor. *Biosensors & Bioelectronics, 26*(12), 4774–4778.

Jensen, J. B., Pedersen, L. H., Carlsen, A., Hoiby, P. E., Nielsen, L. B., & Biarklev, A., et al. (2003). *Photonic crystal fiber based evanescent-wave sensor for detection of biomolecules in aqueous solutions, 2003* (pp. 760–762) IEEE.

Martin, P. A. (2002). Near-infrared diode laser spectroscopy in chemical process and environmental air monitoring. *Chemical Society Reviews, 31*(4), 21.

Muhammad, F. A., Stewart, G., & Jin, W. (1993). Sensitivity enhancement of D-fibre methane gas sensor using high-index overlay. *IEE Proceedings J Optoelectronics, 140*(2), 115.

Polynkin, P., Polynkin, A., Peyghambarian, N., & Mansuripur, M. (2005). Evanescent field-based optical fiber sensing device for measuring the refractive index of liquids in microfluidic channels. *Optics Letters, 30*(11), 1273–1275.

Pristinski, D., & Du, H. (2006). Solid-core photonic crystal fiber as a Raman spectroscopy platform with a silica core as an internal reference. *Optics Letters, 31*(22), 3246–3248.

Sazio, P. J. A., Amezcua-Correa, A., Finlayson, C. E., Hayes, J. R., Scheidemantel, T. J., Baril, N. F., et al. (2006). Microstructured optical fibers as high-pressure microfluidic reactors. *Science, 311* (5767), 1583–1586.

Tian, F., He, Z., & Du, H. (2012a). Numerical and experimental investigation of long-period gratings in photonic crystal fiber for refractive index sensing of gas media. *Optics Letters, 37*(3), 380.

Tian, F., Kanka, J., & Du, H. (2012b). Long-period grating and its cascaded counterpart in photonic crystal fiber for gas phase measurement. *Optics Express, 20*(19), 20951.

Webber, M. E., Baer, D. S., & Hanson, R. K. (2001). Ammonia monitoring near 1.5 μm with diode-laser absorption sensors. *Applied Optics, 40*(12), 2031–2042.

Weidmann, D., Kosterev, A., Tittel, F. K., Ryan, N., & McDonald, D. (2004). Application of a widely electrically tunable diode laser to chemical gas sensing with quartz-enhanced photoacoustic spectroscopy. *Optics Letters, 29*(16), 1837–1839.

Werle, P., Mücke, R., D´AMATO, F., & LANCIA, T. (1998). Near-infrared trace-gas sensors based on room-temperature diode lasers. *Applied Physics B Lasers and Optics, 67*(3), 307–315.

Zheng, S. (2015). Long-period fiber grating moisture sensor with nano-structured coatings for structural health monitoring. *Structural Health Monitoring, 14*(2), 148–157.

Zheng, S., Shan, B., Ghandehari, M., & Ou, J. (2015). Sensitivity characterization of cladding modes in long-period gratings photonic crystal fiber for structural health monitoring. *Measurement, 72,* 43–51.

Zheng, S., Zhu, Y., & Krishnaswamy, S. (2013). Fiber humidity sensors with high sensitivity and selectivity based on interior nanofilm-coated photonic crystal fiber long-period gratings. *Sensors and Actuators B: Chemical, 176,* 264–274.

Zhou, X., Liu, X., Jeffries, J. B., & Hanson, R. K. (2003). Development of a sensor for temperature and water concentration in combustion gases using a single tunable diode laser. *Measurement Science & Technology, 14*(8), 1459–1468.

Zhu, Y., He, Z., Kaňka, J., & Du, H. (2008). Numerical analysis of refractive index sensitivity of long-period gratings in photonic crystal fiber. *Sensors & Actuators: B. Chemical, 129*(1), 99–105.

Part VI
Imaging Degradation in Materials

Chapter 16
Full Field Imaging of High pH Levels in Concrete

Masoud Ghandehari, Engui Liu, Christian Brückner, Gamal Khalil, Jill Worlinsky and Michael Hyland

Abstract In this chapter we discuss an optical method used for direct measurement of pH in Portland cement concrete with high spatial and temporal resolution. This approach is designed to better enable the study and analysis of high pH dependent degradation reactions, and hydration reaction in cement-based composites. We demonstrate that the halochromic sensor molecule is suitable for this purpose. Results of experiments showing spatial distribution of early stage carbonation and reaction involving silica aggregates are highlighted at pH levels between ~11.0 to ~13.5. Results are compared with the commercially available pH indicator Phenolphthalein.

16.1 Introduction

Deleterious chemical reactions cause the premature degradation of concrete and account for the deterioration of roads, bridges, dams, levees and other infrastructure. One of the primary mechanisms of distress in concrete takes place because of reactions when a high level of pH is present. This includes alkali-silica reaction (ASR) and carbonation in concrete.

M. Ghandehari (✉)
New York University, Six Metrotech Center, Brooklyn, NY 11201, USA
e-mail: masoud@nyu.edu

E. Liu
New York University Abu Dhabi, PO Box 129188, Abu Dhabi, UAE
e-mail: engui.liu@nyu.edu

C. Brückner · J. Worlinsky · M. Hyland
Department of Chemistry, University of Connecticut, Storrs, CT 06269, USA
e-mail: c.bruckner@uconn.edu

G. Khalil
Department of Aeronautics & Astronautics, University of Washington,
Box 352250, Seattle, WA 98195, USA
e-mail: gekhalil@gmail.com

M. Ghandehari, *Optical Phenomenology and Applications*,
Smart Sensors, Measurement and Instrumentation 28,
https://doi.org/10.1007/978-3-319-70715-0_16

ASR is a deleterious reaction that takes place between the highly alkaline cement paste matrix and the silica based aggregates. These reactions ultimately result in the cracking of concrete (Taylor 1987). ASR is recognized as a serious durability problem, and the research publications devoted to this topic have been numerous. (FHWA 2017; Eskridge et al. 2009; Fraay et al. 1989; Malvar et al. 2002; ASTM Intl. 2015; Lindgård et al. 2012; Latifee 2016). There have also been a number of laboratory studies focusing on carbonated cement paste and concrete particularly to evaluate the pH induced corrosion of reinforced concrete (Timcakova et al. 2015; Ferrer et al. 2016; Lollini et al. 2012; Kulakowski et al. 2009).

Carbonation is the process by which the concrete becomes less alkaline as a result of exposure to an environment that is more acidic than the concrete material itself. This includes the normal exposure to the highly acidic environments in urban and industrial settings (i.e. acid rain) (Ahmad 2003; Hobbs 2001; Parrott 1994). When reaching the depth of steel reinforcing bars, it leads to the onset of steel corrosion. Accelerated levels of steel oxidation lead to advanced corrosion and dissolution of the steel rebar surface. This is also an expansive reaction, one that leads to the cracking of the surrounding concrete (Parrott 1994). In both the ASR and carbonation process, the pH gradients and fluxes play an important role in initiating and propagating the deleterious reactions, leading to physical damage.

While not covered in this chapter, the measurement of high pH level is also useful for studying fresh concrete. pH levels impact the rate of cement hydration, influence the morphology of the crystalline and amorphous products of cement hydrates, and ultimately affect the strength and durability of concrete structures (Sobhnamayan et al. 2014; Younsi et al. 2013, Yingli et al. 2013).

The current practice for spatial mapping of the pH profile in concrete is accomplished using the pH indicator Phenolphthalein (PHPHT), which is applied as a spray onto a newly fractured concrete surface. The resulting map appears in a magenta color for areas above $\sim$pH 10, versus the concrete native color for areas below pH 10 (Parrott and Killoh 1989; Parrott 1987; Liu et al. 2004). The magenta color at high pH discussed in Sect. 16.4.3 is a result of the optical absorption of the molecular indicator at a wavelength centered at approximately 550 nm (Fig. 16.1a). This is somewhat of a binary shift in response at $\sim$pH 10 (Fig. 16.1c) and poses limitations on the analysis of the early determination of carbonation that typically occurs between pH 10–13.5. PHPHT provides an indication of pH presence below or above pH 10, however does not provide the more granular data for pH levels over 11, needed for the study of early concrete carbonation and its properties.

A number of alternative approaches for the measurement of pH in concrete have been reported. These include fiber optic pH sensors based on pH-sensitive dyes embedded in a polymer matrix (Nguyen et al. 2014; Blumentritt et al. 2008), metal/metal oxide pH electrodes (Du et al. 2006), and water-leaching of powdered concrete (Räsänen and Penttala 2004). These methods each provide specific data and each have some shortcomings; for instance, in the case of optical fibers, the sensors or electrodes provide time-resolved information, but only at the sensor point (Nguyen et al. 2014), while the approach involving water leachate of the powdered

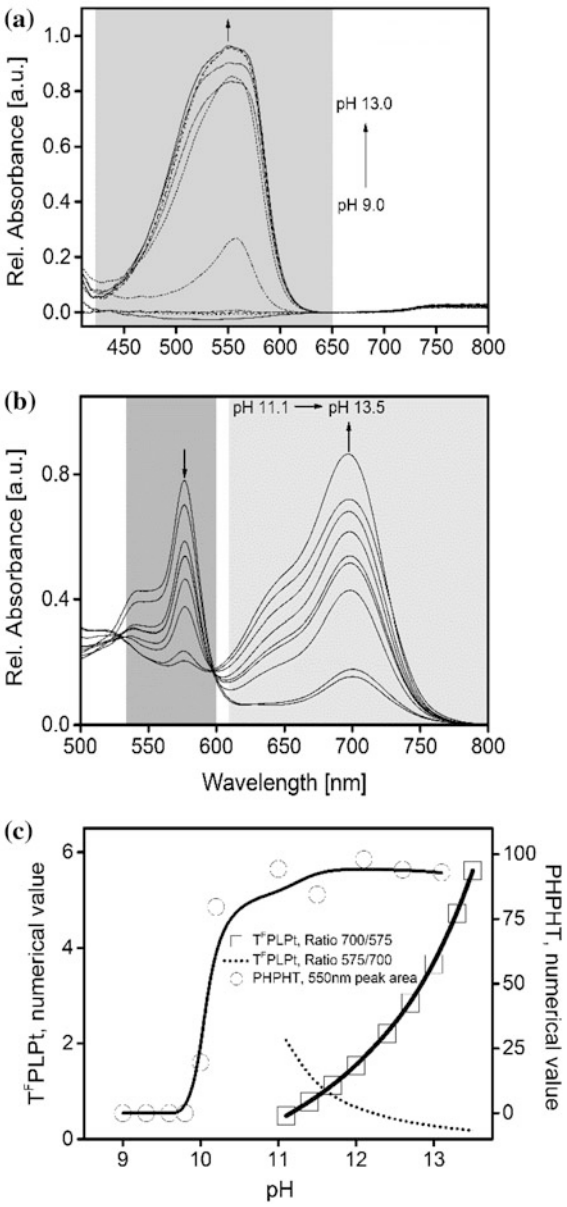

Fig. 16.1 **a** Titration of **PHPHT** and optical absorption measurement; the shaded area indicates the wavelength range (425–650 nm) for integration of area under absorption curve used for calibration show in Fig. 16.1c. **b** Same titration for **T^{F}PLPt**; the shaded areas (regions 537–600 nm and 612–800 nm, respectively) were used for the calibration curve shown in **c**

concrete provides only indirect, and spatially averaged pH readings (Räsänen and Penttala 2004). In the case of techniques for mapping pH levels, a limited number of halochromic dyes are available that are sensitive in the high pH range (Derinkuyu et al. 2007; Ensafi and Kazemzadeh 1999; Werner and Wolfbeis 1993; Safavi and Sadeghi 2007; Safavi and Abdollahi 1998).

16.2 Materials

16.2.1 Sensor Compound

In this study we use a porphyrinoid high-pH indicator, porpholactone platinum(II) complex **T^{F}PLPt** (Khalil et al. 2010), shown to possess a rare dynamic range between ~pH 11 and 13. It is chemically robust and highly specific for OH^- and alkoxide ions even in conditions of high salinity (Worlinsky et al. 2014). While the indicator is also sensitive to cyanide, CN^- (Worlinsky et al. 2014), cyanide is generally not expected in concrete. An attractive feature of the proposed formulation is the possibility of tuning the indicator's dynamic range (Worlinsky et al. 2013). The indicator can also be made water-soluble by means of a derivation of the pentafluorophenyl groups, and/or incorporated into sensor membranes (Worlinsky et al. 2014, 2015). Moreover—and crucial for practical application to mapping pH levels in concrete—this indicator possesses very high extinction values, requiring only small amounts of the indicator for sensitive measurements. Lastly, the two optical absorption wavelengths specific for the neutral and base form of the indicator (Fig. 16.1b) are separated by 125 nm (Khalil et al. 2010; Worlinsky et al. 2013), enabling the separation of the acidic and basic states of the indicator.

Porphyrinoid ([*meso*-tetrakis(pentafluoro-phenyl)porpholactonato]platinum(II), **T^{F}PLPt**; MW = 1195 g/mol) was prepared as described in 2015 by Worlinsky, building on the previous work (Khalil et al. 2010; Worlinsky et al. 2013, 2014, 2015; Gouterman et al. 1989; Yu et al. 2012; Brückner et al. 2012). The concentration of **T^{F}PLPt** in the DMSO stock solution used for the calibrations in homogenous aqueous solutions was 0.4×10^{-3} M (0.48 mg/mL). The concentration of **T^{F}PLPt** in the aqueous hydrophilic polymer solution of DMSO (99.9%)/PVA (Polyvinyl alcohol, average M_w = 31,000)/Culminal C9115 (a nonionic cellulose ether, HPMC, hydroxypropyl methylcellulose)/Cremophor EL® (a synthetic, nonionic polyethoxylated castor oil-based surfactant), weight ratio 5/30/1/4, used for the mapping experiments on concrete surfaces was 0.4×10^{-3} M (0.48 mg/mL). The phenolphthalein (PHPHT) stock solution was 0.1% (w/w) PHPHT in 70% aqueous isopropyl alcohol. The simulated concrete pore solution was prepared by dissolving $Ca(OH)_2$, NaOH, and KOH in deionized water. The $[K^+]$ was 0.4 M, $[Na^+]$ was 0.2 M, and the $[Ca^{2+}]$ was approximately 1.0 M; and the $[OH^-]$ balances the sum of the alkali concentrations at about 0.6 M Diamond (1981). We adjusted the pH levels ranging from pH 13.5 down to pH 8.0 using aqueous Hydrochloric acid (HCl).

To map the pH distribution on fractured concrete surfaces using a sensor compound containing **T^{F}PLPt,** the sensor compound was calibrated in simulated concrete pore solutions at different pH levels from pH 11.0 to 13.5. The solution phase analysis which was done using a spectrometer was repeated using a digital camera. The ratio of intensities corresponding to two optical absorption bands was used for calculation of pH at each pixel. This imaging procedure was then repeated for hardened concrete. The sensor molecule was dissolved in a hydrophilic polymer and applied onto newly fractured concrete surfaces and a ratio-metric imaging procedure was carried out for mapping the pH level.

16.3 Methods

Figure 16.2 shows the experimental set up used to analyze the response of the sensor molecule in concrete pore solution at various pH levels, and the set up for imaging concrete surfaces after application of the sensor molecule.

16.3.1 Solution Phase Calibration Using Transmittance Spectroscopy

In order to gauge the sensitivity of the indicator in typical concrete pore water environment the optical response in simulated pore solutions were measured. 2 mL of simulated concrete pore solution was added at various pH levels to 0.2 mL sensor solution (for **T^{F}PLPt** and PHPHT) and placed in an acrylic cuvette (Fig. 16.3). The

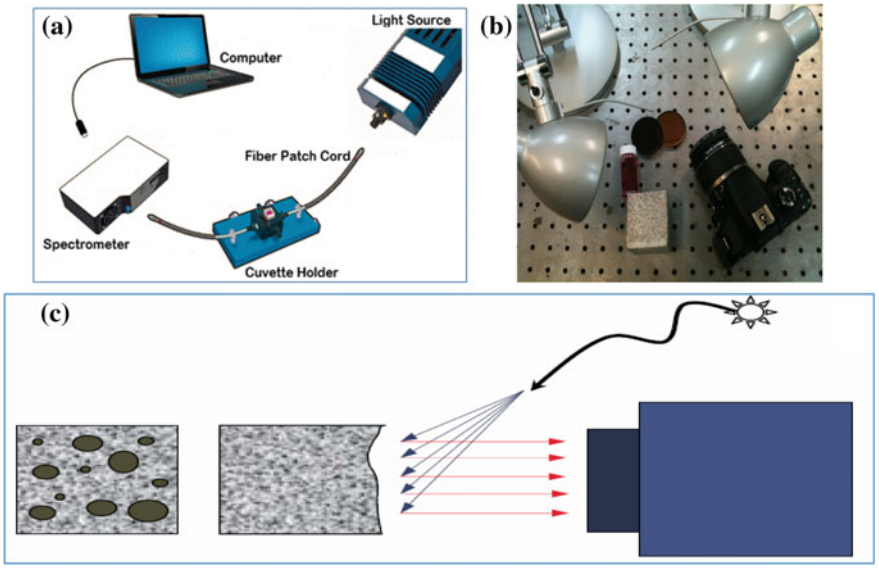

Fig. 16.2 **a** Experimental set-up for a spectrometer, light source and cuvette holder for transmission measurement, **b** camera, filters, and sample concrete specimen for imaging, **c** schematic shown imaging of diffuse reflectance from concrete samples

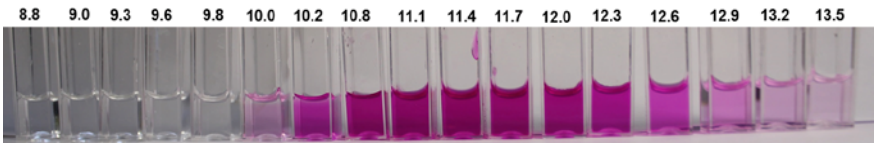

Fig. 16.3 Cuvettes with PHPHT sensor in simulated concrete pore solution at various pH levels

absorbance spectra of each sample were subsequently recorded in transmission mode using a spectrometer and a tungsten halogen light source shown in Fig. 16.2a. Results are shown in Fig. 16.1a for PHPHT and in Fig. 16.1b for **T^{F}PLPt**.

16.3.2 Optical Imaging of Pore Solution and Solid Concrete Surfaces

Corresponding measurements using optical imaging were also carried out (Fig. 16.2). This was done using a digital single lens camera (DSLR—Canon EOS 550D, with 5300 × 3500 pixel density), outfitted with two 575 and 700 nm band-pass filters (Andover Corporation, model 570FS10-50, 575 nm; and 700FS80-50, 700 nm). Concrete surfaces were obtained by cracking pre-notched concrete prisms (Fig. 16.4), was illuminated with two 55 W Xenon lamps and scattered light (Fig. 16.2c) was collected after passing through the band pass filter. MATLAB software was used to process the image data. This involved reading the raw digital images (JPEG format) recorded with each of the two filters, followed by numerical calculations of ratio of the integrated intensity values at each pixel.

16.3.3 Cement Paste and Mortar Sample Preparation

Portland cement Type I (Table 16.1) with alkali content 1.01% (Na_2O equivalent) was used for the preparation of the mortar and cement paste specimens. Cement paste samples were prepared at normal and low pH levels. The low-pH cement paste samples were prepared by partially replacing the Portland cement with micro-silica fume powder (Elkem micro-silica grade 900 W), the low pH mixture

Fig. 16.4 Images of bar samples after and before degradation, showing location of notches where the

Table 16.1 Chemical analysis of Type I Portland cement

Item	SiO_2	Al_2O_3	Fe_2O_3	CaO	MgO	SO_3	CO_2	$CaCO_3$	I.L.	NaEq
(%)	18.10	5.90	2.50	61.30	2.50	4.50	1.30	3.30	2.70	1.01

Table 16.2 Chemical analysis of recycled glass aggregate

Item	SiO_2	Al_2O_3	K_2O, Na_2O	CaO, MgO	SO_3	Fe_2O_3
(%)	73.40	1.80	13.80	10.70	0.22	0.05

had a water to cementitious materials (cement + 30% micro-silica) ratio of 0.50. The same water/cement ratio was used for the cement paste mixture with normal pH. Mortar samples were also used. These were prepared using recycled glass in order to simulate Alkali-Silica Reactions. The glass was obtained from crushed clear bottles with grading of U.S. Standard Sieve #8-#16 (coarse), and #50-#100 (fine) (Table 16.2). The mortar material composition included an aggregate to cement weight ratio of 3:1, coarse to fine glass aggregate weight ratio of 2:1, and water to cement ratio of 0.67. A high shear stand mixer was used for mortar and cement paste mixing, following ASTM C305-14.

Casting of all samples (Fig. 16.4) was done using a mold with dimensions 2″ × 3″ × 12″. Curing was done using a concrete curing chamber at 23 °C and a relative humidity of 90%. The accelerated carbonation experiments were done in a 15 bar pressure plate extractor (Model 1500, Soil Moisture Equipment Corp.) at 23 °C and a relative humidity of 60%. After casting and curing, the mortar and cement paste bars were mechanically fractured along precast notches (Fig. 16.4). The fractured surfaces were not exposed to any other treatment and were immediately treated with the sensing compounds (PHPHT or **T^FPLPt)** and imaged. Both sides of the fracture cross section were used, one side for each of the two sensing compounds, insuring that the same location in the sample is being compared.

16.4 Results and Discussion

16.4.1 Spectral Analysis of the T^FPLPt Sensor Compound in Solution Phase

T^FPLPt has a strong and rapid response in high pH environments, and it is readily detectable at visible wavelengths (Khalil et al. 2010; Worlinsky et al. 2015). A bright pink form of the neutral sensor (present up to pH 10.5) gradually changes to a forest-green form of the sensor at pH 13.5.

The optical response of this sensor molecule is due to a nucleophilic attack of OH^- on the lactone moiety that changes the metalloporphyrin-type of the neutral sensor to a metallochlorin-type (Khalil et al. 2010). The corresponding halochromic

response is insensitive to the high ionic strength of the simulated pore solutions, as the titration curve of this sensor under high ionic strength conditions is very similar to that in low ionic strength aqueous solutions (Khalil et al. 2010). Meanwhile, the wide spectral separation of the diminishing peak at 575 nm, corresponding to the neutral sensor, and the appearing peak at 700 nm, indicative for the basic species, is clearly identifiable.

16.4.2 Imaging of T^FPLPt in Solution

The objective of this study was to develop an imaging approach to map the spatial variation of pH levels on fractured concrete surfaces. Thus, we had to replicate the ratiometric pH calibration commonly practiced in a solution phase and in transmission mode through a cuvette (Figs. 16.2a and 16.3) to a diffuse reflectance mode for concrete surfaces (Fig. 16.2c). Therefore, instead of using a spectrometer, we recorded two images with a digital single lens camera (DSLR) shown in Fig. 16.2b. Unlike a spectrometer which records the full absorbance spectrum of the indicator in a solution, a broad band imager—such as the DSLR –records the intensity of all wavelengths at same time. To allow a quantitative differentiation of the color intensities of the high/low pH species, the DSLR was outfitted with two band pass filters in front of the lens: a green band pass filter center at 575 nm (transmitting from ~540 to 600 nm) and a red band pass filter centered at 700 nm (transmitting from ~610 to 800 nm). These filters were selected to match the **T^FPLPt** absorption peaks. The wavelength covered by these filters is shown superimposed on the absorption spectra of indictor in Fig. 16.1b. Imaging was first carried out on the same cuvettes where the spectra was measured, and the ratio of the integrated intensities of the two filtered images recorded for the sensor molecule in the simulated concrete pore solution at different pH values were measured. Results are shown by the solid squares in Fig. 16.5. This was used as a calibration curve, similar to the ratio-metric calculations done with the spectrometer data. The numerical value of the intensity ratios at the two wavelengths at each pixel would consequently represent a pH value.

16.4.3 Imaging of T^FPLPt on Hardened Cement Paste

Regular hydrated cement paste has pH of ~13.4 (Longuet et al. 1973; Barneyback and Diamond 1981) and low-pH cement paste (cement with 30% silica fume replacement) has pH of ~12.4 (Diamond 1983; Byfors 1987). Cement bars were prepared with regular cement paste and low-pH cement paste, cured and split along pre-cast notches (Fig. 16.4). The newly fractured surfaces were immediately coated

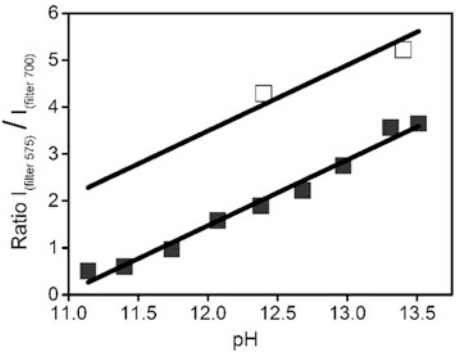

Fig. 16.5 pH versus ratio of the camera recorded intensities of reflected light after passing through the filters ($I_{(filter\ 575)}/I_{(filter\ 700)}$) (bottom trace, solid squares) **T^{F}PLPt** in simulated concrete pore solutions in cuvette; (top trace, hollow squares) **T^{F}PLPt** in a hydrophilic polymer formulation applied on solid concrete surfaces for low pH and normal pH cement paste samples. Experimental data shown in Fig. 16.6 and calculation results shown in Fig. 16.7 were used to obtain the two data points

with the hydrophilic, polymer based solution of **T^{F}PLPt** (0.4×10^{-3} M). The initially red solution turned green and achieved its equilibrium color within minutes, at which time images were collected. The mirror image surface across the fracture was coated with PHPHT for comparison. Comparison of the two surfaces with the two indicators is shown in Fig. 16.6.

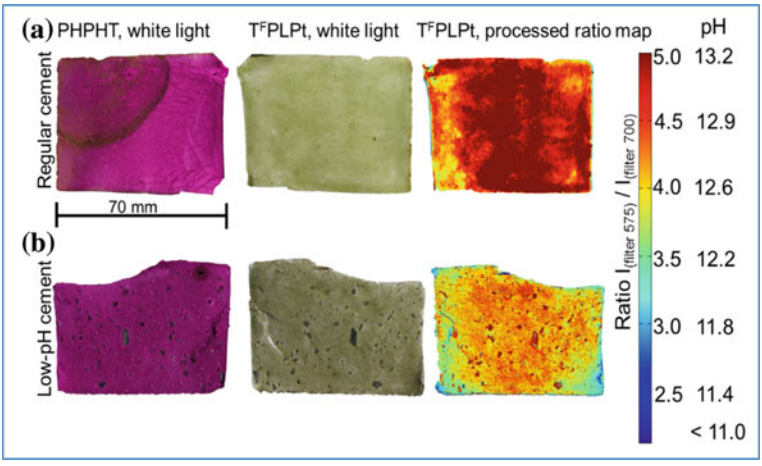

Fig. 16.6 Images of freshly fractured surfaces of cement bar specimens after application of PHPHT (left column) and **T^{F}PLPt** sensor dyes (middle column). The right column shows the processed ratio map of the middle image. **a** Regular cement paste; **b** Low-pH cement paste

16.4.4 Mapping PH Levels in Cured Cement and Mortar Samples After Accelerated Degradation

Further investigations were carried out using mortar samples containing glass aggregate (Figs. 16.7 and 16.8). The pH drop in the glass aggregate samples was more severe than observed in the cement paste sample under nearly similar conditions. According to the PHPHT map, the sample edges for both exposure times of 45 days and 90 days dropped below ~pH 10. **T^{F}PLPt** is unable to map those areas but can resolve the areas with a pH higher than 11. There are two reasons for the more severe drop of the glass aggregate concrete. Firstly, the samples had a

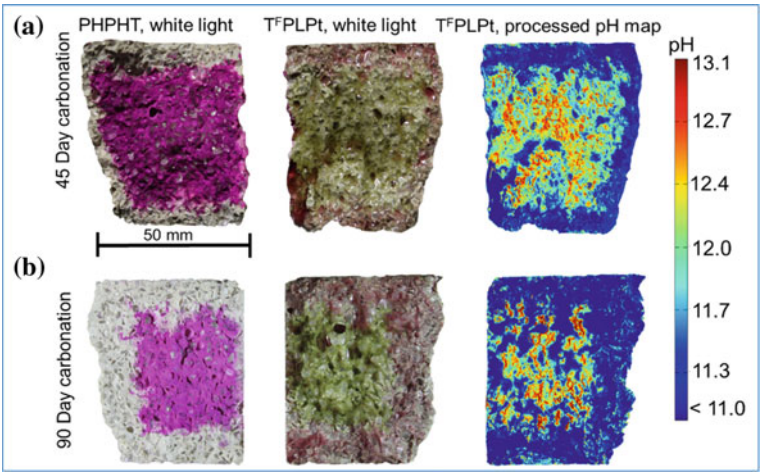

Fig. 16.7 Mortar specimens with Portland cement and recycled glass aggregates after accelerated degradation and application of pH sensors: (left column) PHPHT, (middle column) T^{F}PLPt sensor. Right column shows the pH map post-processed after band pass filtering

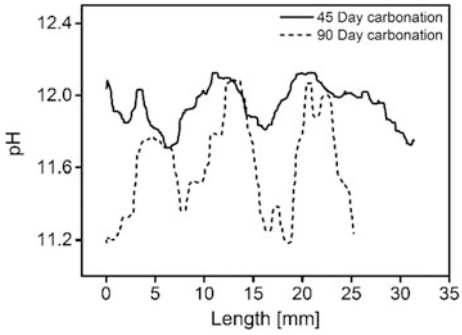

Fig. 16.8 Plot of pH variations along a horizontal line through the center line of the glass aggregate mortar specimen data from Fig. 16.7 (right column)

higher water to cement ratio (w/c 0.67 versus 0.5), and were therefore more porous and permeable. Secondly, glass aggregates lead to ASR, lowering the pH level.

In the case of the PHPHT coated samples, the uniform fuchsia color on both samples indicates pH greater than ~pH 10, but PHPHT is unable to resolve higher pH levels. The pH map of the **T^{F}PLPt** coated surface is designed to resolve the pH level of those areas with pH higher than ~ pH10. A complete review of the chemical and photo-stability of the sensor dye was tested and published (Khalil 2004).

It should be pointed out that while **T^{F}PLPt** has a good dynamic range between pH 11 and 13.5, it has low sensitivity to pH levels below pH 11. Meanwhile PHPHT delineates a shift at pH 10 with some distinction for pH levels between pH 9.75 to 10.25. Therefore, there is an information gap between ~pH 10 and 11. The dynamic range of single-site halochromic sensors is inherently limited, but there is some possibility of tuning (Derinkuyu et al. 2007; Safavi and Abdollahi 1998; Safavi and Sadeghi 2007; Ensafi and Kazemzadeh 1999; Werner and Wolfbeis 1993). We have also reported the fine-tuning of the halochromic response profile of metalloporpholactone-based sensors (Worlinsky et al. 2013), allowing the selection of the appropriate derivative for the imaging range desired. This may be further developed to extend the lower boundaries of the proposed sensing compound down to approximately pH 10.

16.5 Conclusions

The halochromic sensor **T^{F}PLPt** is suitable for the mapping of high pH levels ranging from pH ~11.0 to ~13.5, with potential applications in understanding early stages of carbonation and ASR-related phenomena. The optical response of the sensor allows for ratio-metric measurement, making the analysis invariant to external sources such as the indicator concentration, greatly facilitating its application. The method shown is technically robust, involving a white light source, a commercial grade camera, and two optical filters. Tests were carried out on hardened cement paste with low pH and normal cement, as well as glass aggregate concrete samples subject to accelerated degradation by carbonation. These samples were used to demonstrate the utility of the proposed approach for mapping the spatial distribution of the pH at a fine dynamic range of pH and spatial resolution. We anticipate that this will contribute to a better understanding of alkali aggregate reactivity, the extent and rate of carbonation, and remedial actions such as the role of supplementary cementitious materials in degradation processes in concrete.

References

Ahmad, S. (2003). Reinforcement corrosion in concrete structures, its monitoring and service life prediction—a review. *Cement & Concrete Composites, 25*(4), 459–471.

ASTM Intl. (2015). *Standard test method for determination of length change of concrete due to Alkali-Silica reaction.* West Conshohocken, PA: ASTM C1293–08b.

Barneyback, R. S., & Diamond, S. (1981). Expression and analysis of pore fluids from hardened cement pastes and mortars. *Cement and Concrete Research, 11*(2), 279–285.

Blumentritt, M., Melhorn, K., Flachsbarth, J., Kroener, M., Kowalsky, W., & Johannes, H. (2008). A novel fabrication method of fiber-optical planar transmission sensors for monitoring pH in concrete structures. *Sensors & Actuators: B. Chemical, 131*(2), 504–508.

Brückner, C., Ogikubo, J., McCarthy, J. R., Akhigbe, J., Hyland, M. A., Daddario, P., et al. (2012). Meso-arylporpholactones and their reduction products. *The Journal of organic chemistry, 77*(15), 6480–6494.

Byfors, K. (1987). Influence of silica fume and flyash on chloride diffusion and pH values in cement paste. *Cement and Concrete Research, 17*(1), 115–130.

Derinkuyu, S., Ertekin, K., Oter, O., Denizalti, S., & Cetinkaya, E. (2007). Fiber optic pH sensing with long wavelength excitable Schiff bases in the pH range of 7.0–12.0. *Analytica Chimica Acta, 588*(1), 42–49.

Diamond, S. (1981). Effects of two Danish flyashes on alkali contents of pore solutions of cement-flyash pastes. *Cement and Concrete Research*, *11*, 383–393.

Diamond, S. (1983). Effects of microsilica (silica fume) on pore-solution chemistry of cement pastes. *Journal of the American Ceramic Society,* **66**, pp. C82–84.

Du, R., Hu, R., Huang, R., & Lin, C. (2006). In situ measurement of Cl- concentrations and pH at the reinforcing steel/concrete interface by combination sensors. *Analytical Chemistry, 78*(9), 3179–3185.

Ensafi, A. A., & Kazemzadeh, A. (1999). Optical pH sensor based on chemical modification of polymer film. *Microchemical Journal, 63*(3), 381–388.

Eskridge, A. E., Klahorst, J. T., Klingner, R. E., & Kreger, M. E. (2009). Mitigation techniques for structures with premature concrete deterioration due to ASR/DEF. *ACI Materials Journal, 106* (3), 273.

Ferrer, B., Bogas, J. A., & Real, S. (2016). Service life of structural lightweight aggregate concrete under carbonation-induced corrosion. *Construction and Building Materials, 120,* 161–171.

FHWA. (2017-last update). ASR reference center, Available: https://www.fhwa.dot.gov/pavement/concrete/asr/reference.cfm.

Fraay, A. L. A., Bijen, J. M., & de Haan, Y. M. (1989). The reaction of fly ash in concrete a critical examination. *Cement and Concrete Research, 19*(2), 235–246.

Gouterman, M., Hall, R. J., Khalil, G. E., Martin, P. C., Shankland, E. G., & Cerny, R. L. (1989). Tetrakis(pentafluorophenyl)porpholactone. *Journal of the American Chemical Society, 111* (10), 3702–3707.

Hobbs, D. W. (2001). Concrete deterioration: Causes, diagnosis, and minimizing risk. *International Materials Reviews, 46*(3), 117–144.

Khalil, G. (2004). Dual-luminophor pressure-sensitive paint I. Ratio of reference to sensor giving a small temperature dependency. *Sensors and Actuators B: Chemical, 97*(1), 13–21.

Khalil, G. E., Daddario, P., Lau, K. S. F., Imtiaz, S., King, M., Gouterman, M., et al. (2010). Meso-Tetraarylporpholactones as high pH sensors. *The Analyst, 135*(8), 2125.

Kulakowski, M. P., Pereira, F. M., & Molin, D. C. C. D. (2009). Carbonation-induced reinforcement corrosion in silica fume concrete. *Construction and Building Materials, 23*(3), 1189–1195.

Latifee, E. R. (2016). State-of-the-Art report on alkali silica reactivity mitigation effectiveness using different types of fly ashes. *Journal of Materials, 2016,* 1–7.

Lindgård, J., ANDIÇ-ÇAKIR, Ö., FERNANDES, I., RØNNING, T. F., & THOMAS, M. D. A. (2012). Alkali–silica reactions (ASR): Literature review on parameters influencing laboratory performance testing. *Cement and Concrete Research, 42*(2), 223–243.

Liu, S., Wu, X., Chen, P., & Zhang, J. (2004). Complexity of phenolphthalein changing colors in acidic solution and basic solution. *Journal of Anqing Teachers College (Natural Science), 10,* 63–65.

Lollini, F., Redaelli, E., & Bertolini, L. (2012). Analysis of the parameters affecting probabilistic predictions of initiation time for carbonation-induced corrosion of reinforced concrete structures. *Materials and Corrosion, 63*(12), 1059.

Longuet, P., Burglen, A., & Zelwer, A. (1973). The liquid phase of hydrated cement. *Revue des Materiaux de Construction, 676,* 35–41.

Malvar, L. J., Cline, G. D., Rollings, R., Sherman, T. W., Greene, J., & Burke, D. (2002). Alkali-silica reaction mitigation: State of the art and recommendations. *Materials Journal, 99* (5), 480–489.

Nguyen, T. H., Venugopala, T., Chen, S., Sun, T., Grattan, K. T. V., Taylor, S. E., et al. (2014). Fluorescence based fibre optic pH sensor for the pH 10–13 range suitable for corrosion monitoring in concrete structures. *Sensors and Actuators B: Chemical, 191,* 498–507.

Parrott, L J. (1987). *A review of carbonation in reinforced concrete.* Cement and Concrete Association.

Parrott, L. J. (1994). A study of carbonation-induced corrosion. *Magazine of Concrete Research, 46*(166), 23–28.

Parrott, L. J., & Killoh, D. C. (1989). Carbonation in a 36 year old, in-situ concrete. *Cement and Concrete Research, 19*(4), 649–656.

Räsänen, V., & Penttala, V. (2004). The pH measurement of concrete and smoothing mortar using a concrete powder suspension. *Cement and Concrete Research, 34*(5), 813–820.

Safavi, A., & Abdollahi, H. (1998). Optical sensor for high pH values. *Analytica Chimica Acta, 367*(1), 167–173.

Safavi, A., & Sadeghi, M. (2007). Development of an optode membrane for high pH values. *Spectrochimica Acta Part A: Molecular and Biomolecular Spectroscopy, 66*(3), 575–577.

Sobhnamayan, F., Sahebi, S., Alborzi, A., Ghorbani, S., & Shojaee, N. S. (2014). Effect of different pH values on the compressive strength of calcium-enriched mixture cement. *Iranian Endodontic Journal, 10*(1), 26–29.

Taylor, H. F. W. (1987). A method for predicting alkali ion concentrations in cement pore solutions. *Advances in Cement Research, 1*(1), 5–17.

Timcakova, K., Stefkova, D., & Chobola, Z. (2015). Determination of the influence of carbonation of concrete and corrosion of steel on reinforced concrete condition. *Advanced Materials Research, 1124,* 225.

Werner, T., & Wolfbeis, O. S. (1993). Optical sensor for the pH 10–13 range using a new support material. *Fresenius' Journal of Analytical Chemistry, 346*(6–9), 564–568.

Worlinsky, J. L., Halepas, S., & Brückner, C. (2014). PEGylated meso-arylporpholactone metal complexes as optical cyanide sensors in water. *Organic & Biomolecular Chemistry, 12*(23), 3991–4001.

Worlinsky, J. L., Halepas, S., Ghandehari, M., Khalil, G., & Brückner, C. (2015). High pH sensing with water-soluble porpholactone derivatives and their incorporation into a Nafion® optode membrane. *The Analyst, 140*(1), 190–196.

Worlinsky, J. L., Zarate, G., Zeller, M., Ghandehari, M., Khalil, G., & Brückner, C. (2013). Oxazolochlorins 11: Tuning the dynamic high pH sensing range of meso-tetraarylporpholactonato]M(II) complexes by variation of the central metal ion, the aryl substituents, and introduction of a β-nitro group. *Journal of Porphyrins and Phthalocyanines, 17*(08), 836–849.

Yingli, G., Ling, C., Zheming, G., & Shiying, G. (2013). Effects of different mineral admixtures on carbonation resistance of lightweight aggregate concrete. *Construction and Building Materials, 43,* 506–510.

Younsi, A., Turcry, P., Aït-Mokhtar, A., & Staquet, S. (2013). Accelerated carbonation of concrete with high content of mineral additions: Effect of interactions between hydration and drying. *Cement and Concrete Research, 43,* 25–33.

Yu, Y., Lv, H., Ke, X., Yang, B., & Zhang, J. (2012). Ruthenium-catalyzed oxidation of the porphyrin β, β′-pyrrolic ring: A general and efficient approach to porpholactones. *Advanced Synthesis & Catalysis, 354*(18), 3509–3516.

Chapter 17
Phase Measurement Interferometry for Mapping Fracture

Masoud Ghandehari, Sridhar Krishnaswamy and Surendra Shah

Abstract Phase Measurement Interferometry is introduced as an effective approach for the process of measuring crack growth in concrete. The particular mode of cracking of concrete highlighted in this chapter is caused by composite action between reinforcing bars and concrete. The influence of specimen cross-section size and geometry on the interface stresses and bond slip is evaluated. The measured crack length and crack opening and a finite element material model are used in a hybrid experimental/numerical approach to evaluate the unknown normal component of traction at the interface of concrete and rebar.

17.1 Introduction

The interface shear stress and the associated relative tangential displacement between the steel rebar and concrete have been termed "bond" and "slip" respectively. Due to the material stiffness and strength mismatch and the relatively poor tensile strength of concrete, the interaction of the two materials leads to the cracking of concrete. Considerable effort has been made to understand the cracking of reinforced concrete. This includes research to predict the bond capacity of embedded reinforcing bars (Shah et al. 1995; Lutz and Gergely 1967).

Bond induced tensile cracking of concrete is classified in two main categories. When the rebar axis is in the plane of fracture, the crack is called "longitudinal", and when the rebar axis passes through the fracture plane it is called "transverse". The relative development of the shear stress τ and normal stress σ is an important factor

M. Ghandehari (✉)
New York University, Six Metrotech Center, Brooklyn, NY 11201, USA
e-mail: masoud@nyu.edu

S. Krishnaswamy · S. Shah
Northwestern University, 633 Clark St, Evanston, IL 60208, USA
e-mail: s-krishnaswamy@northwestern.edu

S. Shah
e-mail: s-shah@northwestern.edu

M. Ghandehari, *Optical Phenomenology and Applications*,
Smart Sensors, Measurement and Instrumentation 28,
https://doi.org/10.1007/978-3-319-70715-0_17

governing the sequence of the development of longitudinal versus transverse cracks. The development of these crack types is not entirely independent of each other, adding to the complexity in predicting bond cracks (Gambarova et al. 1989; Modena 1992).

In this study, an experimental program is carried out to evaluate the stages of longitudinal splitting of concrete in the absence of confining effects other than the concrete (Fig. 17.1). These studies are made possible by real-time measurement of the extent (length and opening) of cracking using the phase measurement interferometric imaging (Creath 1985). Keeping the rebar size constant, the influence of concrete cross section size and geometry on concrete cracking is examined. Experiments included rebar pull out tests while simultaneously mapping the fracture using an optical imaging interferometer (Fig. 17.2).

Theory of bond induced longitudinal fracture considers that cracks initiate depending on the specimen size and that the extent of propagation of these cracks depends on the concrete cover (Zulli et al. 2016; Nikoukalam and Sideris 2017; Matsuinoto et al. 2016; Ghandehari 1998). We show in this chapter that longitudinal cracks are not initiated if the mode of failure is changed from splitting to shear failure. It is further shown that this apparent size dependent failure mode also depends on changes in the specimen geometry. A study of the bond in reinforced concrete is carried out with particular attention to the influence of the cross-section size and geometry. The influence of these parameters on cracking of concrete and in particular on the relationship between the normal and tangential stress components, is identified.

One of the first models for studying longitudinal cracking of concrete with an embedded rebar was developed by Tepfers (1979) where the radial component of the bond stress was regarded as hydrostatic pressure acting against a thick wall cylinder. The splitting of the cylinder was evaluated based on the lower bound and the upper bound limits of the strength criteria. In the former, the criterion is satisfied when the tangential stress of the cylinder inside surface reaches the material tensile strength, and in the latter it is satisfied when the tensile strength across the entire thickness of the cylinder is exhausted. A partly cracked model was also formulated but it did not account for the traction across the longitudinal cracks (Tepfers 1979).

Prediction of the load capacity of a concrete cylinder subject to internal pressure using the cohesive crack formulation has been done by number of investigators

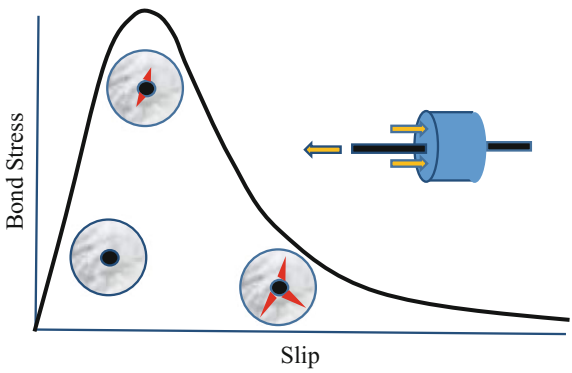

Fig. 17.1 Bond stress induced longitudinal splitting of concrete

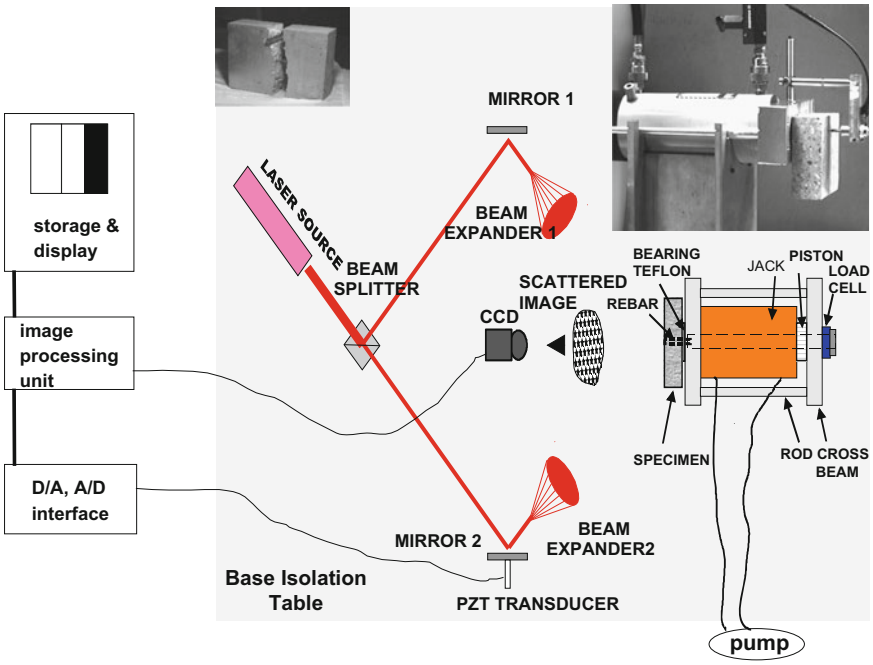

Fig. 17.2 Loading apparatus and the interferometric set-up

(Noghabai 1995; Reinhardt 1992; Rosati and Shumm 1992; Van der Veen 1990). In these studies, the concrete cylinder was considered as an intact elastic outer ring and a cracked cohesive (softening) inner ring, subject to hydrostatic pressure acting on the circumference of the inner surface. An integral equation of equilibrium was solved, by expressing the crack opening in terms of the tangential stress (σ_t) according to the material post peak response in tension. In order to describe the strain variation in the radial direction, certain assumptions were made regarding the tangential displacement variation in the cracked zone. Den Uijl and Bigaj incorporated the radial displacements of concrete in a fracture mechanics model similar to that described above (Den Uijl and Bigaj 1996). The relative magnitude of the displacement components (dn and dt) at the interface were shown to depend on the mode of failure. A linear relation between dt and dn is suggested for the splitting type failure. On the other hand, when the anchorage failure is by shear/pullout, dt was shown to increase at a much faster rate after reaching the vicinity of peak load.

17.2 Method

The study reported in this chapter was designed to observe the process of splitting that occurs in pull-out tests, often used to study the mechanics of bond slip/cracking in reinforced concrete. The quantity of interest that cannot directly be measured is

the normal component of traction at the interface. In this study a hybrid numerical-experimental procedure is carried to estimate the normal stress. The cracking of concrete is monitored while measuring and evaluating the states of stress and displacement at the bar-concrete interface.

Bars in shape of a wedge were fabricated and tested to simulate the rebar splitting force similar to rebar lugs causing a wedging action during pull-out. This simulation is possible as the normal component of the wedge force can be obtained for the wedge.

17.2.1 Speckle Interferometry

In concrete, crack opening displacements at complete separation are typically less than 50 μm (Gopalaratnam and Shah 1985). Electronic Speckle Pattern Interferometry (ESPI) has been shown to be an appropriate technique for measurement from the start to advanced stages of this cracking (Ghandehari et al. 1999). This basic version of the technique is already powerful because the sensitivity is on the order of the wavelength (λ = 633 nm) of the light used. An advanced variation of ESPI, demonstrated in this chapter, involves measurement of the phase and therefore achieves much higher spatial resolution. In our case, even with the ordinary resolution camera used, the spatial resolution was approximately 0.5 nm. This resolution is essential for accurate measurement of the crack opening displacement and calculation of respective cohesive stresses bridging the cracks (Ghandehari et al. 1999).

The experimental setup is shown in Fig. 17.2. Light from a HeNe laser is passed through a beam splitter. One beam is reflected by a mirror which is attached to a piezo-electric transducer used for phase stepping. Prior to illuminating the object, each beam is expanded by passing through an objective lens. The two wave fronts that arrive and mix at the specimen are scattered by the rough specimen surface and onto the CCD array of a camera. The observed random/speckled intensity variation is due to the interference of the scattered wave fronts with random phase. Phase-stepped speckle intensity patterns of the specimen in its reference state are first recorded and then subtracted from the phase-stepped intensity pattern of the object in its deformed states (Ghandehari et al. 2000). The resulting intensity fringe patterns associated with the specimen surface displacement can be expressed as:

$$I_i = I_0 + \{1 + \Upsilon_0 \cos[\emptyset(x,y) + \alpha_i]\},\ i = 1,2,3 \text{ for the three phase steps} \quad (17.1)$$

From which the phase can be extracted:

$$\emptyset(x,y) = \tan^{-1}\left\{\frac{[\sqrt{3}(I_3 - I_2)]}{[2I_1 - I_2 - I_3]}\right\} \quad (17.2)$$

The displacement d mapped by each phase fringe is:

$$d = \frac{\lambda}{2 \sin \theta} \tag{17.3}$$

where,

λ = 0.633 μm (HeNe wave length)

θ = 45° (angle between the illuminating beams and the specimen normal).

17.3 Materials

Normal strength concrete with water, cement, fine and coarse aggregate (8 mm max) content proportions of 0.5, 1, 2, and 2 parts by weight respectively were used for all the specimens. The specimens were cured in 90% relative humidity for 28 days. A compressive strength of 33 MPa and a modulus of elasticity of 25,000 MPa were obtained testing a 76 × 152 mm cylindrical. Tensile strength of 2.5 MPa was obtained using 100 × 30 × 20 mm prism specimens.

The pull-out specimen dimensions are shown in Table 17.1 and geometry shown in Fig. 17.3. Two different specimen geometries used the same rebar size. In the first geometry (edge specimens), the rebar was cast near the specimen edge. In this case a notch was cut on the top so that the splitting crack propagates as an edge crack in one direction only. In the second geometry (center specimens), the rebar was cast in the center of the specimen. The aspect ratio (width/height) of all specimens was 1.5. The specimen dimensions were 50 × 75 (small), 100 × 150 (medium), and 150 × 225 (large) mm, all 50 mm thick. The rebar diameter was 8 mm with ribs at 90° with respect to the longitudinal axis. The rebar was partly milled along the top and bottom surfaces in order to induce pressure in the horizontal direction for obtaining a reliable measure of the normal stress.

Table 17.1 Specimen detail rebar diam. (d_b) = 9 mm, compressive strength (f′c) = 33 MPa

Specimen	Dimensions (Height × Width) (mm)
Edge rebar, small	50 × 75
Edge rebar, medium	100 × 150
Edge rebar, large	150 × 225
Center rebar, small	50 × 75
Center rebar, medium	100 × 150
Center rebar, large	150 × 225
Edge wedge, small	50 × 75
Edge wedge, medium	100 × 150
Edge wedge, large	150 × 225

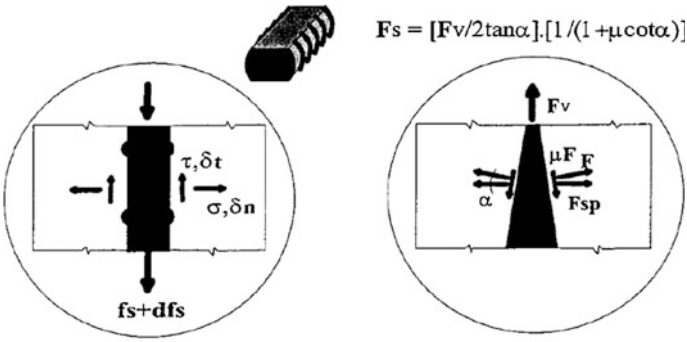

Fig. 17.3 Schematic of components of interface stress for rebar and for wedge

Load was applied by a 200 kN center bore Enerpac hydraulic actuator (Fig. 17.2). The pull-out load was measured with a 25 kN Sensotec load cell. The slip was measured using an LVDT at the free end of the rebar. Teflon pads were placed at the specimen bearing reactions in order to limit the effect of reaction friction against splitting.

17.3.1 Wedge Specimens

Wedge specimens were tested in order to simulate the normal stress induced by the rebar wedging action during pullout (Fig. 17.3). The dimensions of the wedge specimens are the same as the edge rebar specimens. Two Teflon films were placed between the wedge-concrete interface establishing a reliable and known coefficient of friction. The coefficient of friction μ of Teflon against Teflon is 4.5%, smaller than the coefficient of friction of Teflon against concrete or steel. Teflon films were also placed at the specimen bearing reactions in order to limit the effect of bearing friction against splitting.

17.4 Calculation of Interface Stresses Induced by Rebar Pullout

17.4.1 Edge Rebar Specimens

Figures 17.4 and 17.5 show typical phase maps representing the surface displacement of the edge and center rebar specimens. Displacement discontinuities at a crack represented by fringe map discontinuities can be measured to obtain the crack opening displacement profiles (Fig. 17.6). Stable crack propagation was observed

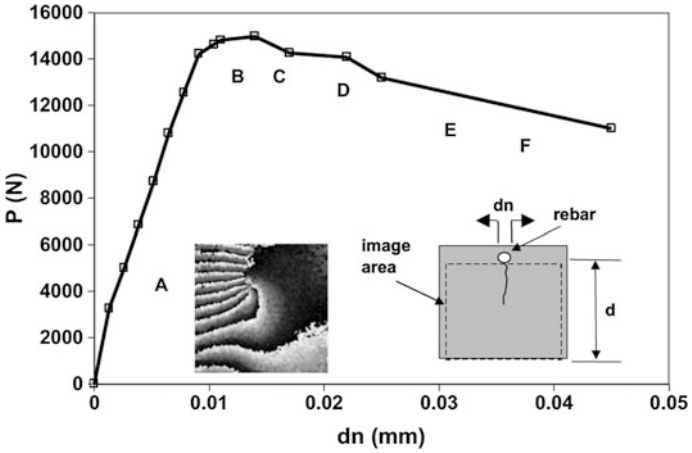

Fig. 17.4 Crack propagation in edge rebar specimen (d = 150 mm)

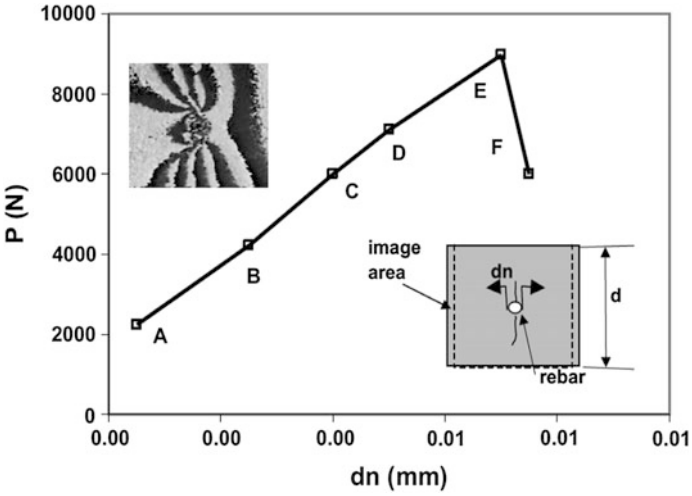

Fig. 17.5 Crack propagation in center rebar specimen (d = 50 mm)

for all edge specimens, which failed by splitting of the concrete. The crack opening displacement was subsequently used to calculate the corresponding crack flank traction (Fig. 17.7). This was achieved using relation of stress and crack opening (Gopalaratnam and Shah 1985). The measured crack length and the crack flank traction at each load step was incorporated into finite element simulation using FRANC2D (Ingraffea and Wawrzynek 1994). The stress intensity factor KI was evaluated using singular crack-tip elements. A fracture mechanics based failure criteria was used, where crack propagation criterion was set to the stress intensity factor reaching the critical stress intensity factor (KI_c). The KI_c was based on an

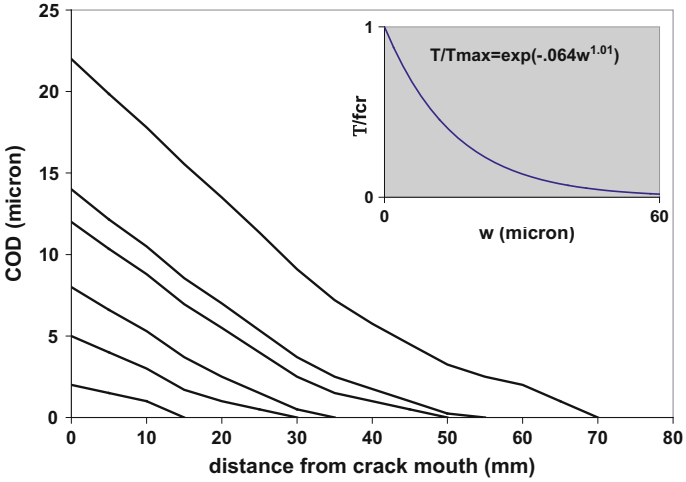

Fig. 17.6 Measured crack profile (edge rebar specimen, d = 150 mm)

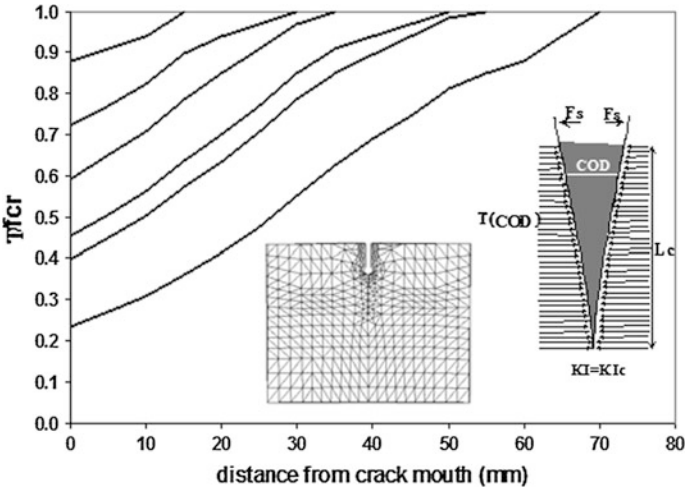

Fig. 17.7 Calculated crack flank traction used as input for numerical simulation

effective, two-parameter, elastic model (Shah and Jenq 1985). The normal force at the rebar required to satisfy this fracture criterion was then calculated. The crack was incrementally propagated to the next experimentally measured length. The numerical simulation was performed in two dimensions, assuming plane strain conditions.

17.4.2 Center Rebar Specimens

Unlike the edge rebar specimens, the mode of failure of the center rebar specimens was size dependent. The small and medium center specimens failed abruptly by splitting of concrete upon developing small longitudinal cracks. However, the large center specimen failed by pullout of rebar with no observable longitudinal cracks. The interface normal stress σ at peak for the small and medium specimens were evaluated in the same way as that outlined for the edge specimens. The normal stress σ in the elastic range was evaluated for both the center and the edge specimens by numerical simulation of the dilatation at the interface and correlating the results with the experimentally measured dilatation.

Since stable crack propagation was not achieved, no optically measured crack opening profile or crack length data were available in this case. Numerical evaluation of the splitting force for the center rebar specimens was therefore performed using an iterative scheme. The scheme is as follows:

1. Start with some small initial guess for the crack length.
2. Guess an initial crack tip opening displacement (CTOD).
3. Assume linear crack profile.
4. Apply crack flank traction T based on the material model shown in Fig. 17.6 insert.
5. Apply and increase the splitting force such that the crack tip stress intensity factor KI = KI_c.
6. Check the corresponding numerical crack profile (COD).

If the output crack profile (COD) and the input T satisfy the material model to within a stipulated accuracy, then consistency is achieved.

Grow the crack to a new length and repeat steps 2–6.

Alternatively, guess a new CTOD and repeat steps 3–6 using the new crack profile as given by the current iteration.

That this iterative algorithm leads to consistent results was established by adopting the same scheme for other specimens where experimental data was available for comparison, see Ghandehari et al. (2000).

17.5 Results and Discussions

17.5.1 Rebar Specimens

Figure 17.8 shows the relation between the pull-out force P and the normal displacement dn. Increase in the size of specimens which failed by splitting, led to an increase in the pullout strength, caused by the additional confinement. In the case of the edge specimens, this effect was pronounced, but to lesser extent for the center specimens. When the size of the center specimen was increased from medium to

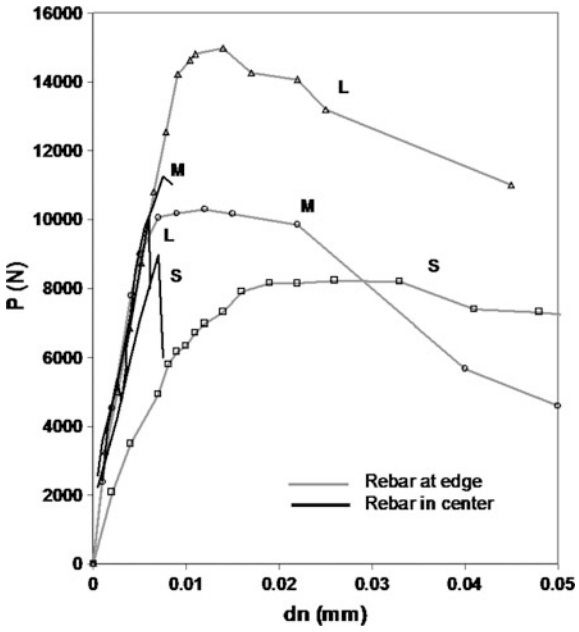

Fig. 17.8 Rebar pullout force versus concrete normal displacement at the rebar

large, the pullout strength was observed to decrease as the failure mode changed from splitting to pullout.

Figure 17.9 shows the relation between the two components of relative displacements at the rebar-concrete interface. The points of crack initiation (as detected on the specimen surface) and the peak load are marked with a cross and a star, respectively. Cracks initiate at approximately 6–10 microns of relative normal displacement (dn), but at larger relative shear displacement (dt) with increasing confinement. The increase in confinement is associated either with increasing the specimen size or with changing the specimen geometry (i.e. rebar location). In the case of small and medium center rebar specimens, the point of crack initiation and peak pullout loads coincide.

Figure 17.10 shows the influence of specimen dimensions (size, and location of rebar) on the Stress Intensity Factor (KI) as obtained from a linear Fracture Mechanics analysis. KI is shown as a function of the non-dimensional crack length (a/d) with constant applied splitting force Fs. Comparing the relative values of KI in the figure, it can be expected that the edge specimens would exhibit a larger splitting tendency than the center rebar specimens. The same tendency is expected as the specimen size is decreased. The evaluated splitting force ($\sigma \times$ projected area) for both edge and the center geometries are shown in Fig. 17.11. The influence of increasing size on pull-out load (Fig. 17.8) is consistent with trends observed on the increase of splitting force (Fig. 17.11) and decrease of stress intensity factor (Fig. 17.10).

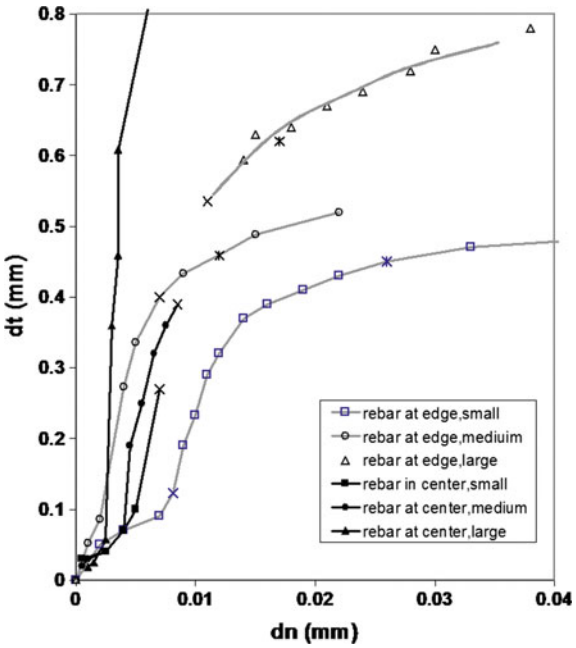

Fig. 17.9 Components of rebar-concrete relative displacement

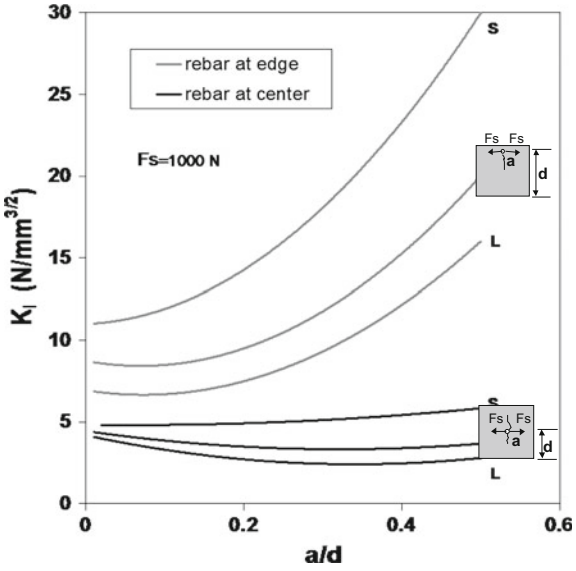

Fig. 17.10 Stress intensity factor (KI) for rebar specimen; effect of specimen size and geometry; numerical simulation (LEFM)

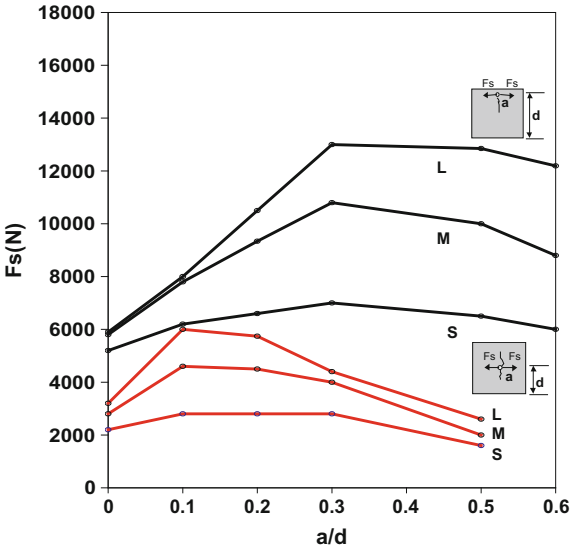

Fig. 17.11 Numerical simulation of 9 mm rebar pullout

17.5.2 Wedge Specimens and Validation of the Hybrid Method

Wedge splitting tests were carried out primarily to validate the selected fracture criterion. Similar measurement of splitting force versus the crack tip opening displacement (CTOD) was done for small, medium, and large wedge specimens. The results show that, as expected, the peak load and the corresponding CTOD increase with increasing specimen size.

The flank traction calculated from the CTOD at various stages of the crack propagation was used for the prediction of the splitting force, in the same way as for the rebar specimens. Good agreements were achieved given that the splitting force is known for the wedge specimen. After accurate measurement of the crack profiles, the numerically predicted wedge splitting force at peak agrees with the experimental results when the fracture criterion $KI = KI_c$ is used. The alternative fracture criterion $KI = 0$ and the tensile strength criterion were also considered. However, those simulations predicted forces much lower than that measured experimentally.

17.6 Conclusion

Full field phase measurement interferometry was used to track the stages of crack propagation in concrete, while measuring the crack tip location and crack opening displacement. Nonlinear fracture mechanics is used to model the bond/splitting

failure in reinforced concrete. Singular cohesive crack modeling provides good prediction of the experimental results. Edge rebar specimens were observed to fail by splitting where increasing the specimen size had a pronounced effect on increasing the pullout load. In the case of the center rebar specimens, small and medium specimens also failed by splitting, however increasing the specimen size did not significantly effect the pullout load. For the center rebar specimens, stable post-peak response was not obtained due to sudden splitting. Meanwhile, the large center rebar specimen failed by pullout without longitudinal cracks which did not propagate to the surface.

References

Creath, K. (1985). Phase-shifting speckle interferometry. *Applied Optics, 24*(18), 3053–3058.

Den Uijl, J. A., & Bigaj, A. J. (1996). A bond model for ribbed bars based on concrete confinement. *Heron*, *41*(3).

Gambarova, P. G., Rosati, G. P., & Zasso, B. (1989). Steel-to-concrete bond after concrete splitting: Test results. *Materials and Structures, 22*(1), 35–47.

Ghandehari, M. (1998). *Bond and cracking in reinforced concrete: Influence of size and geometry*, ProQuest Dissertations Publishing.

Ghandehari, M., Krishnaswamy, S., & Shah, S. (1999). Technique for evaluating kinematics between rebar and concrete. *Journal of Engineering Mechanics, 125*(2), 234–241.

Ghandehari, M., Krishnaswamy, S., & Shah, S. (2000). Bond-induced longitudinal fracture in reinforced concrete. *Journal of Applied Mechanics, 67*(4), 740.

Gopalaratnam, V. S., & Shah, S. P. (1985). Softening response of plain concrete in direct tension. *Journal of the American Concrete Institute, 82*(3), 310–323.

Ingraffea, A., & Wawrzynek, P. (1994). *FRANC2D: A two-dimensional crack propagation simulator. Version 2.7: User's guide.*

Lutz, L. A., & Gergely, P. (1967 November). Mechanics of bond and slip of deformed bars in concrete. *ACI Journal*, 711–721.

Matsuinoto, K., Wang, T., Hayashi, D., & Nagai, K. (2016). Investigation on the pull-out behavior of deformed bars in cracked reinforced concrete. *Journal of Advanced Concrete Technology, 14*(9), 573–589.

Modena, C. (1992). Theoretical prediction of the ultimate bond strength between a reinforcing bar and concrete. In A. Skudra & A. Tepfers (Eds.), *Bond in Concrete.* Latvia, Riga.

Nikoukalam, M. T., & Sideris, P. (2017). Experimental performance assessment of nearly full-scale reinforced concrete columns with partially debonded longitudinal reinforcement. *Journal of Structural Engineering (United States), 143*(4).

Noghabai, K. (1995). *Splitting of concrete in the anchoring zone of deformed bars*. Licentiate thesis / Luleå University of Technology

Reinhardt, H. W. (1992). Bond of steel to strain-softening of concrete taking account of loading rate. In B. Zdenek (Ed.), *Fracture Mechanics of Concrete Structures (*pp. 809–820). United Kingdom: Taylor and Francis.

Rosati, G., & Shumm, C. (1992). Modeling of local bond to concrete bond in reinforced concrete beams. In A. Skudra & A. Tepfers (Eds.), *Bond in Concrete* (pp. 34–43). Riga, Latvia.

Shah, S. P., & Jenq, Y. (1985). Two parameter fracture model for concrete. *Journal of Engineering Mechanics, 111*(10), 1227–1241.

Shah, S. P., Swartz, S. E., & Ouyang, C. (1995). *Fracture mechanics of concrete*. New York [u.a.]: Wiley.

Tepfers, R. (1979). Cracking of concrete cover along anchored deformed reinforcing bars. *Magazine of Concrete Research, 31*(106), 3–12.

Van der Veen, C. (1990). *Cryogenic bond stress-slip relationship*. Delft University of Technology.

Zulli, M., Ghandehari, M., Sidelev, A., & Shah, S. P. (2016). Dimensional factors in oxidation induced fracture in reinforced concrete. *Construction and Building Materials, 122,* 264–272.

Chapter 18
Imaging Strain Localization in Fiber Reinforced Materials

Yilmaz Akkaya, Masoud Ghandehari and Surendra P. Shah

Abstract Composite materials such as Fiber Reinforced Cement or Concrete (FRC) are designed to prevent brittle fracture. FRC is characterized by enhanced ductility and distributed crack formation prior to failure. Mitigation of progressive crack propagation and localization of cracks and stresses are result of the even distribution of fibers throughout the matrix. This chapter presents the utility of full field optical methodology for tracking the progressive development of cracking in cement based FRC. A full field imaging approach is used to better understand the link between microstructural properties, and sequence of cracking. We present the application of Electronic Speckle Pattern phase measurement interferometry (ESPI) for the identification of crack locations, size and progression, and how these features are linked to the uniformity of fiber distribution in the matrix.

18.1 Introduction

In this chapter we review the results of studies on high resolution mapping of surface strain fields, one which is particularly applicable to studying strain localization. The aspect ratio of the specimens used result in a plain strain field distribution, hence the surface measurements are a good approximation of the bulk response. This study highlights the utility of the ESP measurement technique to study the effect of fiber dispersion on crack formation in extruded FRC composites. The mechanical performance of an FRC composite depends on the fiber parameters including volume,

Y. Akkaya
Istanbul Technical University, Maslak, 34467 Sarıyer/İstanbul, Turkey
e-mail: akkayayil1@itu.edu.tr

M. Ghandehari (✉)
New York University, Six Metrotech Center, Brooklyn, NY 11201, USA
e-mail: masoud@nyu.edu

S. P. Shah
Northwestern University, 633 Clark St, Evanston, IL 60208, USA
e-mail: s-shah@northwestern.edu

M. Ghandehari, *Optical Phenomenology and Applications*,
Smart Sensors, Measurement and Instrumentation 28,
https://doi.org/10.1007/978-3-319-70715-0_18

modulus of elasticity, surface properties, length and diameter, as well as fiber alignment and dispersion. In the case of extruded FRC, the extrusion process enables the production with large amounts of short flexible fibers. This results in alignment and a strong bond within the cementitious matrix. (Shao and Shah 2000; Akkaya et al. 2000a; Peled et al. 1999). Short fibers when dispersed homogenously improve mechanical properties of the composites. This is in contrast with unevenly distributed or clumped fibers, often the case when using longer fibers.

These factors, in addition to short fibers limiting the size of initial micro-cracks in the matrix, contribute to the material toughness (Shah and Ouyang 1991; Li and Wu 1992; Li and Maalej 1996; Betterman et al. 1995; Shao and Shah 2000; Akkaya et al. 2000b; Peled et al. 1999).

Interferometric imaging and microscopy was used in this study to relate the mechanical performance of the FRC to microstructural characteristics of the materials. Tracking the fracture process of the FRC during the loading process provides useful insight into when, where and how the cracks form and propagate throughout the composite. The fracture process and multiple cracking of the materials is intimately related to the dispersion of fibers. For example, when there are adequate number of well dispersed fibers, cracks are arrested and the stresses transferred across the matrix, and this mechanism enables the composite to resist higher loads. The multiple cracking with smaller width will result in a pseudo-strain hardening response, eventually an increase in ductility of the material.

Sequences of multiple cracking and corresponding crack width information was evaluated using the optical interferometry approach. Electronic Speckle Pattern Interferometry (ESPI) allowed the measurement of strain localization at the surface. In this case it leads to information on the crack location and extent. The same region is then analyzed for fiber dispersion using microscopic imaging. This will enable linking the microstructural parameters (including fiber distribution) with the process of fracture. The percentage of the fiber clumping in the FRC composite and size of the fiber free areas are estimated and quantified by point process statistics (Akkaya et al. 2001). Correlations between the cracking and the size of the fiber free areas, and toughness of the composite and fiber clumping are investigated.

18.2 Method

Material Composition and Mechanical Testing

Five specimens were made by extruding 25.4 mm × 4 mm cross-sections (Shrinavasan et al. 1999). The materials mix composition was 45% cement, 12% silica fume, 3% PVA fibers (2 mm in length and 14 μm in diameter), 1% super-plasticizer and 39% water, by volume, and water-to-cement ratio was 0.29. Specimens were subjected to steam curing at 90 °C for two days, and cured at 20 °C temperature and 50% relative humidity for three days. They were then oven-dried at 105 °C for one day and kept at laboratory conditions for another day, before testing. The beam was subject to 4 point bending (Fig. 18.1) equipped with a

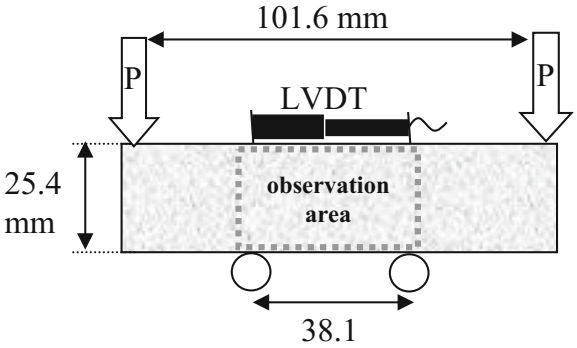

Fig. 18.1 FRC Test specimen

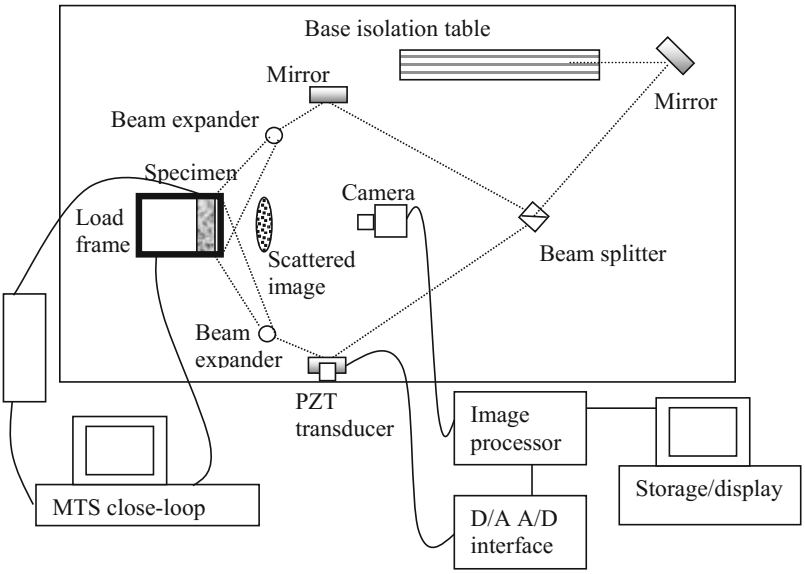

Fig. 18.2 Test set up for ESPI and loading configuration

displacement transducer (gauge length of 38.1 mm) for global measurement of strains. The load setup was part of the optical metrology apparatus (Fig. 18.2).

Optical Metrology

Figure 18.2 shows the experimental set up including the optical metrology, mechanical testing and the data acquisition and storage. The crack measurement technique is done by mapping the surface roughness using the light scattering from the rough (speckled) topology (Ghandehari et al. 1999). This unique finger print will change with specimen surface deformation including discontinuities formed by cracking. The imaging set was tuned to in-plane horizontal displacements, which

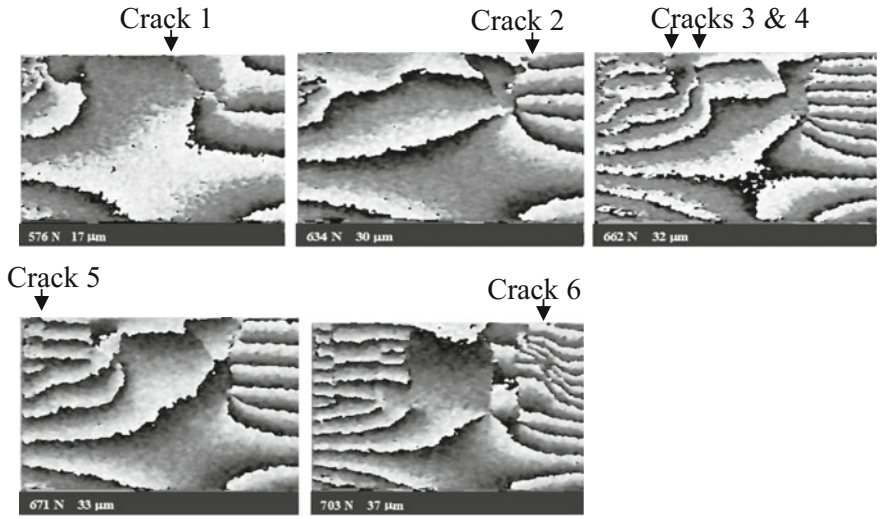

Fig. 18.3 Sequential crack formation as observed by ESPI

also enabled the measurement of crack mouth opening displacement. This was achieved by illuminating the specimen by two beams at 45° to the specimen surface. As the specimen was subject to loading and corresponding deformation, the scattered speckle pattern of the object at one state was stored in the computer image memory and subtracted from the speckle pattern corresponding to another state. The result of the subtraction is an intensity fringe pattern that provides a contour map of horizontal displacement. A standard speckle pattern interferometer is capable of measuring displacements with a resolution defined by the wavelength of the light, the angle between the incoming beam, etc. In a typical set up and with a sufficiently high resolution CCD camera it is possible to map the displacement field with resolution of approximately 0.45 µm. In order to improve the spatial resolution, a modification to this technique known as phase measurement was employed. Full detail of this technique is given in Chap. 17, describing how phase measurement interferometry is used for mapping fracture. In this setup, each fringe shown in Fig. 18.3 represents the same displacement of 0.45 µm but now the inter-fringe (pixel level) gray level carries additional information regarding the displacement shape between each fringe.

18.3 Experimental Results

Load and deflection values for one of the specimens (s1) is shown in Fig. 18.4, pointing along the curve where cracks were detected by the interferometric measurements. This assumed cracks in one cross section does not influence the stress

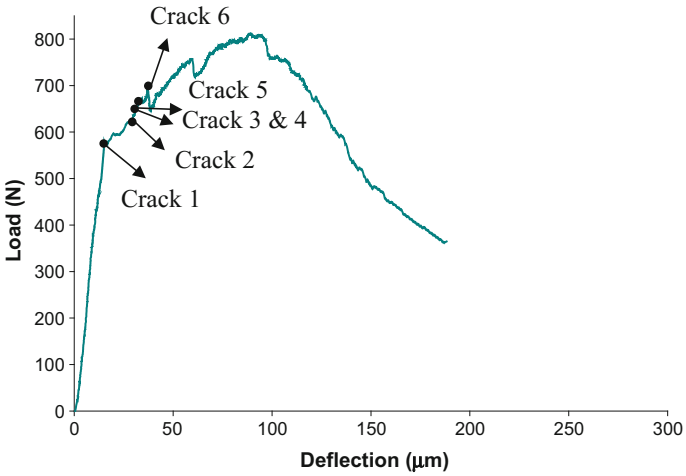

Fig. 18.4 Formation of the sequential cracks

Table 18.1 Stress and displacements at first cracking and flexural strength values

Specimen number	Sequential crack number	1. Cracking stress (MPa)	Displ. at 1st crack (μm)	Flexural strength (MPa)	Displ. at max. stress (μm)
s1	1	25.5	16.3	36.0	88.6
	2	28.1			
	3	29.3			
	4	29.3			
	5	29.7			
	6	31.1			
s2	1	26.2	15.5	30.2	54.0
	2	27.1			
	3	28.0			
	4	29.2			
s3	1	26.8	20.7	37.4	102.7
	2	28.2			
	3	35.3			
s4	1	30.2	26.0	37.2	83.4
	2	33.1			
s5	1	25.6	20.4	34.5	193.0
	2	32.8			

distribution on another cross section. Formation of cracks and corresponding stresses as detected by ESPI are shown in Table 18.1. Although the specimens were all produced from the same batch, the observed flexural behavior and respective cracking were not the same (Fig. 18.5).

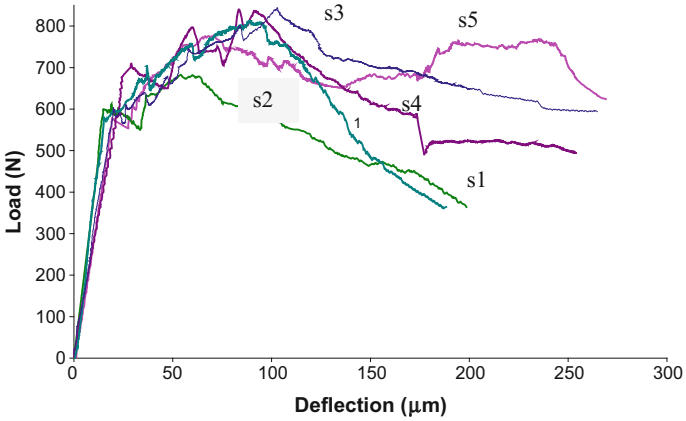

Fig. 18.5 Flexural test results

18.4 Statistical Analysis

After the mechanical testing, specimens were cut and polished at the crack locations for microscopy observations and statistical analysis, quantifying the fiber dispersion characteristics (Diggle 1983; Akkaya et al. 2000c).

The procedure included opening the cracks and separation of the parts of the specimen at the cracks, and preparation of a 10 mm^2 area by polishing. High resolution images of the specimen parts were taken and locations of the fibers were marked (Akkaya et al. 2001). Given the extrusion process, most fibers were aligned along the direction of the extrusion. Examples of images from the cracked cross-sections at the first and sixth cracks are shown in Fig. 18.6. The coordinates of each fiber was determined by the image analysis program, and the distance between each fiber pair was calculated. The point process statistics were calculated based on the coordinates of the fibers.

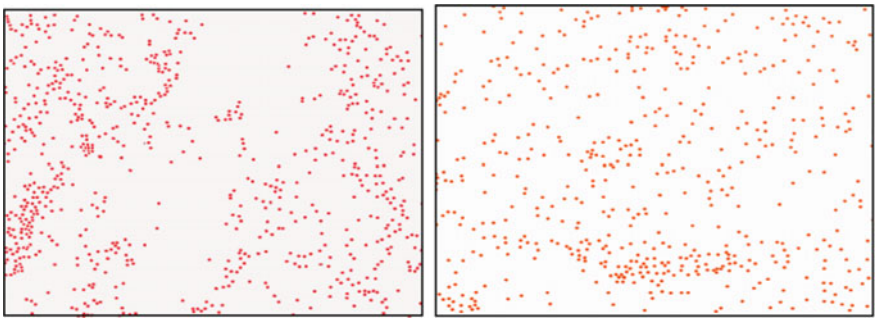

Fig. 18.6 Fiber distribution at the crack cross-sections, ×50 ((left) first crack, (right)) sixth crack

K-Function and F-Function statistical analysis were performed in order to quantitatively describe the fiber dispersion (Diggle 1983; Akkaya et al. 2000c, 2001). K-function was derived as the normalized number of fibers within a distance r of a given fiber. Increase of the K-function means there is fiber clumping. F-function is the distribution of distances between arbitrary points to the nearest fiber, which can be used to describe the size of the fiber-free areas. The F-function gives the probability of any point in the cross-section being at least a certain distance away from the nearest fiber. High values of 1-F(r) would indicate an increase in the fraction of the fiber free areas.

Crack cross-sections with evenly dispersed fibers can be identified by their closeness to the K-function of the random dispersion. Microscopic imaging showed that cross-sections at the first three cracks of the sequential multiple cracking have higher K-function values, implying poor fiber dispersion (Fig. 18.7). Cross-sections with a higher degree of fiber clumping would crack before cross-sections with better fiber dispersion. Fourth, fifth and sixth cracks exhibited fiber dispersions similar to the random dispersion, and thus, higher cracking stresses (Table 18.1).

The cross-section of the first crack has more fiber-free areas, as estimated by the F-function (Fig. 18.8). The largest sizes of the fiber free areas were encountered at the first crack cross-section. The fiber free areas can be considered as defects in the FRC composite and cracks are more likely to initiate around these poorly reinforced cross-sections. The largest fiber free area sizes of Specimen s1 at the various crack locations are shown in Table 18.2.

The ratio of displacement at the maximum stress to the displacement at the first cracking stress, evaluated from the 4-point flexure test, was used as a measure of toughness. A variation in toughness was observed among the specimens (Table 18.3). Fiber dispersion parameters are used to explain these differences

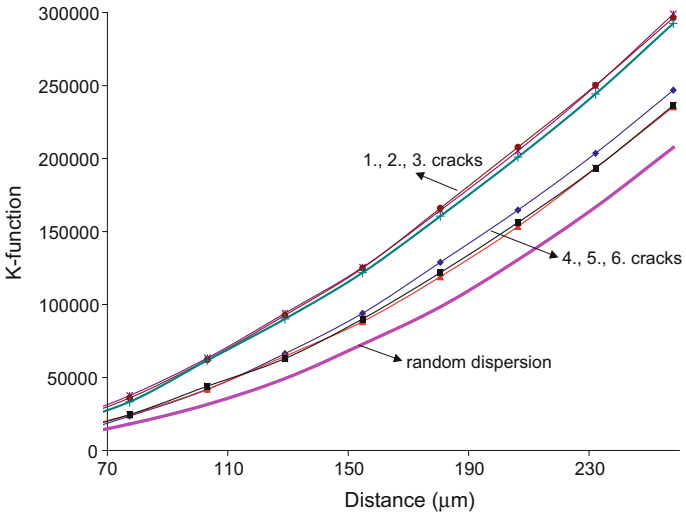

Fig. 18.7 K-function values at the crack locations

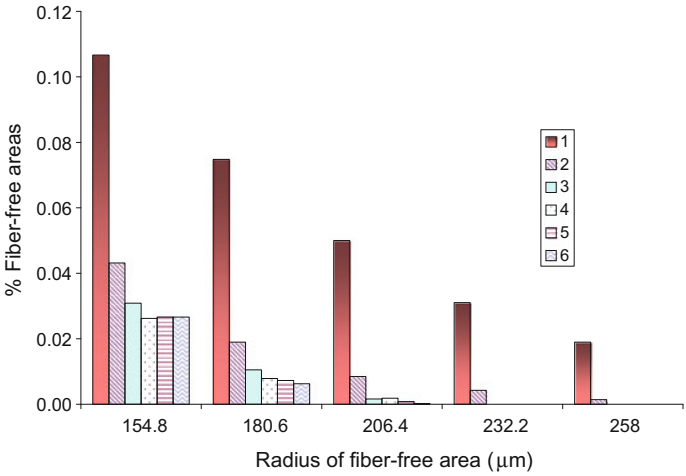

Fig. 18.8 F-Function, radius and percentage of the fiber-free areas with respect to sequential cracking

Table 18.2 Size of the largest fiber-free area at the sequential cracking

Sequential crack number	1	2	3	4	5	6
Radius of the max fiber-free area (μm)	381	271	226	223	219	209

Table 18.3 Toughness and fiber dispersion at the first crack locations of the identical FRC specimens

Specimen number	Displ. at 1. crack (μm)	Displ. at max. stress (μm)	Toughness ratio	Clumping at 1. crack (%)
s1	16.3	88.6	5.4	47
s2	15.5	54.0	3.5	56
s3	20.7	102.7	5.0	48
s4	26.0	83.4	3.2	60
s5	20.4	193.0	9.5	11

among identical specimens. Percentage of the fiber clumping with respect to random dispersion, at the crack locations is also given in Table 18.3. A strong relationship between the fiber dispersion at the first crack location and composite toughness is shown.

18.5 Conclusion

Electronic Speckle Pattern Interferometry (ESPI) was employed to investigate the crack propagation process in Fiber Reinforced Composite (FRC). The technique was instrumental for studying effect of the microstructural properties, such as fiber dispersion characteristics at the crack location, crack sequences, crack locations were observed and quantified. When correlated with measurement of load and displacement, it was possible to relate toughness of the FRC composites to fiber clumping at the cracked cross-sections.

References

Akkaya, Y., Ankenman, B., & Shah, S. P. (2001). Effect of fiber dispersion on multiple cracking of cement composites. *Journal of Engineering Mechanics, 127*(4), 311–316.

Akkaya, Y., Peled, A., Picka, J. D., & Shah, S. P. (2000a). Effect of sand addition on properties of fiber-reinforced cement composites. *ACI Materials Journal, 97*(3), 393–400.

Akkaya, Y., Peled, A., & Shah, S. (2000b). Parameters related to fiber length and processing in cementitious composites. *Materials and Structures, 33*(8), 515–524.

Akkaya, Y., Picka, J., & Shah, S. P. (2000c). Spatial distribution of aligned short fibers in cement composites. *Journal of Materials in Civil Engineering, 12*(3), 272–279.

Betterman, L. R., Ouyang, C., & Shah, S. P. (1995). Fiber-matrix interaction in microfiber-reinforced mortar. *Advanced Cement Based Materials, 2*(2), 53–61.

Diggle, P. (1983). *Statistical analysis of spatial point patterns.* London [u.a.]: Acad. Press.

Ghandehari, M., Krishnaswamy, S., & Shah, S. (1999). Technique for evaluating kinematics between rebar and concrete. *Journal of Engineering Mechanics, 125*(2), 234–241.

Li, V. C., & Maalej, M. (1996). Toughening in cement based composites, part II: Fiber reinforced cementitious composites. *Cement and Concrete Composites, 18*(4), 239–249.

Li, V. C., & Wu, H. (1992). Conditions for pseudo strain-hardening in fiber reinforced brittle matrix composites. *Applied Mechanics Reviews, 45*(8), 390.

Peled, A., Akkaya, Y., & Shah, S. P. (1999). Effect of fiber length in extruded and cast cement composites. *American Concrete Institute*, (SP-190), pp. 1–19.

Shah, S. P., & Ouyang, C. (1991). Mechanical behavior of fiber-reinforced cement-based composites. *Journal of the American Ceramic Society, 74*(11), 2727–2953.

Shao, Y., & Shah, S. P. (2000). Mechanical properties of PVA fiber reinforced cement composites fabricated by extrusion process. *American Concrete Institute Materials Journal, 6*(94), 555–564.

Shrinavasan, R., Deford, D., & Shah, S. P. (1999). The use of extrusion rheometry in the development of extruded fiber reinforced cement composites. *Concrete Science and Engineering, 1*(1), 26–36.

Chapter 19
Optical Characterization of Translucent Stone Subject to Degradation

Federica Rosso, Weihua Jin, Anna Laura Pisello, Marco Ferrero and Masoud Ghandehari

Abstract Marble is an aesthetically appealing and thermodynamically 'cool' building material. However, when subject to weathering, marble building facade elements undergo surface degradation that result in changes to appearance and optical properties. These changes impact both the aesthetics and the thermal characteristics of the marble. This chapter highlights an experimental approach for the characterization of these changes, and numerical simulations for studying the corresponding impact on building energy performance when marble is used as an envelope finishing layer. Optical characteristics studied include gloss, solar reflectance, transmittance and absorbance. Changes in the optical characteristics of marble are used to assess the effect of degradation on it's thermal properties.

F. Rosso · M. Ferrero
Dept. of Civil, Construction and Environmental Engineering,
Sapienza Università di Roma, Via Eudossiana 18, 00184 Rome, Italy
e-mail: federica.rosso@uniroma1.it

M. Ferrero
e-mail: marco.ferrero@uniroma1.it

W. Jin · M. Ghandehari (✉)
New York University, Six Metrotech Center, Brooklyn, NY 11201, USA
e-mail: masoud@nyu.edu

W. Jin
e-mail: wjin@nyu.edu

A. L. Pisello
Dept. of Engineering, University of Perugia,
Via Goffredo Duranti, 67, 06123 Perugia, Italy
e-mail: anna.pisello@unipg.it

M. Ghandehari, *Optical Phenomenology and Applications*,
Smart Sensors, Measurement and Instrumentation 28,
https://doi.org/10.1007/978-3-319-70715-0_19

19.1 Introduction

Marble is a natural material, composed of calcite ($CaCO_3$). It has a long history of being used in architecture, construction and the arts going back to the Greek and Roman Empires; many of these early examples of classic marble architecture are still standing (Malacrino 2010; Zöldföldi et al. 2003). Given its aesthetic properties, such as color and patterns, and optical and thermal properties such as luminescence and reflectivity, marble is still in widespread use today. Because of its aesthetic appeal it is often applied in high value structures such as government, financial and religious buildings. In modern building construction it is often utilized as a component of thin exterior walls systems that include insulation layers, impermeable membranes and marble finishing layers. Some of the optical characteristics that make marble aesthetically pleasing are also responsible for its desirable thermal properties.

In light of the challenges in the construction sector concerning resource management, energy consumption and the associated adverse impact on health and the environment (Haines et al. 2006; Hansen et al. 2010), many governments have established long term sustainability goals for the industry (UNFCCC 2015). 60 billion tons of raw materials are extracted from the earth annually for human building activities. This is despite the advances in alternative and new building materials (Pacheco-Torgal and Labrincha 2013; Pacheco-Torgal and Jalali 2011; Kulatunga et al. 2006). The stone and marble industry alone produces a considerable amount of waste material, as well as pollution during the extracting and manufacturing of end products. The building construction sector accounts for close to 40% of global energy demand (IEA 2013; Pérez-Lombard et al. 2008). Strategies to mitigate energy demand and manage thermal comfort aim at reducing the overall energy demand sector by sector (Cabeza et al. 2010). These strategies include mitigation of elevated heat outdoors in urban areas, know as the Urban Heat Island effect (UHI) (Santamouris 2014). Cool building materials can serve this mitigation objective.

In this case, the optical characteristics of marble and other stone materials result in surface temperatures that are lower than commonly used non-cool materials. The cooling capacity is a result of the intrinsic thermodynamic and optical characteristics of the materials, such as high thermal emissivity and high solar reflectance, properties observed to mitigate both energy need for cooling and outdoor comfort (Pisello et al. 2014; Rosso et al. 2016b). Given the increasing attention to energy efficiency of building envelope materials, we present a study on marble degradation and corresponding optical characteristics and how it relates to energy performance of a building using marble as an envelope material.

When marble is exposed to the exterior environment, it experiences surface degradation. Exposure conditions that may degrade marble includes (i) acid rains (Franzoni and Sassoni 2011), (ii) ultraviolet radiation (Careddu and Marras 2013) and (iii) thermal cycles/thermal stress (Ozcelik et al. 2012). These processes can negatively impact both the aesthetic and thermal properties of marble. This is particularly acute in industrial and urban areas, where the moisture content is more acidic. The mechanisms of degradation of the marble addressed in this chapter is surface degradation as a result of exposure to an acidic environment. We examine these properties in two types of white marble; Bianco Carrara and Statuario.

19.2 Optical Characteristics of Marble

Marble has a high thermal emissivity and a high solar reflectance that contribute to its cool material properties. The optical characteristics of marble that determine what people perceive, are a function of how it reflects light and corresponding colors and texture. Optical characteristics also impact the material energy properties. For example, reflectance influences how much energy from the sun is absorbed. The advantages of using marble as a cool material include a better experience for pedestrians at the street level in warm urban climates, a lower contribution to the Urban Heat Island effect through the reduction in outdoor urban temperatures and a corresponding reduction in the demand for indoor cooling. To quantify the effectiveness of cool marble envelope due to its reflectance, studies were conducted by performing a dynamic simulation on a case study building with a marble envelope (Rosso et al. 2014), by comparing the energy performance of the marble envelope with a more traditional cement-based envelope. Results indicated an energy saving equivalent to 18% of energy demand.

19.2.1 Effect on Color

Color described in a color scale by mean of $L^*a^*b^*$ (Wyszecki et al. 2000) was introduced by *Commission Internationale de l'Eclairage* (CIE) in 1976. This scale includes three coordinates defining the color space represented by L^*, a^* and b^*. L^* refers to lightness ranging from 0 to 100. L^* ranges from 0 (indicating minimum brightness) to 100 (indicating maximum brightness). The a^* ranges between red and green; b^* represents yellow to blue.

In a study carried out by Rosso et al. (2016a) a lightness analysis was carried out by means of High Definition microscope observations and image analysis (Fig. 19.1). This method was employed to quantify the effect of degradation on lightness when the marble was exposed to an acidic environment. Results showed that after one week of exposure to the accelerated weathering test, in solution of nitric and sulfuric acids at pH4, there was a significant decrease of lightness ranging from 7% (Statuario marble) to 33% (Bianco Carrara).

Work by Eren et al. (2016), Urosevic et al. (2010) considered $L^*a^*b^*$ coordinates, evaluating ΔL^*, Δa^*, Δb^* and corresponding ΔE^* using Eq. 19.1. While ΔL^*, Δa^*, Δb^* represent color coordinated variation, ΔE^* expresses human perception of color variation.

$$\Delta E^* = \sqrt{(\Delta L^{*2} + \Delta a^{*2} + \Delta b^{*2})} \tag{19.1}$$

Research reports in the literature highlight the effect of environmental exposure on the optical characteristics of stones. In Eren Sarici's work (2016), various stones including marbles and travertine, were subject to thermal stresses. In the case of

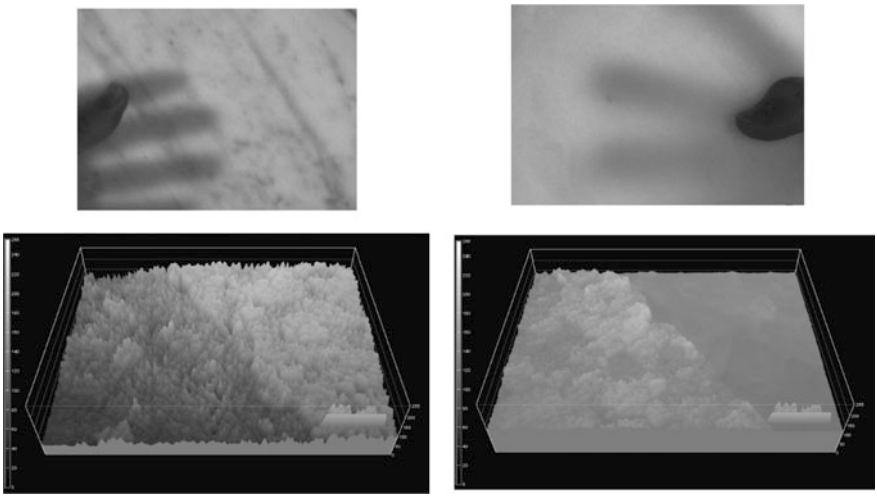

Fig. 19.1 Translucent marble: weathering effect as seen by means of the optical microscope: lightness change after treatments of half of the sample with a solution of nitric acid and distilled water, (Left) Bianco Carrara marble, (right) Statuario marble

marbles, the lighter ones became lighter after degradation due to thermal cycles, while the dark ones became darker. The total color difference, represented by ΔE^*, was approximately 2–3 for all the samples. The exception was travertine, where it is much larger (approximately 20) making the effect much more perceivable.

Urosevic and colleagues (2010) employed a colorimeter to evaluate stone color modifications when exposed to marine aerosol aging, while considering samples with different surface finishing. Their findings demonstrated that color differences are perceivable in almost all the samples, especially in the ones that were polished before the experiment. Such color differences almost always exceed the 3 units of ΔE^*, the value which is the minimum perceivable by human eye.

These findings are confirmed by Rosso et al. (2016a), investigating ΔE^* on samples degraded by accelerated weathering tests: surface color was measured during the weathering process, showing the degradation. Results show that when exposed to accelerated weathering, ΔE^* is greater than 5 for Bianco Carrara, while Statuario color change was perceivable only at the end of the exposure time (Fig. 19.2). Samples were analyzed after 2 and 4 weeks of exposure. As can be seen from Fig. 19.2, the first row shows the Bianco Carrara marble color change after 2 weeks (2w) and 4 weeks (4w), while the second row displays the same for Statuario marble. While Bianco Carrara at 0, 2 and 4 weeks colors are all perceived differently by human eye, Statuario marble 0 and 2w colors are perceived as same color, while 4w is seen as different.

Fig. 19.2 Surface color ($L^*a^*b^*$) at (0w) 0 weeks of exposure to aging, (2w) 2 weeks of exposure, and (4w) 4 weeks of exposure, for both Bianco Carrara and Statuario marbles

19.2.2 Effect on Distinctness of Image and Gloss

In addition to color, other optical characteristics as result of changes to the surface include (i) distinctness of image (DOI) and (ii) gloss. DOI indicates the sharpness of the image reflected by surface: therefore, it is greater on smooth surfaces and lower on rough surfaces. DOI scale ranges from 0 to 10, where 10 refers to perfectly reflective. Gloss is measured on a scale from 0 to 100 gloss units (GU). It refers to how much of the incident light is reflected toward its specular direction by the surface (ASTM D523—14).

DOI and gloss of marble samples vary depending on surface finish (polished/smooth or non-polished/rough), but is also modified by degradation. Studies on the effect of various exposure conditions include (i) acid rains Rosso et al. (2016), (ii) UV radiation (Careddu and Marras 2013) and (iii) thermal cycles (Eren Sarici 2016; Ozcelik et al. 2012). Measurements are carried out using a gloss meter. When samples were exposed to one week accelerated weathering, soaked in an acid solution simulating acid rain, DOI decreased by 7% for Statuario marble and 12% for Bianco Carrara. The solution was used to accelerate weathering for conditions of acid rain in industrialized and or urban areas. This was accomplished by mixing distilled water and nitric acid and sulfuric acid (2/3 SOx- and 1/3 NOx- proportion). The resulting pH4 is approximately ten times more acidic than typical rain water. Lower pH values would result in higher acceleration but results would be farther from reality. The same samples and exposure conditions were used to test for gloss. Results indicated that gloss decreased by as much as 64% for Statuario and 73% for Bianco Carrara according to Rosso et al. (2016). Considering UV radiation, lower differences in gloss before and after the degradation were found, between −0.2 and −13% (Careddu and Marras 2013). Finally, thermal cycles, i.e., freeze-thaw cycles where shown to have strong impact on marbles' gloss, decreasing it from −6% up to −75% (Ozcelik et al. 2012).

19.2.3 Effect on Reflectance, Transmittance, Absorbance

The radiation from the sun arriving to the surface of the earth includes energies in the following ranges: the ultra-violet wavelengths (UV, 200–400 nm), the visible wavelengths (Vis, 400–700 nm), the Near-Infrared radiation (NIR, 700–2500 nm), and the Infrared (IR, above 2500 nm). Reflectance from a surface is often measured using a spectrophotometer (ASTM E903—12). Reflection has important consequences on materials' energy performance. If the material has high reflectance, it is able to maintain a lower surface temperature, and is considered a cool material. The reflectance, and corresponding transmittance and absorbance do not remain constant over time. In the case of marble, these characteristics often follow the same response as color, gloss and DOI (Rosso et al. 2016; Sleiman et al. 2011, 2014). Sleiman and colleagues (2011) found that with the exception of low reflectance materials, reflectance is decreased with material degradation. Rosso et al. (2016) studied marble and found that reflectance in rough surfaces increased with degradation, while it decreased on smooth marble surfaces. Moreover, it was demonstrated that polished samples were less sensitive to degradation than rough samples.

By studying the effects of degradation on the materials optical properties, we have noted that Statuario and Bianco Carrara marbles behave differently in the NIR part of the spectrum. As mentioned above, degradation resulted in a decrease of the solar reflectance in polished samples, and increased the solar reflectance in rough ones. However, in Statuario marble, this trend is confirmed for the UV and Vis spectra, whereas, in the NIR spectrum the opposite occurred. This was observed only in the Statuario samples, while the rough Bianco Carrara samples underwent an increase in reflectance of UV (+7.4), Vis (+8.5), and NIR (+23.1). The polished samples underwent a decrease of reflectance in UV (−1.4), Vis (−4.1) and NIR (−16.3).

19.3 Energy Performance

When the material reflects the largest part of incoming solar radiation back to the sky, surface temperatures remain lower; as a result, less heat enters the building. This behavior on the part of cool materials provides energy savings correlated with a lower demand for cooling during summer. On the other hand, only small penalties in an increased demand for heat are assessed for the cold season, as solar radiation is weaker during this time of the year.

Several studies have been carried out investigating energy savings due to cool envelope materials, to be applied both on vertical envelope and horizontal one (i.e., roof) (Doya et al. 2012; Pisello et al. 2014). With particular reference to cool marble façades, Rosso and colleagues (2014) investigated thermal-energy performance of white marble facades, by means of yearly dynamic simulations with the software Design Builder (Rosso et al. 2014). Their findings demonstrated that this natural stone envelope is able to reduce energy demand by 18% for cooling, when compared to a more traditional cement-based façade. However, since energy performance is

influenced by optic characteristics and degradation affects optic characteristics, the performance of a white marble façade is expected to decrease over time. Further studies using the same dynamic simulation method Rosso et al. (2016a) considered the performance of white marble façade after degradation, and verified significant differences in energy performance due to the interaction with the external environment. As mentioned above, reflectance follows different trends depending on whether samples are rough or polished. On polished samples, degradation did not affect energy performance, while on rough samples degradation acted as a "polishing" mechanism, increasing reflectance and further reducing cooling energy demand by 4.3%. However, these studies demonstrate that degradation affects not only aesthetic performance, but also thermal-energy performance, and that it is necessary to consider the interaction with the external environment when employing such materials.

19.4 Conclusion

Whether or not degradation to the marble surface is visible to the eye, it results in changes to the optical characteristics of the material that influence thermal performance. Indeed, optical characteristics influence not only aesthetic appearance, but also the thermal/energy behavior of the construction element itself. Color change also has implications for the architectural expression of the construction: degradation causes darkening and slight changes in other color coordinates. As described above, modifications in color are perceived by the human eye, and noticeable. Similarly, DOI and gloss determine how the surface finishing of the stone material is perceived. Finally, solar reflectance, transmittance and absorbance are the fundamental properties that support buildings' energy performance. A decrease in reflectance implies a decrease in thermal cooling power, therefore an increase of energy demand for cooling during the summer. An increase in reflectance would provide additional cooling potential, positively contributing to the energy efficiency of the building.

References

Cabeza, L. F., Castell, A., Medrano, M., Martorell, I., Pérez, G., & Fernández, I. (2010). Experimental study on the performance of insulation materials in Mediterranean construction. *Energy and Buildings, 42*(5), 630–636.

Careddu, N., & Marras, G. (2013). The effects of solar UV radiation on the gloss values of polished stone surfaces. *Construction and Building Materials, 49,* 828–834.

Doya, M., Bozonnet, E., & Allard, F. (2012). Experimental measurement of cool facades' performance in a dense urban environment. *Energy and Buildings, 55,* 42–50.

Eren Sarici, D. (2016). Thermal deterioration of marbles: Gloss, color changes. *Construction and Building Materials, 102*, pp. 416–421.

Pacheco-Torgal, F., & Jalali, S. (2011). *Eco-efficient construction and building materials* (1st ed.). London: Springer Verlag.

Franzoni, E., & Sassoni, E. (2011). Correlation between microstructural characteristics and weight loss of natural stones exposed to simulated acid rain. *Science of the Total Environment, 412,* 278–285.

Haines, A., Kovats, R. S., Campbell-Lendrum, D., & Corvalan, C. (2006). Climate change and human health: Impacts, vulnerability and public health. *Public Health, 120*(7), 585–596.

Hansen, J., Ruedy, R., Sato, M., & Lo, K. (2010). Global Surface Temperature Change. *Reviews of Geophysics, 48*(4).

IEA (2013). Transition to sustainable buildings: Strategies and opportunities to 2050. *International Energy Agency*.

Kulatunga, U., Amaratunga, D., Haigh, R., & Rameezdeen, R. (2006). Attitudes and perceptions of construction workforce on construction waste in Sri Lanka. *Management of Environmental Quality: An International Journal, 17*(1), 57–72.

Malacrino, J. (2010). *Constructing the ancient world: Architectural techniques of the Greeks and Romans*. Los Angeles: J Paul Getty Museum.

Ozcelik, Y., Careddu, N., & Yilmazkaya, E. (2012). The effects of freeze–thaw cycles on the gloss values of polished stone surfaces. *Cold Regions Science and Technology, 82,* 49.

Pacheco-Torgal, F., & Labrincha, J. A. (2013). The future of construction materials research and the seventh UN millennium development goal: A few insights. *Construction and Building Materials, 40,* 729–737.

Pérez-Lombard, L., Ortiz, J., & Pout, C. (2008). A review on buildings energy consumption information. *Energy and Buildings, 40*(3), 394–398.

Pisello, A. L., Pignatta, G., Castaldo, V. L., & Cotana, F. (2014). Experimental analysis of natural gravel covering as cool roofing and cool pavement. *Sustainability, 6*(8), 4706–4722.

Rosso, F., Pisello, A. L., Franco, C., & Marco, F. (2014). Integrated thermal-energy analysis of innovative translucent white marble for building envelope application. *Sustainability, 6*(8), 5439–5462.

Rosso, F., Jin, W., Pisello, A. L., Ferrero, M., & Ghandehari, M. (2016a). Translucent marbles for building envelope applications: Weathering effects on surface lightness and finishing when exposed to simulated acid rain. *Construction and Building Materials, 108,* 146–153.

Rosso, F., Pisello, A., Jin, W., Ghandehari, M., Cotana, F., & Ferrero, M. (2016b). Cool marble building envelopes: The effect of aging on energy performance and aesthetics. *Sustainability, 8*(8), 753.

Rosso, F., Pisello, A. L., Cotana, F., & Ferrero, M. (2016c). On the thermal and visual pedestrians' perception about cool natural stones for urban paving: A field survey in summer conditions. *Building and Environment, 107,* 198–214.

Santamouris, M. (2014). On the energy impact of urban heat island and global warming on buildings. *Energy and Buildings, 82,* 100–113.

Sleiman, M., Ban-Weiss, G., Gilbert, H. E., François, D., Berdahl, P., Kirchstetter, T. W., & Levinson, R. (2011). Soiling of building envelope surfaces and its effect on solar reflectance—Part I: Analysis of roofing product databases. *Solar Energy Materials and Solar Cells, 95*(12), 3385–3399.

Sleiman, M., Kirchstetter, T. W., Berdahl, P., Gilbert, H. E., Quelen, S., Marlot, L., & Akbari, H. (2014). Soiling of building envelope surfaces and its effect on solar reflectance–Part II: Development of an accelerated aging method for roofing materials. Solar Energy Materials and Solar Cells, 122, 271–281.

UNFCCC (2015). UN Framework Convention on Climate Change.

Urosevic, M., Sebastián-Pardo, E., & Cardell, C. (2010). Rough and polished travertine building stone decay evaluated by a marine aerosol ageing test. *Construction and Building Materials, 24* (8), 1438–1448.

Wyszecki, G., & Stiles, W. S. (2000). *Color science.* 2nd edn. New York [u.a.]: Wiley.

Zöldföldi, J., & Satir, M. (2003). Provenance of the White Marble Building Stones in the Monuments of Ancient Troia. In: G. A. Wagner, E. Pernicka, & H. Uerpmann, (Eds.), *Troia and the troad: Scientific approaches.* Berlin, Heidelberg: Springer Berlin Heidelberg, pp. 203–222.

Chapter 20
Detection of Subsurface Metal Oxidation with Thermal Imaging

Masoud Ghandehari and Alexey Sidelev

Abstract We introduce thermographic imaging as a non-destructive evaluation method for detection of hidden corrosion or delamination of coating on metals or other substrates. A hybrid experimental-numerical technique using long wave, broad band imaging for the standoff and quantitative analysis of the interface is introduced. Time lapsed measurements of surface temperature is carried out, followed by numerical simulation of the corresponding thermal signature. Results of damage detection using thermal imagery were compared with substrate wall thickness measured by a thickness gauge. It is concluded that imaging approach provides measures of metal loss, at levels less than the variations in the metal wall manufacturing tolerance, highlighting corroded areas which would otherwise be undetectable using sensors for measuring metal thickness.

20.1 Introduction

The Federal Highway Administration reported in 2006 that approximately 14% of all bridges in the US are structurally deficient, primarily due to corrosion (FHWA 2006). FHWA also estimated that the indirect costs to the user, due to traffic delays and loss of productivity, are more than ten times the direct cost of corrosion. The direct cost of corrosion for highway bridges was estimated at $8.3 billion in 1998, resulting in $80 billion in costs to the public and the economy. Similarly, in the utilities sector, such as the oil and gas industry, transmission line failures occur primarily because of corrosion (Lozev et al. 2005; Roberge 2008). When considering all sectors including military, manufacturing etc., the total annual direct cost of corrosion to the United States economy, is estimated at 3% of the total Gross

M. Ghandehari (✉)
New York University, Six Metrotech Center, Brooklyn, NY 11201, USA
e-mail: masoud@nyu.edu

A. Sidelev
Parsons, 100 Broadway, New York, NY 10005, USA
e-mail: a.sidelev@gmail.com

M. Ghandehari, *Optical Phenomenology and Applications*,
Smart Sensors, Measurement and Instrumentation 28,
https://doi.org/10.1007/978-3-319-70715-0_20

Domestic Product (GDP) (NACE et al. 2002). Today, this amounts to approximately $580 billion. Considering indirect costs, the total cost of corrosion to the U.S. economy is estimated at about 6% of U.S. GDP, amounting to over $1.16 trillion. Thus, corrosion is one of the main factors responsible for infrastructure failure and represents a huge cost to the economy.

Studies on the costs and hazards associated with infrastructure degradation have brought wide spread media and public attention to the aging of the infrastructure. Reports by the American Society of Civil Engineers (ASCE) have cited inadequate and deferred maintenance as key factors responsible for degraded infrastructure conditions (ASCE 2001, 2005, 2009). One of the first reports on this issue goes back to 1988 in "*Fragile Foundations: A Report on America's Public Works*" (National Council on Public Works Improvement 1988). The Federal Highway Administration (FHWA) reports that the corrosion of steel remains a serious issue resulting in injuries, fatalities, environmental hazards, reduced infrastructure performance, increased maintenance costs and value reduction due to deterioration (FHWA 2006; NACE et al. 2002). Coating performance is a key factor in protection against corrosion. FHWA reported that approximately 40% of the direct corrosion expenses in all sectors was spent on corrosion control and services (FHWA 2006). Meanwhile, the largest expenditure incurred in corrosion prevention and control was spent on organic coatings. A study on protective coatings (Vincent 2004) revealed that 55% of coating failures are caused by bond failure due to corrosion. Methods for effective and non-destructive field inspection of coatings continue to be in great demand. (Maldague 2001; Hellier 2001; U.S. Department of Defense 1989; ASM 1989; Meola et al. 2004; Laursen et al. 2007; Manegold et al. 2009; Louaayou et al. 2008; Kroon and Lary 2003; Liu et al. 2012) and (Suda et al. 1993). The aim of this study is to further the application of Infrared thermography as a non-destructive testing method for corrosion monitoring and quality control of protective coatings. Applications include corrosion detection for structural elements in bridges, storage tanks, above ground pipes, etc. The method naturally applies to targets with relatively large coated surfaces.

20.2 Approach

Experiments using passive and active Infrared thermography were carried out on laboratory specimens. These included coated steel substrate exposed to accelerated degradation. Modeled defects were also made by inserting cavities in the parent steel filled with products of corrosion. Numerical simulations of heat transfer within the specimens was also carried out. The simulation was done using material properties of the coating, the substrate, and the defects. The steel substrate either had laboratory applied coatings or they were factory coated. The coatings applied in-house include spray lacquer, a multi-component protective coating, and tape coating. The factory applied coatings include coal tar epoxy, coal tar enamel, and fusion bonded epoxy. Results for a selected number of these coatings are presented in this chapter.

The coated plates were subjected to cycles of accelerated corrosion. The specimens were periodically imaged using a broadband Infrared camera and an ultrasonic gauge for measuring changes to the metal thickness. A stepped heating approach allowed the detection of relatively deep defects. Thermal measurements were examined along with observed corrosion induced paint delamination and changes to the steel plate thickness by metal loss. The numerical thermodynamic model included all the material properties and the input energy provided by the lamp in the experiments. The model was tested using specimens with controlled embedded cavities and oxides which were subsequently covered by coatings.

20.3 Experiments

20.3.1 Instruments

A Mikron M7500 camera was used, having un-cooled, focal plane micro-bolometer arrays with spectral sensitivity from 8 to 14 μm and a thermal resolution of 0.06 at 30 °C. The camera had a detector density of 320 × 240 pixels. The camera had a fixed lens with a field of view 21 H and 16 V and range from 0.3 m to ∞. Near-Infrared (NIR) and halogen lamps were used as the heat source. The energy generated by a 1000 W light source adequately stimulates the specimens at distance up to 9 m. Thickness gauges were also used to assess metal loss. Figure 20.1 shows the camera and heat source.

Experiments on Coated Steel Plate with Paint Coating
Steel plate with a thickness of 6.35 mm and dimensions 305 mm by 30 mm was sandblasted to white metal and cleaned according to the standard procedures (ASTM 2008; ASTM 2007). The plate was painted with flat white alkyd multi-purpose spray paint manufactured by Sherwin-Williams. A cycle of heated wet/dry and salted conditions were used in order to accelerate the corrosion process.

Fig. 20.1 Camera and light source

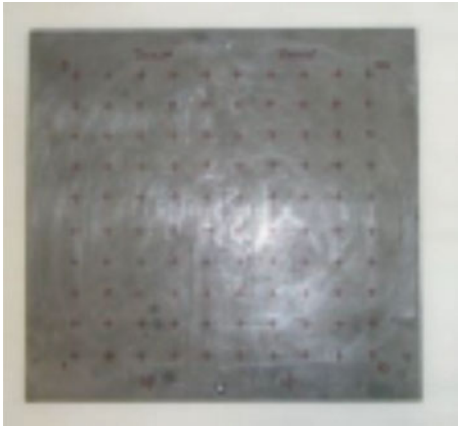

Fig. 20.2 Back side of plate, bare steel with marked points for ultrasonic thickness testing

A typical cycle included a 3% salt solution bath of approximately 4 h, followed by 4 h of drying at elevated temperature (50 °C) using a hot plate in contact with the bare steel surface, followed by 16 h of drying under ambient conditions. The *wet/salt-heat-dry* cycle was carried out 5 days a week. During weekends, the plate was kept at ambient conditions. Every other day the plate was imaged with the infrared camera and the ultrasound thickness gauge. The ultrasound thickness measurements were done on the backside of the plate at marked points shown in Fig. 20.2. The heat source for these tests was a 1000 W halogen NIR lamp placed at a distance of 2 m and thermal input pulse duration ranging from 30 s to 2 min.

Results on Alkyd Paint Coated Steel

There were no signs of surface temperature abnormalities during the first week. The first sign of subsurface corrosion was revealed after 8 days followed by signs of more severe corrosion from day 12 (Fig. 20.3). While at day 8, thermography

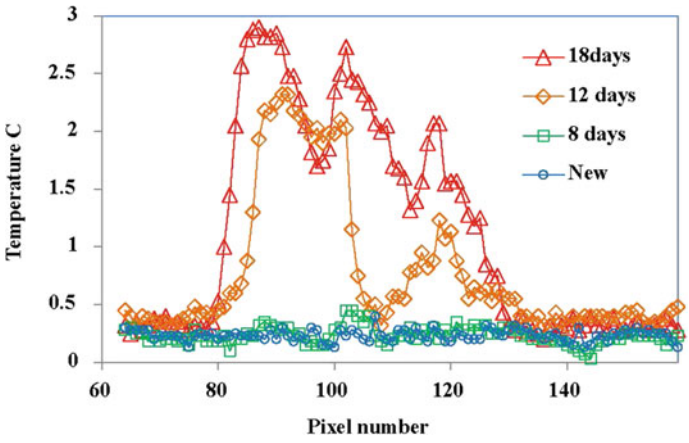

Fig. 20.3 Temperature profile along a line at various levels of coating degradation

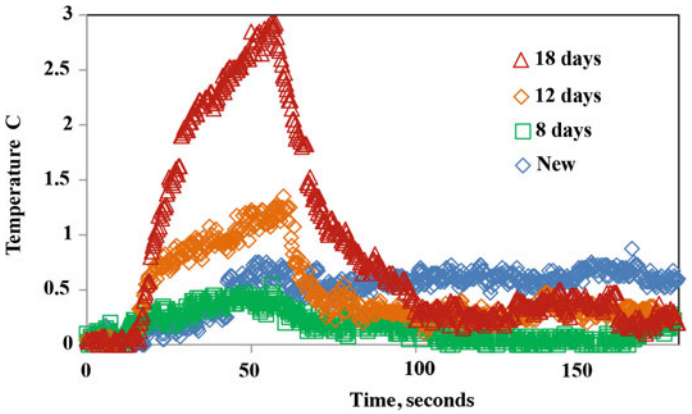

Fig. 20.4 Shows the time response of a location to thermal input at various levels of degradation, using the most severely degraded location

implied signs of subsurface distress, the ultrasound thickness gauge did not pick up any changes to the metal wall thickness. It was assumed that the change in the temperature signal was due to paint disbanding or metal loss due to corrosion, or both. It was therefore concluded that the metal loss, if any, was less than the 0.05 mm resolution of the device. On day 12, the products of corrosion punctured through the paint. Once again, the ultrasound gauge did not register any plate thickness change. On day 16, the paint had significantly dis-bonded from the steel surface, while the ultrasound gauge still did not register a plate thickness change.

Figure 20.3 shows the surface temperature profile along a reference line, at different levels of aging. Note that elevated levels of corrosion, the products of corrosion may migrate away from the interface after the paint layer damage is damaged. Therefore, much of the thermal signature is due to the air gap between delaminated paint and the steel substrate. Figure 20.4 shows the time history response at one point in the delaminated zone, after it was subject to a short heat pulse at the various stages of aging.

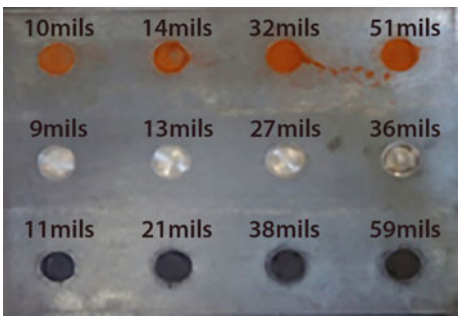

Fig. 20.5 Plate with flat bottom holes to simulate inclusions, specific hole depth indicates various levels of coating degradation

Experiments on Plates with Synthetic Defects

The thermal response observed is a function of thermal conductivity and thickness of the inclusion, whether it is rust or air blisters. It is possible that different types of defects would have the same integrated thermal resistivity depending on their thickness. For example, an air blister or delamination thickness of 0.1 mm would have the same thermal resistivity as 0.5 mm of the metal oxide. Both would create the same surface temperature rise at steady state conditions, after active thermal simulation. In order to uniquely identify and quantify a defect, an independent parameter is needed.

Series of specimens with embedded synthetic inclusions (such as air and oxides and hydroxides of iron) were prepared. The thermal properties of these oxides were evaluated in the laboratory. These tests were done with ¼ steel plates prepared according to the standard procedures (ASTM 2008). The standard requires the steel cleaned down to a shiny level, dust removed and surface wiped with solvent to remove any organic contamination. The surface is then primed and painted according to the manufacturer specifications. After cleaning, one side of the plate was drilled with a 1.25 mm diameter flat bottom milling bit, partially through the metal thickness. These holes were drilled at four depths of 10, 20, 40 and 60 mils, repeated in three rows (Fig. 20.5). The top row was filled with Fe_2O_3; the bottom row with Fe_3O_4, and the middle row was left empty. All holes were coated by 1 mm thick masking tape serving as a paint layer.

The steel plate thickness was measured using the ultrasound thickness gauge, and defect depth was calculated by subtracting the thickness of the plate at the recess from the average plate thickness. The plate was imaged using the infrared camera from a distance of 1 m in both steady state (Fig. 20.6) and active ramp heating (Fig. 20.7). The heat step lasted for 2 min and 45 s. The heat source was a 400 W T3 halogen bulb placed at 1 m distance. Samples were imaged during the heat stimulation and cooling at 3 s intervals.

Results for the Simulated Inclusions

Results of thermal imaging of the synthetic inclusions show reasonable temperature intensities with respect to varying size and type of defects (Fig. 20.7). Temperature fluctuations along a horizontal line through centerline of the holes are shown in the Figure. The inclusions with the iron oxides show higher temperature compared to

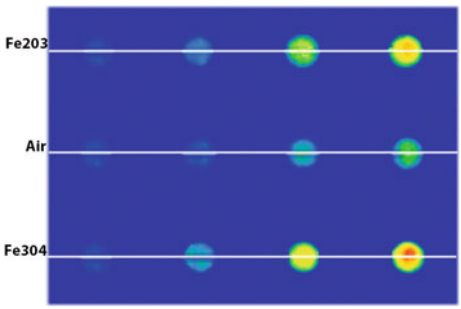

Fig. 20.6 Infrared image of plate after heating

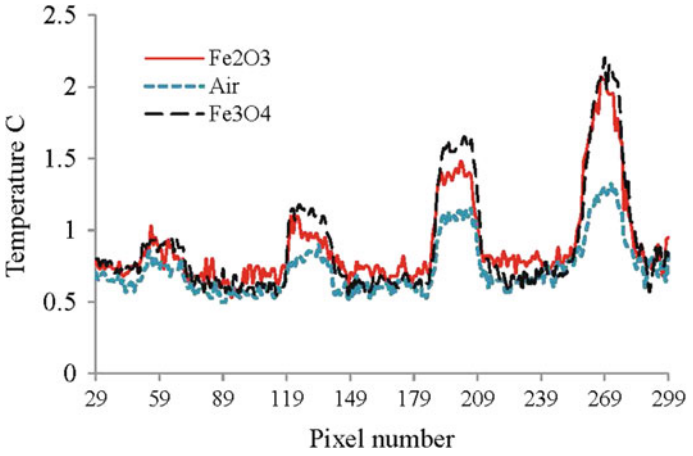

Fig. 20.7 Surface temperature profile on a line along each row

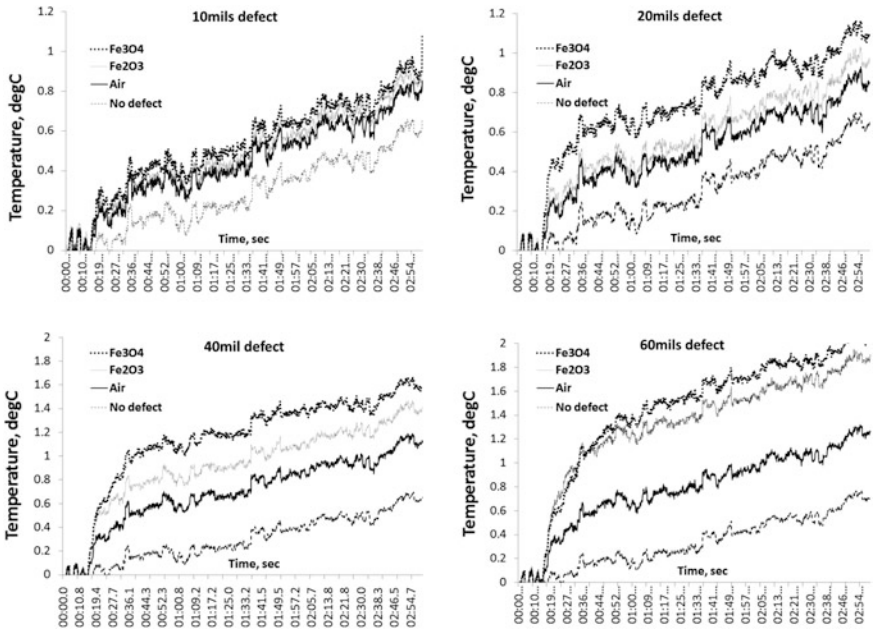

Fig. 20.8 Temperature histories of substrate defects during heating cycle during heating cycle

the areas with air inclusions. This is due to the lower convective cooling in the oxide compared to the air-filled cavity.

This surface temperature history during a heating cycle is shown in Fig. 20.8. The results indicate that in most cases the slope of the temperature rise may be used to differentiate between the subsurface materials, in this case air blister and metal

oxide. The rate of increase in the surface temperature during the surface heating correlates to the heat capacity of the defect. IR cameras with high frame rates and thermal resolution will be capable of providing reliable data to identify these defect properties.

20.3.2 Numerical Simulation

A numerical model was developed to simulate the thermodynamic response of the coating-inclusion-substrate composite. The model used COMSOL software's heat transfer module using automated meshing algorithm. Side boundaries for the plate were assigned as perfectly insulated (no heat transfer). Bottom and top surface were free to achieve thermal equilibrium. The thermal properties of the steel, coating and inclusion are based on the software material library. Properties of iron oxides were obtained from the literature (Cornell and Schwertmann 2006; Tannhauser 1962).

$$\mathrm{Fe_2O_3(Hematite)\ has\ thermal\ conductivity}\ \boldsymbol{k} \approx 1.1\frac{\boldsymbol{W}}{\boldsymbol{m}\cdot\boldsymbol{K}} \tag{20.1}$$

$$\mathrm{Fe_3O_4(Magnetite)\ has\ thermal\ conductivity}\ \boldsymbol{k} \approx 1.6\frac{\boldsymbol{W}}{\boldsymbol{m}\cdot\boldsymbol{K}} \tag{20.2}$$

$$\mathrm{Fe_xO(W\ddot{u}stite)\ has\ thermal\ conductivity}\ \boldsymbol{k} \approx 0.6\frac{\boldsymbol{W}}{\boldsymbol{m}\cdot\boldsymbol{K}} \tag{20.3}$$

The effective thermal conductivity for samples are in the range between the lower limit by Maxwell-Eucken model and the upper limit as defined by the Effective Medium Theory (EMT) model (Carson et al. 2005). Here, effective properties include the external and internal porosity, compactness/density, and moisture. The thermal conductivity of corrosion oxides depends on the type of iron oxide and compactness of rust in bulk. Density of iron oxide crystals vary insignificantly (Tables 20.1 and 20.2). Usual expansion coefficients of corrosion products range from 2 to 4. Calculated values of porosity based on specific and bulk densities of corrosion products are shown.

Table 20.1 Range of effective thermal conductivity based on porosity for different iron oxides

Oxide	Thermal conductivity, W/m K	
	At 60% porosity	At 40% porosity
Fe_2O_3 (Hematite)	0.070	0.673
Fe_3O_4 (Magnetite)	0.071	0.472
Fe_xO (Wüstite)	0.067	0.270

Table 20.2 Iron oxide crystal density

Iron oxide	Crystal density (kg/m^3)	Iron oxide bulk density (kg/m^3)	Porosity (%)
Fe_2O_3 (Hematite)	5200	2400–2800	46.2–53.9
Fe_3O_4 (Magnetite)	5160	2600–3100	40–49.70
Fe_xO (Wüstite)	5460	2300–2700	50.5–57.9

We assumed corrosion products porosity to be 55% and the effective thermal conductivity of the products of corrosion in the experiments to be

$$k_{corrosion} = 0.11 \frac{W}{m \cdot K} \tag{20.4}$$

Assuming a large surface area, the 2-D numerical model consisted of 6 mm thick steel plate with the recess dimensions and spacing similar to the experiment values, and coating thickness of 0.25 mm (Fig. 20.9).

The incident heat onto the surface was estimated based on the observed data from the experiment. The simulated heating step of 2 min and 45 s was used with an average intensity of 85 W/m^2. Air gap conductivity was estimated based on known literature (Çengel and Klein 2007), plus a multiplier to result in thermal resistivity equal to that obtained from the experiments conducted.

The steel plate with defect inclusions and the protective coating was considered as a conduction model. The front and the back surfaces of the specimen are subject to natural convection and heat radiation, while the front surface is subject to additional incident heat flux. The simulated incident heat flux profile on the surface was assigned a Gaussian shape to replicate the non-uniform heating intensity radiated from the source. Some adjustments to the thermal conductivity coefficient and specific heat capacity of the coating were made to account for the effect of the adhesive backing in the tape coating. Summary of material properties used in the numerical model are shown in Table 20.3 (Çengel and Klein 2007; Carson et al. 2005; Çengel and Boles 1995; Howell and Siegel 2002).

The effective thermal conductivity coefficient for air was used to calibrate the correlation between numerical calculations and experimental results. The difference between the effective and actual conductivity compensates for the effect of convection and radiative heat transfer within the blister. For practical purposes, the heat transfer through the air gap was assumed as a simple conduction element in the model (i.e. not including convection and radiation heat transfer).

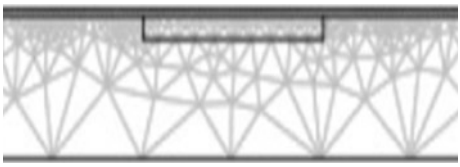

Fig. 20.9 2-D finite element model of coated plate

Table 20.3 Materials properties used in the simulation

Material	Density (kg/m^3)	Thermal conductivity coefficient (W/m K)	Specific heat capacity (W/kg K)	Surface emissivity
Steel	7850	44.5	450	0.95
Coating	1000	0.05	2000	0.98
Air blister	1.188	0.1	1007	–

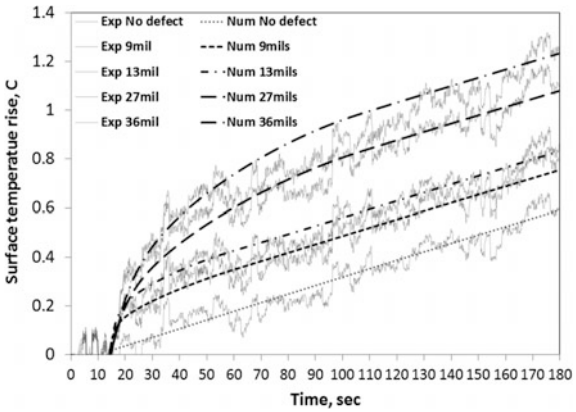

Fig. 20.10 Experimentally measured temperature change for air inclusion during heating cycle; numerical simulation is shown by dashed lines

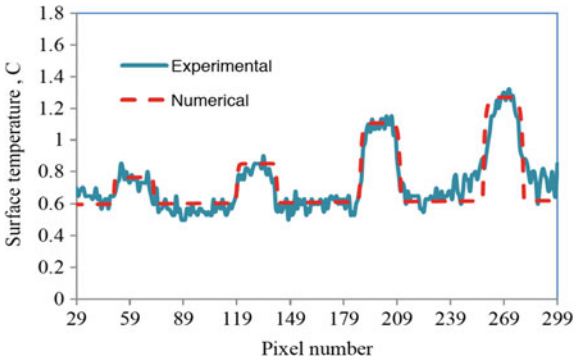

Fig. 20.11 Surface temperature along line through air blisters

The numerical simulation of the dynamic response of the composite with air inclusion is shown in Fig. 20.10. The comparison of the experiment with the simulation is shown. Results of the spatial distribution of static temperature profile for the same data are also in shown Fig. 20.11.

These results refer to the surface temperature at the end of the heat pulse duration. Correlation of surface temperature dynamics and the static state between

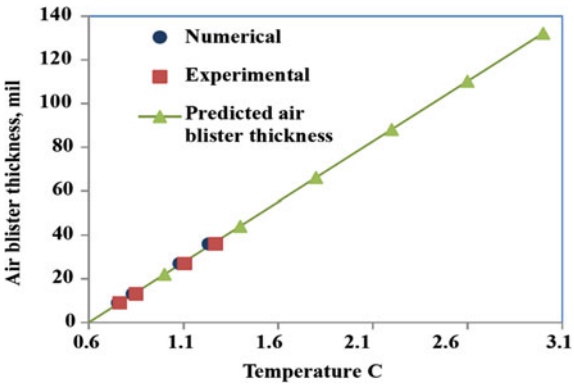

Fig. 20.12 Surface temperature increase versus air blister thickness

the numerical simulation and experimental data are reasonable. Results of the experimental and numerically obtained relations of surface temperature differential and air gap (blister) thickness is shown in Figs. 20.11 and 20.12.

20.4 Conclusion

A hybrid experimental-numerical approach was used for the quantitative analysis of subsurface corrosion in coated metals. Infrared imaging was used to distinguish air blisters versus corrosion beneath coatings on steel. Specimens included laboratory coated specimens subject to accelerated corrosion. The laboratory test was used to calibrate a finite element numerical model for heat transfer. The model was then used to distinguish subsurface corrosion as air blister versus oxides of iron. The comparison of experimental data versus numerical simulation show good prediction of the relation of surface temperature profiles to inclusion beneath coatings. It was further observed that in most practical cases, the variations in the metal wall thickness is too large to allow absolute value measurements of wall thickness as decision point for detection of early onset of corrosion.

References

ASCE. (2001). *2001 Report Card for America's Infrastructure.* America's Infrastructure Advisory Council, ASCE.

ASCE. (2005). *2005 Report Card for America's Infrastructure.* America's Infrastructure Advisory Council, ASCE.

ASCE. (2009). *2009 Report Card for America's Infrastructure*. America's Infrastructure Advisory Council, ASCE.

ASM. (1989). *Nondestructive evaluation and quality control*. Materials Park: American Society for Metals International.

ASTM. (2008). *Standard practice for use of pictorial surface preparation standards and guides for painting steel surfaces*. 2008 ASTM.

ASTM Intl. (2007). *Standard guide for painting inspectors (metal substrates)*. 2007 ASTM.

Carson, J. K., Lovatt, S. J., Tanner, D. J., & Cleland, A. C. (2005). Thermal conductivity bounds for isotropic, porous materials. *International Journal of Heat and Mass Transfer, 48*(11), 2150–2158.

Çengel, Y. A., & Boles, M. A. (1995). Thermodynamics: an engineering approach, second edition. *Applied Mechanics Reviews, 48*(5), pp. B66.

Çengel, Y. A., & Klein, S. A. (2007). *Heat and mass transfer.* 3rd edn. Boston [u.a.]: McGraw-Hill.

Cornell, R. M., & Schwertmann, U. (2006). *The Iron Oxides. 2* (Aufl ed.). US: Wiley-VCH.

FHWA (2006). *Status of the nation's highways, bridges, and transit: Conditions and performance*. Report to Congress.

Hellier, C. J. (2001). *Handbook of nondestructive evaluation.* New York [u.a.]: McGraw-Hill.

Howell, J. R., & Siegel, R. (2002). *Thermal radiation heat transfer.* 4th edn. New York; London: Taylor & Francis.

Kroon, D. H., & Lary, J. T. (2003). External corrosion of water piping systems—Causes and solutions. *New pipeline technologies, security, and safety.* pp. 776–785.

Laursen, P., Mergelas, B., Passaro, P., & Atherton, D. (2007). Inline assessment of transmission pipelines in the oil and gas and water sectors. *Pipelines, 2007,* 1–7.

Liu, Z., Genest, M., & Krys, D. (2012). Processing thermography images for pitting corrosion quantification on small diameter ductile iron pipe. *NDT and E International, 47,* 105–115.

Louaayou, M., Naït-Saïd, N., & Louai, F. Z. (2008). 2D finite element method study of the stimulation induction heating in synchronic thermography NDT. *NDT and E International, 41* (8), 577–581.

Lozev, M. G., Smith, R. W., & Grimmett, B. B. (2005). Evaluation of methods for detecting and monitoring of corrosion damage in risers. *Journal of Pressure Vessel Technology, 127*(3), 244.

Maldague, X. P. V. (2001). *Theory and practice of infrared technology for nondestructive testing.* New York [u.a.]: Wiley.

Manegold, W., Nishenko, S., Lee, C., & Hitchcock, C. (2009). Pacific gas and electric natural gas system preparations for a future Hayward earthquake. *TCLEE, 2009,* 1–12.

Meola, C., Carlomagno, G. M., Squillace, A., & Giorleo, G. (2004). The use of infrared thermography for nondestructive evaluation of joints. *Infrared Physics & Technology, 46,* 93–99.

NACE Intl., FHWA, Koch, G. H., & CC Technology Laboratories (2002). *Corrosion cost and preventive strategies in the United States.* Turner-Fairbank Highway Research Center.

National Council on Public Works Improvement, (U.S.) (1988). *Fragile foundations: A report on America's public works: final report to the President and the Congress*. 1988, United States.

Roberge, P. R. (2008). *Corrosion engineering.* 1st edn. New York [u.a.]: McGraw-Hill.

Suda, K., Misra, S., & Motohashi, K. (1993). Corrosion products of reinforcing bars embedded in concrete. *Corrosion Science, 35*(5), 1543–1549.

Tannhauser, D. S. (1962). Conductivity in iron oxides. *Journal of Physics and Chemistry of Solids*.

U.S. Department of Defense (1989). Nondestructive active testing techniques for structural composites. *Military handbook: MIL-HDBK-793(AR).* Vincent, L. D., 2004. *The protective coating user's handbook.*

Chapter 21
Sensing Metal Oxidation with Chemical Probes

Gamal Khalil, Christian Brückner and Masoud Ghandehari

Abstract The annual cost of corrosion in the US is estimated at roughly 6% of the gross national product. According to a study by the Federal Highway Administration (FHWA 2006), the annual direct cost of corrosion in the transportation infrastructure category alone (highway bridges, waterways and ports, hazardous materials storage facilities, electrical utilities, airports, and railroads) is estimated at tens of billions USD and higher by more recent estimates (Kutz 2012; Nace et al. 2002; Jackson 2017). In general, the costs of repair and remediation to the civil infrastructure are higher than necessary when maintenance schedules are not based on a clear understanding of the onset of damage (for example corrosion), and the degree to which deterioration has occurred, for example, internal cracking. Chemical sensors can play a particularly important role in early detection of deterioration. In corrosion, the processes generally start by releasing ionic components that can be sensed in advance of the appearance of physical signs of damage. This chapter highlights the development of chemical sensors for the detection of iron and zinc.

21.1 Introduction

Addressing the issue of infrastructure degradation due to corrosion requires the ability to measure the extent of oxidation, which can be used to predict the service life of the critical components, and used to plan maintenance and prediction

G. Khalil
Department of Aeronautics & Astronautics, University of Washington,
Box 352250, Seattle, WA 98195, USA
e-mail: gekhalil@gmail.com

C. Brückner
Department of Chemistry, University of Connecticut, Storrs, CT 06269, USA
e-mail: c.bruckner@uconn.edu

M. Ghandehari (✉)
New York University, Six Metrotech Center, Brooklyn, NY 11201, USA
e-mail: masoud@nyu.edu

M. Ghandehari, *Optical Phenomenology and Applications*,
Smart Sensors, Measurement and Instrumentation 28,
https://doi.org/10.1007/978-3-319-70715-0_21

strategies. The costs for the development and installation of sensing tools for detection of early onset of corrosion damage will be easily offset by the reduction in maintenance costs. Information generated by corrosion monitoring tools also provides several things: a phenomenological understanding of the onset, process and acceleration of damage due to corrosion, a better understanding of the rates of aging and transport processes, guidance for better infrastructure design and for optimizing remedial strategies. The corrosion monitoring technology discussed in this chapter is based on a sensor molecule for detection of metal ions, particularly iron and zinc. When integrated with optical waveguides the sensor may be embedded for monitoring the subsurface environment and materials in situ.

21.2 Sensor Molecules for Infrastructure Corrosion Monitoring

Figure 21.1 describes a typical timeline for a degrading infrastructure. Most deterioration processes in materials involve deleterious chemical reactions, rate controlled by ionic/molecular transport, which produce micro-structural changes in materials that degrade its physical properties. Deterioration of reinforced concrete is an example where the ingress of moisture, particularly acids in soft water and chlorides, leads to the corrosion of steel reinforcing bars.

Rust from steel reinforcing bars is a formation of various iron oxides such as FeO, FeO(OH), Fe_2O_3, or Fe_3O_4. There are a number of well-established prevention and remedial strategies used to protect reinforced concrete, (Böhni 2005; Cramer et al. 2002; Gjørv 2014; Jasbir et al. 2016). Application of moisture

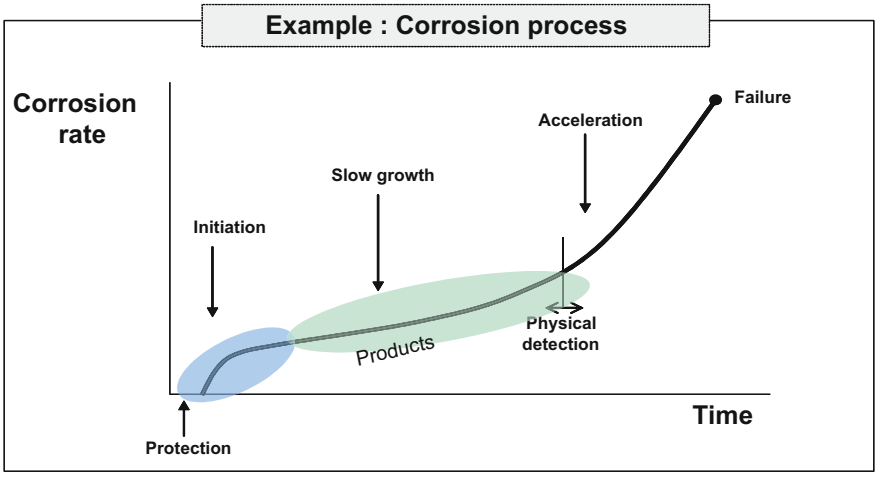

Fig. 21.1 A time line of a series of phases during the corrosion

barriers, implementation of cathodic protection in the form of sacrificial anodes, re-alkalization, and chloride extraction are well known.

In the early stages, deterioration of materials is localized and relatively inexpensive to remediate. Technologies that provide early warning of this aging process—such as the appearance of iron ions—would enable the implementation of timely prevention strategies and remedial action where needed, resulting in a greater service life for the facilities and substantial cost savings in infrastructure maintenance.

Sensors based on optically detectable signals are particularly desirable, since they eliminate the need for wires and electrical leads, which are also prone to corrosion. For example, an optical wave guide can be used for sensing of oxides when integrated with sensor molecules. Such optical sensors can be used for in situ detection of corrosion in steel-reinforced concrete, pre-stressed and post-tension concrete, bridge wires, bridge cables, utility pipelines and fuel storage containers.

21.3 Sensor Molecules for Corrosion Detection of Iron and Zinc

Sensor molecules have long been used in biomedical applications and more recently have proven utility in environmental applications. For example, porphyrins highlighted in this chapter have widespread applications in analytical chemistry (Biesaga et al. 2000). For the purpose of this chapter we discuss the utility of sensor molecules in applications to infrastructure monitoring and early detection of corrosion; one for steel rebar and other for zinc coated reinforcing steel bars. The highlighted sensor molecules are chosen for their optical response in the presence of corrosion products, whether iron or dissolved zinc.

Porphyrins and similar macrocyclic compounds readily form into complexes with a number of metals, such as iron and zinc, and show corresponding diagnostic changes in their optical properties (Buchler 1978). Many porphyrins also conform to the strict durability requirements in typical applications to civil infrastructure monitoring. Thus, porphyritic indicators can be used for detection of dissolution of the base metal structure such as steel, as well for zinc-based galvanized coatings.

Absorption properties of metal porphyrins depend on the particular metal, its oxidation state, and its electronic configuration (Buchler 1978; Gouterman 1978). The metal may possess a closed shell (diamagnetic) or open shell (paramagnetic) electron configuration. The optical spectra of iron porphyrins and their electronic structure have been studied extensively for their important role in biology. Generally, iron is bound to porphyrins only readily in their +II oxidation states but once chelated to a porphyrin, the iron can assume +II and +III and, under strongly oxidizing conditions, higher oxidation states, both in different coordination geometries and high/low spin states.

Iron and steel undergo an electrochemical corrosion process in the presence of water and oxygen that produces rust, liberating soluble iron (II) species in the

process. Chelation of these ions by porphyrins will produce iron porphyrins with distinct absorption spectra. Free base (non-metallated) porphyrin in the presence of Fe_2+ involves the following equilibrium equation: (Buchler 1978):

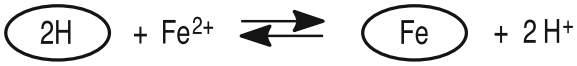

(21.1)

The chelation process usually results in spectral changes and a reduction in the number of absorption bands (Fig. 21.2). In general, ferric iron porphyrin absorption spectra have well defined bands especially in the infra-red region, one which can be used for diagnostic purposes. Similarly, N-methyl protoporphyrin IX, mesotetrakis (N-methyl-4-pyridyl) porphyrin tetratosylate, and mesotetra (n-propyl)—porphyrin produce notable spectral changes in the presence of ferrous chloride (Si-Nae and Khalil 2006).

Figure 21.2 also displays the spectral changes when free base *meso*-tetraphenylporphyrin (TPP) is coordinated to zinc (in the form of $ZnCl_2$), forming ZnTPP. Notice the disappearances of the 515 nm and 650 nm bands from the H_2TPP spectrum and the appearance of a strong 560 nm band in the ZnTPP spectrum. These distinct optical changes can be utilized for corrosion monitoring in processes that liberate zinc ions. Free base porphyrin in the presence of zinc shown in the equilibrium Eq. 21.2 are characterized by very rapid kinetics:

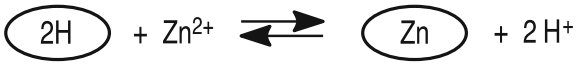

(21.2)

The absorbance properties of zinc porphyrin are used for early detection of the environmental conditions that lead to metal corrosion (Bentur et al. 1997; Kutz 2012). The sensor molecule in the form of a free base porphyrin can be embedded

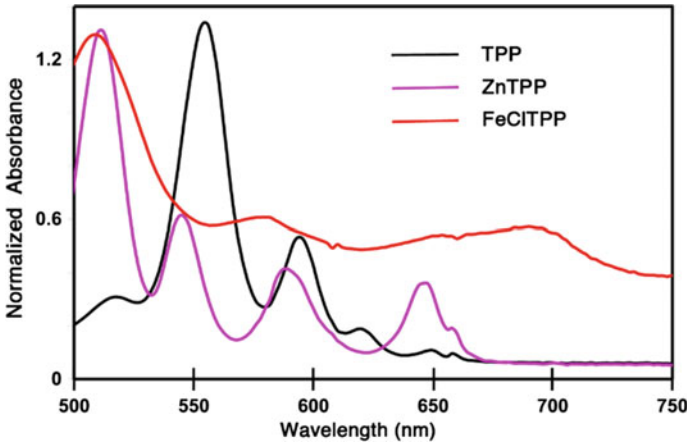

Fig. 21.2 UV-visible absorption spectra (in CH_2Cl_2) associated with the chelation process with normalized absorption units for TPP starting at 0.25, ZnTPP at 0.7 and FeCLTPP at 1.2

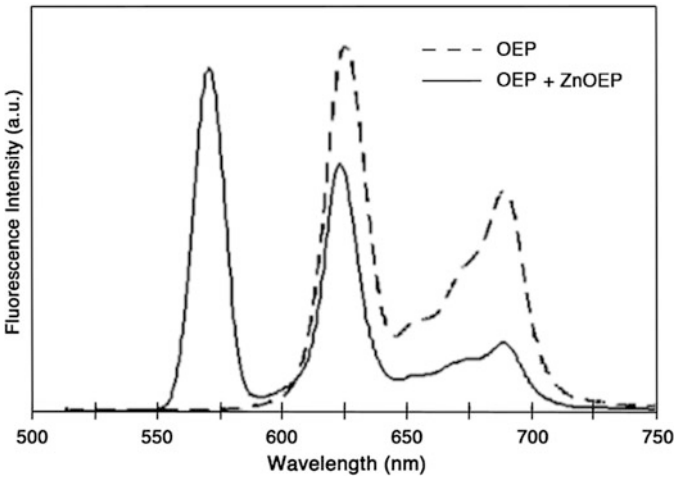

Fig. 21.3 Emission spectra of pure OEP after the addition of Zn^{2+}, forming also ZnOEP, $\lambda_{excitation}$ = 400 nm

in an appropriate zinc ion-transducing polymer, and used as a sensor compound. This compound can be combined with an optical fiber and used for remote sensing.

The emission of free base porphyrins also changes upon metal chelation. Figure 21.3 shows the fluorescence emission spectral changes of free base octaethylporphyrin (OEP) before and after the addition of $ZnCl_2$, forming ZnOEP. Notice the appearances of a 570 nm band when zinc was added. The determination of the intensity ratio of the 570 nm band and 625 nm band will provide a measure for the zinc concentration. In this example, both dyes A and B are emitting species and use of their emission can be done in two ways. We can use two excitation wavelengths, λ_1 and λ_2, that are absorbed differently by A and B and monitor an emission wavelength λ_3 that is strongly emitted by both species. Alternatively, we can use an exciting wavelength λ_1 that is strongly absorbed by both A and B and monitor an emission at λ_2 that is strongly emitted by A but not B, and an emission at λ_3 that is strongly emitted by B but not A.

In applications where a metal (such as iron) is covered by zinc or zinc-rich coatings, luminescent dyes with strong optical signals can be used to directly monitor the dissolution of zinc. Figure 21.4 below shows results of zinc detection using fluorescent imaging of two dyes, free base OEP and acetylacetatepyrene (AcAcpy). Results clearly show the color differences of the dyes in the absence and presence of zinc ions. Other fluorescent chemosensor dyes for zinc are also known. Examples include: TSQ (*N*-(6-methoxy-8-quinolyl)-*p*-toluenesulfonamide), its derivative Zinquin (2-methyl-8-*p*-toluenesulfonamido-6-quinolyloxy acetic acid), dansylamidoethylcyclen and acetylacetatepyrene (Kimura and Koike 1998; Valeur and Leray 2000). Likewise, a number of other optical sensor molecules for iron have been reported (Sahoo et al. 2012; Faizi et al. 2016).

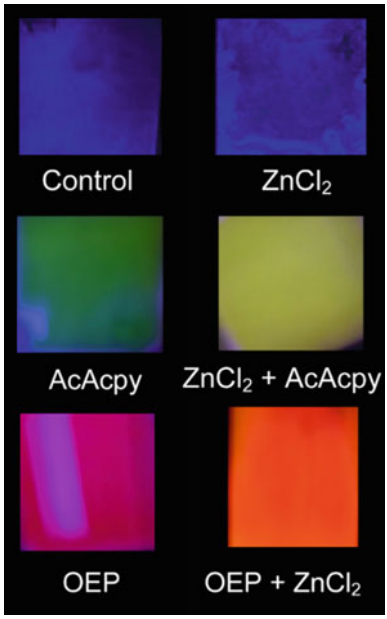

Fig. 21.4 Luminescence images of 1 in. square aluminum plates treated with the compounds indicated. Image adopted from (Chin and Khalil 2004)

21.4 Optical Measurements

The remarkable growth in photonics imaging in the past decade has contributed immensely to developments in chemical sensing. The successful employment of sensors in general relies on accurate measurement of changes in the absorption and or luminescent signals, which in turn requires careful control of the placement of the light sources and detectors, whether is for surface imaging or for embedded applications using optical waveguides. To offset these variables, dual luminophore methodologies were developed. To take full advantage of a dual-luminophore approach, simultaneous signal at two emission wavelengths can be used. Experiments shown in Fig. 21.4 were carried out using an image multiplexer. This device uses a lens that incorporates an internal beam splitter prism and two mirrors, thus taking one image and splitting them into two. The two images are then passed through bandpass filters and refocused onto a single camera CCD chip. In this way, the emission of light from the dual luminophore can be observed on two channels, one for corrosion sensitive luminophore, and the other for the reference luminophore. In the case of the optical fiber sensing, a simple spectrometer is adequate.

In both the open space and embedded applications, the sensor compound can be illuminated with an LED device, simultaneously exciting both luminophores. A number of possible instrumental setups can be developed which would be suitable for applications to infrastructure corrosion monitoring.

21.5 Conclusion

This chapter presented initial development of preparation of sensor molecules for early detection of oxidation. The optical signals for the detection iron and zinc ions show strong spectral signatures in wavelength range from 500 to 750 nm, pointing to opportunities for detection of steel corrosion and dissolution of galvanized protective coatings. Subsurface applications can include the use of optical fibers with embedded sensor molecules at the distal end.

References

Bentur, A., Diamond, S., & Berke, N. (1997). *Steel corrosion in concrete: Fundamentals and civil engineering practice.* Taylor & Francis.

Biesaga, M., Pyrzyńska, K., & Trojanowicz, M. (2000). *Porphyrins in analytical chemistry. A review.* England: Elsevier B.V.

Böhni, H. (2005). *Corrosion in reinforced concrete structures*. Cambridge: Woodhead Publishing.

Buchler, J. W. (1978). Synthesis and properties of metalloporphyrins. In: D. Dolphin (ed.), *The Porphyrins.* New York: Acedemic Press, pp. 389–483.

Chin, A., & Khalil, G. (2004) Senior Project Chemistry Report, University of Washington.

Cramer, S. D., Covino, B. S., Bullard, S. J., Holcomb, G. R., Russell, J. H., Nelson, F. J., et al. (2002). Corrosion prevention and remediation strategies for reinforced concrete coastal bridges. *Cement & Concrete Composites, 24*(1), 101–117.

Faizi, M. S. H., Gupta, S., Mohan, K. V., Jain, V. K., & Sen, P. (2016). Highly selective visual detection of Fe3+ at ppm level. *Sensors and Actuators B: Chemical, 222,* 15–20.

FHWA (2006). Status of the nation's highways, bridges, and transit: Conditions and performance. Report to Congress.

Gjørv, O. E. (2014). *Durability design of concrete structures in severe environments.* CRC Press.

Gouterman, M. (1978). Optical spectra and electronic structure of Porphyrins and related ring. In: D. Dolphin (ed.), *The Porphyrins* (pp. 1–165). New York: Academic Press.

Jackson, D. (2017)-last update. Cost of corrosion annually in the US over $1.1 trillion in 2016. Available: www.g2mtlabs.com/corrosion/cost-of-corrosion/.

Jasbir, N. P., Andre, C., Haleh, S., & Bozena, K. (2016). Adaptive corrosion protection system using continuous corrosion measurement, parameter extraction, and corrective loop. *International Journal of Corrosion, 2016,* 1–11.

Kimura, E., & Koike, T. (1998). Recent development of zinc-fluorophores. *Chemical Society Reviews, 27*(3), 179–184.

Kutz, M. (2012). *Handbook of environmental degradation of materials.* 2nd edn. Amsterdam [u.a.]: Elsevier, William Andrew.

NACE International, FHWA, Koch, G. H., & CC Technology Laboratories (2002). *Corrosion cost and preventive strategies in the United States.* Turner-Fairbank Highway Research Center.

Sahoo, S. K., Sharma, D., Bera, R. K., Crisponi, G., & Callan, J. F. (2012). Iron(iii) selective molecular and supramolecular fluorescent probes. *Chemical Society Reviews, 41*(21), 7195–7227.

Si-Nae, K., & Khalil, G. (2006) Senior Project Chemistry Report, University of Washington.

Valeur, B., & Leray, I. (2000). Design principles of fluorescent molecular sensors for cation recognition. *Coordination Chemistry Reviews, 205*(1), 3–40.